CUMULATIVE DISSERTATION

Cosmic-Ray Neutron Sensing for the estimation of soil moisture

From the atmosphere to the near-surface and to larger depths

by Daniel Rasche, M.Sc.

A thesis presented for the degree
doctor rerum naturalium (Dr. rer. nat.)

in the academic discipline of
hydrology

Submitted to the
Faculty of Science, Institute of Environmental Science and Geography,
University of Potsdam, Germany

Prepared at the
Department: Geosystems, Section: Hydrology,
Helmholtz Centre Potsdam - GFZ German Research Centre for Geosciences

Submitted: 23.01.2024
Defended: 02.05.2024

Referees:

Prof. Dr. Andreas Güntner

Faculty of Science, Institute of Environmental Science and Geography,
University of Potsdam, Germany

Department: Geosystems, Section: Hydrology,
Helmholtz Centre Potsdam - GFZ German Research Centre for Geosciences

Dr. Theresa Blume

Department: Geosystems, Section: Hydrology,
Helmholtz Centre Potsdam - GFZ German Research Centre for Geosciences

Prof. Dr. Peter Dietrich

Faculty of Science, Department of Geoscience, Center for Applied Geoscience,
University of Tübingen, Germany

Department of Monitoring and Exploration Technologies,
Helmholtz Centre for Environmental Research – UFZ Leipzig, Germany

Published online on the
Publication Server of the University of Potsdam:
https://doi.org/10.25932/publishup-63646
https://nbn-resolving.org/urn:nbn:de:kobv:517-opus4-636465

Summary

Water stored in the unsaturated soil as soil moisture is a key component of the hydrological cycle influencing numerous hydrological processes including hydro-meteorological extremes. Soil moisture influences flood generation processes and during droughts when precipitation is absent, it provides plant with transpirable water, thereby sustaining plant growth and survival in agriculture and natural ecosystems.

Soil moisture stored in deeper soil layers e.g. below 100 cm is of particular importance for providing plant transpirable water during dry periods. Not being directly connected to the atmosphere and located outside soil layers with the highest root densities, water in these layers is less susceptible to be rapidly evaporated and transpired. Instead, it provides longer-term soil water storage increasing the drought tolerance of plants and ecosystems.

Given the importance of soil moisture in the context of hydro-meteorological extremes in a warming climate, its monitoring is part of official national adaption strategies to a changing climate. Yet, soil moisture is highly variable in time and space which challenges its monitoring on spatio-temporal scales relevant for flood and drought risk modelling and forecasting.

Introduced over a decade ago, Cosmic-Ray Neutron Sensing (CRNS) is a non-invasive geophysical method that allows for the estimation of soil moisture at relevant spatio-temporal scales of several hectares at a high, subdaily temporal resolution. CRNS relies on the detection of secondary neutrons above the soil surface which are produced from high-energy cosmic-ray particles in the atmosphere and the ground. Neutrons in a specific epithermal energy range are sensitive to the amount of hydrogen present in the surroundings of the CRNS neutron detector. Due to same mass as the hydrogen nucleus, neutrons lose kinetic energy upon collision and are subsequently absorbed when reaching low, thermal energies. A higher amount of hydrogen therefore leads to fewer neutrons being detected per unit time. Assuming that the largest amount of hydrogen is stored in most terrestrial ecosystems as soil moisture, changes of soil moisture can be estimated through an inverse relationship with observed neutron intensities.

Although important scientific advancements have been made to improve the methodological framework of CRNS, several open challenges remain, of which some are addressed in the scope of this thesis. These include the influence of atmospheric variables such as air pressure and absolute air humidity, as well as, the impact of variations in incoming primary cosmic-ray intensity on observed epithermal and thermal neutron signals and their correction. Recently introduced advanced neutron-to-soil moisture transfer functions are expected to improve CRNS-derived soil moisture estimates, but potential improvements need to be investigated at study sites with differing environmental conditions. Sites with strongly heterogeneous, patchy soil

moisture distributions challenge existing transfer functions and further research is required to assess the impact of, and correction of derived soil moisture estimates under heterogeneous site conditions. Despite its capability of measuring representative averages of soil moisture at the field scale, CRNS lacks an integration depth below the first few decimetres of the soil. Given the importance of soil moisture also in deeper soil layers, increasing the observational window of CRNS through modelling approaches or in situ measurements is of high importance for hydrological monitoring applications.

By addressing these challenges, this thesis aids to closing knowledge gaps and finding answers to some of the open questions in CRNS research. Influences of different environmental variables are quantified, correction approaches are being tested and developed. Neutron-to-soil moisture transfer functions are evaluated and approaches to reduce effects of heterogeneous soil moisture distributions are presented. Lastly, soil moisture estimates from larger soil depths are derived from CRNS through modified, simple modelling approaches and in situ estimates by using CRNS as a downhole technique. Thereby, this thesis does not only illustrate the potential of new, yet undiscovered applications of CRNS in future but also opens a new field of CRNS research. Consequently, this thesis advances the methodological framework of CRNS for above-ground and downhole applications. Although the necessity of further research in order to fully exploit the potential of CRNS needs to be emphasised, this thesis contributes to current hydrological research and not least to advancing hydrological monitoring approaches being of utmost importance in context of intensifying hydro-meteorological extremes in a changing climate.

Zusammenfassung
(in allgemeinverständlicher Sprache)

Wasser, das als Bodenfeuchte in der ungesättigten Bodenzone gespeichert ist, beeinflusst zahlreiche hydrologische Prozesse. Sie ist von großer Bedeutung für hydrometeorologische Extremereignisse, da sie sowohl die Prozesse zur Entstehung von Hochwassereignissen beeinflusst als auch pflanzenverfügbares Wasser in Dürreperioden bereitstellt, in denen Regen ausbleibt. Vor allem Bodenfeuchte in tieferen Schichten des Bodens wird zum Beispiel durch die geringere Dichte an Pflanzenwurzeln langsamer aufgenommen und reduziert. Die Bodenfeuchte in diesen tieferen Schichten kann daher vor allem in Trockenperioden zum Überleben der Pflanzen in landwirtschaftlichen Gebieten und natürlichen Ökosystemen beitragen. Im Kontext hydro-meteorologischer Extremereignisse kommt der Bodenfeuchte so eine besondere Bedeutung zu und ist daher Teil nationaler Monitoring- und Anpassungsstrategien an sich verändernde Klimabedingungen.

Cosmic-Ray Neutron Sensing (CRNS) ist ein geophysikalisches Messverfahren, das natürlich vorkommende Neutronen aus kosmischer Strahlung zur Bodenfeuchtebestimmung nutzt. Die Intensität der über dem Boden gemessenen Neutronen ist dabei abhängig von der Menge an Wasserstoff in der Umgebung des Neutronendetektors. Da in den meisten Bereichen an Land die Bodenfeuchte den größten Teil des Wasserstoffs ausmacht, lassen Veränderungen in der gemessenen Neutronenintensität auf veränderte Bodenfeuchtebedingungen schließen. Ein Vorteil dieser nichtinvasiven Methode ist ihr großer Messbereich von mehreren Hektar. Die, selbst über kurze Distanzen und Zeiträume auftretenden, Unterschiede werden somit repräsentativ gemittelt und gemessene Bodenfeuchtewerte können so besser für Vorhersagemodelle von Hochwasser- und Dürreereignissen genutzt werden.

Trotz des Potentials von CRNS für das Monitoring von Bodenfeuchte bleiben zahlreiche offene Forschungsfragen, von denen einige im Rahmen dieser Arbeit betrachtet werden. Hierzu zählt die Bestimmung und Korrektur von Einflussgrößen, die das Neutronensignal zusätzlich zur Bodenfeuchte beeinflussen. Ebenso gehört die Ableitung von Bodenfeuchte aus dem Neutronensignal selbst sowie der Umgang mit stark unterschiedlichen Bodenfeuchtebedingungen im Messbereich dazu. Obwohl CRNS einen großen horizontalen Messbereich besitzt, ist die Messtiefe auf die oberen ca. 30 cm des Bodens begrenzt. Hierzu werden Ansätze untersucht, die Bodenfeuchte mathematisch in größere Tiefen zu extrapolieren und sie direkt dort zu messen, indem Neutronendetektoren in Bohrlöchern installiert werden.

Mit der Betrachtung der Forschungsfragen kann diese Arbeit einen wichtigen Beitrag zur Weiterentwicklung von CRNS und der Anwendbarkeit der Methode z.B. im Rahmen nationaler Monitoring-Programme leisten, denen im Kontext zunehmend intensiverer hydro-meteorologischer Extremereignisse eine besondere Bedeutung zukommt.

Contents

List of Publications

This thesis comprises the following peer-reviewed publications

D. Rasche, M. Köhli, M. Schrön, T. Blume, and A. Güntner. 2021. Towards disentangling heterogeneous soil moisture patterns in cosmic-ray neutron sensor footprints. *Hydrology and Earth System Sciences*, 25(12):6547–6566. doi: 10.5194/hess-25-6547-2021

Author's contribution: Concept and design of the study, conducting simulations, processing and analysis of observation data. Preparation and writing of the manuscript, corresponding author for publishing procedure.

D. Rasche, J. Weimar, M. Schrön, M. Köhli, M. Morgner, A. Güntner, and T. Blume. 2023. A change in perspective: downhole Cosmic-Ray Neutron Sensing for the estimation of soil moisture. *Hydrology and Earth System Sciences*, 27(16):3059–3082. doi: 10.5194/hess-27-3059-2023

Author's contribution: Idea for this study, design of the experiment, observation data processing and analysis. Preparation and writing of the manuscript, corresponding author for publishing procedure together with J. Weimar.

D. Rasche, T. Blume, and A. Güntner. 2024. Depth-extrapolation of field-scale soil moisture time series derived with Cosmic-Ray Neutron Sensing using the SMAR model. *SOIL (submitted)*

Author's contribution: Concept for this study (together with T. Blume and A. Güntner), data processing and analysis. Preparation and writing of the manuscript (together with T. Blume and A. Güntner), corresponding author for publishing procedure.

M. Schrön, D. Rasche, J. Weimar, M. Köhli, K. Herbst, B. Boehrer, L. Hertle, S. Kögler, and S. Zacharias. 2023b. Buoy-based detection of low-energy cosmic-ray neutrons to monitor the influence of atmospheric, geomagnetic, and heliospheric effects. *Earth and Space Science (submitted)*. doi: 10.22541/au.170319441.16528907/v1

Author's contribution: Concept for this study, data processing and analysis (together with M. Schrön). Preparation and writing of the manuscript (together with M. Schrön.)

Contributions to additional peer-reviewed publications during the doctoral studies

H. R. Bogena, M. Schrön, J. Jakobi, P. Ney, S. Zacharias, M. Andreasen, R. Baatz, D. Boorman, M. B. Duygu, M. A. Eguibar-Galán, B. Fersch, T. Franke, J. Geris, M. G. Sanchis, Y. Kerr, T. Korf, Z. Mengistu, A. Mialon, P. Nasta, J. Nitychoruk, V. Pisinaras, D. Rasche, R. Rosolem, H. Said, P. Schattan, M. Zreda, S. Achleitner, E. Albentosa-Hernández, Z. Akyürek, T. Blume, A. del Campo, D. Canone, K. Dimitrova-Petrova, J. G. Evans, S. Ferraris, F. Frances, D. Gisolo, A. Güntner, F. Herrmann, J. Iwema, K. H. Jensen, H. Kunstmann, A. Lidón, M. C. Looms, S. Oswald, A. Panagopoulos, A. Patil, D. Power, C. Rebmann, N. Romano, L. Scheiffele, S. Seneviratne, G. Weltin, and H. Vereecken. 2022. COSMOS-Europe: a European network of cosmic-ray neutron soil moisture sensors. *Earth System Science Data*, 14 (3):1125–1151. doi: 10.5194/essd-14-1125-2022

B. Fersch, T. Francke, M. Heistermann, M. Schrön, V. Döpper, J. Jakobi, G. Baroni, T. Blume, H. Bogena, C. Budach, T. Gränzig, M. Förster, A. Güntner, H.-J. Hendricks Franssen, M. Kasner, M. Köhli, B. Kleinschmit, H. Kunstmann, A. Patil, D. Rasche, L. Scheiffele, U. Schmidt, S. Szulc-Seyfried, J. Weimar, S. Zacharias, M. Zreda, B. Heber, R. Kiese, V. Mares, H. Mollenhauer, I. Völksch, and S. Oswald. 2020. A dense network of cosmic-ray neutron sensors for soil moisture observation in a highly instrumented pre-alpine headwater catchment in Germany. *Earth System Science Data*, 12(3):2289–2309. doi: 10.5194/essd-12-2289-2020

M. Heistermann, H. Bogena, T. Francke, A. Güntner, J. Jakobi, D. Rasche, M. Schrön, V. Döpper, B. Fersch, J. Groh, A. Patil, T. Pütz, M. Reich, S. Zacharias, C. Zengerle, and S. Oswald. 2022. Soil moisture observation in a forested headwater catchment: combining a dense cosmic-ray neutron sensor network with roving and hydrogravimetry at the TERENO site Wüstebach. *Earth System Science Data*, 14(5):2501–2519. doi: 10.5194/essd-14-2501-2022

M. Heistermann, T. Francke, L. Scheiffele, K. Dimitrova Petrova, C. Budach, M. Schrön, B. Trost, D. Rasche, A. Güntner, V. Döpper, M. Förster, M. Köhli, L. Angermann, N. Antonoglou, M. Zude-Sasse, and S. E. Oswald. 2023. Three years of soil moisture observations by a dense Cosmic-Ray Neutron Sensing cluster at an agricultural research site in north-east Germany. *Earth System Science Data*, 15(7):3243–3262. doi: 10.5194/essd-15-3243-2023

J. Jakobi, J. A. Huisman, M. Köhli, D. Rasche, H. Vereecken, and H. R. Bogena. 2021. The footprint characteristics of cosmic ray thermal neutrons. *Geophysical Research Letters*, 48(15). doi: 10.1029/2021GL094281

M. Pätzig, F. Geiger, D. Rasche, P. Rauneker, and A. Eltner. 2020. Allometric relationships for selected macrophytes of kettle holes in northeast Germany as a basis for efficient biomass estimation using unmanned aerial systems (UAS). *Aquatic Botany*, 162:103202. doi: 10.1016/j.aquabot.2020.103202

D. Rasche, C. Reinhardt-Imjela, A. Schulte, and R. Wenzel. 2019. Hydrodynamic simulation of the effects of stable in-channel large wood on the flood hydrographs of a low mountain range creek, Ore Mountains, Germany. *Hydrology and Earth System Sciences*, 23(10):4349–4365. doi: 10.5194/hess-23-4349-2019

List of Figures

List of Tables

Chapter 1

Introduction

1.1 Hydro-meteorological extremes in a changing climate

Hydro-meteorological extreme events are intensifying on a global scale [Tabari, 2020; Rodell and Li, 2023] with human and economic losses of river flood events are being expected to increase with a warming climate [Dottori et al., 2018]. In the past 25 years, Germany alone experienced severe flood events with high amounts of tangible and intangible losses, ranging from large-scale river floods e.g. of the Elbe river in 2002 and 2013 [e.g. Schröter et al., 2015] to events on a smaller spatio-temporal scale. These include, for instance, the flash flood events in Braunsbach in 2016 [e.g. Bronstert et al., 2018] or in the Ahr valley in 2021 [e.g. Apel et al., 2022]. A warming climate alters both the timing of flood events [Blöschl et al., 2017] and increases the frequency of floods on a global scale [Hirabayashi et al., 2013]. Yet, regionally varying trends can be found for the timing, magnitudes and frequencies of flood events. While some regions in Europe experience earlier floods, a delay can be observed in others [Blöschl et al., 2017]. Similar differences have been found for flood discharges arising from regionally changing patterns in precipitation, evaporation and snowmelt, showing that climate change impacts on flood events and the hydrological cycle can already be observed [Blöschl et al., 2019b].

Decreasing trends of flood discharges in some regions of Europe, due to reduced precipitation and increased evapotranspiration, illustrate the regionally opposing effects of a changing climate and underline the findings of Rodell and Li [2023] showing that extreme dry events are intensifying along with extreme wet events. Thus, a warming climate can be expected to increase the severity and frequency of drought events in Europe [Spinoni et al., 2018] as well as on a global scale [Pokhrel et al., 2021]. Recent examples of drought events in Germany occurred in 2018 and 2019, also affecting large parts of central Europe [Boergens et al., 2020] and impacting agriculture, forestry and the transportation sector [e.g. Madruga de Brito et al., 2020; Boergens et al., 2020] on different temporal scales. For example, droughts can impact forest ecosystems beyond their own duration [e.g. Senf and Seidl, 2021] while immediately impacting agriculture [Madruga de Brito et al., 2020]. An associated effect of the 2018/2019 events were drought-induced forest fires [Madruga de Brito et al., 2020], which not only affect the respective forest ecosystems and related economic losses in forestry, but also affect human health [Xu et al., 2020]. Although the drivers of wildfires are complex, droughts contribute to the likelihood wildfires

especially in woody ecosystems [Pausas and Keeley, 2021] and with more frequent and severe droughts, a potential increase in frequency of wildfires can be expected.

More frequent and intense hydro-meteorological extreme events associated with a global rise in temperatures lead to severe direct and indirect impacts on ecosystems, economy and human health. Gaining further knowledge on the driving key hydrological variables, their interconnectivity and monitoring on different spatio-temporal scales is a prerequisite for developing and advancing the forecasting of hydro-meteorological extremes as well as risk mitigation and adaption strategies in a changing climate.

1.2 On the role of soil moisture

1.2.1 The importance of soil moisture in the context of hydrological extremes

Defined as the water located in the unsaturated, i.e. vadose zone of the soil [Seneviratne et al., 2010], soil moisture represents one key variable in hydrology [Vereecken et al., 2008, 2014] and the climate system [Seneviratne et al., 2010] driving energy and water fluxes [e.g. Vereecken et al., 2008; Seneviratne et al., 2010]. Despite its small share of below 0.01 % of the total amount of water on earth [Dingman, 2015], it has a high importance for several hydrological and environmental processes as reviewed in numerous studies [e.g. Daly and Porporato, 2005; Robinson et al., 2008; Seneviratne et al., 2010; Wang et al., 2018]. This includes the modulating process from precipitation to runoff generation [Wang et al., 2018]. The role of the antecedent soil moisture state for the runoff generation has been analysed by Merz and Blöschl [2009] for catchments of various sizes, illustrating that antecedent soil moisture conditions can exert a strong influence on runoff coefficients and runoff generation, although the impact of antecedent soil moisture on runoff volumes depends on the runoff generating process [Scherrer et al., 2007]. For example, runoff volumes from Hortionian overland runoff, caused by precipitation intensity exceeding the infiltration rate, can be expected to be little influenced by antecedent moisture [Scherrer et al., 2007]. In contrast, runoff from saturation excess due to a decreased soil water storage volume available through higher soil moisture contents is expected to influence runoff and flood generation [Merz et al., 2021].

In the large catchment of the Elbe river, Nied et al. [2013] found that soil moisture patterns are among the flood-initiating conditions and that both, weather patterns and soil moisture conditions influence flood generation and characteristics [Nied et al., 2014, 2017]. In addition to floods on a larger spatio-temporal scale, small scale flash flood events were also found to be influenced by antecedent soil moisture conditions. For example, Grillakis et al. [2016] report a sensitivity of flash flood peak discharges on antecedent soil moisture conditions. Although lower antecedent soil moisture contents indicate a higher water storage capacity and hence, potentially dampening effect on flood discharges, the opposite may also occur. Dry conditions can result in hydrophobicity which reduces the infiltration rate into the soil and thus, increasing surface runoff and runoff coefficients [e.g. Ferreira et al., 2000; Lemmnitz et al., 2007].

Although regional differences can be observed, on a continental scale, soil moisture excess is the most important flood driver in Europe [Berghuijs et al., 2019],

with increasing importance being found for the British Isles, north and central Europe [Kemter et al., 2020]. Due the high importance of soil moisture conditions for runoff generation and thus, the characteristics and magnitudes of floods on different spatio-temporal scales, soil moisture information can improve flood modelling [e.g. Massari et al., 2014; Chifflard et al., 2018] and flood forecasting efforts [e.g. Wanders et al., 2014], illustrating the high value of soil moisture information for forecasting as well as the risk assessment and management of flood events in a changing climate.

In addition to the importance for flood events, soil moisture provides the plant-available water for transpiration, plant growth and photosynthesis, thereby driving biogeochemical processes such as the carbon and nitrogen cycles [e.g. Seneviratne et al., 2010]. Several interaction and feedback processes between soil moisture, vegetation and climatic variables show that that climatic conditions and vegetation cover exert an influence on soil moisture and vice versa [e.g. Seneviratne et al., 2010; Wang et al., 2018]. Changing soil moisture contents are observed in many regions of the world, with 48 % of vegetated area showing a long-term decrease in soil moisture [Lal et al., 2023] and hence, potentially available water for plants and ecosystems. Depending on the affected ecosystem, this may lead to an increased vulnerability to globally intensifying droughts (see chapter 1.1), as vegetation becomes increasingly sensitive to soil moisture in many parts of the world, especially in arid and semi-arid regions [Li et al., 2022b]. This may be of special importance as droughts are developing more rapidly in many parts of the world [Yuan et al., 2023], making monitoring and forecasting more difficult [Pendergrass et al., 2020]. Depleting soil moisture contributes to the development of these rapidly developing flash droughts [e.g. Qing et al., 2022] which not least illustrates the importance of long-term soil moisture monitoring for drought modelling, forecasting and early warning efforts [Boeing et al., 2022].

Droughts not only affect local ecosystems but also the production of agricultural crops through low soil moisture contents and associated water stress. More intense and rapidly developing droughts can therefore be expected to negatively affect the global food production. Accurate crop yield modelling and forecasting are vital to sustain food security. Incorporating soil moisture information into crop yield models has been found to improve modelling results [Proctor et al., 2022].

Similarly, other drought-associated hazards such as wildfires, can also be linked to spatio-temporal fire-promoting soil moisture patterns [e.g. Krueger et al., 2015; O et al., 2020], making soil moisture an important variable for wildfire danger rating and management [Krueger et al., 2022] and highlighting the importance of soil moisture information beyond the monitoring, modelling and forecasting of droughts as hydro-meteorological extremes themselves.

Not least because of the significance of soil moisture against the background intensifying hydro-meteorological extremes in a warming climate, soil water storage in agricultural soils and soil moisture in forest soils have been defined as indicators and described in the latest monitoring report on the official „German Strategy for Adaption to Climate Change“[van Rüth et al., 2023], underlining the importance of monitoring soil moisture for the development of adaption and mitigation strategies for a changing climate.

1.2.2 Soil moisture in deeper layers

In general, the importance of soil moisture described in the previous chapter refers to the amount of water stored in the entire unsaturated zone. However, the soil surface is directly connected to the atmosphere, making the soil close to the surface most important for processes of infiltration, runoff, evaporation and hence, water and energy fluxes. Globally, the majority of plant roots are located within the upper 100 cm of the soil [Jackson et al., 1996], making this soil layer also essential for transpiration, photosynthesis and plant growth as well as biogeochemical processes. As a consequence, soil moisture is often monitored close to the surface. For instance, stations of the International Soil Monitoring Network ISMN [Dorigo et al., 2011] observe in situ soil moisture to a maximum depth of 200 cm with the vast majority of stations monitoring soil moisture to 100 cm only [Dorigo et al., 2021b]. Similarly, studies which aim for the estimation of root zone soil moisture from measurements of surface soil moisture in the first centimetres of the soil usually consider depths down to approx. 100 cm when assessing the root zone soil moisture content [e.g. Peterson et al., 2016; Manfreda et al., 2014; Zhang et al., 2017; Mishra et al., 2020; Tian et al., 2020; Franz et al., 2020; Carranza et al., 2021; Guo et al., 2023], while only some studies consider larger depths of e.g. 200 cm [e.g. Pasik et al., 2023]. Globally available gridded soil moisture products based on, for example, satellite data, modelling approaches and data reanalysis cover similar vertical extents as summarised in Xu et al. [2021] and Zheng et al. [2023].

Although most of the roots are located in the upper 100 cm of the soil, the maximum rooting depths of vegetation usually exceed this depth with a global average of 4.6 m [Canadell et al., 1996], depending on vegetation type, soil properties and hydroclimatic conditions [e.g. Fan et al., 2017] including soil moisture through its influence on root growth [e.g. Maan et al., 2023]. As a consequence, the root distribution in the entire vadose zone is difficult to quantify and the commonly used exponential model to describe the cumulative root distribution remains under debate [Pierret et al., 2016] and may only be considered as a first estimate. As most roots can be found in the upper soil layer, roots below a threshold depth of 100 cm have been defined as deep roots [Maeght et al., 2013] and deep soil moisture may be defined correspondingly to water stored in the vadose zone in depths greater 100 cm. Infiltrating water from precipitation percolating to depths below 100 cm is less susceptible to being removed via root water uptake compared to soil layers with higher root densities. Consequently, water may be stored in deeper layers of the unsaturated zone, or percolates further contributing to groundwater recharge. Depending on the site-specific soil physical and hydroclimatic conditions, plants can access water in deeper unsaturated soil layers or even groundwater through deep root growth [e.g. Fan et al., 2017]. For instance, the common Scotts pine (*Pinus sylvestris*) may develop a height-to-depth ratio of 0.6 [Pierret et al., 2016] meaning that for a tree height of 20 m, a maximum rooting depth of more than 30 m can be expected allowing the tree to access groundwater resources via tap roots in many regions.

As the density of roots is much higher close to the soil surface, the highest amount root water uptake and hence, water supply of plants occurs in the shallow root zone by uptaking infiltrated water from precipitation while the root water uptake from deeper layers is comparably marginal [Pierret et al., 2016]. Nevertheless, deep roots can play an important role for root water uptake in dry periods [Pierret et al., 2016]

for both forest ecosystems and agricultural crops, as reviewed in Germon et al. [2020] and Li et al. [2022a]. Therefore, it represents an important factor for drought tolerance of plant ecosystems. The process of hydraulic lift allows plants to transport infiltrating water either into deeper layers or water from moist deep layers upwards [e.g. Nadezhdina et al., 2010; Neumann and Cardon, 2012] and is documented for many tree species and forest ecosystems [e.g. Neumann and Cardon, 2012]. An example for a typical hydraulic lift signal in soil moisture time series observed with in situ sensors can be found in Fig. 1.1 for a mixed forest site in north-eastern Germany indicating the presence of roots down to at least 450 cm. The signature of hydraulic lift is characterised by an increase of soil moisture during the night and a depletion of soil moisture during the day, differing from the typical „descending staircase “evapotranspiration signal characterised by a depletion during the day, only [Brooks et al., 2002]. Brooks et al. [2002] indicate that hydraulic redistribution of water from e.g. deeper to shallow layers can delay the soil drying of the upper soil layers and hence, elongate water availability for transpiration in shallow soil layers during droughts which increases the drought tolerance of plants.

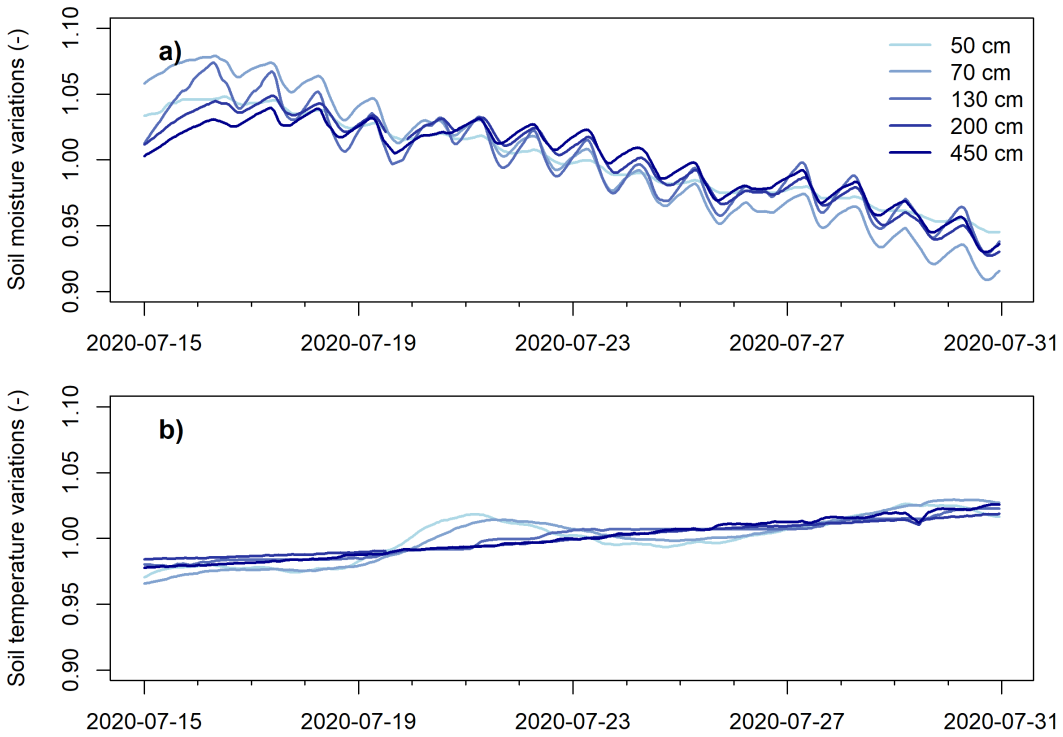

Figure 1.1: (a) Diurnal soil moisture variations and (b) soil temperature variations observed by selected in situ point-scale sensors installed in different depths at a forest monitoring site in north-eastern Germany in July 2020.

Furthermore, roots form macropores in the soil which act as flowpaths enabling preferential flow along living and dead roots [e.g. see review by Nimmo, 2021]. This allows infiltrating water to bypass shallow layers and to percolate into deeper soil increasing the amount of water transported and potentially stored in deeper soil layers. For instance, Hu et al. [2022] found that preferential flow associated with macropores along roots can be higher compared to macropores not associated with roots. Consequently, roots contribute to both, increasing infiltration to greater depths and

thereby increasing soil water storage which can lead to reduced runoff on the one hand as well as increased stored water in deeper layers potentially accessible during periods of drought on the other. Maysonnave et al. [2022] recently confirmed the importance of water stored in deeper layers for enabling plant water supply during dry periods in a mixed forest in France, finding that root water uptake in layers below 150 cm depth increases over the growing season when the superficial layers dry up. Moreover, water in deep soil layers contributed up to 60 % of the transpired water during the central European drought event in August 2018 [Maysonnave et al., 2022] indicating their importance for sustaining plant growth during droughts. A widespread access of vegetation to water in soil layers below 100 and 200 cm has been indicated by Stocker et al. [2023] on a global scale underlining the importance of water stored below 100 cm, e.g. as deep soil moisture in the unsaturated zone, for the water supply of vegetation. Monitoring water stored in the deeper unsaturated zone may therefore become especially important in a warming climate, accompanied with intensifying hydro-meteorological extremes such as droughts in order to support forecasting efforts and to improve mitigation and adaptation strategies.

1.2.3 Measuring soil moisture at relevant scales

Soil moisture is highly variable in time and space and may change intensely, even over small horizontal distances in the centimetre range [Vereecken et al., 2014]. The spatio-temporal variability is driven by a complex interaction of several factors [Rosenbaum et al., 2012] including topography, soil physical properties, meteorological forcing, groundwater, the average soil moisture content and vegetation [Famiglietti et al., 2008; Rosenbaum et al., 2012]. The degree of surface soil moisture variability on the point scale (approx. measurement volume of 1 dm^3, [Robinson et al., 2008]) is dependent on the scale itself, with an increasing variability reported for larger spatial scales [e.g. Famiglietti et al., 2008]. Due to the driving meteorological forcing, surface soil moisture can be expected to vary stronger than soil moisture in deeper layers in both the spatial and temporal domain [e.g. Rosenbaum et al., 2012]. This can be also be related to the degree of interception and transpiration [e.g. Schume et al., 2003] and throughfall patterns [e.g. Fischer-Bedtke et al., 2023] as well as infiltration patterns due to species dependent root distributions of forest vegetation [e.g. Jost et al., 2012]. The influence of vegetation on spatio-temporal variability of soil moisture is not limited to forest ecosystems but has also been reported for e.g. grasslands [Demir et al., 2022]. An example of spatio-temporal variability of point-scale soil moisture close to the surface can be found in Fig. 1.2. It shows the differing response of several electromagnetic in situ soil moisture sensors installed in a depth of 10 cm in a mixed forest in north-eastern Germany. Although installed only a few metres apart from each other, it can be seen that not only the average soil moisture differs between sensors but also their temporal dynamics.

This exemplifies the high spatio-temporal variability of point-scale soil moisture and illustrates the need to observe representative averages of soil moisture at the spatial and temporal scales of the process and application of interest [Dorigo et al., 2021a]. For instance, environmental model applications such as rainfall-runoff modelling for flood risk assessment and foresting or land-surface modelling for drought forecasting may require soil moisture information on the process scale of the respective model domain [e.g. Robinson et al., 2008], e.g. grid cell sizes from tens of metres

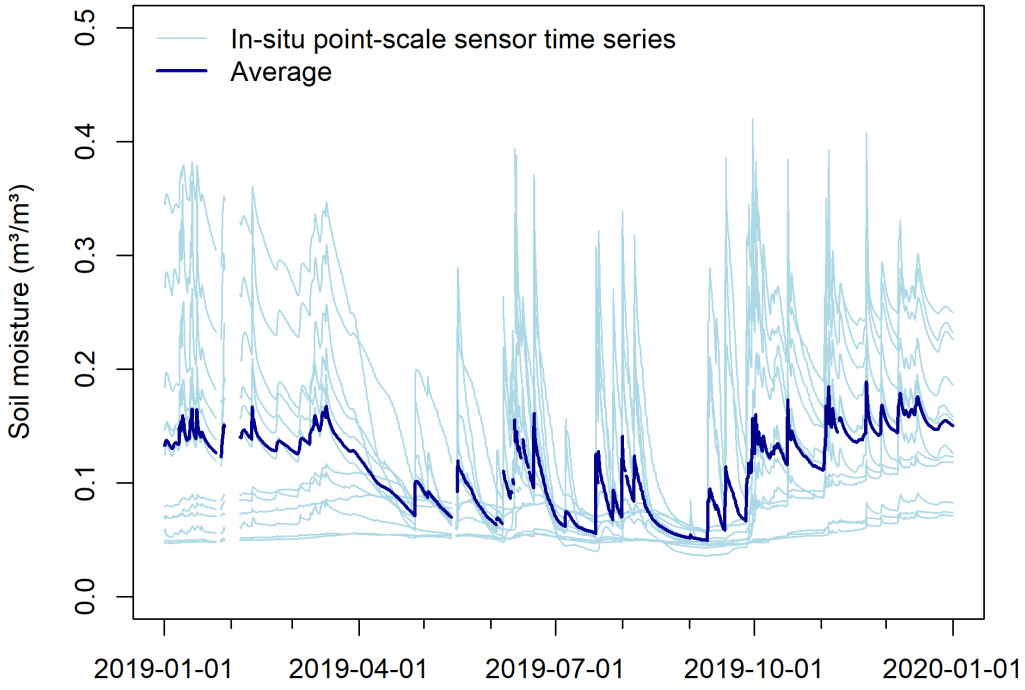

Figure 1.2: Soil moisture time series measured by 12 in situ points-scale sensors installed in 10 cm depth at a forest monitoring site in north-eastern Germany in 2019.

to tens of kilometres [Dorigo et al., 2021a]. Similarly, agricultural applications require soil moisture information on the scale of agricultural fields to aid agricultural management practices such as irrigation for optimising crop yield [Vereecken et al., 2014]. The required field-scale data in the range from 1 to 10 [Vergopolan et al., 2021] or 100 ha [Brown et al., 2023] lies between the point scale which can be observed using, for instance, electromagnetic in situ sensors and the coarser scale of satellite-derived soil moisture products. Observational techniques to measure soil moisture at the field scale range from networks of co-located in situ point-scale measurements [Robinson et al., 2008; Vereecken et al., 2014] to non-invasive geophysical methods such as electrical resistivity tomography (ERT) [e.g. Cimpoiaşu et al., 2020], terrestrial gravimetry [e.g. Van Camp et al., 2017] and lower resolution soil moisture products derived from airborne and space-borne remote sensing. Detailed reviews on observing soil moisture at different spatio-temporal scales can be found in Robinson et al. [2008], Vereecken et al. [2008, 2014] and Babaeian et al. [2019].

All techniques for monitoring field-scale soil moisture come with their individual limitations and challenges. For example, point-scale sensor networks comprising several electromagnetic in situ soil moisture sensors can be used to derive continuous field-scale averages of soil moisture in different depths and on a high temporal, e.g. sub-hourly, resolution [e.g. Vereecken et al., 2014]. However, a very large number of sensors are required to capture the variability of soil moisture at the field scale and to derive representative field-scale average values [Babaeian et al., 2019]. The large number of sensors required are cost and labour intensive which hampers their

installation and usage [Babaeian et al., 2019] and often their installation depth does not exceed 100 cm, as exemplary shown for the ISMN [Dorigo et al., 2021b]. Furthermore, agricultural management practices such as ploughing and harvest make their use impractical in these settings [e.g. Stevanato et al., 2019]. Other geophysical methods such as time-lapse ERT are non-invasive and can be used to derive soil moisture changes along transects and to greater depths of a few metres allowing to assess e.g. two-dimensional soil moisture distributions [e.g. de Jong et al., 2020; Vanella et al., 2022; Rieder and Kneisel, 2023]. However, they require additional information to derive absolute soil moisture contents from raw measurements through empirical models or calibration [Fäth et al., 2022] and measurements are often carried-out as snap-shot campaigns with a limited temporal resolution. Field to landscape-scale soil moisture changes in the entire vadose zone can also be derived non-invasively from relative terrestrial gravimetry [e.g. He et al., 2022]. However, additional information such as groundwater storage variations are required to reduce observed gravity variations to soil moisture storage variations in the vadose zone, complicating the approach and adding to the high instrumental costs [Van Camp et al., 2017]. Airborne and space-borne remote sensing soil moisture estimates with sufficient spatial resolution may also be used to derive field-scale soil moisture averages [Vereecken et al., 2014]. Nevertheless, their temporal resolution is limited and the measurement depth is restricted to the first few centimetres of the soil [e.g. Babaeian et al., 2019].

As a consequence, hydrological monitoring efforts for observing soil moisture on relevant scales for e.g. informing flood and drought modelling, would benefit from non-invasive methods that are capable to continuously monitor soil moisture at the field scale with a sufficient temporal resolution and a measurement depth exceeding the upper centimetres of the soil, thereby coming at a reasonable cost and reduced complexity by requiring only a comparably small amount of additional data.

1.3 Field-scale soil moisture estimation with Cosmic-Ray Neutron Sensing

1.3.1 Principles of Cosmic-Ray Neutron Sensing

Cosmic-Ray Neutron Sensing (CRNS) is a non-invasive geophysical method which allows for the estimation of representative spatial averages of field-scale soil moisture on a high temporal resolution [Schrön et al., 2018b]. CRNS makes use of the sensitivity of neutrons with energies below 1 MeV to hydrogen. As the hydrogen nucleus has the same mass as a neutron, elastic scattering causes an energy loss of the neutron upon collision with the hydrogen nucleus [e.g. Köhli et al., 2015]. Hydrogen effectively slows down neutrons from higher to lower thermal energies ($\leq$ 0.25 eV) in which a neutron is in thermal equilibrium with its surrounding material and where the probability for absorption by nuclei, e.g. hydrogen, is highest. A change in the hydrogen content of the interacting medium, e.g. the soil, results in a change of the observed intensity of neutrons in the water-sensitive epithermal energy range between thermal energies and 1 MeV [e.g. Köhli et al., 2015; Weimar et al., 2020]. Assuming that the dominating fraction of hydrogen is stored in the soil as water, changes in soil moisture lead to changes in the observed neutron intensity

following an inverse relationship.

The potential of the effectiveness of hydrogen to slow down neutrons for hydrological applications has already been described in the mid 20th century by Gardner and Kirkham [1952] who introduced the active neutron probe for soil moisture measurements. Equipped with a neutron source and a co-located neutron detector, the ratio of emitted higher energy to detected lower energy neutrons in different depths via access tubes or at the soil surface can be related to the water content in a few tens of centimetres of the surrounding soil [e.g. IAEA - International Atomic Energy Agency, 1970; Gardner, 1986; Babaeian et al., 2019]. As the active neutron method requires a radioactive neutron source, high safety requirements and regulations need to be fulfilled which hamper its application and make it impractical [e.g. Gardner, 1986; Babaeian et al., 2019].

Being among the first, Kodama et al. [1975, 1979, 1985] showed the potential of naturally occurring secondary neutrons from cosmic-rays for passively estimating snow water equivalents and soil moisture, respectively. While Dorman [2004] summarises several potential fields of applications of cosmic-rays, including soil moisture measurements, Zreda et al. [2008] and Desilets et al. [2010] were the first to introduce the methodological framework of CRNS for the non-invasive estimation of soil moisture from the intensity of naturally occurring secondary neutrons from cosmic radiation above the soil surface.

High-energy cosmic-ray neutrons penetrate the soil and produce water-sensitive neutrons in nuclear evaporation processes [Köhli et al., 2015] which interact with the soil constituents including soil moisture and the contained hydrogen before eventually leaving the soil column. Above the ground, a neutron detector can measure the intensity of neutrons in the water-sensitive energy range reflected from the soil. The first devices used for CRNS applications were composed of two proportional gas-filled neutron detectors [Zreda et al., 2012]. One for detecting neutrons in the thermal energy range and second detector for neutrons in the water-sensitive, epithermal energy range which is shielded by high-density polyethylene to slow down, i.e. moderate, impinging neutrons to energy levels detectable by the instrument. In these detectors ^{3}He gas acts as a converter material, by creating a measurable electronic pulse once a neutron interacts with the detector gas by absorption. Originating from refurbishing nuclear warheads [Weimar et al., 2020], ^{3}He is expensive which lead to the development of a variety of detector types and the use of different converter materials. Apart from ^{3}He, proportional detectors filled with BF_3 gas are most common and installed in CRNS networks around the world [Hawdon et al., 2014; Cooper et al., 2021; Upadhyaya et al., 2021; Bogena et al., 2022]. However, as BF_3 gas is toxic, in the context of CRNS, further alternative instrumental concepts to ^{3}He have been introduced including proportional neutron detectors based on solid boron [Weimar et al., 2020] and solid lithium [Patrignani et al., 2021] as well as scintillators [Stevanato et al., 2019; Stowell et al., 2021] where neutrons interacting with the scintillator material create detectable photon, i.e. light, pulses.

Depending on the neutron detector type and converter material, different neutron detectors have different efficiencies in detecting neutrons in the desired energy range. As the detection of neutrons follows Poisson statistics [Bogena et al., 2013], the capability of a neutron detector to count more neutrons per time interval leads to a higher statistical accuracy and lower noise levels in the detected neutron signal. In order to reduce the Poisson noise in neutron data, moving averages are commonly

applied in order to reduce the Poisson noise through an extension of the counting interval and hence, the increase of the total neutron counts per time interval [Zreda et al., 2008; Bogena et al., 2013; Schrön et al., 2018b]. As moving averages smooth the signal and reduce, e.g. flatten sharp decreases of the neutron signal during rainfall events, alternative filtering approaches have been tested [Davies et al., 2022]. Nevertheless, applying a centred 12 or 24 hour moving average remains the standard procedure in CRNS data processing as it was done for European network of CRNS detectors [Bogena et al., 2022].

Due to their high sensitivity to hydrogen, epithermal neutrons observed by the shielded, i.e. moderated neutron detector are used for estimating soil moisture in the CRNS approach [Desilets et al., 2010]. Consequently, many CRNS instruments are equipped with an epithermal neutron detector, only, as it is the case for the Australian CRNS network [Hawdon et al., 2014] and the majority of sites in the network of the United Kingdom [Cooper et al., 2021]. Although most CRNS research focused on epithermal neutrons, thermal neutrons observed by unshielded, bare detectors remain an important topic in CRNS research with different studies investigating their response to influencing environmental factors [e.g. Andreasen et al., 2017b; Jakobi et al., 2021] and exploring potential fields of application [e.g. Tian et al., 2016; Jakobi et al., 2018, 2022].

1.3.2 Travelling to the earth's surface

CRNS relies on secondary neutrons produced by naturally occurring cosmic radiation penetrating the earth's atmosphere and eventually reaching the ground. On their path through the atmosphere primary cosmic-ray particles, mainly protons, interact with the atmospheric components and producing secondary particles through e.g. nuclear evaporation processes in the atmosphere [e.g. Köhli et al., 2015; Weimar et al., 2020]. A higher air density, through more atmospheric mass per volume, and a higher air humidity lead to a decrease in the distance a neutron can travel before it is thermalised [Köhli et al., 2015]. Therefore, changing attributes and composition of the atmosphere influence the neutron signal observed by a CRNS instrument above the soil surface.

Consequently, epithermal neutron signals observed by a CRNS instrument need to be corrected for variations of atmospheric mass, which can be expressed as the shielding depth in $\mathrm{g\,cm^{-2}}$ and related to air pressure variations [e.g. Heidbüchel et al., 2016; Andreasen et al., 2017a] as well as absolute air humidity [e.g. Zreda et al., 2012; Rosolem et al., 2013] before soil moisture can be estimated. The correction procedures described in Zreda et al. [2012] and Andreasen et al. [2017a] became common standard in CRNS research and can be applied with observations of local air pressure, temperature and relative humidity observations which are standard meteorological variables and comparably easy to measure.

In addition to the atmosphere modulating the neutron signal observed at the ground level, variations in the incoming primary cosmic-rays reaching the earth's atmosphere from space influence the neutron signal at the ground level and need to be corrected for [e.g. Zreda et al., 2012]. High-energy cosmic-rays are difficult to measure and usually observed with large high-energy neutron monitors which are also commonly used to correct epithermal neutron signals in the scope of CRNS applications [e.g. Zreda et al., 2012]. Neutron monitors only exist at selected loca-

tions around the globe [Bogena et al., 2022]. For instance, Väisänen et al. [2021] identified 147 neutron monitors with publicly available data covering varying time periods of the past 70 years. As datasets are available from different data bases and varying data quality levels, Väisänen et al. [2021] identified 29 neutron monitors stations with the longest record and most reliable data. One of these stations is the Jungfraujoch neutron monitor in Switzerland which became the standard neutron monitor for correcting epithermal neutrons observed by CRNS instruments for variations in incoming primary radiation in different observational networks [e.g. Zreda et al., 2012; Evans et al., 2016; Cooper et al., 2021; Bogena et al., 2022].

However, differences of geomagnetic cutoff rigidity, which expresses the energy a cosmic-ray particle must have in order to reach a certain point on earth [Herbst et al., 2013], and altitude between a neutron monitor station and the respective CRNS observation site may lead to an insufficient correction. Thus, the Jungfraujoch neutron monitor may not be representative for the variations of incoming primary radiation at a CRNS observation site with a different cutoff rigidity and altitude. Scaling approaches have been developed to scale neutron monitor signals of incoming primary radiation according to the difference in cutoff rigidity and altitude of the neutron monitor and the CRNS location for an improved correction of epithermal neutron signals and in turn, soil moisture estimates [Hawdon et al., 2014; McJannet and Desilets, 2023]. Yet, evaluating the improvement of these approaches is challenging as the locally measured epithermal neutron signal by the CRNS instrument always depends on the hydrogen and especially soil moisture dynamics in its surroundings. This would either require a constant water content of the soil and surroundings, or an exact knowledge of the soil moisture distribution and dynamics surrounding the CRNS instrument which difficult to observe given the high spatio-temporal variability of soil moisture.

Furthermore, neutron monitor data is distributed through different databases with the Jungfraujoch neutron monitor being available from the neutron monitor database (`www.nmdb.eu`). In the latter, data are updated and revised by the individual neutron monitor operators [Väisänen et al., 2021] and the persistence of certain monitors and their data availability in future remains uncertain. As CRNS research and the CRNS approach for soil moisture estimation rely on the availability of information on the incoming primary cosmic-ray flux, finding alternative options for observing its variations are a key challenge in CRNS research. A potential approach utilizes cosmic-ray muons which have been shown to respond similar to cosmic radiation events as neutron monitors [e.g. Braun et al., 2009]. Like high-energy neutrons, long-term muon data is available from global monitoring networks such as the Global Muon Detector Network but comprising only a small number of stations [e.g. Rockenbach et al., 2014]. However, compared to high-energy neutrons, muons are easier to measure with relatively small and comparably inexpensive detectors [Stevanato et al., 2022]. Therefore, some commercially available CRNS instruments already include a muon detector and provide a muon product intended to be used for an on-site correction of observed neutrons for variations of incoming cosmic-rays [Stevanato et al., 2019] and first attempts to compare the correction with locally observed muons and available neutron monitors have already been made [e.g. Stevanato et al., 2022; Gianessi et al., 2022]. Another option is the use of existing CRNS instruments in environments with constant hydrogen, i.e. water content where ideally only atmospheric factors influence the observed neutron signal. Under

these circumstances, the neutron signal corrected for variations in air pressure and absolute air humidity would only represent variations in incoming primary radiation and could be subsequently used for correcting the neutron signal at observation sites intended for soil moisture measurements. First experiments have been made by Schrön [2017], designing a floating CRNS instrument on a buoy comprising a bare, thermal and moderated, epithermal neutron detector and installing it on a lake. However, the potential and applicability of such approaches remain under debate and require further research.

In contrast to epithermal neutrons, commonly accepted correction procedures for thermal neutrons counted by the bare neutron detector are not existing. Studies which make use of thermal neutrons or investigate their response under varying environmental conditions correct observed thermal neutron intensities differently. For example, Tian et al. [2016] used uncorrected thermal neutron observations while Andreasen et al. [2016] correct thermal neutrons for incoming primary cosmic-ray flux and air pressure but not for variations in absolute humidity. In contrast, based on empirical findings, Jakobi et al. [2018, 2022] do not correct thermal neutrons for the incoming primary cosmic-ray flux but for air pressure and absolute air humidity variations although the absolute humidity correction was developed for epithermal neutrons [Rosolem et al., 2013]. Hence, its validity for thermal neutrons remains uncertain and illustrates an important knowledge gap regarding the thermal neutron signal of CRNS instruments. Gaining further understanding of how atmospheric parameters influence the thermal neutron signal will allow for more standardised and expedient research on potential use-cases of thermal neutrons in CRNS research.

1.3.3 From neutrons to soil moisture

Deriving soil moisture from corrected and filtered epithermal neutron intensities requires mathematical transfer functions. Desilets et al. [2010] were the first to develop a generally applicable non-linear transfer function including a site-specific calibration parameter representing the site-specific neutron intensity above dry soil. The parameter can be calibrated against reference measurements of soil moisture in the sensitive measurement area around the CRNS instrument usually acquired through soil sampling and subsequent laboratory analyses. Although a single representative reference measurement of soil moisture is sufficient to calibrate the site-specific parameter in the transfer function [Zreda et al., 2012], a calibration against multiple reference measurements has been recommended [Iwema et al., 2015]. Soil bulk density estimates are required to transform the transfer function after Desilets et al. [2010] from gravimetric percent to volumetric soil moisture [Bogena et al., 2013]. More detailed analyses on the influence of bulk density and its changes on the performance of neutron-to-soil moisture transfer functions can be found in Kasner et al. [2022]. Observed epithermal neutrons are sensitive to all hydrogen. Additional below-ground hydrogen pools such as soil organic matter and lattice water need to be accounted with when deriving soil moisture from observed neutron intensities [e.g. Zreda et al., 2012; Bogena et al., 2013] in order to derive accurate soil moisture estimates. Similarly, hydrogen stored in above-ground biomass influences the observed neutron signal. Although its influence may be compensated through determining the site-specifc calibration parameter, temporal changes in biomass have been found to influence the estimated soil moisture contents [e.g. Baatz et al., 2015;

Vather et al., 2020] and require correction approaches. Different biomass correction approaches have been developed and evaluated [e.g. Hawdon et al., 2014; Baatz et al., 2015; Jakobi et al., 2018, 2022] with the approach by Baatz et al. [2015] may be considered the most common.

Since the introduction of the initial neutron-to-soil moisture transfer function by Desilets et al. [2010], other transfer approaches have been developed, including the universal calibration function [Franz et al., 2013b] as well as the COSMIC operator [Shuttleworth et al., 2013]. As comparisons of the individual methods revealed differences but generally similar performances [e.g. Baatz et al., 2014; Iwema et al., 2015] and due to the simplicity of the equation after Desilets et al. [2010], the latter became the standard approach for converting epithermal neutron intensities and is used in observational CRNS networks around the world [e.g. Zreda et al., 2012; Hawdon et al., 2014; Cooper et al., 2021; Bogena et al., 2022]. However, alternative approaches are still being developed, including site-specific conversion functions [Andreasen et al., 2020] and the recently introduced universal transport solution (UTS) [Köhli et al., 2021]. The most important novelty of the latter approach is that it takes the variability of the neutron-to-soil moisture transfer function to changes in absolute air humidity into account. In contrast, the use of the air humidity correction [Rosolem et al., 2013] with other transfer approaches only adjusts the neutron intensities to changes in air humidity, leaving the shape of the functional relationship unchanged. Additionally, the UTS has been derived from different neutron transport models providing slightly different fitting coefficients for the UTS equation. Although it has been shown that the UTS can outperform the standard transfer function [Köhli et al., 2021], a validation at different study sites and comparing the different available fitting coefficients has yet to be done in order to fully assess the potential of the UTS approach for future CRNS applications.

1.3.4 Sensitive measurement footprint

Zreda et al. [2008] provide the first quantification of the CRNS sensitive measurement footprint with respect to epithermal neutrons and show that the measurement radius can extent up to over 600 m and covers a depth of several decimetres. The measurement footprint is non-linearly dependent on soil moisture content, air pressure and air humidity [Zreda et al., 2008; Desilets and Zreda, 2013] and a comparison with reference in situ measurements from soil samples or point-scale soil moisture requires the calculation of a weighted average of reference soil moisture information according to match the sensitive footprint of the CRNS approach. The first weighting approach of reference measurements was introduced by Franz et al. [2012b] and tested by Franz et al. [2012a]. It includes the dependence of the sensitive measurement depth on the soil moisture content and other hydrogen sources such as lattice water in the soil as well as the soil bulk density [Franz et al., 2012b,a] in order to increase the comparability between the reference soil moisture values and the areal average soil moisture content from CRNS. The latter is not only important for a comparison of CRNS-derived soil moisture estimates with reference measurements, but also for the calibration of neutron-to-soil moisture transfer functions against reference measurements and the derivation of soil moisture from CRNS in the first place.

Given the high importance of the sensitive measurement area for the under-

standing and interpretation of the CRNS-derived soil moisture values, Köhli et al. [2015] provided a more extensive characterisation of the measurement volume revealing a sensitive measurement radius between 130 to 240 m and sensitive depth of 15 between 83 cm under wet and dry soil conditions, respectively. In contrast to the initial analyses from Zreda et al. [2008] as well as Desilets and Zreda [2013], both the horizontal and vertical footprint dimensions, were found to depend on the soil moisture content as well as air pressure, absolute air humidity and vegetation cover [Köhli et al., 2015]. A higher soil moisture content leads to a smaller horizontal measurement radius and shallower measurement depth. Furthermore, a decreasing sensitivity of the CRNS signal on soil moisture changes in greater distance and depth has been found [Köhli et al., 2015]. These findings lead to the development of revised weighting procedures [Köhli et al., 2015] for in situ reference soil moisture information which outperform previous approaches at various study sites [e.g. Schrön et al., 2017].

While the sensitive measurement footprint of epithermal neutrons has been investigated intensively since the introduction of CRNS by Zreda et al. [2008] due to their importance for soil moisture estimation, the thermal neutron footprint remained long unexplained [e.g. Andreasen et al., 2017a] and often assumed similar in studies which use and investigate thermal neutron observations [e.g. Vather et al., 2020]. The first horizontal measurement radius for thermal neutrons of approx. 35 m and thus, a much smaller footprint compared to epithermal neutrons was stated in Bogena et al. [2020]. In a subsequent study, Jakobi et al. [2021] characterised the thermal neutron footprint in greater detail. The smaller footprint of was confirmed and weighting functions similar to those for epithermal neutrons [Köhli et al., 2015] were derived. Yet, the results remain to be confirmed and weighting functions to be tested in research applications as it was done previously for epithermal neutrons [e.g. Schrön et al., 2017].

The large sensitive horizontal and vertical measurement footprint of eptithermal neutrons is an important advantage allowing to derive an representative weighted soil moisture average at the field scale [Schrön et al., 2018b]. This aids to bridge the spatio-temporal scale gap between soil moisture estimates from coarse-scale remote sensing techniques and e.g. point-scale electromagnetic in situ sensors observing soil moisture at small scales but with a high temporal resolution [e.g. Vereecken et al., 2014] as illustrated in Fig. 1.3. Several studies investigate and illustrate the potential of CRNS for calibrating, validating and evaluating satellite-derived and modelled soil moisture products [e.g. Holgate et al., 2016; Montzka et al., 2017; Upadhyaya et al., 2021; Zheng et al., 2023]. Reducing the spatial mismatch between the spatial discretisation of the model and the observation scale, Iwema et al. [2017] showed that CRNS-derived soil moisture information can improve the model calibration compared to point-scale sensors in some cases. Moreover, research conducted by Dimitrova-Petrova et al. [2020] revealed a stronger correlation between catchment water storage and near-surface water storage from CRNS-derived soil moisture estimates compared to storage information derived from single point-scale sensors again indicating the higher spatio-temporal representativity of the CRNS-derived soil moisture estimates.

Despite the large sensitive measurement footprint being advantageous in many applications, in some cases it might be obstructive. For example, on the one hand, in cases where the sensitive footprint of the CRNS instrument exceeds the area

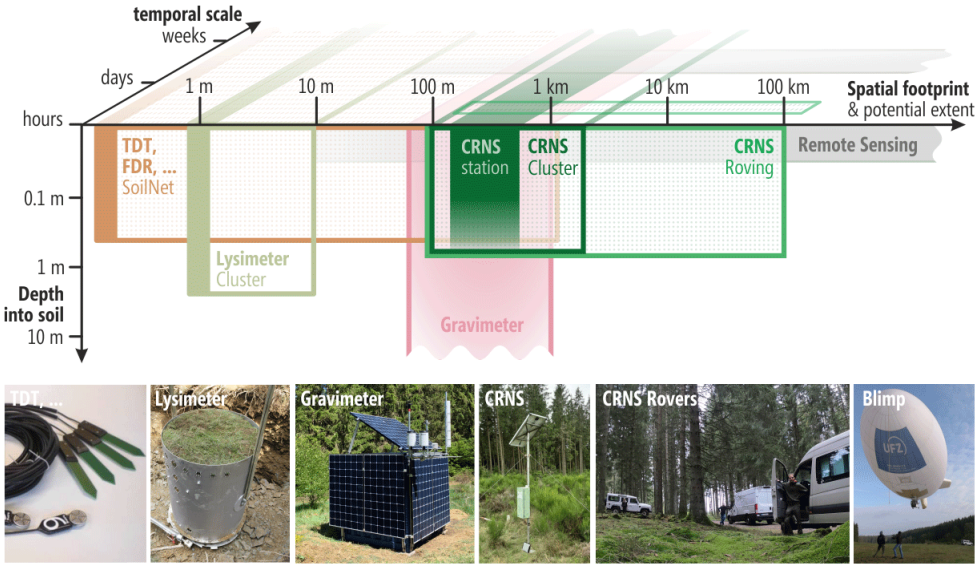

Figure 1.3: Exemplary selection of soil moisture measurement techniques across spatio-temporal scales. The footprint of an individual sensor is displayed solid while minimum temporal resolution and maximum spatial extent of typical applications (e.g. clusters of points-scale in situ TDT and FDR sensors) are depicted by frames in the respective colour [Figure taken from Heistermann et al., 2022].

of interest. This has been addressed by Brogi et al. [2022, 2023] with respect to irrigation monitoring in agricultural fields smaller than the CRNS measurement footprint. On the other hand, difficulties may arise when CRNS-derived soil moisture estimates are used in the scope soil hydraulic modelling efforts. Soil water flow under unsaturated conditions is described by the Richards' equation [e.g. Hopmans et al., 2002]. The required soil hydraulic parameters are highly variable in space and given the strong non-linearity in the functional relationships, averaging hydraulic properties from small-scale measurements such as soil samples to larger scales is difficult [Hopmans et al., 2002]. As a consequence of the high spatial variability of soil hydraulic properties and non-linearities in the functional relationships, soil moisture estimates observed on a larger spatial scale may not be well reproduced by using a single set of soil hydraulic properties in a soil hydraulic model for the entire footprint. Although, some studies showed the potential to inversely derive field-scale soil hydraulic properties from CRNS-derived soil moisture information in combination with soil hydraulic models [e.g. Rivera Villarreyes et al., 2014], this may become difficult in cases where the soil hydraulic properties are not homogeneously distributed with small spatial variability, such as the occurrence of two or more distinctly different soil moisture regimes in the sensitive measurement footprint.

If soil moisture contents and dynamics in the area of interest and the entire CRNS footprint follow a Gaussian distribution with the same average soil moisture content and short correlation lengths, the soil moisture content in the subfootprint area of interest equals the soil moisture content in the entire footprint and its estimation is straightforward. However, if this is not the case and the area of interest exhibits differences in the absolute soil moisture content as well as its temporal dynamics, the estimation is challenging. For example, in case of a binary soil moisture distribution where the entire sensitive measurement footprint comprises two subfootprint areas

with distinct different soil moisture contents, an influence on the observed epithermal neutron intensity can be expected [Franz et al., 2013a]. Here, the interpretation of the integral soil moisture content estimated with CRNS becomes challenging and differentiating between the two soil moisture regimes in order to derive soil moisture estimates in the subfootprint area of interest is difficult. One approach has been suggested by Schrön et al. [2018b] who correct the epithermal neutron signal for binary soil moisture distribution. In their study, a sealed area with no soil moisture changes covered parts of the footprint and dampened the observed neutron count rate. Correcting the neutron signal in order to derive a neutron signal which would occur without the sealed area with constant soil moisture in the footprint, improved the soil moisture estimates for non-sealed areas [Schrön et al., 2018b]. However, challenges remain for heterogeneous CRNS footprints comprising two or more subfootprint areas which have different soil moisture contents varying in time instead of, e.g. a sealed area where a constant moisture content can be assumed.

1.3.5 Vertical footprint limits

Although the large horizontal measurement footprint allows for the estimation of representative soil moisture averages at the field scale, the sensitive measurement depth is limited to a maximum of approx. 80 cm close to the neutron detector and below 50 cm in 300 m distance under extremely dry soil conditions [Köhli et al., 2015]. Under wet conditions, the measurement depth reduces to 15 cm close to the detector and below 10 cm in greater distances which results in a measurement depth around 30 cm for the entire measurement footprint averaged over different soil moisture conditions and distances to the CRNS instrument, i.e. neutron detector. Although this value exceeds the measurement depth of field-scale soil moisture products from e.g. remote sensing, large parts of the root zone and deeper root zone below 100 cm depth remain outside the observational window of the method.

Due to the importance of monitoring soil moisture in layers below the measurement depth of CRNS for several hydrological applications, different studies attempted to derive soil moisture information in greater depths from CRNS-derived soil moisture information [e.g. Peterson et al., 2016; Zhu et al., 2017; Nguyen et al., 2019; Franz et al., 2020]. However, these approaches require either permanently installed in situ reference sensors in the specific depths for continuous estimates of soil moisture in deeper layers or reference measurements in the respective depth of interest for calibrating mathematical models to extrapolate CRNS-derived soil moisture estimates to greater depths. This hampers their applicability when reference measurements in greater depths are not available.

Similarly, the use of CRNS-derived soil moisture estimates for calibrating and evaluating existing e.g. physically-based environmental models including land-surface and rainfall-runoff models is limited to the upper layers of the soil. For example, Boeing et al. [2022] evaluated drought simulations in Germany with soil moisture information from different measurement techniques including CRNS but only assessed the upper 60 cm of the soil as soil moisture information in greater depths is often unavailable. This raises the question if soil moisture in deeper layers can be directly estimated using CRNS in below-ground applications and poses potential for further research.

1.4 Overall aim and research questions

CRNS allows for the estimation of soil moisture at relevant scales of several hectares and in depths exceeding the upper 5 cm of the soil. Therefore, it can provide important information to aid hydrological models for assessing risks and forecasting hydro-meteorological extremes such as floods and droughts and environmental monitoring in general. Yet, several challenges remain to be addressed in order to gain better understanding of the method and its underlying processes as well as to explore potential new fields of application.

Consequently, the overall aim of this thesis is to further advance the CRNS method by gaining further knowledge on the influencing factors on the CRNS signal, the sensitive measurement footprint and to explore the use of CRNS for deriving soil moisture information in greater depths. By addressing the research questions listed below, this thesis not only aims for advancing CRNS from a methodological point of view and thereby addressing one of the unsolved problems in hydrology identified by the scientific community [Blöschl et al., 2019a] but also contributes to improving environmental monitoring efforts. These are pivotal for improved environmental risk assessments and forecasting as well as mitigation and adaption strategies, being of utmost importance against the background of intensifying hydro-meteorological extremes in a changing climate.

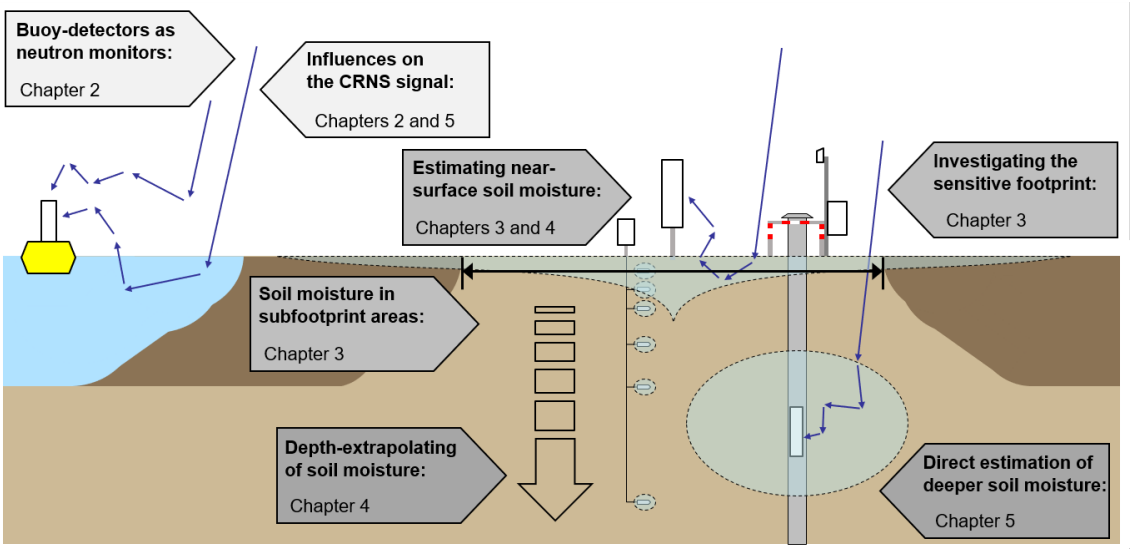

Figure 1.4: Schematic illustration and summary of the research questions in the three parts (grey scale) of CRNS research addressed in this thesis.

This thesis comprises four main chapters addressing research questions in three parts of CRNS research, which are schematically illustrated in Fig. 1.4. The first part concerns the variables other than soil moisture influencing the neutron signals observed in the scope of CRNS:

- What is the influence of air pressure, incoming primary radiation and air humidity on observed thermal and epithermal neutron intensities?

- Which potential yield thermal and epithermal neutron detectors installed above water as an alternative for neutron monitors to correct for variations in incoming primary radiation?

The second part addresses the sensitive measurement footprint and the estimation of soil moisture from CRNS:

- How do newly developed transfer functions perform in comparison with the standard approach in estimating field-scale soil moisture?
- What is the size difference between the footprint of thermal and epithermal neutrons and can it be useful at heterogeneous study sites?
- How can soil moisture be estimated for selected subfootprint areas?

In the third and last part, the potential of CRNS to derive soil moisture information for deeper soil layers is explored:

- To what extent can surface soil moisture information from CRNS be extrapolated to greater depth without reference information of deeper soil moisture?
- What is the potential of downhole CRNS for the direct estimation of soil moisture in the depth of interest?

Chapter 2

The influence of atmospheric, geomagnetic and heliospheric effects on observed CRNS signals

A version of this chapter has been submitted as:

Buoy-based detection of low-energy cosmic-ray neutrons to monitor the influence of atmospheric, geomagnetic, and heliospheric effects

Martin Schrön, Daniel Rasche, Jannis Weimar, Markus O. Köhli, Konstantin Herbst, Bertram Boehrer, Lasse Hertle, Simon Kögler, and Steffen Zacharias

Earth and Space Science (submitted), doi: 10.22541/au.170319441.16528907/v1 (preprint), 2023.

2.1 Abstract

Cosmic radiation on Earth responds to heliospheric, geomagnetic, atmospheric, and lithospheric changes. In order to use its signal for soil hydrological monitoring, the signal of thermal and epithermal neutron detectors needs to be corrected for external influencing factors. However, theories about the neutron response to soil water, air pressure, air humidity, and incoming cosmic radiation are still under debate. To challenge these theories, we isolated the neutron response from almost any terrestrial changes by operating a bare and a moderated neutron detector in a buoy on a lake in Germany from July 15 to December 02, 2014. We found that the count rate over water has been better predicted by a theory from Köhli et al. [2021] compared to the traditional approach from Desilets et al. [2010]. We further found strong linear correlation parameters to air pressure ($\beta = 0.0077\,\mathrm{mb}^{-1}$) and air humidity ($\alpha = 0.0054\,\mathrm{m}^3/\mathrm{g}$) for epithermal neutrons, while thermal neutrons responded with $\alpha = 0.0023\,\mathrm{m}^3/\mathrm{g}$. Both approaches, from Rosolem et al. [2013] and from Köhli et al. [2021], were similarly able to remove correlations of epithermal neutrons to air humidity. Correction for incoming radiation proved to be necessary for both thermal and epithermal neutrons, for which we tested different neutron monitor stations and correction methods. Here, the approach from Zreda et al. [2012] worked best with the Jungfraujoch monitor in Switzerland, while the approach from McJannet and Desilets [2023] was able to adequately rescale data from more remote neutron monitors. However, no approach was able to sufficiently remove the signal from a major Forbush Decrease event on September 13th, to which thermal and epithermal neutrons showed a comparatively strong response. The buoy detector experiment provided a unique dataset for empirical testing of traditional and new theories on CRNS. It could serve as a local alternative to reference data from remote neutron monitors.

2.2 Introduction

The natural background radiation on Earth is mainly produced by the omnipresent and continuous exposure to galactic cosmic rays, which are modulated by solar activity, filtered by the geomagnetic field, and moderated by the Earth's atmosphere [Hess et al., 1961; Dorman, 2004; Usoskin et al., 2011]. Since 1951, neutron monitors have been in operation at various places around the globe to continuously monitor high-energy cosmogenic neutrons as a proxy for space weather [Väisänen et al., 2021]. About half a century ago, Kodama et al. [1975] revealed the potential of the lower energetic component of cosmic-ray neutrons for estimating water content in snow. Two decades after Kodama [1980] and Kodama et al. [1985] presented more experimental findings also related to soil moisture, Dorman [2004] proposed the broader use of this concept for hydrological applications. Yet, Zreda et al. [2008] were the first to introduce the methodological framework of Cosmic-Ray Neutron Sensing (CRNS) and to demonstrate its potential for large-scale monitoring of soil moisture. Soon after, Desilets et al. [2010] proposed an empirical but turned-out-to-be robust relationship to convert neutrons to soil moisture, followed by Zreda et al. [2012] presenting the concept and establishment of a continental CRNS network. To date, CRNS is a growing non-invasive and low-maintenance technique providing continuous hectare-scale root-zone soil moisture to inform and validate products of

hydrological models [Baatz et al., 2014; Iwema et al., 2017; Patil et al., 2021] and remote sensing [Montzka et al., 2017; Döpper et al., 2022; Schmidt et al., 2024].

The ambient epithermal neutron radiation above the ground is of key interest for CRNS, as this energy band shows the highest sensitivity to hydrogen in soils [Desilets et al., 2010; Zreda et al., 2012; Köhli et al., 2015]. Some CRNS probes additionally measure thermal neutrons as a potential proxy for soil chemistry, snow, biomass, or spatial heterogeneity [Tian et al., 2016; Jakobi et al., 2022; Rasche et al., 2021]. In order to isolate the response of neutrons to the ground from external influences, CRNS data processing heavily relies on accurate corrections for changes in atmospheric shielding depth (i.e., air pressure), atmospheric hydrogen content (i.e., air humidity), and incoming cosmic rays (i.e., high-energy hadron flux). For epithermal neutrons, such corrections have been proposed based on literature about high-energy cosmic rays [Desilets et al., 2006; Zreda et al., 2012] or on dedicated simulations [Rosolem et al., 2013]. However, no commonly accepted correction approaches exist for thermal neutrons, while the transferability of the epithermal correction functions is under debate [Andreasen et al., 2016; Jakobi et al., 2018, 2022; Rasche et al., 2021].

There is an ongoing debate about many aspects of CRNS theory and the traditional correction approaches since correlations to external signals were sometimes not removed sufficiently, and unexplained variations in the data remained. For example, Köhli et al. [2021] used new simulation approaches to explain neutron variations specifically in semi-arid regions, where limitations of the widely established approaches from Desilets et al. [2010] and Rosolem et al. [2013] became evident. However, the simulations from Köhli et al. [2021] were also insufficient to conclude on a final choice out of many offered correction models. Moreover, many authors have found inconsistencies in using the neutron monitor "Jungfraujoch" in Switzerland as a reference for the incoming cosmic-ray flux at different periods and locations on Earth [e.g. Hawdon et al., 2014; Schrön, 2017; Hands et al., 2021]. The main reason is the dependence of the cosmic-ray flux on the geomagnetic field, which changes continuously in space and time [Belov et al., 2005; Kudela, 2012; Herbst et al., 2013]. To account for that, authors suggested different correction approaches to rescale data from a neutron monitor site to a CRNS location [Hawdon et al., 2014; McJannet and Desilets, 2023], while their performance is yet to be tested. Nevertheless, more issues complicate the use of the neutron monitor network as a reference for CRNS stations across the world: the instruments measure different neutron energies than CRNS, they are sometimes prone to weather effects, the few neutron monitors have only scarce coverage on Earth, the data exhibits varying consistency and quality, and a single institute is responsible for the data provision and processing [Bütikofer, 1999; Aplin et al., 2005; Korotkov et al., 2011; Oh et al., 2013; Abunin et al., 2016; Ruffolo et al., 2016; Väisänen et al., 2021]. Consequently, the future availability of incoming cosmic-ray reference data may not be guaranteed, which explains the current search for alternative concepts [e.g. Schrön et al., 2016; Fersch et al., 2020; Gugerli et al., 2022; Stevanato et al., 2022].

An empirical and objective evaluation of traditional and new theories on the neutron response to the ground, to the atmosphere, and to the magnetosphere, is a challenging endeavour. Any ground-based CRNS measurement inherently depends on the spatial and temporal variability of nearby hydrogen pools, such as soil moisture, biomass, ponding water, etc. [Iwema et al., 2021; Schrön et al., 2023a].

However, such variability can be considered negligible above lakes or other water bodies, where even rain events would not introduce a significant addition of water. Neutron measurements on a lake with a detector that has a comparable energy sensitivity to CRNS could provide a unique data set to investigate the local and "actual" influence of non-terrestrial variability on thermal and epithermal neutrons. In terrestrial CRNS applications, many of the external, ground-related influencing factors are often unknown and thus challenging to model, leading to uncertainties in the interpretation of the CRNS signal. A buoy detector on a lake, however, has a clear pure-water boundary condition and would allow for a more direct comparison of the observations with simulations of the sensor response. Moreover, a lake-based buoy CRNS detector might be even suitable as a reference monitor for the incoming cosmic-ray flux.

The advantage of water bodies beneath a neutron detector has been first reported by Krüger and Moraal [2010], who performed intercalibration measurements of high-energy neutron monitors all over the world by placing a miniature detector over a small nearby pool. CRNS detectors, however, are sensitive to the surrounding environment up to radii of 300 meters [Desilets and Zreda, 2013; Köhli et al., 2015]. Hence, Franz et al. [2013b] suggested short measurements on a lake to calibrate the pure-water limit of the sensor response, which was conducted using rafts for a few days by McJannet et al. [2014], Andreasen et al. [2016] and Rasche et al. [2023]. The first long-term experiment of CRNS detectors on a lake was proposed and conducted in 2014 and later reported by Schrön et al. [2016] and Schrön [2017]. The idea was further extended by Weimar [2022] with static and mobile measurements. The present study performs a first detailed analysis of the data set from 2014 and uses it to challenge traditional correction functions and recent CRNS theories.

The first hypothesis of this study is that state-of-the-art theories about the neutron-to-water relationship can predict the drop in neutron count rates from land to water. Here, we will challenge the widely established method from Desilets et al. [2010] and the more recent findings from Köhli et al. [2021]. With any ground-related changes of water content removed, we further hypothesise that the hitherto established and partly debated correction functions for air pressure [Desilets et al., 2006; Zreda et al., 2012], air humidity [Rosolem et al., 2013; Köhli et al., 2021], and incoming cosmic radiation [Zreda et al., 2012; Hawdon et al., 2014; McJannet and Desilets, 2023] can adequately remove all remaining temporal variations during the study period. The performance of these approaches will also be tested for thermal neutrons, for which no study has yet confirmed their applicability. Finally, we propose using the buoy detector as an alternative for neutron monitors as a reference for incoming radiation, and test this hypothesis at a nearby CRNS research site.

2.3 Methods

2.3.1 Detection of cosmic radiation on Earth

Cosmic radiation mainly consists of protons and heavier ions, permanently penetrating the Earth's magnetic field and interacting with the Earth's atmosphere [Simpson, 1983]. Their collision with nitrogen, carbon, or oxygen atoms in the air produces high-energy particle showers, which consist of neutrons, protons, muons, and other particles. Neutrons and protons can be detected by high-energy neutron monitors

(NM) on Earth [Mavromichalaki et al., 2011; Väisänen et al., 2021]. The muon component is regularly monitored by the global muon detector network [Rockenbach et al., 2014]. Both their signals are a measure of the incoming cosmic radiation on Earth's surface and, as such, highly correlated to space weather and solar activity. Besides typical periodicities, such as the 22-year solar cycle, also irregular short-term events may change the incoming cosmic-ray flux significantly. Examples of these striking solar events are Forbush Decreases (FD) or Ground-Level Enhancement (GLE). They are temporary reductions or enhancements of the cosmic ray flux observed on Earth, caused by the passage of a solar flare or coronal mass ejection [Laken et al., 2011; Mishev et al., 2014; Lingri et al., 2019; Hands et al., 2021].

As the cosmic-ray particles interact with the atmosphere, their signal on the ground additionally carries information on atmospheric conditions, such as air pressure, air humidity, and atmospheric temperature. For research on space weather, it is important to correct for such atmospheric factors, while research on the response of cosmic rays to the ground surface requires both atmospheric and heliospheric influences to be corrected for. To investigate these corrections empirically with ground-based sensors, however, it is necessary to exclude any ground-related influencing factors.

The interaction of high-energy cosmic rays with the ground usually produces lower energetic neutrons, which are, in turn, sensitive to environmental factors such as water content [Zreda et al., 2012]. NMs make use of thick high-density polyethylene shields and lead producers to do both, reduce the influence of those low-energy neutrons that have already interacted with the ground, and tailor the sensitivity to direct high-energy cosmic radiation. Data from NMs available from the global neutron monitor database (`https://www.nmdb.eu`) is already corrected for atmospheric pressure and acts as a reference of incoming cosmic radiation on Earth for many adjacent research fields [Mavromichalaki et al., 2011]. The distribution of NM stations across the globe aims at covering a range of geomagnetic locations, since the intensity and variability of cosmic rays are a function of the so-called *vertical cutoff rigidity* of the geomagnetic field, R_c. This quantity relates to the alignment of the magnetic field lines, which acts as an energy filter of the primary cosmic-ray particles that leads to higher radiation exposure at the poles compared to the equator. Table 2.1 shows an overview of the NMs used in this study: Jungfraujoch (JUNG) is the standard reference for incoming radiation correction in CRNS research, Athens (ATHN) exhibits high vertical cutoff rigidity in Europe, Kiel (KIEL) is the closest NM to the study site, Oulu (OULU) exhibits the lowest cutoff rigidity in Europe, South pole (SOPO) the lowest globally, while Daejeon (DJON) and Doi Inthanon (PSNM) may serve as promising candidates to test the correction performance with NMs at very high cutoff rigidities and in very large distance to the study site.

2.3.2 Cosmic-Ray Neutron Sensing (CRNS)

Detectors with a reduced amount of shielding are more sensitive to low-energy neutrons and, thus, to the local environment on the ground. A technology with reduced shielding is called Cosmic-Ray Neutron Sensing (CRNS) and is based on the response of low-energy neutrons to nearby environmental water content [Zreda et al., 2008]. The main energies used in hydrological CRNS applications are the epithermal

Table 2.1: Overview of the Neutron Monitors (NM) and the buoy detector site used in this study, including their coordinates and geomagnetic cutoff rigidity, R_c, from two different sources (values for 2010 from `https://www.nmdb.eu` and for 2014 from `https://crnslab.org/util/rigidity.php`).

Neutron Monitor	Acronym	Country	R_c (2010)	R_c (2014)	Altitude	Latitude	Longitude
Doi Inthanon	PSNM	Thailand	16.80 GV	16.72 GV	2565 m	18.59°	98.49°
Daejeon	DJON	South Korea	11.22 GV	10.75 GV	200 m	36.24°	127.22°
Athens	ATHN	Greece	8.53 GV	8.27 GV	260 m	37.97°	23.78°
Jungfraujoch	JUNG	Switzerland	4.50 GV	4.54 GV	3570 m	46.55°	7.98°
Buoy	Buoy	Germany	2.99 GV	2.93 GV	78 m	51.58377°	12.41423°
Kiel	KIEL	Germany	2.36 GV	2.31 GV	54 m	54.34°	10.12°
Oulu	OULU	Finland	0.80 GV	0.63 GV	15 m	65.05°	25.47°
South Pole	SOPO	Antarctica	0.10 GV	0.06 GV	2820 m	-90°	0°

neutrons (with energies between 0.5 eV and 10^5 eV), and thermal neutrons (energies below 0.5 eV), as they show the strongest variation with water content [Köhli et al., 2015]. In dry soil, the epithermal neutrons produced by the penetration of high-energy particles may leave the ground almost unhindered. In wet soil, on the other hand, the higher concentration of hydrogen efficiently moderates the neutrons on their way, leading to less epithermal neutron counts above the surface. While epithermal neutron variations are mainly dependent on the hydrogen abundance, thermal neutron radiation shows an additional dependency on chemical components and is still a subject of research. Thermal neutrons can be detected with standard neutron detectors, such as proportional counters. Epithermal neutrons can be detected with an additional layer of high-density polyethylene around these bare detector tubes [Zreda et al., 2012; Schrön et al., 2018b].

The wetness of the ground is usually expressed as the soil moisture θ in units of g/g. Conversion functions exist to describe its relationship to epithermal neutrons, $N(\theta)$. The traditional function has been introduced by Desilets et al. [2010]:

$$N^{\mathrm{Des}}(\theta) \propto \frac{0.0808}{\theta + 0.115} + 0.372. \tag{2.1}$$

It is independent on hydrogen in air, for instance, which could be addressed by a separate correction factor on the neutrons (see section below). A recent study by Köhli et al. [2021] introduced a universal transfer solution (UTS) for soil moisture conversion which is inseparable from the air humidity, h in g/m^3, of the environment:

$$N^{\mathrm{UTS}}(\theta, h) \propto \left(\frac{p_1 + p_2\,\theta}{p_1 + \theta} \cdot \left(p_3 + p_4\,h + p_5\,h^2\right) + e^{-p_6\,\theta}\,\left(p_7 + p_8\,h\right) \right), \tag{2.2}$$

where p_i represents a range of parameter sets out of many possible candidates offered by Table A1 in Köhli et al.. They either depend on different simulation approaches or employ different energy response functions [see also Köhli et al., 2018]. The parameter set "MCNP drf" was derived from MCNP [Goorley et al., 2012] simulations, which include interaction processes of neutrons, protons, muons, and other particles. It also integrates the actual detector energy response function (drf) of the CRNS instrument. In contrast, the parameter set "MCNP THL" uses the MCNP model

with a less accurate energy threshold window. Parameter sets "URANOS drf" and "URANOS THL" express similar detector models, while URANOS has been used instead of MCNP to simulate the neutron response to soil and water, which includes only neutron particle interactions and some effective and less accurate representation of other particles [see Köhli et al., 2023, for details].

Both approaches, Desilets et al. [2010] and Köhli et al. [2021], have in common that they provide a relative value for neutron count rates that can be scaled with a factor N_0, usually referred to as a calibration parameter. It is different for each approach and parameter set but essentially mimics the detector-specific count rate at a very dry state of the soil. From calculations using typical ranges of θ and h it follows that the N_0 values for the UTS function are larger than N_0 for the Desilets approach by factors of 1.61, 2.09, 1.58, and 2.03 for the parameter sets "MCNP drf", "MCNP THL", "URANOS drf", and "URANOS THL", respectively.

To date, there is no published evidence of a preferred parameter set for CRNS data processing with the UTS approach. Standard evaluation procedures would require a high number of auxiliary measurements of soil moisture in the sensor footprint and different depths, in addition to consideration of spatial heterogeneity and other disturbing factors typically present at most field sites. However, an experiment with $\theta = \text{const.}$ could facilitate an empirical determination of $N(h)$ to shine a light on a suitable parameter set that describes this part of the model realistically.

A water body is expected to produce a minimal number of neutrons, which, unlike for soils, does not change as a result of rainfall events (i.e., $\theta = \text{const.}$). Hence, it is expected that neutrons measured above a lake are only dependent on atmospheric conditions or solar activity. In the pure-water environment, we follow the limes approach by Schrön et al. [2023a], $\theta \to \infty$, with which Eq. (3.1) reduces to:

$$\lim_{\theta\to\infty} N^{\mathrm{Des}}(\theta) = 0.372\,, \tag{2.3}$$

while Eq. (2.2) reduces to:

$$\lim_{\theta\to\infty} N^{\mathrm{UTS}}(\theta, h) = p_2\,(p_3 + p_4\,h + p_5\,h^2)\,. \tag{2.4}$$

The latter varies from 0.15 to 0.28 depending on air humidity and on the chosen parameter set [Table A1 in Köhli et al., 2021].

2.3.3 Atmospheric and geomagnetic corrections

Previous studies have introduced correction functions for the measured neutrons to remove the effect of air pressure P, air humidity h, and incoming radiation I. Conventionally, these functions are usually treated as factors on the neutron counts (except for Eq. (2.2)):

$$\begin{aligned}
\text{humidity-corrected} \quad & N_h = N(\theta)\cdot C_h\,,\\
\text{pressure-corrected} \quad & N_P = N(\theta)\cdot C_P\,,\\
\text{incoming-corrected} \quad & N_I = N(\theta)\cdot C_I\,,\\
\text{fully-corrected} \quad & N_{hPI} = N(\theta)\cdot C_h\cdot C_P\cdot C_I\,.
\end{aligned} \tag{2.5}$$

Air humidity can be corrected by two different approaches. The established approach by Rosolem et al. [2013] uses a separate correction factor based on the air humidity h (in g/m^3):

$$C_h = 1 + \alpha\,(h - h_{\mathrm{ref}})\,. \tag{2.6}$$

The parameter α accounts for water vapor in the near or total atmosphere. It was determined by Rosolem et al. [2013] using neutron transport simulations. However, systematic experimental validation has not been reported, yet. The other approach refers to Eq. (2.2), which intrinsically accounts for air humidity in a non-separable way. In this case, $N_h \equiv N(\theta, h)$ or $C_h = 1$.

Air pressure can be corrected for using an established exponential function:

$$C_P = e^{\beta(P - P_{\mathrm{ref}})}\,. \tag{2.7}$$

The attenuation coefficient β equals the inverse attenuation length, L^{-1}, and has been used for decades to process atmospheric correction of cosmic rays. It can be determined using different analytical relations [Clem et al., 1997; Dunai, 2000; Desilets et al., 2006], by minimising the correlation between incoming radiation and air pressure [Sapundjiev et al., 2014], or by comparing neutron time series with a reference station, where β is known [Paschalis et al., 2013]. These various approaches show that β might be a complex variable that depends on several factors, such as latitude, altitude, type and energy of incident particles [Clem and Dorman, 2000; Dorman, 2004, and references therein], on variations during the solar cycle and during solar flare events [Dorman, 2004; Kobelev et al., 2011], and on properties and yield function of the detector device [Bütikofer, 1999].

We make use of an established calculation of L following Dunai [2000] and Desilets and Zreda [2001]:

$$\beta^{-1} = L(i) = y + \frac{a}{\left(1 + e^{(x-i)/b}\right)^c}\,, \tag{2.8}$$

where i is the Earth's magnetic field inclination and the empirical parameters are: $a = 19.85$, $b = -5.43$, $x = 62.05$, $y = 129.55$. The inclination at the buoy's location can be determined from National Centers for Environmental Information [2015] and was $i = 66.9\,^\circ$. This leads to a theoretical prediction of $L = 129.7\,\mathrm{g/cm^2}$ or $\beta = 0.0077\,\mathrm{mbar}$. An alternative tool that is often used by the CRNS community, is the website http://crnslab.org/util/rigidity.php, which predicts $L = 137.0\,\mathrm{g/cm^2}$ or $\beta = 0.0073\,\mathrm{mbar}$ for the buoy location. However, both tools are also based on calculations derived for high-energy particles and a specific temporal state of the magnetosphere, while the neutron attenuation has never been explicitly identified for the lower-energetic CRNS detectors. Given the uncertainty in determining the correct value for the attenuation coefficient, in this study, we have initialised our analysis with an average value of $L = 133.0\,\mathrm{g/cm^2}$.

The approach for correcting incoming radiation has been first formulated by Zreda et al. [2012] and generalised by Schrön et al. [2016]:

$$C_I = \left(1 - \gamma \left(1 - I/I_{\text{ref}}\right)\right)^{-1} . \tag{2.9}$$

It uses reference data I from the neutron monitor database that measures only the incoming, high-energy component of the cosmic radiation at a few selected locations on Earth. The parameter γ depicts the amplitude scaling of signal variations depending on geomagnetic location. The conventional approach has been assuming $\gamma = 1$, but it failed to remove the incoming cosmic-ray variability, especially for large distances between CRNS and NM sites. The underlying challenge is the dependency of the incoming signal on the geomagnetic location, expressed by the cutoff rigidity, R_{c} in GV, of the geomagnetic field. For example, sites near the geomagnetic poles see different cosmic-ray particles than sites near the equator. So ideally, reference data for incoming radiation should be collected from an NM near the CRNS measurement site, i.e., at a similar cutoff rigidity.

Hawdon et al. [2014] presented a scaling concept to account for this geomagnetic effect using $\gamma = 1 - 0.075\,(R_{\text{c}} - R_{\text{c}}^{\text{ref}})$, however, this approach has not been tested globally. A more recent approach by McJannet and Desilets [2023] uses so-called scaling factors that depend on R_{c} and on the atmospheric depth x for both the location of the site and of the neutron monitor used as a reference:

$$C_I = \tau^{-1} , \tag{2.10}$$

$$\tau(x, R_c) = \tau_{\text{ref}}^{-1} \cdot \epsilon\ \left(-p_0\, x + p_1\right) \left(1 - \exp\left(-\left(p_2\, x + p_3\right) R_{\text{c}}^{p_4\, x - p_5}\right)\right) , \tag{2.11}$$

with parameters p_i fitted on historical NM data. An empirical test of these approaches for the correction of incoming radiation is still missing.

Besides various correction functions, the neutron data presented in this study has been smoothed by temporal aggregation or moving average filters. These temporal smoothing approaches are useful to reduce noise in highly resolved time series in order to improve further comparative calculations, correlations, or visualisations. In the current processing scheme, the correction functions have been applied on the raw data first, followed by subsequent smoothing. Since there is also a debate about the correct order of these processing steps, we elaborated on this discussion in more detail in 2.6.

2.3.4 The buoy deployment

To address the open questions on an empirical evaluation of atmospheric and geomagnetic correction approaches for the CRNS method, we decided to deploy a CRNS detector system on a lake. With a minimum amount of surrounding material, a detector system with a thermal and an epithermal neutron counter would mainly "see" the surrounding lake water. As the amount of water surrounding a floating device remains the same, the CRNS detector was not effected by precipitation or evapotranspiration and the total ground-related influence on the neutrons could be assumed constant. The remaining variations of neutrons should be induced by atmospheric conditions or solar activity only. An ideal set of correction functions would be able to reduce the neutron variations over time to zero ± stochastic errors.

For this experiment, we chose the lake *Seelhausener See*, which was located about 100 km southwest of Berlin, Germany, at the border between the federal states Saxony and Saxony-Anhalt (Fig. 2.1a). The lake had formed in the abandoned opencast of a lignite mine [e.g. Geller et al., 2013]. The lake is still not accessible for public use and thus offered the perfect place for exposing sensible technology in the environment. The surrounding is flat land with mainly natural vegetation.

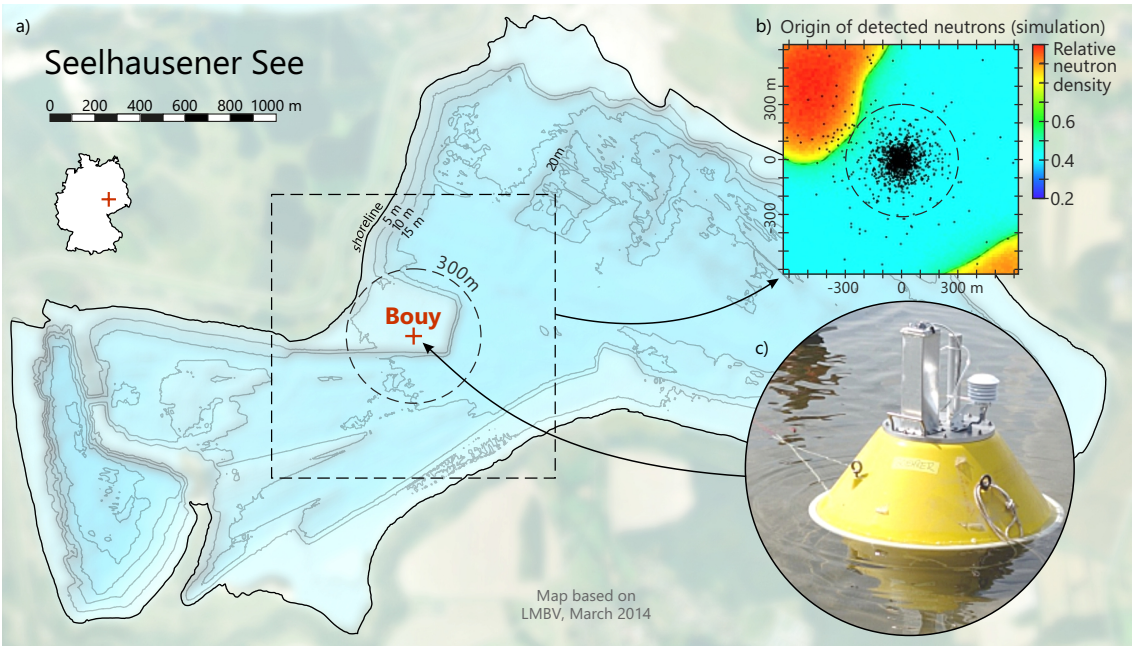

Figure 2.1: a) Location of the CRNS buoy detector at lake *Seelhausener See*. b) The distance of 300 m from the shoreline was chosen such that more than 98,% of detected neutrons had contact to water only (black dots, simulated with URANOS). c) Photograph of the buoy in operation. Map credits: adapted from LMBV, March 2014.

In the preparation of this study, the URANOS model by Köhli et al. [2023] has been used to simulate the origin of the detected neutrons, following the signal contribution concept presented by Köhli et al. [2015] and Schrön et al. [2023a]. The environment has been modelled in a $700 \times 700\,\mathrm{m}^2$ domain (Fig. 2.1b) with a virtual detector above water, a given land structure with 10 % soil moisture, and air with $10\,\mathrm{g/m^3}$ humidity. We found that a distance of ≈ 300 m from the shore is appropriate to limit the influence of the land on the buoy detector to less than 2 %.

Instruments were placed inside a buoy of type `601 Profiler` from Idronaut S.r.l. and then tied between two anchors at the coordinates (51.58377 °, 12.41423 °) (Fig. 2.1c). Each rope was put under tension by mounting a trawl net ball (see Fig. 2.2). Other then usual anchoring techniques [e.g. Boehrer and Schultze, 2008], this arrangement kept the buoy in place within about 1 m and in the same orientation independently of rising or falling water levels over the entire study period.

The moderated and the bare tube was taken from a standard stationary CRNS system of type CRS1000 (Hydroinnova LLC, Albuquerque, US) that had previously been operated at the UFZ Leipzig [Schrön et al., 2018b]. The detectors were disassembled and integrated in a tailor-made aluminium lid, protruding upwards from the buoy (Fig. 2.2). The system was powered by eight batteries of type Yuasa NPL,

38 Ah, using lead-fleece technology to guarantee proper functioning under wobbling conditions. After installation on July 15th, 2014, the batteries had to be recharged by the end of September as the power supply lasted 2.5 months. Finally, the buoy was retracted under frosty conditions on December 2nd, 2014. An antenna regularly transmitted sensor data and GPS coordinates to an FTP server to allow scientists to remotely keep track of the battery status, and for the sake of protection against theft and tempest. The system further included external sensors for air temperature, relative air humidity, and air pressure to facilitate atmospheric corrections.

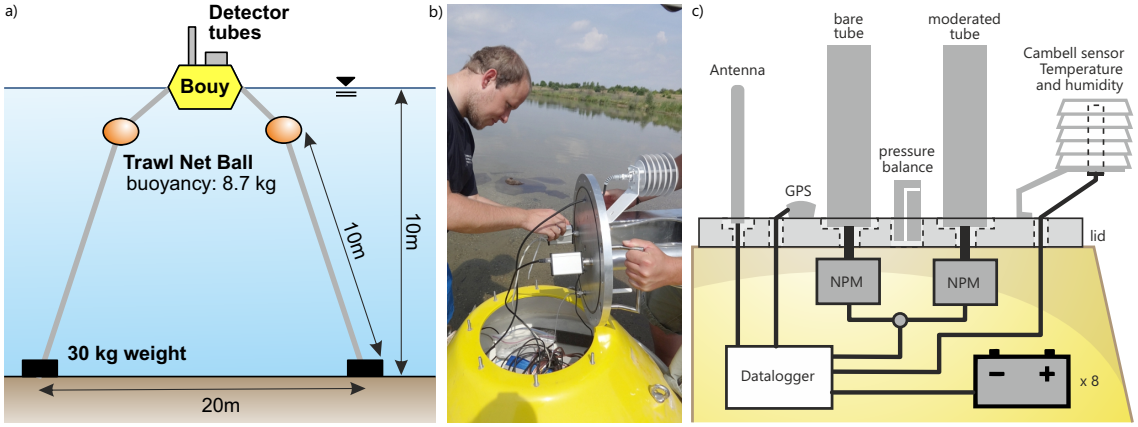

Figure 2.2: a) Setup of the buoy in the lake at around 10 m depth using trawl net balls and weights. b) Final checks with an open lid near the shore before the final launch into the water. c) Detector housing inside the tailor-made lid of the buoy, including GPS, antenna for data transmission, external sensors for air conditions, and a large battery array.

2.4 Results and Discussion

2.4.1 Buoy dataset

The measurement data of the buoy system is shown in Fig. 2.3. From July to December 2014, the air pressure varied by 30 mbar, while air temperature decreased from 20 °C to 0 °C and relative air humidity increased from 40 to 100 %. We have also calculated the absolute air humidity, h, following Rosolem et al. [2013]. The epithermal neutron count rate has been 416 ± 41 cph, while thermal neutrons showed on average 240 ± 31 cph. According to counting statistics following Schrön et al. [2018b], the expected stochastic error of the epithermal neutron count rate would be ± 20 cph (hourly) or ± 4 cph (daily), and of thermal neutrons ± 15 cph (hourly) or ± 3 cph (daily). In this context, the actually measured count rate already indicates a non-negligible influence of atmospheric and heliospheric factors. The time series has been gap-free with the exception of a short maintenance period in September 30th. Additionally, a Forbush Decrease event has been captured on September 13th, which led to a significant drop of neutron count rates by ≈ 10 %.

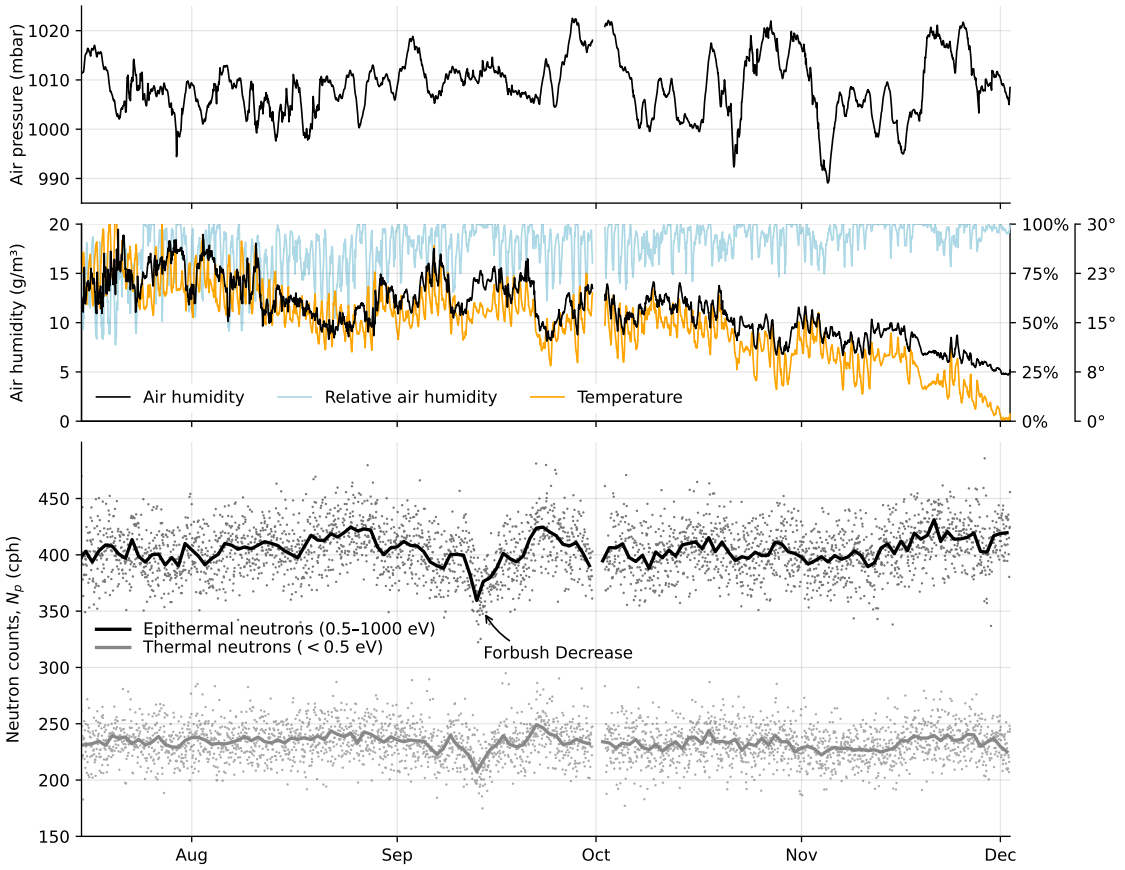

Figure 2.3: Data collected with the buoy instrument in 2014. Top: Air pressure. Middle: External air humidity and temperature. Bottom: pressure-corrected neutron counts of epithermal (0.5–1000 eV, black) and thermal energies (0–0.5 eV, grey). Dots depict hourly measurements, and solid lines depict the daily aggregation. A Forbush Decrease event has been detected on September 13th. Maintenance work, including battery exchange, has been conducted on September 30th.

2.4.2 Challenging the neutrons-to-water relationship

Compared to typical over-land locations, the detector showed a significant drop of neutron counts over water by almost 50 % [compare Schrön et al., 2018b, , Fig. 3]. Based on this observation, it was possible to test whether the existing concepts to describe the relationship between neutrons and water content, $N(\theta)$ (Eqs. (3.1), (2.2)), make the correct predictions following Eqs. (2.3) and (2.4).

The same detector type used in the buoy, CRS1000, has also been used on other locations, where $N_0^{\mathrm{Des}} \approx 1000$ cph has been determined through calibration [see e.g., Bogena et al., 2022]. This corresponds to $N_0^{\mathrm{UTS}} = 1610$ cph, 2090 cph, 1580 cph, and 2030 cph for the UTS parameter sets "MCNP drf", "MCNP THL", "URANOS drf", and "URANOS THL", respectively (section 2.3.2). Based on the assumption that these N_0 parameters are also applicable to the buoy detector, the expected count rate in a pure-water environment (Eqs. (2.3), (2.4)) would become 372 cph, 411 cph, 322 cph, 302 cph, 315 cph for the five approaches, respectively. Hence, the measured average count rate of 416 cph on the lake is in best agreement with the theoretical value of the "MCNP drf" parameter set from Köhli et al. [2021] for

$\theta \to \infty$. The agreement is certainly within the uncertainty band of the data (see Fig. 2.3), while the remaining discrepancy could arise from a non-negligible effect of neutrons produced by the buoy material and the lead batteries themselves.

From this analysis, we can draw two conclusions. Firstly, the recently suggested parameter set for $N(\theta, h)$ derived from the full particle-physics model (MCNP) and the full detector response model (drf) fits best to the measured data and thus creates evidence for its potential superiority over the other parameter sets, including the approach from Desilets et al. [2010]. Secondly, the buoy detector in this study seems to be a suitable representation of a pure-water scenario despite the substantial extent and material of the buoy itself and despite the finite distance to the shore.

2.4.3 Correlation of epithermal and thermal neutrons to external factors

The influences of (i) air pressure, (ii) air humidity, and (iii) incoming radiation on epithermal neutrons have been addressed in the literature, where various approaches exist to correct for these effects (section 2.3.3). Corrections for thermal neutrons have not been investigated so far, usually following the assumption that the same functions apply for them, too. For both neutron energies, however, empirical validation remains difficult, since neutron measurements above soils are always governed by the spatial and temporal variability of soil moisture, as well as by the site-specific heterogeneity [Schrön et al., 2023a]. In contrast, it is expected that neutron observations on a lake would not show terrestrial variability, thereby allowing for an evaluation of non-terrestrial correction approaches.

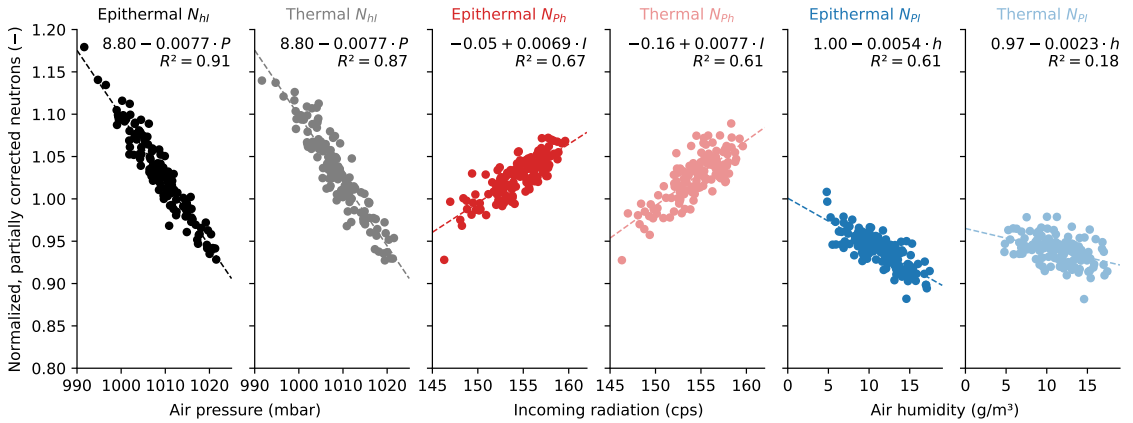

Figure 2.4: Partially corrected daily epithermal and thermal neutron observations normalised by their mean, correlated with three meteorological variables. Left two panels: neutrons corrected for air humidity and incoming radiation versus air pressure. Middle two panels: neutrons corrected for air humidity and air pressure versus incoming radiation. Right two panels: neutrons corrected for air pressure and incoming radiation versus air humidity. Each panel also shows the parameters of a linear model fit (dashed line).

Fig. 2.4 shows the correlation between the daily relative neutron intensity and atmospheric variables. In each panel, neutron counts have been corrected for two variables and correlated to the corresponding third variable (compare section 2.3.3).

Variations in air pressure exert the strongest influence on epithermal neutrons ($R^2 = 0.91$), followed by variations in incoming radiation ($R^2 = 0.67$), represented by data from the JUNG NM, and absolute air humidity ($R^2 = 0.61$). Thermal neutrons follow the same rank order.

For air pressure, the correction parameter $\beta = 0.0077\,\mathrm{mb}^{-1}$ seems to be an adequate choice for both thermal and epithermal neutrons. It matches exactly (within the uncertainty bounds) with the theoretical value of 0.0077 predicted by Dunai [2000]. However, it differs slightly from the value of 0.0073 suggested by Desilets et al. [2006] and the corresponding and typically used calculation tool http://crnslab.org/util/rigidity.php. Note that β can change in time and space, such that the value determined in this experiment is not globally transferable. Further research should investigate the performance of the two methods with experimental data at other locations.

The regression coefficient for absolute air humidity, $0.0054\,\mathrm{m}^3/\mathrm{g}$, exactly matches the linear correction factor α derived by Rosolem et al. [2013], confirming the robustness of this approach. Unlike for epithermal neutrons, the correction procedure required for thermal neutrons has remained under debate. For instance, Andreasen et al. [2016] and Rasche et al. [2021] did not correct thermal neutrons for variations in air humidity, arguing that the traditional correction functions have been derived for epithermal neutrons only. From dedicated simulations, Rasche et al. [2023] found a new value for thermal neutron correction, $\alpha = 0.0021\,\mathrm{m}^3/\mathrm{g}$. In contrast, based on empirical findings, Jakobi et al. [2018, 2022] correct thermal neutron intensities for air pressure and absolute humidity but not for variations in incoming radiation. They claimed that their empirical findings suggested better performance against biomass estimations.

The buoy-detector observations shed light on the required correction procedures for thermal neutrons as the effect of other hydrogen pools (e.g., biomass and soil moisture) on the empirical relationship can be excluded. Fig. 2.4 indicates that thermal neutrons are similarly dependent on variations in air pressure and incoming radiation compared to epithermal neutrons. The largest difference between epithermal and thermal neutrons by applying the same correction occurs in respect to variations in absolute air humidity. We found that the linear regression slope, 0.0023, is less than half of that of epithermal neutrons and very close to the value recently found by Rasche et al. [2023]. The difference of thermal to epithermal neutron response to air humidity is likely linked to the generally higher production rate of thermal neutrons by epithermal neutron moderation than the thermal neutron absorption rate which leads to a weaker response of thermal neutrons to variations in environmental hydrogen [Weimar et al., 2020].

Consequently, the observations in this study indicate that epithermal and thermal neutron intensities need to be corrected for all three atmospheric variables. With respect to existing correction approaches, it is evident that the correction factor for air humidity should be different for epithermal and thermal neutrons, using $\alpha = 0.0054\,\mathrm{m}^3/\mathrm{g}$ [Rosolem et al., 2013] and $\alpha = 0.0021\,\mathrm{m}^3/\mathrm{g}$ [Rasche et al., 2023], respectively.

2.4.4 Apparent correlation of thermal neutrons to water temperature

The observation that the air humidity correction parameters for epithermal and thermal neutrons are different may have significant impact on the growing number of studies related to thermal neutron monitoring. Some previous studies applied the same correction approach from epithermals also to the thermal neutrons without accounting for this difference [Jakobi et al., 2018, 2022; Bogena et al., 2020]. This may introduce a risk of overcorrection and apparent correlation to other variables. In the case of the buoy experiment, the conventional air humidity correction would cause an apparent correlation of thermal neutrons to lake water temperature. In fact, the observed corrected count rate of thermal neutrons in Fig. 2.5a showed a significantly higher correlation to the lake temperature ($R^2 = 0.26$) compared to corrected epithermal neutrons ($R^2 = 0.01$). We will explain below that this connection appears logical at first glance, but it is a fallacy on closer inspection.

By definition, the energy range of thermal neutrons corresponds to the mean kinetic energy of atoms in the environment, and thus their temperature. The theoretical foundation for this phenomenon is the temperature dependency of neutron cross sections [Glasstone and Sesonske, 1981]. The cross section σ represents the probability of an interaction with an atomic nucleus. Interaction is less likely for larger relative velocities between target and particle v, i.e., $\sigma \propto 1/v$. In equilibrium, velocity and temperature are related by the Maxwell-Boltzmann distribution, where the (mean) particle energy is given by $E \propto mv^2 \propto kT$. Hence, σ ultimately depends on the temperature T of the scattering target: $\sigma(T) \propto \sqrt{1/T}$. Since water has a much higher density than humid air, the temperature of the lake might be more relevant than the air temperature.

While the higher temperature increases the thermal neutron density in air and water, it reduces the detection probability of the helium-3 counting gas in the same way [Krüger et al., 2008]. The total observable influence on the thermal neutron count rate is a combination of two effects as air and lake temperatures decrease towards the winter: (i) increasing cross sections of nuclei in air and water, which removes more neutrons on their way to the detector and leads to a decreasing thermal neutron density in the system, and (ii) at the same time, increasing cross sections of nuclei in the Helium-3 gas, enabling higher detection efficiency which leads to higher count rates. Both processes scale with $\sqrt{1/T}$ in different directions. Since lake water temperature and detector temperature show the same dynamics (2.7), the two effects should almost annihilate each other. Fig. 2.5b shows the calculated temperature effect of the lake on the thermal neutron production (blue) and the thermal neutron detection (orange). The combined effects (black) almost cancel each other out and leave a nearly constant influence on the thermal neutron count rate.

Hence, the remaining correlation of thermal neutrons to lake temperature results from the wrong correction coefficient of $\alpha = 0.0054\,\mathrm{m^3/g}$. The observation data in Fig. 2.4 demonstrate that the thermal neutrons response to air humidity is much smaller compared to epithermal neutrons. Using the recently published correction factor, $\alpha = 0.0021\,\mathrm{m^3/g}$ [Rasche et al., 2023], which is very close the empirical observation from the buoy, the new correlation becomes $R^2 = 0.01$ for thermal neutrons and thereby confirms the insignificance of the temperature effect.

The example demonstrates the risk of overcorrection and false conclusions from data when the physical process understanding is incomplete. On the other hand, we cannot exclude remaining features in the data that could indicate systematic influences on the neutron count rate. For example, dew formation or ice on the buoy lid could be responsible for additional neutron moderation in autumn and winter, while extreme variations of shore moisture could impact the count rate in the summer. After a finalised analysis of the known external influences, we have further investigated the remaining correlations in section 2.4.7.

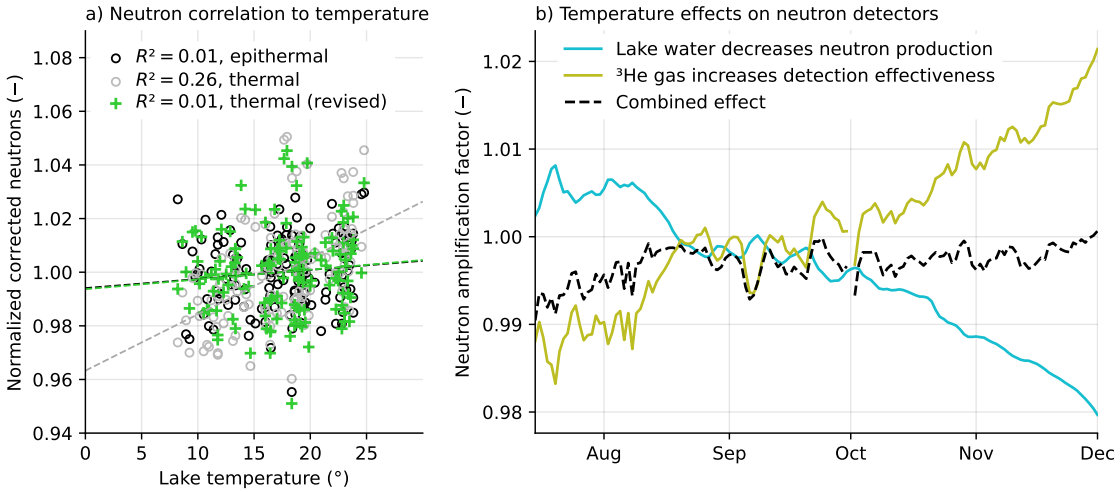

Figure 2.5: The effect of temperature on the measured buoy neutrons. a) Correlation of epithermal (black) and thermal neutrons (grey) to the lake temperature after conventional atmospheric corrections. This introduced an overcorrection for thermal neutrons. A revised air humidity correction approach simulated by Rasche et al. [2023] and confirmed by this study removed this remaining correlation. (b) Processes relevant for neutron production and absorption based on temperature over time. The reduced production of colder water essentially cancels out the enhanced detection efficiency of the detector gas.

2.4.5 Challenging the air humidity correction for epithermal neutrons

As discussed before, air humidity can have a significant effect on the neutron count rate due to varying density and amount of hydrogen atoms in the atmosphere. Rosolem et al. [2013] and Köhli et al. [2021] derived mathematical relationships from neutron transport simulations, but they are difficult to validate experimentally due to the high amount of other influencing environmental variables. With the exclusion of terrestrial factors, such as soil moisture and biomass, the use of lake-side measurements can be again an advantageous solution here.

To investigate which correction approach performs best at the buoy site, we correct the epithermal neutrons with air pressure and incoming radiation (N_{Pi}). If the remaining variability is only related to air humidity changes, the P, i-corrected neutrons should equal the inverse correction factor C_h^{-1}. In this ideal case, this difference is expected to become zero. To quantify the performance of each air

Table 2.2: Root mean square error (RMSE) between the observed corrected epithermal intensity for air pressure and incoming radiation, N_{Pi}, and the inverse air humidity correction C_h^{-1} for the approaches from Rosolem et al. [2013] and UTS (see section 2.3.3). The analysis has also been performed for three different approaches of incoming radiation to test its robustness.

Incoming correction for N_{Pi}	Rosolem et al.	MCNP drf	MCNP THL	URANOS drf	URANOS THL
Zreda et al. [2012]	**5.39**	5.50	6.18	6.42	6.94
Hawdon et al. [2014]	**5.40**	5.48	6.09	6.31	6.82
McJannet and Desilets [2023]	**5.38**	5.48	6.13	6.37	6.88

humidity correction approach, we calculate the root-mean square error (RMSE) between N_{Pi} and C_h^{-1} over the whole measurement period.

Table 2.2 shows the result of this calculation. The hitherto approach from Rosolem et al. [2013] exhibits the lowest RMSE, again confirming a good performance for air humidity correction, see also section 2.4.3. However, the UTS approach with the parameter set "MCNP drf" is comparable in performance with an insignificantly larger error, while other parameter sets show weaker performance. This confirms the results from section 2.4.2 and the robustness of the full particle-physics and detector models. The fact that the approach from Rosolem et al. provides slightly better results than the UTS may be linked to the fact that the UTS was not tailored to describe the neutron response to changing air humidity alone. UTS has been optimised to solve the neutron response to the complex combination of soil moisture and air humidity, which could introduce lesser accuracy for air humidity variations alone.

2.4.6 Challenging the incoming cosmic-ray correction

Buoy-detector observations of neutrons in the epithermal and thermal energy range above a water surface and over a period of several months also allows for a comparison of the different correction approaches available for correcting neutron observations for variations in incoming radiation. The three available correction approaches described in the methods section were tested with seven different neutron monitors shown in Tab. 2.1 and compared with a thermal and epithermal neutron observations corrected for variations in air pressure and absolute air humidity (N_{Ph}), as this correction level should represent variations from changes in incoming radiation, only. In order to reduce the statistical noise in the data from the buoy detector, a 25-hour moving average was applied after applying the corrections. The epithermal and thermal N_{Ph} was then compared to the inverted correction factors for incoming radiation based on Zreda et al. [2012], Hawdon et al. [2014] and McJannet and Desilets [2023] (see section 2.3.3).

Table 2.3 shows the results from the analysis performed for selected neutron monitor stations. The Kling-Gupta Efficiency (KGE) was chosen as the goodness-of-fit measure in order to equally account for variation, correlation, and bias. The analysis reveals that the performance is generally lower for thermal neutrons compared to epithermal neutrons. This can be linked to the higher statistical uncertainty in the thermal neutron data due to the lower count rates. Likewise, a higher difference in cutoff rigidity between the locations of the neutron monitor and the study site

leads to a lower KGE for both neutron energies. However, the Jungfraujoch neutron monitor still reveals the highest KGE, although its cutoff rigidity and altitude are higher than at the study site (compare Tab. 2.1).

Table 2.3: Performance measured by the Kling-Gupta Efficiency (KGE) of different correction approaches to rescale incoming neutron intensities from different neutron monitor stations compared with the observed and P, h-corrected epithermal (E) and thermal (T) neutron counts of the buoy. See also Tab. 2.1 for the corresponding cutoff rigidities and altitudes.

	C_I approach	PSNM	DJON	ATHN	JUNG	KIEL	OULU	SOPO	Average
E	Zreda et al. [2012]	0.269	0.34	0.465	0.737	0.678	0.667	**0.765**	0.560
E	Hawdon et al. [2014]	0.560	0.543	0.640	**0.790**	0.651	0.566	0.692	0.634
E	McJannet and Desilets [2023]	0.639	0.703	**0.761**	0.760	0.647	0.613	0.619	0.677
T	Zreda et al. [2012]	0.220	0.280	0.408	**0.635**	0.594	0.587	0.714	0.491
T	Hawdon et al. [2014]	0.481	0.460	0.567	**0.689**	0.569	0.493	0.614	0.553
T	McJannet and Desilets [2023]	0.627	0.624	**0.699**	0.657	0.565	0.537	0.545	0.608

Furthermore, it can be seen that the approaches from Hawdon et al. [2014] and McJannet and Desilets [2023] improve the KGE for the comparison with neutron monitors with higher cutoff rigidity than the study site compared to the approach after Zreda et al. [2012]. In contrast, for neutron monitors with a lower cutoff rigidity, this improvement disappears and the approach according to Zreda et al. [2012] reveals a higher KGE with the data from the buoy detector. This effect is evident for both epithermal and thermal neutrons. The recent approach from McJannet and Desilets [2023] outperforms the approach by Hawdon et al. [2014], while both only lead to improvements for higher cutoff rigidities compared to the standard approach after Zreda et al. [2012]. On average and over all neutron monitors investigated, the approach after McJannet and Desilets [2023] performs best in scaling neutron monitor signals to the location of the buoy detector, followed by the approach after Hawdon et al. [2014] and Zreda et al. [2012].

All three approaches provided robust results using data from the JUNG NM, with a slightly superior performance of Hawdon et al. [2014] at the study site. Additionally, the correct selection of a reference monitor seems to be more influential than then correction method. The results generally indicate the advanced correction approaches from Hawdon et al. [2014] and particularly McJannet and Desilets [2023] improve the performance only for higher cutoff rigidities (i.e., regions near the equator). These findings may be also linked to the complex behaviour of incoming radiation with different effects occurring at different cutoff rigidities, altitudes, latitudes, and longitudes [López-Comazzi and Blanco, 2020, 2022]. The time series of epithermal and thermal neutrons are shown in Fig. 2.6 together with the time series of the JUNG, PSNM, and SOPO neutron monitors. Especially during the Forbush Decrease in September 2014, a dampening of the neutron signal of the PSNM neutron monitor compared to the JUNG neutron monitor can be seen, which is linked to the higher R_c of PSNM. In addition, a temporal shift between PSNM and JUNG indicates differences between neutron monitor intensities due to different longitudinal locations. Lastly, the epithermal and thermal intensities decrease stronger than JUNG and PSNM, but similar to SOPO. This is an unexpected behaviour, as the cutoff rigidity of SOPO is much lower than at the buoy location. The coincidence

could indicate that low-energy neutron counters generally respond stronger to geomagnetic changes than high-energy NMs. Particularly with regards to the Forbush Decrease, the observed discrepancy could also be linked to a change of the primary cosmic-ray energy spectrum during solar events [Bütikofer, 2018], which may lead to stronger changes of secondary low-energy cosmic-ray neutrons.

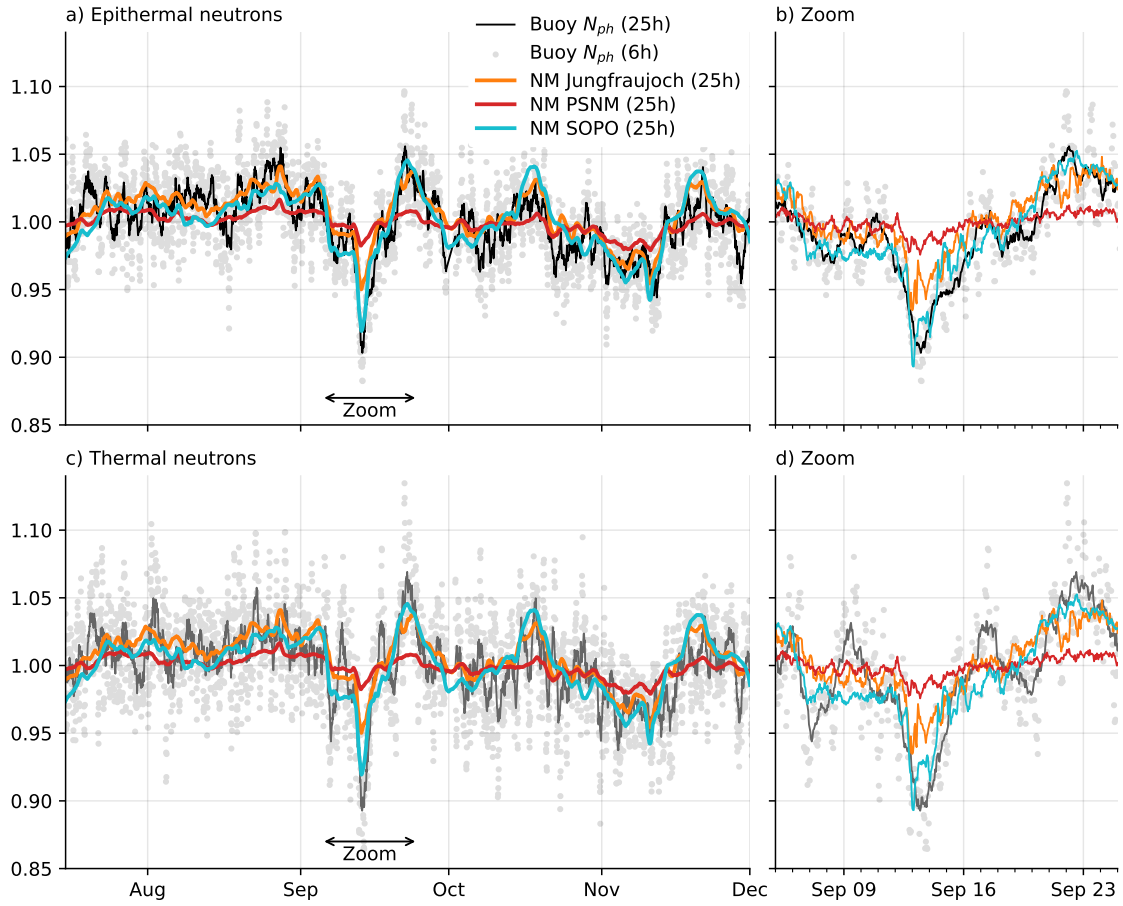

Figure 2.6: Normalised pressure- and humidity-corrected neutron count rates of the buoy detector compared with neutron monitor data. a) Epithermal buoy neutrons with a moving average window of 6 hours (grey dots) and 25 hours (black line). The latter filter was also applied to the NM data from JUNG in Switzerland (orange), PSNM in Thailand (red), and SOPO near the South Pole (blue). b) Zoom-in to the Forbush Decrease event. c-d) Same as a-b for thermal buoy neutrons.

Depending on the moderator material and material thickness, proportional neutron detectors show varying sensitivity to neutrons of different energies [Garny et al., 2009; Köhli et al., 2018]. A difference in the response of a bare thermal neutron detector and a neutron monitor has been shown by Nuntiyakul et al. [2018]. Furthermore, Hubert et al. [2019] found a different response to solar events for neutrons of different energies. For the correction of neutron intensities for incoming radiation in the scope of CRNS, it, therefore, may not be sufficient to scale the neutron monitor response to different cutoff rigidities and atmospheric shielding depths only [Hawdon et al., 2014; McJannet and Desilets, 2023], but also to account for the different response of low-energy neutron detectors and neutron monitors.

The question about the choice of the most suitable neutron monitor for CRNS

correction is equivalent to the question of which monitor better represents the local changes of cosmic-ray neutrons at the CRNS site. Sometimes, the answer is not obvious considering just geographical location parameters. For example, compared to the location of the buoy experiment, the KIEL monitor has more similar distance, altitude, and cutoff rigidity than JUNG. However, the neutron dynamics of the buoy can be better explained by JUNG, while KIEL behaves differently during and beyond the Forbush Decrease event. These findings indicate the need for further research on the role of primary incoming radiation for low-energy Cosmic-Ray Neutron Sensing.

2.4.7 Residual correlations

The proper correction of all influencing factors on the neutrons should result in a time series, where residual deviations from the mean represent Poissonian noise. To test this hypothesis, a correlation analysis of N_{Phi} was conducted using a selection of atmospheric variables. In addition, different aggregation levels have been applied to further test the either random or systematic character of the relationships. The Spearman's rank correlation coefficient is shown in Tab. 2.4. It indicates that the influence of air pressure, incoming radiation, and absolute humidity is removed by the previously discussed correction procedures. However, a significant correlation between the N_{Phi} and relative air humidity remained for all aggregation levels and for both neutron energies.

Table 2.4: Spearman's rank correlation coefficient between the corrected intensity (N_{Phi}) of epithermal (E) and thermal (T) neutrons aggregated to different temporal resolutions. Asterisk indicates statistical significance with $p < 0.05$.

	Variable	aggregation: 1 hour	6 hour	12 hour	24 hour
E	Air pressure	0.04	0.07	0.07	0.1
E	NM (Jungfraujoch)	0.003	0.02	−0.006	0.01
E	Abs. air humidity	−0.02	−0.04	−0.05	−0.09
E	Air temperature	0.003	0.02	0.01	0.0009
E	Rel. air humidity	−0.07*	−0.2*	−0.2*	−0.3*
E	Water temperature	0.01	0.03	0.03	0.008
E	Moist air density	0.006	−0.000004	0.01	0.03
E	Precipitation	0.0005	−0.09	−0.10	−0.20
T	Air pressure	0.03	0.08	0.06	0.03
T	NM (Jungfraujoch)	−0.006	−0.02	−0.04	−0.08
T	Abs. air humidity	−0.04*	−0.08	−0.10	−0.20*
T	Air temperature	−0.0007	−0.01	−0.07	−0.1
T	Rel. air humidity	−0.07*	−0.1*	−0.2*	−0.2*
T	Water temperature	−0.002	0.02	0.03	0.08
T	Moist air density	0.009	0.03	0.08	0.1
T	Precipitation	0.01	−0.006	−0.08	−0.10

High values of relative air humidity may indicate the formation of dew and, thus, a thin film of water on the buoy-detector, which reduces the observed neutron intensity of the epithermal and thermal detector due to higher neutron absorption. For example, Sentelhas et al. [2008] use a threshold of $\geq 90\,\%$ relative humidity

to distinguish periods with leaf wetness. Applying this threshold to the neutron observations reveals that epithermal and thermal N_{Phi} are, on average, 0.44 and 0.56 % lower in periods with dew, respectively. This indicates that some influencing atmospheric variables are not yet considered in the standard correction procedures and illustrates the need for further research.

Furthermore, the statistical accuracy increases strongly with increasing integration times. Already at the 6-hour aggregation level, the Poisson standard deviation of the uncorrected neutron observations becomes lower than 2 %. However, neutron transport simulation revealed that approx. 2 % of epithermal neutrons reach the buoy-detector from the shore, indicating that with higher statistical accuracy, terrestrial variables such as soil moisture variations could influence the neutron observations of the buoy detector. This indicates some limitations of the measurement design in this study and illustrates potential improvements for future lake-side neutron measurements.

2.4.8 Potential for the buoy as a reference for CRNS probes

Typical CRNS stations are located on natural ground to monitor soil moisture dynamics or agricultural fields, grass lands, or even snow dynamics in the alps. The conventional correction approach uses incoming radiation from neutron monitors (e.g., Jungfraujoch) to remove unwanted effects from solar activity, such as Forbush Decreases.

We used data from a nearby terrestrial CRNS site at the UFZ Leipzig (25 km distance), where six identical CRNS stations were co-located on a $20 \times 20\,\mathrm{m}^2$ grassland patch. The sum of their signals mimics a larger CRNS station with up to 6000 cph (≈ 1.4 % uncertainty).

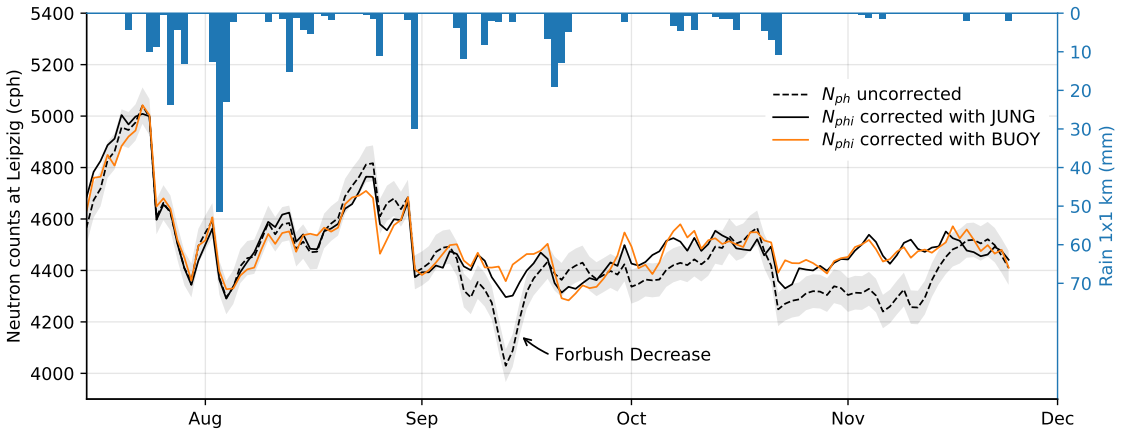

Figure 2.7: Epithermal neutrons aggregated from six collocated CRNS stations at the UFZ Leipzig, 25 km away [Schrön et al., 2018b, data from]. Neutron counts were corrected for air pressure and air humidity (dashed black) and corrected for incoming radiation using NM Jungfraujoch (solid black) and the buoy data (solid orange). Daily precipitation is indicated from Radolan measurements.

Figure 2.7 shows the epithermal neutron data from this aggregated sensor corrected for air pressure and air humidity (dashed line). The solid line shows the data conventionally corrected for incoming neutrons with the NM Jungfraujoch. It is

evident that the correction generally improves the obvious response to rain events, but the correction of the Forbush Decrease in September 13 was not strong enough. The orange line shows the same correction approach with the epithermal neutron data measured at the same time by the buoy. The data was filtered by a 3-day moving average to reduce the buoy's noise level. The correction using the local buoy data better removes the Forbush Decrease from the corrected CRNS neutron counts (September 13) and is also able to strengthen the response to some rain events (e.g., August 24 and September 17).

The results demonstrate that the concept of buoy detector can be used as an alternative to neutron monitors to correct for the incoming radiation. However, measurements on the buoy are limited by the low count rate due to the surrounding water and small detectors, such that there is a risk of introducing additional noise to the CRNS station data by this correction approach.

2.5 Conclusions

This study presents the concept of a thermal and an epithermal neutron detector in a buoy on a lake. The arrangement depicts an innovative opportunity to monitor the response of low-energy cosmic-ray neutrons to atmospheric conditions and to space weather without the influence of the ground, soil moisture, or any other nearby terrestrial heterogeneity that can influence the neutron counts. The experiment conducted on a lake in East Germany covered an almost gap-free period of five months from July 15th to December 2nd, 2014, including temperatures from 30 to 0 °C, and - by chance - a major solar event (Forbush Decrease). The unique data set facilitates empirical research on challenging conventional theories and traditional correction functions for atmospheric, geomagnetic, and heliospheric variations. The experiment revealed the following insights:

1. The epithermal neutron count rate over water dropped by more than 50 % compared to values over typical soil. The measured count rate was not in agreement with the theoretical value predicted by the previous $N(\theta)$ model [Desilets et al., 2010]. In contrast, the value was almost exactly predicted by the UTS approach [Köhli et al., 2021] using the parameter set "MCNP drf". This finding might indicate a potential superiority of UTS for the conversion from neutrons to soil moisture also for other CRNS applications.

2. The buoy data showed strong correlation to air pressure, which was similar for both, epithermal and thermal neutrons. The thereby empirically determined neutron attenuation length was in very good agreement with the theoretical prediction by Dunai [2000], while it was 5 % lower than the conventional calculation for this region. This indicates that further research is needed to better adapt traditional calculation methods on the special requirements of low-energy neutron detectors.

3. The different approaches for air humidity correction have been challenged by their ability to remove undesired variations of the buoy signal. The conventional approach by Rosolem et al. [2013] performed best and its parameter $\alpha = 0.0054$ has been confirmed for epithermal neutrons. Almost similar performance was achieved by the UTS approach using the parameter set "MCNP

drf", while all other parameter sets were not able to fully remove air humidity variations.

4. Conventional thermal neutron corrections for air humidity, however, led to a significant overcorrection. A potential influence of lake water temperature on the thermal neutrons has been excluded by analysis of the nuclear interaction cross sections. A different correction parameter for thermal neutrons has been identified, which confirmed independent results from Rasche et al. [2023].

5. The response to incoming cosmic radiation is almost similar for both, epithermal and thermal neutrons, in contrast to assumptions by some previous studies. We challenged three existing correction approaches by comparing the buoy data with data from various neutron monitors and found robust performance for NM Jungfraujoch and the approach from Zreda et al. [2012]. The more sophisticated approaches by Hawdon et al. [2014] and McJannet and Desilets [2023] showed particularly good skills in rescaling data from NMs with higher cut-off rigidities than the measurement site.

6. The remarkable Forbush Decrease (FD) observed in Sept 2014 was more pronounced in the buoy data than in data from the NMs, particularly for thermal neutrons. In addition to the findings from the pressure correction above, this is another indication that the scaling of incoming radiation from NMs to CRNS is not well enough understood, probably due to the sensitivity to different particle energies.

7. After all corrections were applied, the remaining variations of the buoy signal have been investigated. For both, thermal and epithermal neutrons, a significant correlation to relative air humidity became evident, which could be an indication for yet unnoticed sensitivity to dew.

In a final test, we used the buoy data as a reference signal for the incoming radiation correction of a nearby CRNS site. Here, a slightly better correction capability was evident, particularly during the FD event. This experiment demonstrated that a buoy could act as a suitable local alternative for a neutron monitor, especially since it measures similar energy levels as the CRNS, it is much cheaper than an NM, and it could be installed more closer to CRNS sites, thereby avoiding any geomagnetic or location-specific biases. However, buoys are limited in size, such that their data is highly uncertain due to the low count rates. Daily temporal resolution was the minimum for our system to be applicable as a reference monitor. To overcome this weakness, future studies could deploy buoy detectors on high-altitude lakes or glaciers, which would equally well resemble a pure-water environment for the neutrons with much higher count rates [e.g. Gugerli et al., 2019, 2022].

We encourage the usage of the presented data set for further research on new theories or correction functions. One more example is the debate of whether to apply temporal smoothing algorithms before or after atmospheric corrections. With the buoy data, we were able to show that correction prior to smoothing is crucial for maintaining correlation to the incoming radiation data, for instance (see sect. 2.6).

2.6 Appendix A

The buoy experiment provides a perfect test for meteorological correction functions. For example, it has been discussed in the community whether smoothing prior [Heidbüchel et al., 2016] or after correcting neutron data [Franz et al., 2020; Davies et al., 2022] is recommended. With the buoy data, this hypotheses can be tested without influence of ground-based variations.

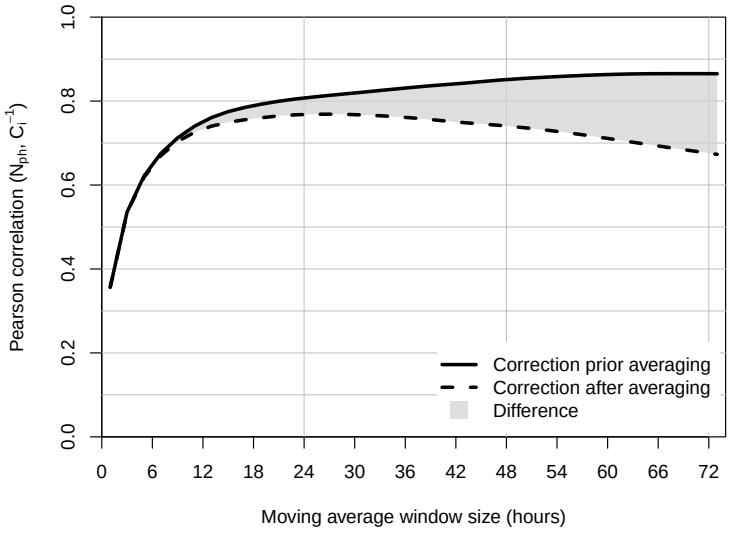

Figure 2.8: Pearson correlation coefficient between the epithermal N_{ph} vs. inverted influx correction after Zreda et al. [2012] using the JUNG neutron monitor, when the correction is applied prior or after smoothing with a moving average.

In general, temporal smoothing of a time series is a linear operation f, since

$$f: \quad x(t) = \sum_{t-\tau}^{t+\tau} w \cdot x(t') / \sum_{t-\tau}^{t+\tau} w \,,$$

where 2τ is the window size over which the data is averaged, and w is a weighting factor (e.g., 1 for a uniform average, or $e^{-\tau}$ for exponential filters). In contrast, some correction functions can be non-linear, e.g., the correction for air pressure or for incoming radiation. For the combination of linear f and non-linear functions g, the following rule generally holds:

$$f(g(x)) \neq g(f(x)) \,.$$

For this reason, the order of processing operations generally matters. In the case of neutron count variations, corrections should be applied on the raw data, and only the final product should then be averaged (smoothed). Otherwise, it is not guaranteed that a measurement $N(t)$ is corrected for the air pressure $P(t)$ at the same time t, for instance. Fig. 2.8 shows that the correlation between the buoy experimental epithermal neutron intensity corrected for variations in atmospheric pressure and absolute humidity and the inverted primary influx correction from Zreda et al. [2012]

generally increases with increasing moving average window size when the correction procedures are applied *before* averaging the raw data. In contrast, a correction *after* averaging the raw data leads to (i) a lower maximum correlation and (ii) a decrease of the correlation at window sizes larger than 25 hours. This is in line with recent findings by Davies et al. [2022], who found a general improvement of the CRNS-derived soil moisture when the correction procedure is applied prior filtering of the neutron intensity time series. In general, for filtering approaches based on a moving window, the window size needs to be odd in order to create a centred filter to avoid a temporal shift in the filtered time series. For example, a centred 24-hour moving average equals a 25-hour moving average.

2.7 Appendix B

At the study location, lake *Seelhausener See*, direct measurements of the water temperature were not available. However, it is possible to use measurements of a nearby lake as a proxy.

Surface temperatures in lakes are mainly determined by the local weather. Hence lakes located close to each other at the same geographic altitude show similar temperatures. This was verified in a comparison of surface temperatures of mine pit lakes in the Central German and Lusatian Mining District, in which also *Seelhausener See* is located. Boehrer et al. [2014] found that the lake temperatures measured in 0.5 m depth were nearly identical. Only in cases of rapidly rising temperatures (e.g., in spring time), a difference of up to 2 °C was detected between very small and larger lakes. Numerical models that are calibrated specifically for the conditions of a single lake often reach about the same accuracy [e.g. Weber et al., 2017], while models that are not specifically calibrated (e.g. occasional local temperature measurements) will show greater deviations. Alternative methods, such as satellite imaging and thermometry, only provide sporadic measurements and do not reach a similar accuracy without additional support from numerical models [Zhang et al., 2020].

Lake *Rassnitzer See* is situated in 31 km distance south west of the study area and was previously called "Mine Pit Lake Merseburg-Ost 1b" [Heidenreich et al., 1999]. The lakes *Seelhausener See* and *Rassnitzer See* exhibit similar morphology, similar size, and are exposed to similar air temperatures [Böhrer et al., 1998]. Since it can be assumed that temperatures will hardly differ by more than 1 °C, the surface temperatures (i.e., at 0.5 m depth) from *Rassnitzer See* can be used as an accurate approximation for temperatures in *Seelhausener See* at the same depth. This assumption has been supported by the fact that the observed air temperatures were very similar at both lakes throughout the investigation period (shown in Fig. 2.9).

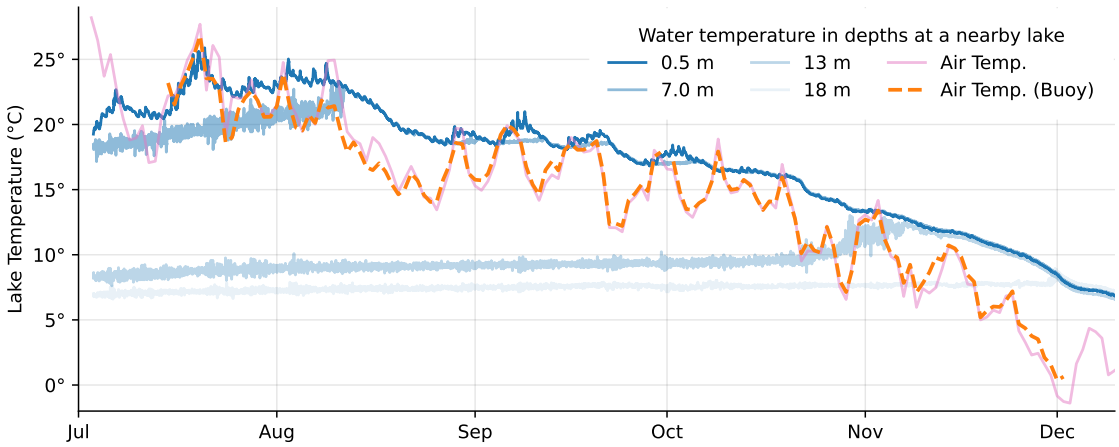

Figure 2.9: Water temperatures measured by an anchored weather station with attached thermistor chain in *Rassnitzer See* from July 2014 to January 2015 in several depths (blue shading). Air temperature has been measured at both lakes, *Rassnitzer See* (pink solid) and *Seelhausener See* (orange dashed).

Chapter 3

The sensitive footprint of CRNS at heterogeneous study sites

A version of this chapter has been published as:

Towards disentangling heterogeneous soil moisture patterns in cosmic-ray neutron sensor footprints

Daniel Rasche, Markus Köhli, Martin Schrön, Theresa Blume, and Andreas Güntner

Hydrology and Earth System Sciences, 25(12):6547–6566, doi: 10.5194/hess-25-6547-2021, 2021.

3.1 Abstract

Cosmic-Ray Neutron Sensing (CRNS) allows for non-invasive soil moisture estimations at the field scale. The derivation of soil moisture generally relies on secondary cosmic-ray neutrons in the epithermal to fast energy ranges. Most approaches and processing techniques for observed neutron intensities are based on the assumption of homogeneous site conditions or of soil moisture patterns with correlation lengths shorter than the measurement footprint of the neutron detector. However, in view of the non-linear relationship between neutron intensities and soil moisture, it is questionable whether these assumptions are applicable.

In this study, we investigated how a non-uniform soil moisture distribution within the footprint impacts the CRNS soil moisture estimation and how the combined use of epithermal and thermal neutrons can be advantageous in this case. Thermal neutrons have lower energies and a substantially smaller measurement footprint around the sensor than epithermal neutrons.

Analyses using the URANOS (Ultra RApid Neutron-Only Simulation) Monte Carlo simulations to investigate the measurement footprint dynamics at a study site in northeastern Germany revealed that the thermal footprint mainly covers mineral soils in the near-field to the sensor while the epithermal footprint also covers large areas with organic soils.

We found that either combining the observed thermal and epithermal neutron intensities by a rescaling method developed in this study or adjusting all parameters of the transfer function leads to an improved calibration against the reference soil moisture measurements in the near field compared to the standard approach and using epithermal neutrons alone. We also found that the relationship between thermal and epithermal neutrons provided an indicator for footprint heterogeneity. We, therefore, suggest that the combined use of thermal and epithermal neutrons offers the potential of a spatial disaggregation of the measurement footprint in terms of near- and far-field soil moisture dynamics.

3.2 Introduction

Soil moisture is a key variable in the hydrological cycle [e.g. Vereecken et al., 2008, 2014; Seneviratne et al., 2010], driving e.g., energy fluxes, groundwater recharge, runoff generation processes and biomass production, which, in turn, influence climatic variables on varying spatio-temporal scales [e.g. see, Daly and Porporato, 2005; Vereecken et al., 2008; Seneviratne et al., 2010; Wang et al., 2018]. Consequently, observations of soil moisture have a high importance for the estimation of landscape water balances and hydrological modelling. However, these applications would profit especially from field-scale observations covering several hectares. At this scale, the spatial (and temporal) resolution of satellite-derived soil moisture products is too coarse, and in situ soil moisture sensors would need to be installed in very large numbers due to the high spatial variability in soil moisture [Famiglietti et al., 2008; Vereecken et al., 2014; Babaeian et al., 2019]. In agricultural areas, this in situ installation is additionally hampered by management practices such as ploughing, tillage and harvest [Stevanato et al., 2019].

Introduced about a decade ago, Cosmic-Ray Neutron Sensing [CRNS; e.g. Zreda et al., 2008; Desilets et al., 2010] partly overcomes these issues and allows

for non-invasive soil moisture estimation at the field scale. It provides a representative spatially averaged soil moisture value across the instrument's measurement footprint [Schrön et al., 2018b] of approximately 12 ha. The resulting field-scale soil moisture products were successfully used for the calibration and validation of satellite-derived soil moisture products, as well as improved land-surface and rainfall-runoff models [e.g. Holgate et al., 2016; Montzka et al., 2017; Iwema et al., 2017; Duygu and Akyürek, 2019; Dimitrova-Petrova et al., 2020]. Combining soil moisture products of different spatial scales may overcome scale gaps as exemplarily shown by Fersch et al. [2018]. Roving CRNS-devices [e.g. McJannet et al., 2017; Schrön et al., 2018a; Vather et al., 2019] as well as dense sensor networks [e.g. Fersch et al., 2020; Heistermann et al., 2021] pose further opportunities for covering even larger areas.

Cosmic-Ray Neutron Sensing relies on a number of naturally occurring secondary cosmic-ray neutrons in the water-sensitive epithermal energy range from $> 0.2\,\mathrm{eV}$ to $1\,\mathrm{MeV}$ [Köhli et al., 2015], which are counted by a neutron detector above the soil surface. Neutrons in the epithermal energy range are highly sensitive to the amount of hydrogen in the surrounding area due to their energy loss by elastic scattering processes. As a result, an increase in hydrogen results in a decrease in epithermal neutrons counted by the instrument as the neutrons are slowed down more effectively. In turn, thermal neutrons have energies below $0.2\,\mathrm{eV}$ and show a more complex response to the dynamics of hydrogen and other elements. The interaction with hydrogen shows two competing effects. On the one hand, the thermal neutron abundance is positively correlated with the amount of hydrogen as more thermal neutrons are generated due to thermalisation of epithermal neutrons. On the other hand, neutron absorption leads to a decrease in thermal neutrons with increasing hydrogen abundance [e.g. Hubert et al., 2016]. As a consequence, thermal neutrons may show a similar response to variations in hydrogen and, thus, soil moisture (the largest terrestrial near-surface hydrogen storage). However, this response may be less distinct than the one of epithermal neutrons [Weimar et al., 2020], which are mainly driven by elastic scattering. An example for the more complex behaviour of thermal neutrons is the moderation optimum describing the amount of hydrogen at which the thermalisation is most effective [Hubert et al., 2016].

The measurement footprint size of CRNS varies with air pressure, air humidity and soil moisture conditions and ranges from 130 to 240 m in radius with a depth of 15 to 83 cm during wet and dry conditions, respectively [Köhli et al., 2015]. Additionally, topographic features such as open water or strong topographic gradients may influence the footprint size [e.g. Köhli et al., 2015; Schattan et al., 2019; Mares et al., 2020].

Although neutrons in the epithermal energy range are the basis for deriving soil moisture contents, thermal neutrons remain the focus of CRNS research as they can provide valuable information for estimating biomass [e.g. Tian et al., 2016; Jakobi et al., 2018; Vather et al., 2020] or snow water equivalent [SWE; Bogena et al., 2020], e.g. by using the ratio of epithermal and thermal neutrons. Compared to epithermal neutrons, little is known about the behaviour of thermal neutrons. For instance, when thermal and epithermal neutrons are combined, a measurement footprint of a similar size is assumed for both energy ranges [e.g. Vather et al., 2020]. However, the integration radius of thermal neutrons at the CRNS sensor can be expected to be much smaller (a footprint of approx. 35m) compared to epithermal neutrons [200 m;

see, e.g., Bogena et al., 2020]. This was recently confirmed by Jakobi et al. [2021], who estimated a radius of 43 to 48 m. Considering different footprint sizes of thermal and epithermal neutrons, a combination of both through calculating neutron ratios requires all hydrogen to be distributed homogeneously in the measurement footprints. As a result, uncertainties may arise when hydrogen is not distributed homogeneously in the footprints, as mentioned by Bogena et al. [2020], and this limits the applicability of combining thermal and epithermal neutrons. This may be of particular importance, as most studies with stationary CRNS assume quasi-homogeneous site conditions or spatial patterns of different soil moisture states and dynamics with correlation lengths smaller than the CRNS footprint. For instance, neutron transport modelling so far assumes homogeneous soil water distributions when characterising footprint dynamics and weighting functions [e.g. Köhli et al., 2015; Schrön et al., 2017; Jakobi et al., 2021] or developing transfer functions for deriving soil moisture from epithermal neutron intensities [e.g. Desilets et al., 2010; Franz et al., 2013b; Andreasen et al., 2020; Köhli et al., 2021]. However, different footprint sizes may offer the opportunity for a horizontal differentiation between near- and far-field soil moisture dynamics. Although previous studies confirmed the applicability of CRNS at heterogeneous study sites for deriving spatially averaged soil moisture time series [e.g. Franz et al., 2016; Sigouin et al., 2016; Schrön et al., 2017; Pang et al., 2021], approaches for the spatial disaggregation of CRNS-derived soil moisture values at heterogeneous observation sites have not yet been assessed in detail.

Against this background, this study investigates the footprint size and neutron dynamics of epithermal and thermal energies at a heterogeneous study site in the TERENO (TERrestrial ENvironmental Observatories) lowland observatory in northeastern Germany. Consisting of mineral soils in the near-field and partly surrounded by groundwater-influenced organic peatland soils in the far field, different approaches for a spatial disaggregation of the measurement footprint can be tested at this site. This is aided by the distinct hydraulic characteristics of organic peatland soils [e.g. Dettmann et al., 2014; Rezanezhad et al., 2016] and mineral soils which lead to different soil water dynamics and water contents.

Due to the general decrease in thermal neutron count rates with increasing soil moisture, but with a smaller integration radius, we hypothesise that Spearman's rank correlation coefficient between normalized thermal and epithermal neutron intensities can serve as measure for footprint heterogeneity. Second, we hypothesise that both, adjusting the neutron transfer function to near-field soil moisture observations or a combination of the normalised epithermal and thermal neutron intensities allow for a spatial disaggregation of the measurement footprint by improving the estimation of near-field soil moisture. To test these hypotheses, we first set up Monte Carlo neutron transport simulations using the URANOS (Ultra RApid Neutron-Only Simulation) code [Köhli et al., 2015]. This code is often used in CRNS research [e.g. Köhli et al., 2015, 2021; Schrön et al., 2017, 2018a,b; Schattan et al., 2019; Li et al., 2019a; Weimar et al., 2020] to develop transfer functions and weighting procedures. In our study, we use it to identify the footprint size and dynamics of neutrons in the thermal and epithermal energy ranges under different soil moisture conditions at the heterogeneous study site. Second, we adjust the standard transfer function used for deriving soil moisture from neutron observations and apply a combination of observed thermal and epithermal neutrons in order to improve the

calibration of CRNS-derived soil moisture estimates against reference soil moisture observations in the near-field. Finally, we illustrate the potential of deriving differentiated soil moisture dynamics under heterogeneous footprint conditions by either adjusting the transfer function or by adjusting the neutron signal.

3.3 Material and methods

3.3.1 Study site

The study site is located at the TERENO-NE [Zacharias et al., 2011; Heinrich et al., 2018] in the lowlands of northeastern Germany (Fig. 3.1). The average annual temperature is 8.8 °C, and rainfall amounts to 591 mm per year at the Waren weather station, which is approx. 35 km away from the study site [station ID: 5349; period 1981–2010; DWD - German Weather Service, 2020a,b]. Geologically, the study site is situated on a glacial outwash plain south of a terminal moraine formed during the Pomeranian phase of the Weichselian glaciation [Börner, 2015]. Within the outwash plain we still find non-eroded outcrops of glacial till of previous glaciation phases while fens formed subsequently in depressions and local sinks [Börner, 2015] due to rising temperatures and groundwater levels in the Holocene.

The CRNS site (site A) itself is located on a slightly elevated outcrop of Weichselian glacial till surrounded by peatland (Fig. 3.1). Dominating soil types in areas with glacial till are Cambisols formed on sandy loam, while the peatland areas are characterised by Histosols rich in clay and silt and low water table depths. Soil samples were taken from mineral and organic soils in depths from 0 to 30 cm, in 5 cm increments, at 21 random locations within a 200 m radius in February 2020 and were analysed to retrieve local soil properties. Within a 10 m, 10 to 50 m and 50 to 200 m radius, 5, 6 and 10 samples were taken, respectively, thus matching the decreasing sensitivity of the neutron detector with increasing radius. The analyses revealed an average bulk density of 1.43 g cm^{-3} in areas with mineral soils and 0.29 g cm^{-3} in areas with organic soils. The site average bulk density calculated from all available samples is 1.11 g cm^{-3}. Based on the material density of quartz (2.65 g cm^{-3}), these values were used to estimate soil porosities of 89 and 46 % for organic and mineral soils. The average percentage of soil organic matter determined from the loss-on-ignition analyses (550 °C, 24 hours) revealed 0.70 g g^{-1} for organic soils and 0.02 g g^{-1} for mineral soils. A subsequent loss-on-ignition analysis (1000 °C, 24 hours) revealed an average lattice water content of 0.03 g g^{-1} for organic and 0.001 g g^{-1} for mineral soils, respectively. Based on these soil samples, the average gravimetric water content in organic soils in the far field was 0.62 m^3 m^{-3}, while it was only 0.15 m^3 m^{-3} for near-field mineral soils, thereby illustrating the two distinct soil moisture regimes at the study site. Regardless of the soil type, pasture is the prevailing type of land cover, mainly used for cattle grazing, while larger areas that are forested with *Pinus sylvestris* are found in greater distances of more than 1 km towards the east (Fig. 3.1). The observation site is one of three sites in the TERENO-NE observatory equipped with a CRS1000 neutron detector (Hydroinnova LLC, USA) and also includes a weather station that permanently monitors the relative humidity, wind speed and temperature, as well as the long and short-wave solar radiation. Additionally, irregular monthly groundwater measurements are available. The other two CRNS observation sites (B and C; Fig. 3.1b)

represent forest sites with a rather homogeneous distribution of soil moisture in the measurement footprint of the CRNS. Further details regarding site C can be found in Heidbüchel et al. [2016].

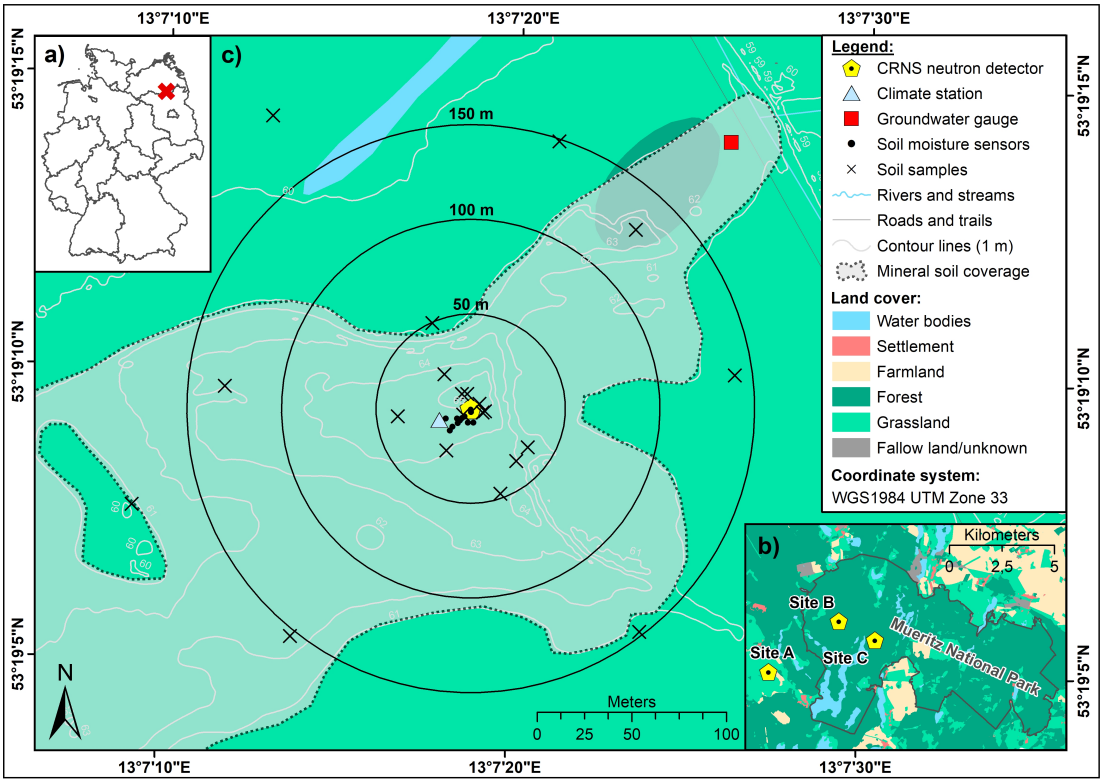

Figure 3.1: The location of the study area and within Germany (a), the positions of all CRNS locations of the TERENO lowland observatory in the Mueritz National Park (b) and the heterogeneous CRNS observation site of this study (c). Sources: digital elevation model from LAIV-MV - State Agency for Interior Administration Mecklenburg-Western Pomerania [2011]; land cover from BKG - German Federal Agency for Cartography and Geodesy [2018a]; administrative units from BKG - German Federal Agency for Cartography and Geodesy [2018b].

The neutron detectors are composed of two proportional counter tubes filled with ^{3}He gas (see Zreda et al. [2012] and Schrön et al. [2018b] for a detailed description). There is one bare, unshielded, tube to detect neutrons in the thermal energy range and a second moderated counter tube shielded with a 2.5 cm high-density polyethylene housing to measure neutrons in the epithermal energy range. It should be noted that the bare counter tube may observe about 5 % of the epithermal neutrons and the moderated tube observes up to 45 % of the thermal neutrons [Andreasen et al., 2016], which should be considered when comparing the different detector systems and the results of neutron transport simulations. The time series of in situ soil moisture point sensors of the two different types are available at the site. A total of six SMT100 sensors (Truebner GmbH, Germany) are installed, with two sensors each in 10, 20 and 30 cm depths. They record soil moisture at 10 min intervals. Time domain reflectometry (TDR) sensors (Campbell Scientific Ltd, UK) are installed at the same depths, with four sensors in 10 cm depth, three sensors in 20 cm and five sensors at 30 cm depth. The record interval for the TDR probes is

15 min. Measurements are converted to soil moisture by using the manufacturers' calibrations. All point sensors are installed within a 30 m radius around the neutron detector and, thus, only cover the near-field composed of mineral soils. Continuous reference observations from the far-field peatland soils are not available. Given the higher noise level of the TDR time series, but soil moisture dynamics that are very similar to the SMT100 sensors in the respective soil depths, only SMT100 data are used in the following analyses and presented in the paper. An identical processing procedure was used for the soil moisture time series from TDR soil moisture sensors (for results, see the Appendix).

3.3.2 Neutron simulations

In the present study, we apply the Monte-Carlo-based neutron transport model of URANOS (version v0.99 ω19; see Köhli et al. [2015] for details). By simulating 200 million source neutrons, we intend to estimate the influence of water content variations in areas with organic soils in the far field of the neutron detector on the neutron flux and footprint size of epithermal and thermal neutrons. The model set-up uses a simplified representation of soil distributions (Fig. 3.1) within a rectangular 900 by 900 m sized model domain, with a horizontal resolution of 1 m around the neutron detector. The following three simplifications had to be made in order to set up the model: a flat topography was assumed, soil porosities derived from field samples were assumed to be valid for the entire simulated soil column of 2 m depth and organic soils are only differentiated by their significantly higher porosities, while their chemical composition is equal to that of mineral soils. This last simplification is due to the limitations of the neutron transport model. Although these simplifications will hamper a direct comparison with observed neutron intensities as the hydrogen stored in soil organic matter or vegetation will reduce the footprint sizes and dampen the neutron intensity response to changes in soil water content under real-world conditions, the simulations will provide valuable information on the neutron intensity dynamics at the study site. All simulations were made with a single set of atmospheric boundary conditions, namely an assumed cutoff rigidity of 3 GV, based on Andreasen et al. [2017a], an absolute humidity of 8.3 g m^{-3} and an atmospheric shielding depth of 1028.5 g cm^{-2}. In the case of absolute humidity and atmospheric shielding depth, these values represent site averages derived from local measurements for the study period from 2015 to 2018.

To investigate the footprint variability caused by soil water changes in the peatland soils of the far field, we calculate the footprint radius as the 86 % quantile of distances (R_{86}) to the detected neutron origins for thermal (0.001 eV to 0.2 eV) and epithermal (¿ 0.2 eV to 0.01 MeV) neutrons. For detected epithermal neutrons, the distance to the point of the first soil contact is considered as being the point of origin, as secondary epithermal neutrons generated from nuclear evaporation processes in the soil are sensitive to hydrogen by elastic scattering [e.g. Köhli et al., 2015]. In contrast, to our knowledge, the definition of the origin of detected thermal neutrons has not yet been assessed in detail. On the one hand, the point of thermalisation (i.e. point where a neutron first reached an energy in the thermal range) may be a suitable definition of the origin because, as neutrons reach thermal energies, absorption adds to elastic scattering as a second important interaction process between neutrons and hydrogen, as well as matter in general. On the other

hand, if thermal neutrons are generated from higher energetic epithermal neutrons, the amount of detected thermal neutrons may partly be influenced by the amount of epithermal neutrons and their origin. As a consequence, we apply and compare both options, i.e. the point of thermalisation and the point of first soil contact, to define the origin of detected thermal neutrons and the resulting footprint radius. The measurement depth of epithermal and thermal neutrons is derived similarly. For thermal neutrons, the average measurement depth D_{86} is defined as the 86 % quantile of either the depth of the thermalisation point or the maximum depth along the neutron transport path while for epithermal neutrons we use only the latter.

It should be noted that the virtual detector in the simulations is significantly larger (9 m radius) than a real neutron detector; this is in order to enhance the count rate and decrease the computational time. However, this means that neutrons originating below the detector (i.e. originating within the 9 m radius) are considered to have a travel distance of 0 m. Furthermore, in this study, we consider an energy window for defining thermal and epithermal neutrons scattering in the virtual detector. Although detector response functions [see, e.g., Köhli et al., 2018, 2021] mimic the sensitivity of a real neutron detector and would provide a more realistic neutron intensity, we deliberately decided to keep our model simple and general (also due to a lack of information on soil moisture dynamics and soil chemistry in the peatlands). We are, thus, not aiming at a detailed reproduction of field conditions but at more general understanding. Although different studies refer to different upper energy boundaries for thermal neutrons in simulation studies which depend on the specific neutron detector and applied shielding material, we decided to use the physical energy threshold in which thermal neutrons are in equilibrium with the energy of environmental nuclei and neutron absorption becomes a relevant process as a more general definition of thermal neutrons.

On the one hand, the simulation scenarios described in the following sections allow the investigation of thermal and epithermal measurement footprint changes when soil moisture is either stable or dynamic in the near-field where the CRNS method is most sensitive. Additionally, we can derive potentially valuable information on neutron intensity variations when the water content varies at different rates in the near-field and far field. This may be of particular importance at study sites influenced by peatland soils, as these are characterised by, e.g., higher storage capacities. An overview of all simulation sets and the included simulation scenarios performed in the scope of this study can be found in Table 5.1.

Simulation set 1: static near-field soil moisture and variable far-field soil moisture

In the first simulation set that consists of seven neutron transport simulation scenarios, the simulated soil moisture was kept constant in the near-field mineral soil areas. The soil moisture in areas with peatland soils was altered for each scenario and ranges from 0.1 to 0.7 m^3 m^{-3} across the entire soil column at a porosity of 89 %. During all scenarios, the soil moisture in areas with mineral soil remains constant at 0.1 m^3 m^{-3} at a porosity of 46 % (Table 5.1). This fixed low water content in the near-field was chosen as the measurement radius from which detected thermal or epithermal neutrons originate can be expected to be largest at dry soil conditions [Köhli et al., 2015; Schrön et al., 2017]. Therefore, the largest influence of far-field soil water dynamics on neutron count rates at the detector location can

be expected at low soil moisture conditions in the near-field. Hence, simulating constant low near-field soil water contents and solely varying far-field soil water contents allows for the isolated investigation of the impact of peatland soil water variations on the observed neutron intensities and the corresponding footprint variations.

Simulation sets 2 and 3: varying soil moisture in both the near-field and far field

The second set of simulation scenarios included variations in soil moisture contents in the far field and in the near-field. All other simulation parameters remained equal to previous simulations. We simulate six simulation scenarios with an equal decrease in soil water contents in near-field mineral soils and far-field peatland soils. The highest soil moisture content simulated is 0.35 m^3 m^{-3} for mineral soils and and 0.70 m^3 m^{-3} for peatland soils. These soil water contents are decreased in equal intervals of 0.05 m^3 m^{-3} in both soils (Table 5.1). In the third set of simulations, we investigate the effect when soil moisture is reduced more strongly in peatland soils compared to mineral soils. Here, the soil moisture in peatland areas is reduced in 0.10 m^3 m^{-3} intervals, from 0.70 to 0.20 m^3 m^{-3}, while soil moisture in the mineral soils is reduced from 0.35 to 0.10 m^3 m^{-3} in 0.05 m^3 m^{-3} intervals.

Table 3.1: Overview of the different Monte-Carlo-based neutron transport simulation scenarios conducted within the different simulation sets. Near-field soil moisture refers to soil moisture in areas covered with mineral soils, while far-field soil moisture refers that in the peatland soils.

Simulation set	Simulation scenario no.	Near-field soil moisture (m^3 m^{-3})	Far-field soil moisture (m^3 m^{-3})
(1) Static near-field soil mositure	1	0.10	0.70
	2	0.10	0.60
	3	0.10	0.50
	4	0.10	0.40
	5	0.10	0.30
	6	0.10	0.20
	7	0.10	0.10
(2) Equal decrease in near- and far field	1	0.35	0.70
	2	0.30	0.65
	3	0.25	0.60
	4	0.20	0.55
	5	0.15	0.50
	6	0.10	0.45
(3) Unequal decrease in near- and far field	1	0.35	0.70
	2	0.30	0.60
	3	0.25	0.50
	4	0.20	0.40
	5	0.15	0.30
	6	0.10	0.20

3.3.3 In situ neutron observations

Processing of measured neutron intensities

For our 4-year study period from January 2015 to December 2018, neutron intensities were aggregated from sub-hourly intervals to hourly values and smoothed by a 13-hour moving average in order to reduce noise in the data [e.g. Bogena et al.,

2013]. Data gaps were caused by power cuts, technical issues or maintenance activities. Outliers were identified by a threshold of 4 times the standard deviation and were excluded from the analyses. Raw neutron observations were corrected for variations in atmospheric shielding depth or air pressure and primary neutron influx [e.g. Zreda et al., 2012]. The standard correction procedure for air humidity is defined for neutrons in the epithermal energy range [Rosolem et al., 2013] and may not be valid for thermal neutrons. As a consequence, in this study, we corrected thermal and epithermal neutron intensities only for variations in atmospheric shielding depth and primary neutron influx in order to maintain comparability. It should be noted that the correction procedures applied to thermal and epithermal neutron intensities differ among previous studies [e.g. Andreasen et al., 2016; Jakobi et al., 2018] and illustrate the need for further research. To correct raw neutron intensities for varying atmospheric shielding depths, air pressure values in hectopascals measured by the neutron detector are converted to atmospheric shielding depth in grams per squared centimetre by multiplication with 1.0194 s^2 m^{-1} [Heidbüchel et al., 2016]. The required reference value is the average atmospheric shielding depth for the 4-year study period, and the attenuation length (135.6 g cm^{-2}) is adapted from Heidbüchel et al. [2016]. The correction for variations in primary neutron flux is done using pressure- and efficiency-corrected primary neutron data from the Jungfraujoch neutron monitor in Switzerland (JUNG; `www.nmdb.eu`). Again, the reference value is defined as the average influx during the study period. The corrected thermal (bare) and epithermal (moderated) neutron intensities for the study period are illustrated in Fig. 3.2.

Corrected epithermal neutron intensities can be converted to volumetric soil moisture θ_{CRNS} in cubic metres per cubic metre (m^3 m^{-3}), using the standard transfer function introduced by Desilets et al. [2010], as follows:

$$\theta_{\mathrm{CRNS}} = \left(\frac{a_0}{\frac{N}{N_0} - a_1} - a_2 \right) \times \frac{\rho_{\mathrm{soil}}}{\rho_{\mathrm{water}}}. \tag{3.1}$$

Here, a_0 (0.0808), a_1 (0.372) and a_2 (0.115) are the shape-defining parameters of the hyperbolic transfer function. N describes the corrected neutron intensity, ρ_{soil} is the average soil bulk density in the measurement footprint (kilograms per cubic metre; hereafter kg m^{-3}), ρ_{water} is the density of water in kg m^{-3}, and N_0 is a free calibration parameter describing the site-specific neutron intensity over dry soil at 0.0 m^3 m^{-3}. In this study, we used the revised standard transfer function recently introduced by Köhli et al. [2021], which provides a physical meaning for each of the shape-defining parameters from eq. (3.1). The three variables in the revised transfer function (eq. (3.2)) can be calculated from the variables of the standard transfer function.

$$\theta_{\mathrm{CRNS}} = \left(\tilde{a_0} \frac{1 - \frac{N}{N_{\mathrm{max}}}}{\tilde{a_1} - \frac{N}{N_{\mathrm{max}}}} \right) \times \frac{\rho_{\mathrm{soil}}}{\rho_{\mathrm{water}}}, \tag{3.2}$$

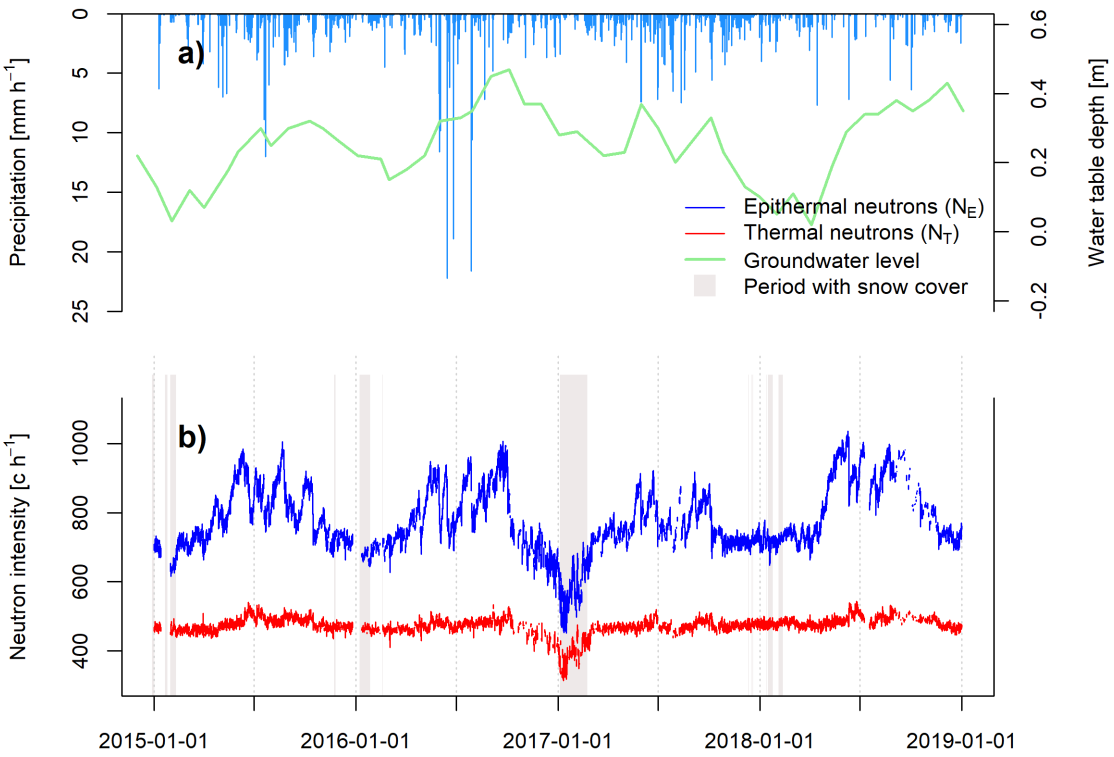

Figure 3.2: Field observations for the period from January 2015 to December 2018, showing the (a) hourly rainfall and approximate monthly groundwater table depth in far-field peatland soils and (b) the corrected neutron intensities in the thermal (N_T) and epithermal energy range (N_E) (b).

where, in the following:

$$\tilde{a_0} = -a_2, \tag{3.3}$$

$$\tilde{a_1} = \frac{a_1 a_2}{a_0 + a_1 a_2}, \tag{3.4}$$

$$N_{\text{max}} = N_0 \times \frac{a_0 + a_1 a_2}{a_2}. \tag{3.5}$$

The calibration procedure is performed for the entire time series of observed, corrected neutron intensities of epithermal neutrons N_E. There are two possible options for deriving soil moisture based on the standard transfer function (eq. (3.1)). The first option requires eq. (3.1) to be solved for N_0 in order to approximate the calibration parameter. The calculated N_0 is then used in eq. (3.1). In the second procedure, the N_0 parameter of eq. (3.1) is calibrated iteratively against reference soil moisture measurements in order to derive the site-specific neutron intensity over dry soils N_0.

We used the revised transfer function (eq. (3.2) – (4.4)) and iteratively calibrated N_0 because continuous in situ soil moisture measurements offer a high number of

reference points. Regardless of which equation is used for deriving soil moisture values from neutron observations and the corresponding calibration option, reference soil moisture observations need to be weighted according to their depth and distance to the neutron detector in order to match the sensitivity regarding the origin of the epithermal neutrons [Schrön et al., 2017].

We weighed all available point sensor measurements per time step in order to derive a depth-distance weighted soil moisture time series after Schrön et al. [2017]. The weighting approach takes, e.g., soil moisture, bulk density (1.43 g cm^{-3}), additional hydrogen pools (organic matter of 0.02 g g^{-1} and lattice water of 0.001 g g^{-1} excluded in this study), air humidity and vegetation height (0.2 m) into account. Hourly time series of all SMT100 soil moisture sensors at depths of 10, 20 and 30 cm for all snow-free periods from January 2015 to December 2018 were weighted accordingly. For SMT100 probes, we also excluded soil moisture observations during soil temperatures below 0 °C. Lastly, the N_0 is iteratively adjusted to derive a soil moisture time series from observed neutron intensities resulting in the highest goodness of fit in terms of the highest Kling-Gupta Efficiency [KGE; Gupta et al., 2009], compared to the weighted reference time series from the in situ sensors in the near-field. To assess the impact of the weighting on the calibration result, we also compare the depth-distance weighted calibration with a calibration based on the arithmetic mean of all available in situ sensors. This calibration approach is referred to as the standard calibration approach throughout the paper.

Improving the CRNS-derived soil moisture estimation

To achieve a better calibration result against the observations of the reference sensors in the near-field, we adjusted the shape of the transfer function by tuning the parameters a_0, a_1 and a_2. The tuning of all shape-defining parameters was done in previous studies and resulted in a better goodness of fit between CRNS-derived soil moisture values and reference measurements [e.g. Rivera Villarreyes et al., 2011; Lv et al., 2014; Heidbüchel et al., 2016; Tan et al., 2020] and may be especially necessary at sites with binary soil moisture distributions [e.g. Franz et al., 2013a]. In this study, we adjust parameters N_0, a_0, a_1 and a_2, using a Monte-Carlo based approach, by testing 10,000 random combinations of the parameters and selecting the parameter set that produces the highest statistical goodness of fit in terms of the KGE. This approach will be referred to as alternative approach 1 in the following sections.

Furthermore, we tested a second approach in which we made use of the simultaneously recorded and corrected thermal neutron intensity N_T to create a rescaled neutron time series N_{ET}, using equation (3.6) as follows:

$$N_{ET} = \left(\frac{N_E + N_T}{\overline{N_E + N_T}} \right) \times \overline{N_E} \tag{3.6}$$

Here, $\overline{N_E + N_T}$ is the average of the sum of epithermal and thermal neutrons, while $\overline{N_E}$ is the average of the epithermal neutron intensity only. The result from equation (3.6) is a neutron time series which averages the dynamics of thermal and epithermal neutron intensities and, thus, leads to a rescaled epithermal neutron time series N_{ET}, which now shows a different relationship with the reference soil moisture measurements characterised by a shallower slope compared to N_E. The

rescaled time series may be less influenced by peatland soil moisture variations due to the expected smaller footprint of thermal neutrons while the more distinct intensity change of epithermal neutrons with soil moisture variations is at least partly conserved. More importantly, the slope of the functional relationship between soil moisture and the neutron intensity of N_{ET} becomes less steep due to the generally weaker response of thermal neutrons to soil moisture changes [e.g. Weimar et al., 2020]. For our study site, especially the shallower slope could be used as a proxy to partly account for, e.g. the stronger soil moisture changes expected to occur in far-field peatland areas. These would lead to changes that are too strong in epithermal neutron intensity and would hamper the standard approach for deriving near-field soil moisture estimates. We would like to note that, in this study, we did not consider using thermal neutrons alone as this would require a transfer function specifically designed to the response of thermal neutrons to changes in soil moisture.

The calibration was performed iteratively by adjusting N_0 only. In terms of normalized neutron intensity dynamics, this equation is equal to summing the absolute epithermal and thermal neutron intensity, which would, consequently, lead to a much higher N_0 after calibration. The latter approach will be referred to as alternative approach 2 for the remainder of the paper.

To test if the CRNS-derived soil moisture from one of the alternative approaches 1 and 2 differs significantly from the traditional standard approach, using N_E and calibrating N_0 only, we performed a time series comparison based on bootstrapping residuals and the Wilcoxon rank sum test. First, the CRNS-derived soil moisture time series based on (i) N_E and calibrating N_0, (ii) N_E and calibrating all parameters and (iii) N_{ET} and calibrating N_0 were smoothed with a normal Nadaraya-Watson kernel regression smoother, using a large bandwidth of 1,000 in order to achieve an intense smoothing effect. Based on the smoothing method applied, the seasonal variations in soil moisture remain, while short-term soil moisture changes, i.e. on the event scale, are removed. Missing values were excluded before applying the smoothing algorithm and reintroduced to the smoothed time series. Then the residuals were calculated between the smoothed and original soil moisture time series. Next, a random sample of 5,000 residuals was generated and used to produce a random distribution of 5,000 soil moisture values per time step for each of the smoothed time series of the three variants mentioned above. This is done to obtain a distribution of soil moisture values per time step of each CRNS-derived soil moisture time series which can be compared in the next step. For each time step, an unpaired Wilcoxon rank sum test was performed in order to determine time steps where significant differences ($p < 0.05$) occur between the CRNS-derived soil moisture time series calculated with the classic approach and with the two alternative approaches.

In a first attempt to find a measure to characterise footprint heterogeneity, the Spearman rank correlation coefficients between normalized thermal and epithermal neutron counts were calculated for the study site and for the two nearby CRNS sites that are located in forested terrain (see Fig. 3.1) with rather homogeneous soil characteristics in their footprint. The Neutron intensities of those two sites were corrected in the same way as described above. Unless otherwise stated, all calculations were performed in R statistical software [R Core Team, 2018] using, for instance, the hydroGOF package [Zambrano-Bigiarini, 2017] for calculating the goodness-of-fit parameters.

3.4 Results

3.4.1 Simulated neutron response to soil moisture changes in the far-field peatland soils

The results of all neutron transport simulation scenarios with a constant soil moisture in mineral soils of the near-field reveal that the sensitive measurement footprint radius is distinctively smaller for thermal neutrons than for epithermal neutrons (Fig. 3.3). The footprint radius of epithermal neutrons decreases from 141 m in the 0.1 m^3 m^{-3} scenario to 111 m in the 0.7 m^3 m^{-3} scenario, with an average R_{86} of 122 m based on all simulation scenarios. In comparison, the thermal footprint radius is distinctively smaller but depends on the definition of a detected neutrons origin in the model domain. If the point of thermalisation is considered as the point of origin, the thermal footprint only exhibits a minor change in simulation scenarios with increasing soil moisture in the peatland soils of the far field. It remains rather constant with a minimum and maximum R_{86} of 42 m and 45 m, respectively (Fig. 3.3). The average footprint radius of thermal neutrons from all simulation scenarios is 44 m, and thus, the average epithermal footprint radius is 2.8 times larger than the thermal footprint radius. However, if the first soil contact is considered as the point of origin, then the thermal footprint is larger and decreases with increasing peatland soil moisture from 107 m to 81 m, with an average footprint radius of 88 m. Thus, the neutron transport simulations led to an average horizontal integration area of 0.6 ha and 2.4 ha for thermal neutrons, depending on which footprint definition is applied. The average horizontal integration area of epithermal neutrons has a size of 4.7 ha. The average integration depth D_{86} remains constant for thermal neutrons with an average D_{86} of 0.27 m if the point of thermalisation is considered as the origin, while it is distinctively larger if the maximum depth is used. Here, the average measurement depth increases to 0.52 m and is larger than the average measurement depth of epithermal neutrons, revealing a D_{86} of 0.31 m. Even though thermal neutrons show a smaller integration radius, the integration depth might be larger than that of epithermal neutrons.

The number of neutrons detected by the virtual detector decreases with increasing soil moisture in the peatland soils (Fig. 3.4) during the different simulation scenarios from 0.1 to 0.7 m^3 m^{-3}. The total number of detected neutrons, i.e. of neutrons with any origin in the model domain, illustrates the decrease in detected epithermal and thermal neutrons with increasing peatland soil moisture and a generally lower number of detected thermal neutrons (Fig. 3.4). The number of detected epithermal neutrons decreases by 10.3 %, from about 27700 to 24800, in the 0.1 and 0.7 m^3 m^{-3} scenario. The number of thermal neutrons detected decreases to a lesser degree, by 5.4 %, from about 25200 to 23800. Thus, the total number of epithermal neutrons decreases 1.9 times more than the number of thermal neutrons with increasing far-field soil moisture.

The visible influence of far-field soil moisture variations on both epithermal and thermal neutrons raises the question of the impact on the fraction of detected neutrons, i.e. the fraction of detected neutrons originating from areas covered with peatland soils and minerals soils. We investigated the influence of peatland soil moisture variations in the far field on the fractional contribution to the total number of thermal neutrons when either the point of thermalisation or the point of first

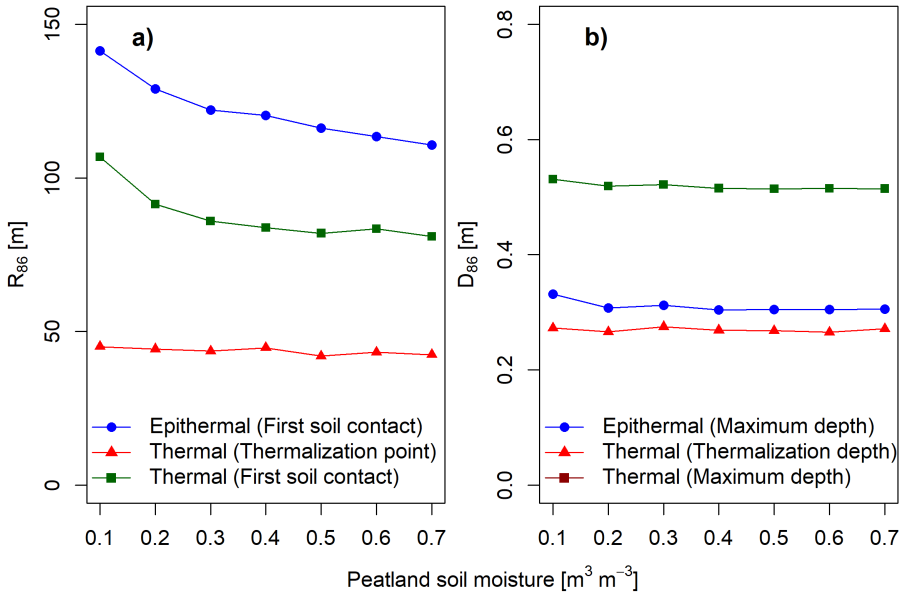

Figure 3.3: Simulation results for the measurement footprint radius (a) and depth (b) of detected thermal and epithermal neutrons.

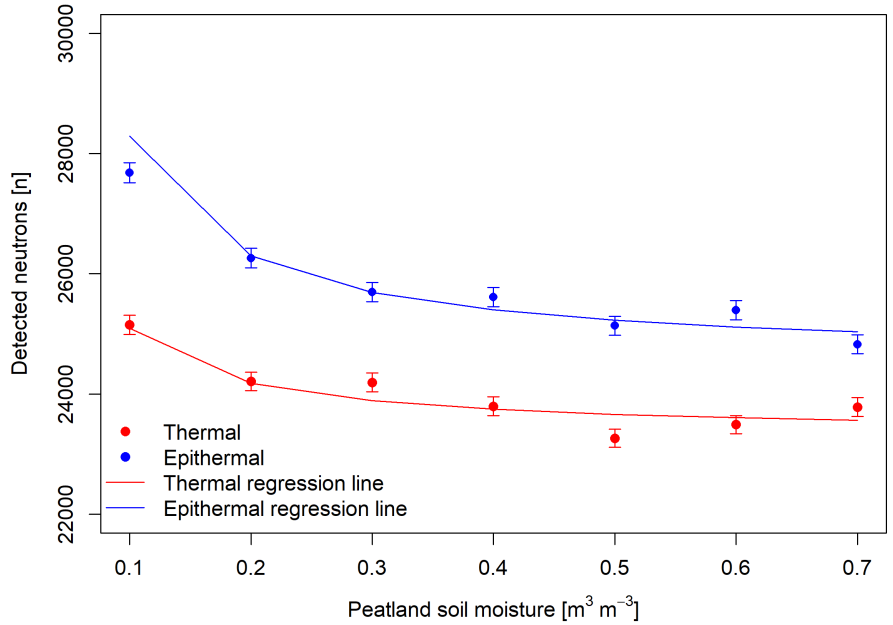

Figure 3.4: The total number of neutrons in the thermal and epithermal energy range observed by the virtual detector per simulated peatland soil moisture

soil contact is considered as being the origin of the specific neutron. The latter represents the position of the first soil contact of a neutron within its life cycle in the model domain, i.e., the position at which the simulated neutron had its first soil contact before it further slowed down and reached the virtual detector as a neutron with thermal energy. For detected epithermal neutrons, the fraction of neutrons with peatland origin decreases with increasing peatland soil moisture from 19 to 12 % and contributes, on average, 14 % to the total number of detected epithermal

neutrons (Fig. 3.5). For thermal neutrons, the fraction of neutrons originating from peatland areas depends on the definition of the point of origin. If the point of thermalisation is used, then the average fraction of thermal neutrons originating from peatland areas is much lower at only 4 %. Furthermore, the fraction does not change with increasing peatland soil moisture. In contrast, if the point of first soil contact is used for thermal neutrons as well, then the contribution of thermal neutrons with peatland origin decreases from 14 to 8 % with increasing soil moisture. On average, the contribution from peatland is 10 %.

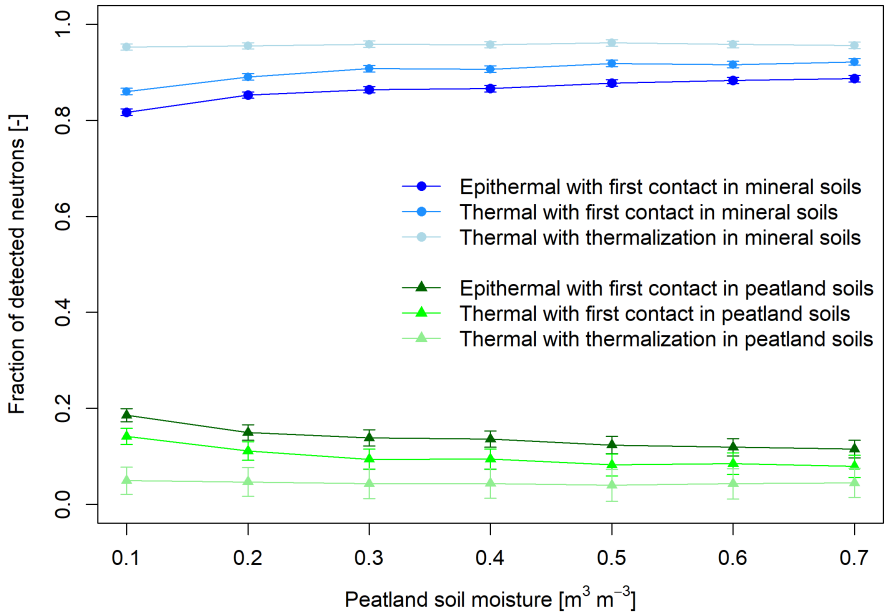

Figure 3.5: The fraction of detected epithermal and thermal neutrons with increasing soil moisture originating from areas covered with peatland soils and mineral soils in the model domain. For epithermal neutrons, the point of origin is defined as the point of first soil contact while for thermal neutrons, both calculations, for the point of first contact and the point of thermalisation are shown.

3.4.2 Simulated neutron response to soil moisture changes in both near-field mineral and far-field peatland soils

In addition to keeping soil moisture values in mineral soils of the near-field constant, we simulated a second set of scenarios where both near-field and far-field soil water contents were adjusted (Table 5.1). The results of the measurement radius and depth for the same decrease in soil moisture in areas covered with mineral soils and peatland soils can be found in Fig. 3.6. The epithermal R_{86} does not show a visible increase if soil moisture is reduced equally and reveals an average footprint radius of 117 m. An increase in the R_{86} can be observed when soil moisture is decreased by twice as much in the peatland soils compared to the decrease in the mineral soils. In this case, R_{86} increases from 118 to 128 m. A similar behaviour can be observed for thermal neutrons if the point of first soil contact is considered as the origin in the model domain. While in this case the R_{86} remains constant at 81 m if soil moisture is decreased equally in mineral and peatland soils, R_{86} increases from 80 to 92 m

when soil moisture is reduced by twice as much in peatland compared to mineral soil areas. Similar to the simulation set described in the previous chapter where the soil moisture is kept constant in the near-field, the thermal R_{86} is much smaller and does not change with varying soil moisture when the point of thermalisation is considered. It remains constant at an average value of 43 m for the simulation sets where soil moisture is decreased both equally and unequally.

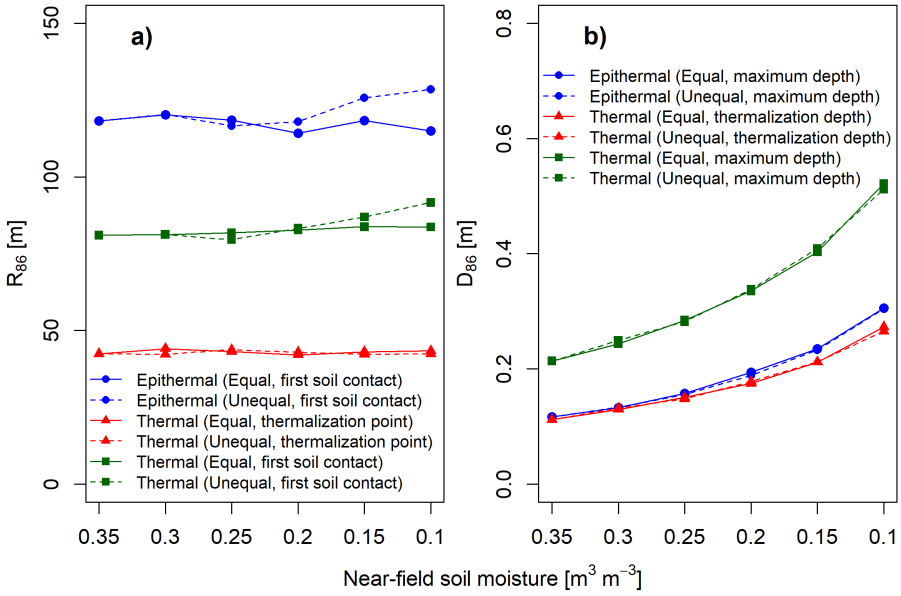

Figure 3.6: The simulated measurement footprint radius R_{86} (a) and depth D_{86} (b) of thermal and epithermal neutrons when soil moisture in areas with mineral and peatland soils decreases by the same amount (solid lines) and when peatland soil moisture decreases twice as much (dashed lines).

Unlike for the previous scenarios with constant near-field soil moisture, the measurement depth varies noticeably in both neutron energy ranges when soil moisture is also reduced in the near-field of the neutron detector. The epithermal integration depth D_{86} increases from 0.12 to 0.3 m while the thermal integration depth changes from 0.11 to 0.27 m if the depth of the point of thermalisation is used to define the measurement depth. In contrast, if the thermal integration depth is calculated as it is done for epithermal neutrons, by using the maximum depth along the neutron transport path, then the thermal integration depth becomes much larger and exceeds the integration depth of epithermal neutrons. It increases from 0.21 to 0.52, if soil moisture is reduced equally, and to 0.51 m if soil moisture is reduced unequally, in near-field mineral and far-field peatland soils.

A stronger increase in the detected epithermal neutrons normalised by the average detected neutrons of all simulation scenarios for sets 2 and 3, respectively, can be observed when soil water contents decrease twice as fast in peatland soils compared to mineral soils (Fig. 3.7). Simulated thermal neutrons exhibit a more complex behaviour because the number of thermal neutrons increases with decreasing soil moisture in the model domain when the general soil water content is high; however, when the overall soil moisture in the model domain is low, the detected thermal neutrons tend to either remain constant or even decrease if the soil moisture

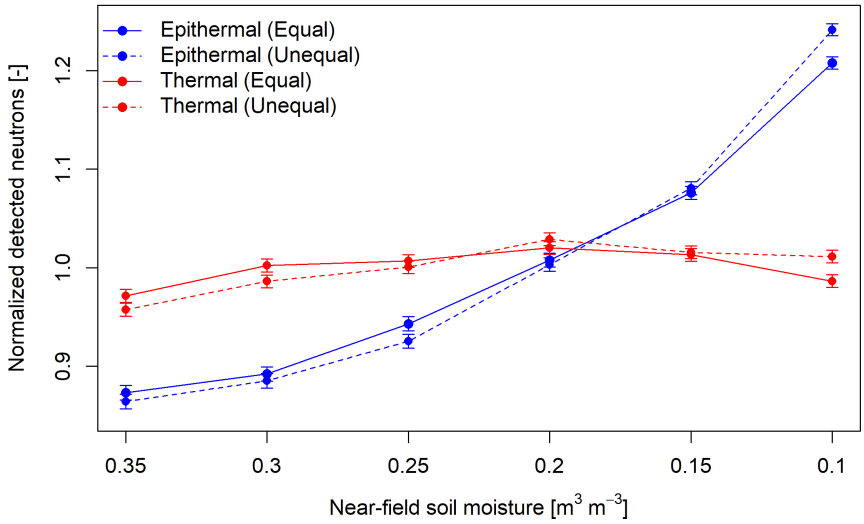

Figure 3.7: The simulated normalised thermal and epithermal neutron response when soil moisture in areas covered with mineral and peatland soils decreases at equal intervals (solid lines) and when peatland soil moisture decreases twice as much (dashed lines).

decrease is stronger in peatland soils. Overall, the thermal neutrons tend to increase with decreasing soil water content.

3.4.3 Relationship between thermal and epithermal neutron observations

Spearman's rank correlation coefficient is calculated between the normalised corrected hourly intensities of thermal and epithermal neutrons for the observation site (site A; Fig. 3.8a) and, for comparison, also at the two other nearby CRNS observation sites (sites B and C; Fig. 3.8b,c). The Spearman rank correlation coefficient for the other two sites is 0.95, showing a high correlation between the neutrons observed by the shielded (epithermal) and unshielded (thermal) counter tube. In contrast, the correlation coefficient at our main observation site is much lower, with only 0.58 (Fig. 3.8). Figure 3.8 illustrates the relationship between the relative observed neutron intensities in both energy ranges per study site. Apart from having higher Spearman's rank correlation coefficients, the point clouds for both sites that are assumed to have a more uniform soil moisture (Fig. 3.8b,c) are close to the 1:1 line, although a slight non-linearity is visible. In contrast, the scatterplot for site A (Fig. 3.8a) reveals a strong heteroscedasticity, with deviations occurring during high relative neutron count rates in the epithermal and thermal energy range.

Adding the simulated normalised detected neutrons to the scatterplot of site A results in all simulated data points being located within the range of the observed values (Fig. 3.9). Data points of simulation sets 2 and 3 with varying near-field soil moisture cross the 1:1 line while the data points of simulation set 1, where the near-field soil moisture was kept constantly low, remains on the right side of the 1:1

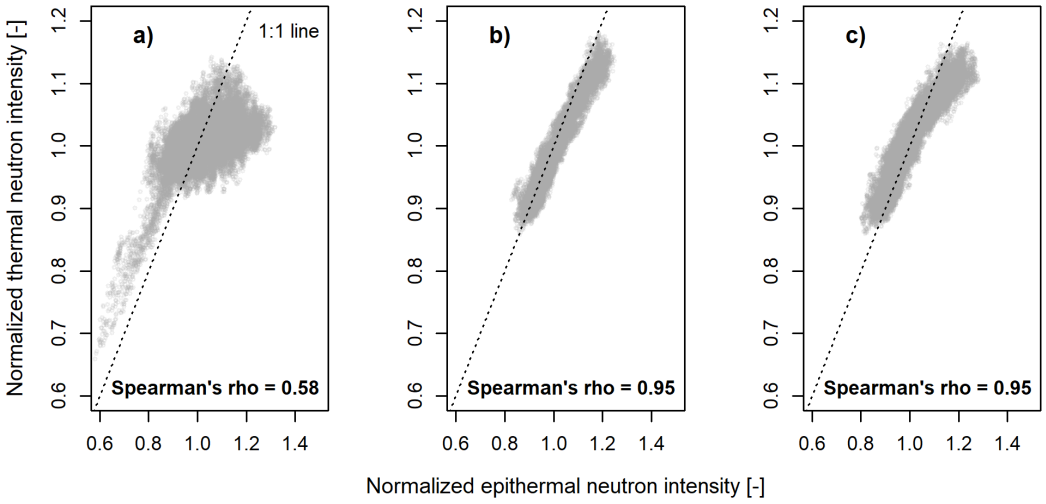

Figure 3.8: Relationship between observed normalised thermal and epithermal neutron intensity at the three CRNS sites; namely (a) site A, the main study site, (b) site B (soil moisture assumed to be uniform) and (c) site C (soil moisture assumed to be uniform). Normalised intensities were calculated by dividing by the respective time series mean.

line.

3.4.4 Estimation of soil moisture from observed neutron intensities

We estimated the soil moisture time series from the CRNS signal with three different calibration approaches. We first applied the standard calibration approach by using the corrected epithermal neutron intensities (N_E) and iteratively calibrating N_0 in equation (3.2) – (4.4). We then compared this standard approach to alternative approach 1, where N_E is used but all parameters (N_0, a_0, a_1, a_2) from equation (3.2) – (4.4) are adjusted. Last, we compare the standard calibration approach and alternative approach 1 with alternative approach 2. Here, we rescale the epithermal neutron intensity (N_E) by calculating the normalised sum of the thermal and epithermal neutrons (N_{ET}), based on equation (3.6), and use the rescaled neutron intensities in equation (3.2) – (4.4) by iteratively calibrating N_0. The approaches are applied by using a depth-distance weighted reference soil moisture time series and the arithmetic average of the reference measurements which result in the statistical goodness of fit presented in Table 5.3.

The calibration of the CRNS-derived soil moisture time series by iteratively adjusting N_0, based on the standard calibration approach and a weighted reference soil moisture time series, results in a KGE of 0.57 (Table 5.3). When all variables are adjusted in alternative approach 1, the KGE can be increased to 0.84. Similarly, the KGE increases to 0.85 when alternative approach 2 with rescaled neutron intensities N_{ET} is applied. This improvement is also expressed by a higher Nash-Sutcliffe efficiency (NSE) and lower root mean square error (RMSE) for alternative approaches 1 and 2, either by using a rescaled neutron time series N_{ET} and only adjusting N_0 or by using N_E and tuning all the parameters. In contrast, using the arithmetic

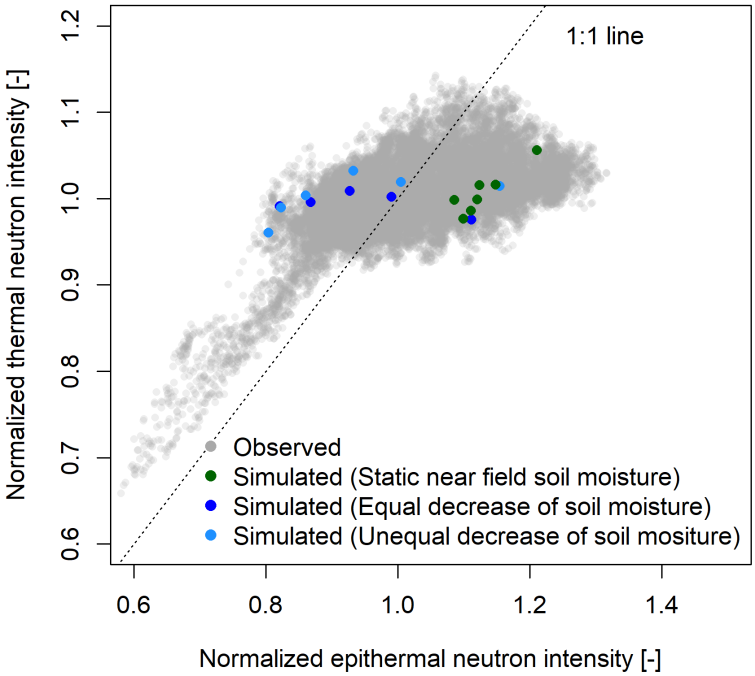

Figure 3.9: The relationship between normalised thermal and epithermal neutron intensities for in situ observations and the relationship between the normalised detected epithermal and thermal neutrons for simulated data. The simulated values refer to the simulation set and scenarios summarised in Table 5.1. Simulated neutrons are normalised by the average number of detected neutrons of all simulations in the respective energy range.

Table 3.2: Statistical goodness of fit when calibrating equations (3.2) – (4.4) with (applying) the three different calibration approaches.

Calibration	Reference soil moisture	Neutron intensities	a_0	a_1	a_2	N_0	KGE	NSE	RMSE
Standard		N_E	0.0808	0.372	0.115	907.3	0.57	-0.01	0.032
Approach 1	Weighted	N_E	0.2080	0.155	0.117	595.7	0.84	0.72	0.017
Approach 2		N_{ET}	0.0808	0.372	0.115	956.4	0.85	0.71	0.017
Standard		N_E	0.0808	0.372	0.115	896.9	0.46	-0.84	0.04
Approach 1	Arithmetic	N_E	0.1400	0.083	0.103	926.4	0.84	0.61	0.019
Approach 2		N_{ET}	0.0808	0.372	0.115	955.4	0.79	0.61	0.019

average reference soil moisture time series leads to a lower KGE of 0.46 compared to the calibration against a depth-distance weighted average with the standard calibration approach. However, the KGE again increases strongly if either alternative approach 1 or alternative approach 2 are optimized against the arithmetic average of reference soil moisture observations to generate a CRNS-derived soil moisture time series. The derived KGE increases to 0.84 and 0.79, respectively, which is close to the goodness of fit derived using the weighted reference soil moisture time series. Similarly, the additional goodness-of-fit parameters for NSE and RMSE improve when using alternative approaches 1 and 2 instead of the standard approach. In

general, for alternative approaches 1 and 2, the calibration result in terms of the KGE improves by at least 0.25 over the 4-year study period when compared to the standard calibration approach (see also Fig. 3.12 and Table 5.2).

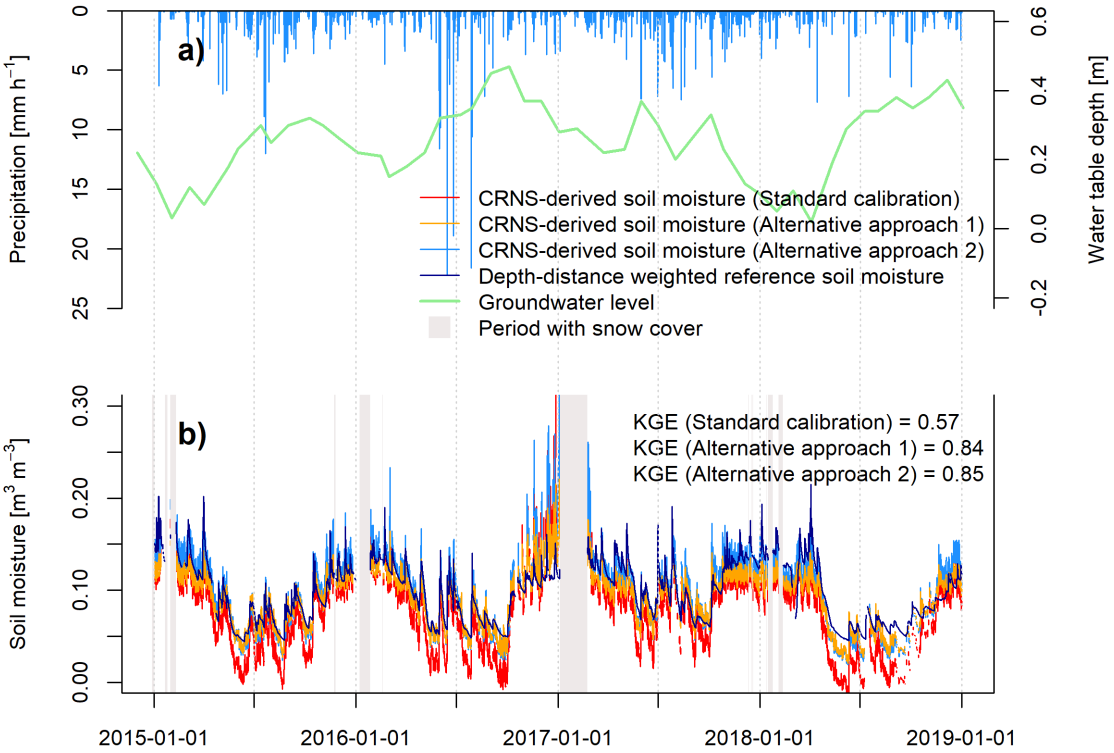

Figure 3.10: On-site observed hourly rainfall sums (a) and CRNS-derived soil moisture time series based on the standard calibration approach, as well as calibration approaches 1 and 2, in comparison to the depth-distance weighted reference soil moisture time series derived from SMT100 sensors (b).

The CRNS-derived soil moisture time series based on the three calibration approaches both over- and underestimate the dynamics of the weighted reference time series (Fig. 3.10). The largest differences from using the standard calibration approach to either tuning all parameters of the transfer function in alternative approach 1 or applying the rescaled N_{ET} in alternative approach 2 occur in summer periods when the weighted near-field reference soil moisture is generally low. In these periods, using N_E in the standard calibration approach results in a distinct underestimation of the reference soil moisture while both alternative calibration approaches produce a CRNS-derived soil moisture time series fitting the weighted reference more closely (Fig. 3.11). In contrast, differences between the CRNS-derived soil moisture time series and the reference time series are less pronounced in winter periods when the near-field reference soil moisture is high.

Although differences between the CRNS-derived soil moisture time series vary seasonally, an overall closer fit to the weighted reference time series can be achieved when estimating soil moisture based on the two tested approaches for improving calibration against near-field reference measurements as previously illustrated by the statistical goodness-of-fit parameters. Last, we compared the CRNS-derived soil moisture time series based on the three calibration approaches. A bootstrap-

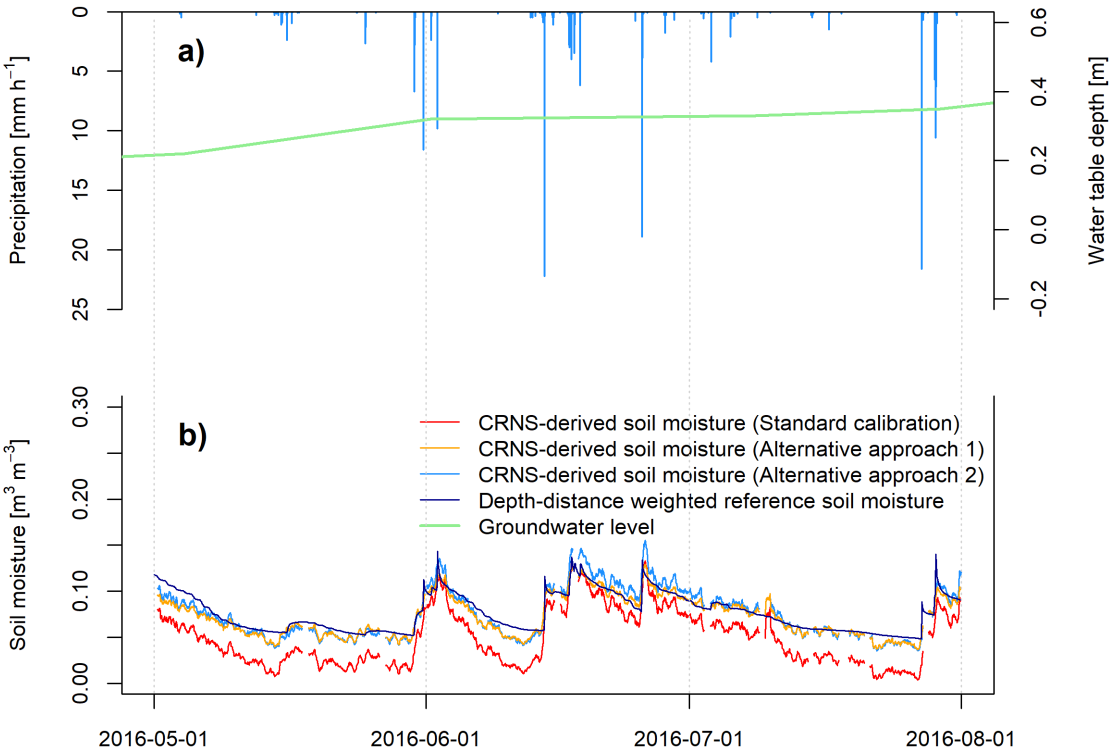

Figure 3.11: On-site observed hourly rainfall sums (a) and CRNS-derived soil moisture time series based on the standard calibration approach and alternative approaches 1 and 2 in comparison to the depth-distance weighted reference soil moisture time series derived from SMT100 sensors (b) for a 3-month period in the summer of 2016.

ping of the residuals and subsequent Wilcoxon rank sum tests per time step revealed significant differences ($p < 0.05$) between CRNS-derived soil moisture time series calculated from the standard calibration approach and the two alternative approaches tested for improving the calibration. For both alternative calibration approaches and both reference soil moisture time series, the CRNS-derived soil moisture time series are significantly different from the time series based on the standard calibration approach for at least 97 % of the time steps.

3.5 Discussion

3.5.1 Neutron-energy-dependent variations in footprint size and neutron intensity

Our neutron transport simulations resulted in footprint radii of epithermal neutrons, which lie in the ranges reported by Köhli et al. [2015] and are shown in Schrön et al. [2017], for all simulation scenarios. In contrast, little is known about the measurement footprint radius of thermal neutrons. Previous studies assume a similarly sized footprint [e.g. Vather et al., 2020] or a significantly smaller measurement radius [e.g. Bogena et al., 2020]. Our simulation results reveal that the derived measurement radii strongly depend on the definition of the point of origin of the thermal neutrons

detected by the virtual neutron detector. If the point of thermalisation is used to calculate the measurement radius R_{86}, then the footprint radius has an average size of about 43-44 m and only exhibits a slight response to changes in soil moisture. This estimate comes close to what is stated in Bogena et al. [2020] and lies in the range of what was recently reported by Jakobi et al. [2021]. In our simulations with constant soil moisture in near-field mineral soils, the fraction of detected neutrons being thermalised in areas covered with mineral soils and peatland soils remains constant, although soil moisture in peatland soils is altered (Fig. 3.5). This could lead to the interpretation that the footprint of thermal neutrons is too small to cover a significant portion of peatland soils and, thus, peatland soil moisture variations do not influence the simulated thermal neutron intensity. However, even if the footprint based on the point of thermalisation is small, an influence of peatland soil moisture variations on the number of thermal neutrons reaching the virtual detector is visible (Fig. 3.4). As a consequence, the alternative definition may be more suitable. If the point of first soil contact is defined as the origin for both epithermal and thermal neutrons, then the thermal neutron footprint becomes twice as large (compared to using point of thermalisation as the origin). It then covers larger parts of peatland areas, and the fraction of detected thermal neutrons originating from peatland areas changes with varying peatland soil moisture. This definition better explains the variations visible in the detected thermal neutron intensity because the number of detected thermal neutrons generated from higher-energy neutrons with peatland soil contact is likely to vary with peatland soil moisture.

The average measurement depths of epithermal neutrons simulated here also lie in the range of the values reported in previous studies [Zreda et al., 2008; Köhli et al., 2015]. For the case of constant soil moisture conditions in the highly sensitive near-field, the average measurement depth of epithermal neutrons only shows a slight decrease with increasing peatland soil moisture. In the scenarios with varying soil moisture contents in both the near-field and the far field, a change in the CRNS measurement depth is clearly visible. The integration depth of the thermal and epithermal neutrons shows a very similar response to soil moisture variations, with thermal neutrons having a slightly shallower D_{86} when based on the point of thermalisation. In contrast, if the maximum depth along the neutron transport path is considered as the measurement depth, then the thermal neutron integration depth becomes nearly twice as deep (compared to epithermal neutrons). This observation might be explained in the following way: after a high-energy neutron enters the soil column, it is slowed down to an epithermal neutron. This epithermal neutron either leaves the soil or is further slowed down to a thermal neutron before then leaving the soil. The deeper in the soil an epithermal neutron is generated by a high-energy neutron, the more likely it will be thermalised before leaving the soil column. Consequently, thermal neutrons might contain information of soil moisture from even greater depths than epithermal neutrons (see fig. 3.3 and 3.6). This would have implications for, e.g., soil sampling campaigns for calibration as larger sampling depths might be required if thermal neutrons are of interest. However, little is known about the vertical and horizontal footprint dynamics of thermal neutrons in general and care should be taken when interpreting the presented results based on a heterogeneous model domain and a narrow range of simulated boundary conditions. Further research is required to investigate the footprint of thermal neutrons for a homogeneous study site and under a wide range of boundary conditions to eventu-

ally derive weighting functions similar to those developed for epithermal neutrons during the past decade [e.g. Zreda et al., 2008; Franz et al., 2012a; Köhli et al., 2015; Schrön et al., 2017; Scheiffele et al., 2020]. Very recently, Jakobi et al. [2021] investigated the footprint of thermal neutrons and developed weighting functions based on the point of thermalisation as the origin generated the first valuable conclusions to understand the footprint of thermal neutrons. However, as stated before, our study shows that the footprint of thermal neutrons seems to be larger than estimated, based on the point of thermalisation, and that the point of first soil contact may be a better definition for assessing the footprint of thermal neutrons which again illustrates the need for further research.

Besides the varying dimensions of the integration volume, epithermal and thermal neutrons show a different response to the simulated changes in peatland soil moisture. This applies to both the simulation set, with a constant near-field soil moisture, and to the simulation set, with the soil moisture in the near-field and in the peatland soils changing at different degrees. In general, the total number of detected epithermal and thermal neutrons decreases with an increasing peatland soil moisture and, thus, with an increasing amount of hydrogen in the model domain. However, the response of epithermal and thermal neutrons to the different simulated soil moisture contents in mineral and peatland soils differs. Differences in the response of epithermal and thermal neutrons have also been observed in previous modelling studies [e.g. Andreasen et al., 2017b] for variations in soil moisture or liquid water layer thickness [e.g. Hubert et al., 2016]. Thermal neutrons show a much smaller response to variations in hydrogen [Weimar et al., 2020], and they show a moderation optimum occurring just below $0.10\,\mathrm{m^3\ m^{-3}}$ soil moisture [Sato and Niita, 2006; Weimar et al., 2020]. The latter is caused by the two competing processes influencing thermal neutron abundance, i.e. slowing down of epithermal neutrons (moderation) and absorption of thermal neutrons, for example, by hydrogen [e.g. Hubert et al., 2016].

Several assumptions need to be considered when interpreting the neutron transport simulation results presented here. In this study, a simplified model domain was created where topography was neglected. However, while topography may play a more important role in mountainous terrain [e.g. Schattan et al., 2019; Mares et al., 2020], smaller topographic gradients, as at our study site, are unlikely to have a considerable influence on footprint sizes [Köhli et al., 2015]. Nevertheless, the slightly elevated position of the observation site compared to the surrounding peatland (Fig. 3.1) may cause slightly larger real-world footprint radii than those obtained from the simulations. Additional simplifications include the estimation of soil porosities based on the density of quartz and the use of the same soil chemistry for organic and mineral soils. The higher amount of hydrogen stored in the soil organic matter of the peatlands is likely to shift the simulation results towards lower ratios of epithermal and thermal neutrons, smaller footprint sizes in the real world and a shallower response of epithermal and thermal neutrons with changing soil water content in all simulations, for example. Last, we did not add a vegetation layer to the simulations as most of the study site is pasture assumed to represent static sources of additional hydrogen. Nevertheless, the latter will likewise have a reducing influence on the general footprint size, as is can be exemplary seen when applying the weighting functions developed by Köhli et al. [2015] and Schrön et al. [2017] which include a vegetation height parameter.

As a consequence of the simplifications and limitations of the neutron transport simulations, care needs to be taken when using the model results to explain the real-world observations.

3.5.2 Towards a quantification of footprint heterogeneity

The high correlation between thermal and epithermal neutron intensities at the more uniform sites and the low correlation at the heterogeneous site can be explained by the fact that both energy ranges have different footprint sizes, as indicated by Bogena et al. [2020] and partly supported by the neutron simulations shown here. The heterogeneous observation site has a lower correlation coefficient which indicates larger differences between the soil water contents and dynamics of the near-field and of far field with organic peatland soils. However, our simulations indicate that the thermal neutron intensity is influenced by far-field soil moisture changes occurring in areas covered with peatland soils. The scatterplot for our heterogeneous site A (in Fig. 3.8a) shows deviations from the narrow point cloud and, thus, the close non-linear relationship observed at study sites where soil moisture is more uniform in terms of absolute values and relative changes. The strongest deviations occur at high normalised intensities, leading to the heterocedasticity observed and, in turn, the lower correlation coefficient. Adding the results from all simulations conducted in the scope of this study to the scatterplot with the observed values (Fig. 3.9) further illustrates this effect. The simulated intensities comprising different absolute soil moisture values for mineral soils of the near-field and peatland soils of the far field, as well as different soil water dynamics, are located in the area representing deviations from the relationship observed at the two homogeneous observation sites. In particular, the simulated normalised numbers of detected neutrons with low static near-field soil moisture and changing peatland soil moisture are located in the area of the scatter plot considered as having deviations. Under real-world conditions, this response may be expected during summer periods when mineral soil moisture contents reached a minimum, while peatland soil moisture continues to change due to, e.g., high water storage capacities and the variations in shallow groundwater visible in Fig. 3.2 and Fig. 3.10.

Hence, a twofold influence may be considered. On the one hand, the total soil moisture content differs between the mineral soils of the near-field and the far-field peatland soils leading to a different response of thermal and epithermal neutrons when soil water contents change in the near-field and the far field. On the other hand, the differences in the moisture content between the near-field and the far field may fluctuate over time and result in a varying influence on the observed neutron intensities in the two energy ranges.

Against this background, the simple Spearman rank correlation coefficient can serve as a first indicator for footprint heterogeneity in terms of soil moisture conditions in the near- and the far field of the neutron detector and could be used to characterise observation sites and select processing procedures accordingly. Detailed knowledge of the functional relationship between thermal and epithermal neutrons at heterogeneous observation sites poses great potential for an improved assessment of the footprint heterogeneity and the development of advanced indices. However, this requires further research regarding the relationship of the thermal and epithermal neutron intensities under changing soil moisture and with respect to different

environmental factors such as soil chemistry. As study sites are always restricted to local boundary conditions, large-scale irrigation experiments using, e.g., centre pivots [see also Franz et al., 2015] combined with neutron transport simulations could improve and extend the insights gained in this study regarding indicators for footprint heterogeneity and the definition of measurement footprints in general. Additionally, this may also require the need to develop transfer functions for thermal neutrons which are similar to those already available for estimating soil moisture from epithermal neutron intensities [e.g. Desilets et al., 2010; Franz et al., 2013b; Köhli et al., 2021].

3.5.3 Improving the estimation of near-field soil moisture

The calibration of neutron observations against the near-field reference soil moisture time series from in situ soil moisture sensors revealed an improvement of the calibration result in terms of the statistical goodness of fit when either all parameters of the transfer function are adjusted (N_0, a_0, a_1 and a_2) or the combination of thermal and epithermal neutrons based on (3.6) was used and only N_0 was calibrated. Using the standard calibration approach, the calibration against a weighted average reference soil moisture time series resulted in a better KGE compared to a simple arithmetic average. This illustrates the positive effect of the weighting procedure developed by Köhli et al. [2015] and advanced by Schrön et al. [2017], to match the sensitivity of the CRNS.

Adjusting all parameters in alternative approach 1, instead of only calibrating N_0, and combining the thermal and epithermal neutrons in the scope of alternative approach 2 leads to an improvement in the calibrated KGE by at least 0.25. As the analyses revealed a significant ($p < 0.05$) difference between the CRNS-derived soil moisture based on the standard calibration approach and both alternative calibration approaches for at least 97 % of the data points of the time series, a significantly improved representation of the near-field soil moisture dynamics can be achieved by either adjusting all parameters (approach 1) or combining both neutron energy ranges (approach 2). However, this does not represent an uncertainty analysis that considers various statistical sources of uncertainty as was done in previous studies [e.g. Andreasen et al., 2017b; Baroni et al., 2018; Gugerli et al., 2019; Schattan et al., 2019; Jakobi et al., 2020].

In this study, reference soil moisture sensors were installed in the near-field of the CRNS only, and no information on far-field peatland soil moisture dynamics were available. Although this poses the largest limitation of this study, marked differences in soil water dynamics can be expected for mineral and peatland soils due to the distinct hydraulic behaviour of the latter [e.g. Rezanezhad et al., 2016]. In addition, peatland areas at the study site are characterised by groundwater influence and potentially higher soil water content, as observed in the reference soil samples taken from mineral and peatland soils in February 2020 (section 2.1). The obtained calibration results of CRNS-derived soil moisture time series clearly show an improvement in the representation of near-field soil moisture dynamics when accounting for these peatland soil moisture dynamics through alternative approaches 1 or 2.

The transfer function developed by Desilets et al. [2010], and revised by Köhli et al. [2021], was designed for a uniform soil water content within the measurement

footprint. In the example presented in this study, the epithermal neutron response is stronger than the soil water changes observed in the mineral soils of the near-field, causing the underestimation of the near-field reference soil moisture during summer periods. Therefore, adjusting the shape-defining variables of eq. (3.2) – (4.4) in addition to the calibration parameter N_0 alone in alternative approach 1 allows for the adjustment of the transfer function for the soil moisture dynamics of the near-field. Different studies already adjusted the shape-defining parameters of the standard calibration function (eq. (3.1)) [e.g. Heidbüchel et al., 2016] and achieved better calibration results compared to adjusting N_0 only. However, the reasons for changing the physical meaning of eq. (3.1) or (eq. (3.2) – (4.4)) by tuning all variables of the transfer function remain disputable. The results of this study shed more light on the potential reasons for an improved calibration against reference measurements by changing the shape of the transfer function. Distinct differences in soil moisture states and dynamics within the measurement footprint over time may lead to neutron responses deviating from the shape of the original transfer function (eq. (3.1) or (eq. (3.2)). This is in line with findings from previous studies [e.g. Lv et al., 2014; Heidbüchel et al., 2016]. Nevertheless, care should be taken when tuning the shape-giving parameters to optimise the goodness of fit against different reference measurements. This can lead to different optimised values for the shape-giving parameters (N_0, a_0, a_1 and a_2) depending on the reference soil moisture time series (see also Table 5.2). This illustrates that the shape-giving parameters can be fitted to different reference measurements, and that the objective for the site-specific optimisation needs to be considered. For example, optimising for a site-specific areal average requires sufficient spatio-temporal coverage of reference measurements, while optimising for reference soil moisture in defined parts of the footprint requires representative reference measurements from these areas.

In contrast, in alternative approach 2, we produced a rescaled neutron time series N_{ET} based on observed epithermal (N_E) and thermal N_T neutron intensities and, thus, adjusted the signal instead of the transfer function. As the thermal neutron response to soil water changes is generally weaker [Weimar et al., 2020], summing the observed normalised intensities of the thermal and epithermal neutrons and rescaling them using eq. (3.6), leads to a less steep slope of the functional relationship between the neutron intensity and reference soil moisture. Consequently, the rescaling approach presented here makes use of thermal neutrons (N_T) as a proxy for a different response to soil water changes, leading to a rescaled neutron time series N_{ET} that is more similar to the epithermal neutron intensities N_E if the entire measurement footprint has the lower soil water content and dampened dynamics of the near-field where the reference point sensors are installed. Hence, the second alternative approach tested in this study is suitable for a separation of near- and far-field soil moisture at the heterogeneous observation site investigated.

Both approaches tested in this study allow for an improvement of the estimation of near-field soil moisture and illustrate the potential for separating the measurement footprint where approach 1 is generally applicable, while approach 2 may be most suitable at sites with conditions similar to those at the study site investigated. We would like to note that further instrumental adjustments based on additional shielding may also offer the potential to limit the measurement footprint. These include downward-looking detectors [Badiee et al., 2021] or side-looking devices [Francke et al., 2022]. However, using a non-modified detector allows the possibility to also

retrieve an area-averaged soil moisture time series in the entire footprint.

Several limitations need to be considered when assessing the improvement achieved with the different approaches tested in this study. Besides the horizontal footprint of the thermal neutrons being smaller than for epithermal neutrons, the integration depth can be considered to be different as well. This may complicate the joint interpretation and combination of both neutron energies and intensities. Additionally, the differing influences of other factors on thermal and epithermal neutron observations should be considered. In this study, raw thermal and epithermal neutron observations were corrected equally for the influence of variations in atmospheric shielding depth and incoming high-energy neutron radiation but not for variations in air humidity as the latter was determined for epithermal neutrons only. The correction procedures applied to the observed thermal neutrons differ among studies [e.g. Andreasen et al., 2016; Jakobi et al., 2018], and in addition to the need for detailed knowledge about the dynamics of the integration volume, further research is required concerning appropriate correction procedures for thermal neutrons to varying environmental conditions.

3.6 Conclusions

The neutron transport simulations performed here support previous studies that indicate a distinctively smaller horizontal measurement footprint of thermal compared to epithermal neutrons. However, the thermal neutron footprint radius strongly depends upon the definition of the origin of the detected neutrons. Our study suggests that the point of thermalisation alone may not be suitable for characterising the sensitive measurement footprint size, as detected thermal neutrons do vary with far-field soil moisture variations. Instead, as with epithermal neutrons, the point of first soil contact may be more suitable. In this case, the integration radius almost doubles but still remains smaller than that of epithermal neutrons. The integration depth also increases strongly even surpassing that of epithermal neutrons.

The relationship between normalised observed thermal and epithermal neutron intensities is likely to differ between homogeneous and heterogeneous conditions and may be used to characterise the footprint heterogeneity. The simple Spearman rank correlation coefficient between the normalized thermal and epithermal neutron intensities proved to a be a suitable first indicator for the footprint heterogeneity, with lower values indicating a larger (and varying) difference between soil water contents in the near- and the far field.

Either adjusting all parameters of the transfer function or rescaling the observed epithermal neutron intensities by averaging the normalized dynamics of thermal and epithermal neutrons leads to a significant improvement in the calibration result against the reference soil moisture sensors in the near-field. This is achieved by changing the neutron intensity dynamics towards a more dampened response that would occur if the entire epithermal footprint had the lower soil moisture conditions and dampened dynamics of the near-field.

In conclusion, both approaches tested for improving the estimation of near-field soil moisture pose great value for the use of CRNS at study sites with heterogeneous soil water contents and dynamics. On the one hand, complementary observations of thermal and epithermal neutrons offer the opportunity to test for footprint heterogeneity using simple correlation measures. On the other hand, in addition to

adjusting the transfer function, the thermal neutron intensity proved to be a useful proxy for rescaling the epithermal neutron intensities in order to improve the representation of near-field soil water time series at the study site. Several limitations of this study need to be considered and also illustrate the need for further research, especially regarding the general response of thermal neutrons to environmental conditions, suitable correction procedures for these phenomena and the behaviour of both neutron energies at study sites with heterogeneous distributions of soil water and pools of hydrogen in general. Nevertheless, this study illustrates the possibility of achieving a spatial disaggregation of soil moisture at heterogeneous study sites and the potential of using both neutron energies for improving CRNS-derived soil water estimates.

3.7 Appendix

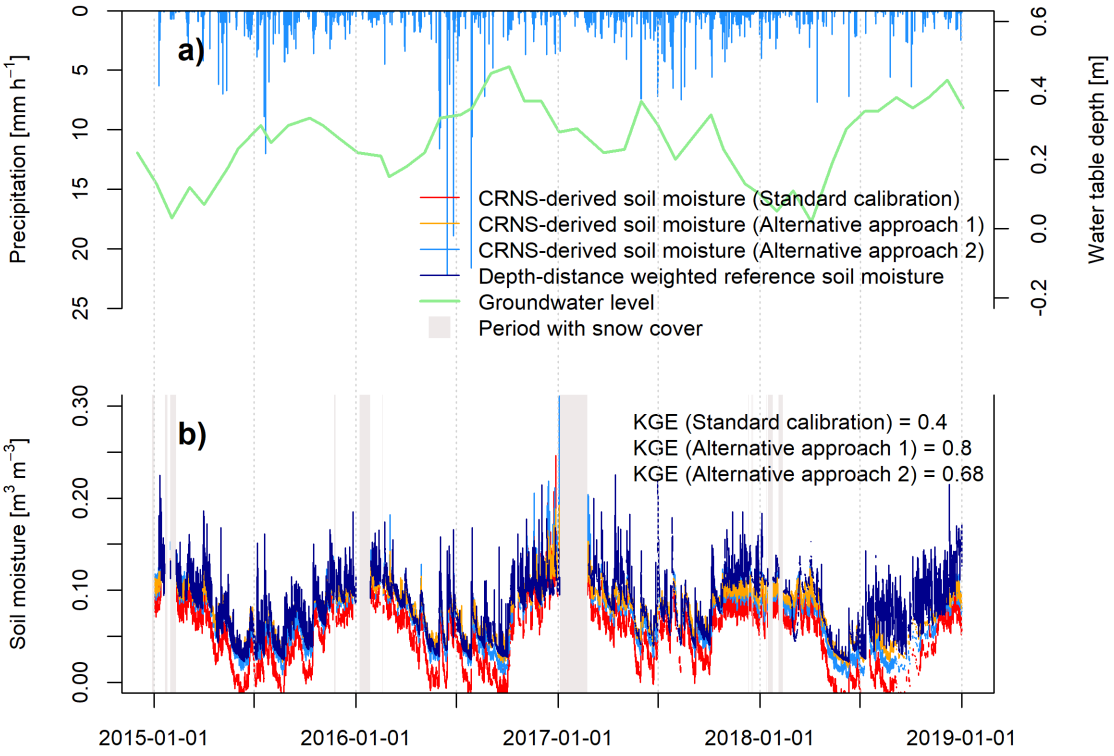

Figure 3.12: On-site observed hourly rainfall sums (a) and CRNS-derived soil moisture time series based on the standard calibration approach and calibration approaches 1 and 2 in comparison to the depth-distance weighted reference soil moisture time series derived from TDR sensors (b).

Table 3.3: Statistical goodness of fit when calibrating equations (3.2) – (4.4) with (applying) the three different calibration approaches using reference soil moisture observations from TDR sensors with a higher noise and lower signal quality.

Calibration	Reference soil moisture	Neutron intensities	a_0	a_1	a_2	N_0	KGE	NSE	RMSE
Standard		N_E	0.0808	0.372	0.115	849.5	0.40	-0.58	0.040
Approach 1	Weighted	N_E	0.1420	0.153	0.100	724.6	0.80	0.64	0.019
Approach 2		N_{ET}	0.0808	0.372	0.115	899.9	0.68	0.31	0.026
Standard		N_E	0.0808	0.372	0.115	842.6	0.33	-1.03	0.044
Approach 1	Arithmetic	N_E	0.1420	0.153	0.100	724.6	0.78	0.58	0.020
Approach 2		N_{ET}	0.0808	0.372	0.115	898.4	0.64	0.19	0.028

Chapter 4

Depth-extrapolation of surface soil moisture estimates derived with CRNS

A version of this chapter has been submitted as:

Depth-extrapolation of field-scale soil moisture time series derived with cosmic-ray neutron sensing using the SMAR model

Daniel Rasche, Theresa Blume, and Andreas Güntner

SOIL (submitted), 2024.

4.1 Abstract

Soil moisture measurements at the field scale are highly beneficial for different hydrological applications including the validation of space-borne soil moisture products, landscape water budgeting or multi-criteria calibration of rainfall-runoff models from field to catchment scale. Many of these applications require information on soil water dynamics in deeper soil layers. Cosmic-Ray Neutron Sensing (CRNS) allows for non-invasive monitoring of field-scale soil moisture across several hectares around the instrument but only for the first few tens of centimetres of the soil. Simple depth-extrapolation approaches often used in remote sensing applications may be used to estimate soil moisture in deeper layers based on the near-surface soil moisture information. However, most approaches require a site-specific calibration using depth-profiles of in situ soil moisture data, which are often not available. The physically-based soil moisture analytical relationship SMAR is usually also calibrated to sensor data, but could be applied without calibration if all its parameters were known. However, in particular its water loss parameter is difficult to estimate. In this paper, we introduce and test a simple modification of the SMAR model to estimate the water loss in the second layer based on soil physical parameters and the surface soil moisture time series. We apply the model at a forest site with sandy soils with and without calibration. Comparing the model results against in situ reference measurements down to depths of 450 cm shows that the SMAR models both with and without modification do not capture the observed soil moisture dynamics well. The performance of the SMAR models nevertheless meets a previously used benchmark RMSE of ≤ 0.06 $cm^3\,cm^{-3}$ in both, calibrated and uncalibrated scenarios. Only with effective parameters in a non-physical range, a better model performance could be achieved. Different transfer functions to derive surface soil moisture from CRNS do not translate into markedly different results of the depth-extrapolated soil moisture time series simulated with SMAR. However, a more accurate estimation of the sensitive measurement depth of the CRNS improved the soil moisture estimates in the second layer. Despite the fact that the soil moisture dynamics are not well represented at our study site using physically reasonable parameters, the modified SMAR model may provide valuable first estimates of soil moisture in a deeper soil layer derived from surface measurements based on stationary and roving CRNS as well as remote sensing products where in situ data for calibration are not available.

4.2 Introduction

Soil moisture is a key parameter in the hydrological cycle [e.g. Vereecken et al., 2008, 2014; Seneviratne et al., 2010]. It controls several aspects of the environment such as soil infiltration, runoff dynamics, plant growth and biomass production which in turn influence evapotranspiration as well as the climatic conditions on varying spatio-temporal scales [see reviews by e.g. Daly and Porporato, 2005; Vereecken et al., 2008; Seneviratne et al., 2010; Wang et al., 2018]. Thus, information on soil water dynamics at the field scale have great importance for various larger-scale hydrological applications ranging from landscape water budgeting to multi-criteria calibration approaches in rainfall-runoff modeling. However, due to the high spatio-temporal variability of soil water content [Famiglietti et al., 2008; Vereecken et al., 2014] which is highest in surface soil layers [Babaeian et al., 2019], measuring field-

scale soil moisture and its dynamics proves difficult based on invasive point-scale soil moisture measurement methods as for example reviewed in Vereecken et al. [2014] and Babaeian et al. [2019]. For instance, the installation of electromagnetic point sensors measuring at high temporal resolution would require a very large number of sensors to obtain a representative field-scale average [Babaeian et al., 2019]. Additionally, sensor networks are not always feasible as agricultural management practices hamper a permanent installation of point sensors [Stevanato et al., 2019]. As a consequence, extensive point sensor networks which allow for the estimation of field-scale soil moisture are often restricted to a rather small number of research related monitoring sites such as the Terrestrial Environmental Observatories (TERENO, `www.tereno.net`) in Germany [e.g. Zacharias et al., 2011; Bogena et al., 2018; Kiese et al., 2018; Heinrich et al., 2018].

Kodama et al. [1979], Kodama et al. [1985] and Dorman [2004] suggested the potential of naturally occuring secondary neutrons produced by high-energy cosmic rays for estimating soil and snow water. About a decade ago Zreda et al. [2008]; Desilets et al. [2010], introduced a methodological framework for soil moisture estimation using cosmic-ray neutrons. The Cosmic-Ray Neutron Sensing (CRNS) approach is a non-invasive geophysical method for estimating representative field-scale soil moisture [Schrön et al., 2018b] based on the measurement of cosmic-ray neutrons which are inversely related to the amount of hydrogen in the vicinity of the neutron detector. As soil water is the largest pool of hydrogen in the footprint of the neutron detector in most terrestrial environments, CRNS allows for the measurement of integrated soil moisture of several hectares around the instrument and the first decimetres of the soil [e.g. Zreda et al., 2008; Desilets et al., 2010; Köhli et al., 2015; Schrön et al., 2017].

Estimating soil moisture using CRNS has a high potential for various hydrological applications, which require soil moisture observations at the field scale. Several studies demonstrate the potential of CRNS-derived soil moisture estimates for example for a comparison with satellite derived soil moisture products, their validation and the improved calibration of environmental models [e.g. Holgate et al., 2016; Montzka et al., 2017; Iwema et al., 2017; Duygu and Akyürek, 2019; Dimitrova-Petrova et al., 2020]. Besides stationary CRNS probes for the retrieval of field scale soil moisture time series, roving CRNS-devices have been successfully used, mapping CRNS-derived surface soil moisture in even larger areas with instruments mounted on vehicles [e.g. McJannet et al., 2017; Schrön et al., 2018a; Vather et al., 2019] and [Fersch et al., 2018] illustrate potential synergies between CRNS, airborne radar and in situ point sensor networks for soil moisture estimation across spatial scales. Due to the sensitivity of CRNS to any hydrogen in the measurement footprint, snow monitoring [e.g. Schattan et al., 2017, 2019; Gugerli et al., 2019], irrigation management [e.g. Li et al., 2019a] as well as biomass estimation [e.g. Baroni and Oswald, 2015; Tian et al., 2016; Jakobi et al., 2018; Vather et al., 2020] pose further fields of application and are reviewed in Andreasen et al. [2017a].

Although the large areal footprint of the CRNS-instrument allows estimating field-scale integral soil moisture, the CRNS-derived time series lack soil moisture information from greater depths. However, soil moisture at these greater depths becomes highly relevant as soon as the rooting depth of crops or forest extends past the first decimeters. The maximum rooting depth and hence, root zone extent as well as root density along the soil profile varies with vegetation type and biome

[e.g. Canadell et al., 1996; Jackson et al., 1996]. According to Jackson et al. [1996], on global average across all biomes, the 75 % of plant roots occur in the first 40 centimetres of the soil, which would be largely covered by the CRNS. However, the global average maximum rooting depth, and thus, root zone depth is about 4.6 m [Canadell et al., 1996] where the rooting depth also depends on prevailing soil hydrological conditions [Fan et al., 2017]. Even grassy vegetation and crops can have rooting depths of more than 200 cm [Canadell et al., 1996], thus exceeding the measurement depth of CRNS. Deep roots play a significant role for the water supply of plant ecosystems especially during dry conditions [Canadell et al., 1996] i.e. through hydraulic redistribution [see e.g. Neumann and Cardon, 2012] or increased root water uptake from deeper soil layers under drought conditions [Maysonnave et al., 2022]. Furthermore, plant species influence infiltration and vertical soil moisture patterns through species dependent root distributions [e.g. Jost et al., 2012] and horizontal soil moisture patterns through species dependent evapotranspiration and interception rates [e.g. Schume et al., 2003]. Hence, field-scale soil water information from the deeper vadose zone overcoming these smaller scale heterogeneities can be important for the quantification of water storage variations, potential influences on vegetation dynamics, matter fluxes and the characterisation of the local hydrological cycle.

Given the importance of soil moisture in the deeper root zone, extending CRNS-measurements to greater depths is of high importance for broadening the applicability of CRNS for soil water estimations [Peterson et al., 2016]. Numerous studies extrapolate surface soil moisture time series to greater depths using different empirical approaches [e.g. Zhang et al., 2017; Li and Zhang, 2021] including regression analyses, machine learning techniques or other approaches such as the soil water index (SWI) [Wagner et al., 1999; Albergel et al., 2008]. Few studies address the depth-extrapolation of field-scale CRNS-derived soil moisture time series [e.g. Peterson et al., 2016; Zhu et al., 2017; Nguyen et al., 2019; Franz et al., 2020] to the shallow root zone (approx. 100 cm) by applying and comparing extrapolation approaches with the SWI being the most commonly used approach [e.g. Peterson et al., 2016; Dimitrova-Petrova et al., 2020; Franz et al., 2020]. All these approaches require reference soil moisture information in the depth of interest to either build an empirical model or calibrate the depth-extrapolated soil moisture time series. This information may not always be available in sufficient quantity and quality. In contrast, the physically-based soil moisture analytical relationship (SMAR) [Manfreda et al., 2014], applied and modified in recent studies [e.g. Faridani et al., 2017; Baldwin et al., 2017, 2019; Gheybi et al., 2019; Zhuang et al., 2020; Farokhi et al., 2021], allows for the extrapolation of daily surface soil moisture information to a second, lower soil layer by solely relying on soil physical information and a water loss term. This method does not require calibration if the environmental parameters are known.

Against this background, we investigate the potential to depth-extrapolate hourly and daily surface soil moisture time series without calibration and thus without the need for reference soil moisture information in the depth of interest by applying the SMAR algorithm at a highly equipped study site in the TERENO-NE observatory located the lowlands of north-eastern Germany. While soil physical parameters may be determined from soil analyses, the water loss parameter describing the water loss per unit time from the second soil layer is more difficult to estimate. Therefore, we

propose a simple modification of the SMAR algorithm to estimate the water loss term from soil physical characteristics and from the surface soil moisture time series derived from CRNS. We first compare the standard SMAR that uses a constant, calibrated water loss term (calibrated against in situ reference sensors) with the modified, uncalibrated SMAR that uses the estimated water term loss for different depths of the second soil layer down to 450 cm depth. Secondly, we calibrate all soil parameters in the original and modified version of the SMAR model in order to assess its best possible performance at the study site for the given in situ reference data. In addition, we apply different neutron-to-soil moisture transfer functions available to derive the surface soil moisture time series. This is done to assess which transfer function performs best and if a better CRNS-derived surface soil moisture time series translates into better estimates of the depth-extrapolated soil moisture. Lastly, we test the influence of the choice of the depth of first soil layer, i.e. the sensitive measurement depth of CRNS, on the goodness of fit of the depth-extrapolated to soil moisture estimates.

4.3 Material and methods

4.3.1 Study site

The study site is located in the TERENO-NE observatory [Heinrich et al., 2018] in the young Pleistocene landscape of north-eastern Germany (Fig. 4.1). The site hosts the CRNS sensor „Serrahn“ [Bogena et al., 2022]. The site has a mean annual temperature of 8.8°C and mean annual precipitation of 591 mm per year, measured at the long-term weather station in Waren (in a distance of approximately 35 km) operated by the German Weather Service (station ID: 5349, period 1981–2010) [DWD - German Weather Service, 2020a,b]. It is situated on the southern ascent of a glacial terminal moraine formed during the Pomeranian phase of the Weichselian glaciation in the Pleistocene [Börner, 2015]. The dominating soil types in the vicinity of the sensor are Cambisols formed on aeolian sands with depths down to 450 cm deposited during the Holocene [Rasche et al., 2023]. Continuing downwards, these are followed by deposited glacial till of the terminal moraine, glacio-fluvial sediments and glacial tills originating from earlier glaciations with the latter forming the aquitarde the upper groundwater aquifer with water level depths ranging between 13 and 14 m below the surface [Rasche et al., 2023]. A mixed forest dominated by European beech (*Fagus sylvatica*) and Scots pine (*Pinus sylvestris*) is the dominant landcover type. A clearing covered by grassy vegetation can be found nearby.

In order to calibrate the CRNS sensor, soil samples were taken at different distances around the instrument in February 2019 as shown in Fig. 4.1. Soil samples were taken in 5 cm depth increments from 0–35 cm using a split tube sampler containing sampling rings in order to derive soil moisture, soil physical characteristics, average grain size distributions, soil organic matter and lattice water from laboratory analyses as shown in Tab. 4.1. Soil moisture and soil bulk density were determined from oven-drying at 105°C for 12 h and gravimetric analyses of all individual soil samples. Subsequent loss-on-ignition analyses at 550 and 1000°C with a duration of 24 h were used to determine the amount of soil organic matter and lattice water from bulk samples per depth assuming that no inorganic carbon is present in the acidic aeolian sands. Soil porosity was estimated based on the material density of

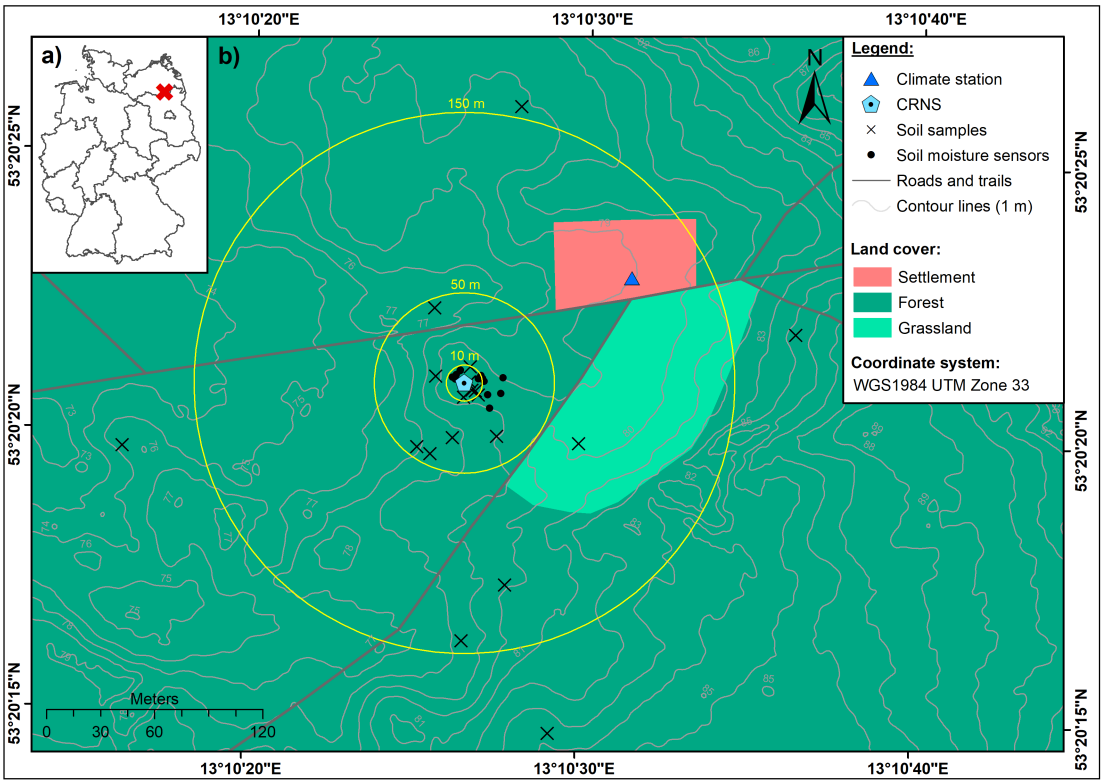

Figure 4.1: Location of the study area within Germany (a) and location of the CRNS observation site „Serrahn“ (b) (digital elevation model: LAIV-MV - State Agency for Interior Administration Mecklenburg-Western Pomerania [2011], land cover: BKG - German Federal Agency for Cartography and Geodesy [2018a]).

quartz ($2.65\,\mathrm{g\,cm^{-3}}$) and corrected for the amount of soil organic matter based on the density of cellulose ($1.5\,\mathrm{g\,cm^{-3}}$).

In addition to the stationary CRNS instrument, the study site is equipped with a groundwater observation well, a weather station and a network of in situ point-scale soil moisture sensor profiles (type SMT100; Truebner GmbH, Germany). A total of 59 in situ soil moisture sensors is deployed in depths down to 450 cm depth with 12 sensors in 10 cm, 6 sensors in 20 cm, 8 sensors in 30 cm, 8 sensors in 50 cm, 6 sensors in 70 cm, 4 sensors in 130 cm, 7 sensors in 200 cm, 4 sensors in 300 cm as well as 450 cm. The sensors are located in distances up to 22 m from the CRNS instrument and continuously monitor the volumetric soil moisture content based on the manufacturer's calibration function.

4.3.2 Field-scale surface soil moisture derived with CRNS

Secondary neutrons are produced by primary cosmic-rays interacting with matter in the atmosphere and in the ground. Depending on their energy level, secondary neutrons may be classified as fast (0.1-10 MeV), epithermal ($>$ 0.25-100 keV) and thermal neutrons ($<$ 0.25 eV) [e.g. Köhli et al., 2015; Weimar et al., 2020]. Cosmic-Ray Neutron Sensing for soil moisture estimation relies on the amount of neutrons in the epithermal energy range produced by nuclear evaporation in the atmosphere and ground [Köhli et al., 2015]. Epithermal neutrons are sensitive to elastic scattering by

Table 4.1: Soil physical characteristics at the CRNS site Serrahn obtained from laboratory analyses of soil samples [Rasche et al., 2023, modified]. Below the maximum sampling depth of 35 cm and down to the maximum depth of the aeolian sand deposits, the soil physical are assumed to have the same soil physical parameters as the layer between 30 and 35 cm. The soil moisture content at field capacity and wilting point were taken from tabulated values in Sponagel et al. [2005] according to the respective soil grain size class (medium-fine sand) and the soil bulk density of the individual layers.

Depth (cm)	Grain size fractions (weight-%)					Bulk density ($g\,cm^{-3}$)	Porosity (-)	Organic matter ($g\,g^{-1}$)	Lattice water ($g\,g^{-1}$)	Field capacity ($cm^3\,cm^{-3}$)	Wilting point ($cm^3\,cm^{-3}$)
	> 2 mm	2 - 0.63 mm	0.63 - 0.2 mm	0.2 - 0.063 mm	< 0.063 mm						
0–5	2.7	19.7	42.2	33.7	2.1	0.24	0.91	0.32	0.003	0.16	0.06
5–10	1.1	8.7	43.5	45.7	2.4	0.77	0.70	0.10	0.002	0.16	0.06
10–15	0.7	7.2	41.5	47.9	2.8	1.25	0.52	0.05	0.002	0.16	0.06
15–20	1.2	7.8	38.7	44.3	2.2	1.43	0.45	0.02	0.002	0.14	0.05
20–25	1.7	7.7	42.2	46.5	2.2	1.55	0.41	0.02	0.002	0.14	0.05
25–30	1.7	8.5	43.5	45.4	1.2	1.59	0.40	0.01	0.002	0.12	0.04
30–35	1.1	8.0	42.8	46.8	1.5	1.63	0.38	0.01	0.002	0.12	0.04
35–450	1.1	8.0	42.8	46.8	1.5	1.63	0.38	0.01	0.002	0.12	0.04

collision with hydrogen and are further moderated to thermal neutrons (< 0.25 eV). Thus, the amount of epithermal neutrons detected by the instrument is inversely correlated with the amount of hydrogen in the sensitive measurement footprint of the sensor.

Epithermal neutron counts detected by the instrument are influenced by atmospheric pressure, the amount of primary high-energy cosmic-ray neutrons entering the earth's atmosphere from space [Zreda et al., 2012] as well as variations of absolute air humidity [Rosolem et al., 2013] and need to be corrected for these influencing factors before soil moisture information can be derived. In this study, we use the correction procedure for air pressure and incoming primary cosmic-ray flux presented in Zreda et al. [2012]. The correction factor for the shielding effect of the atmosphere can be calculated from local air pressure measurements where the attenuation length L is set to 135.9 g cm^{-2} for the study area [Heidbüchel et al., 2016]. The correction factor for the incoming high-energy primary neutron flux was obtained from hourly pressure and efficiency corrected primary neutron intensities (cps) of the Jungfraujoch neutron monitor (JUNG, `www.nmdb.eu`). Furthermore, the neutron data was corrected for the influence of absolute air humidity introduced by Rosolem et al. [2013]. The absolute humidity is calculated from relative humidity and temperature observations of the weather station at the observation site according to Rosolem et al. [2013]. For all correction approaches, the time series averages of air pressure, incoming radiation and air humidity are used as the required reference values. Finally, a 25 h moving average filter is applied to the corrected neutron time series to reduce noise and uncertainty in the data [e.g. Schrön et al., 2018b].

$$\theta_{\text{Standard}} = \left(\left(\tilde{a_0} \frac{1 - \frac{N_{\text{pih}}}{N_{\text{max}}}}{\tilde{a_1} - \frac{N_{\text{pih}}}{N_{\text{max}}}} \right) \times \frac{\rho_{\text{soil}}}{\rho_{\text{water}}} \right) - (\theta_{\text{SOM}} + \theta_{\text{LW}}), \tag{4.1}$$

where

$$\tilde{a_0} = -a_2, \tag{4.2}$$

$$\tilde{a_1} = \frac{a_1 a_2}{a_0 + a_1 a_2}, \tag{4.3}$$

$$N_{\max} = N_0 \cdot \frac{a_0 + a_1 a_2}{a_2}. \tag{4.4}$$

Desilets et al. [2010] introduced a transfer function to convert neutron counts into soil moisture by calibration against reference measurements. Although other approaches exist [e.g. Franz et al., 2013b; Köhli et al., 2021], the Desilet's equation became the methodological standard and can be rewritten as eq. (4.1) – (4.4) [Köhli et al., 2021] with $a_0 = 0.0808$, $a_1 = 0.372$, $a_2 = 0.115$ and N_0 being a local calibration parameter describing the neutron intensity above dry soil [Desilets et al., 2010]. As observed epithermal neutron intensities are sensitive to any hydrogen present in the measurement footprint, the water equivalent of soil organic matter θ_{SOM} and the amount of lattice water θ_{LW} in $\mathrm{cm^3\,cm^{-3}}$ need to be subtracted. Additionally, ρ_{soil} describes the average soil bulk density in the measurement footprint ($\mathrm{g\ cm^{-3}}$) and ρ_{water} the density of water assumed to be 1 $\mathrm{g\ cm^{-3}}$. In this neutron-to-soil moisture transfer function the neutron intensity corrected for variations in air pressure, incoming primary neutron flux and absolute humidity N_{pih} is used. However, the more recent study by Köhli et al. [2021] suggests that the influence of absolute air humidity and soil moisture on the observed epithermal neutron signal are interdependent, i.e. the shape of the neutron-soil moisture relationship changes with absolute humidity. The universal transport solution (UTS), eq. (4.5) – eq. (4.6), [Köhli et al., 2021] accounts for the changing relationship between neutrons and soil moisture under different conditions of absolute humidity.

$$N_{\mathrm{pi}} = N_D \cdot \left(\frac{p_1 + p_2\,\theta_{\mathrm{total}}}{p_1 + \theta_{\mathrm{total}}} \cdot \left(p_3 + p_4\,h + p_5\,h^2\right) + e^{-p_6\,\theta_{\mathrm{total}}}\ \left(p_7 + p_8\,h\right) \right), \tag{4.5}$$

where

$$\theta_{\mathrm{total}} = \left(\theta_{\mathrm{UTS}} + \theta_{\mathrm{SOM}} + \theta_{\mathrm{LW}}\right) \cdot \frac{1.43\,\mathrm{g\,cm^{-3}}}{\rho_{\mathrm{soil}}} \tag{4.6}$$

The UTS is designed to describe the neutron intensity response caused by changes in total soil water content and absolute air humidity and therefore, the predicted neutron intensity represents the intensity corrected for variations in atmospheric pressure and incoming primary neutron flux N_{pi}. Soil moisture can be derived from the UTS using numerical inversion or a look-up table approach which is used in this study. Analogously to the standard transfer function, the UTS needs to be calibrated locally. The calibration parameter N_D may be interpreted as the average neutron intensity of the local neutron detector under the boundary conditions defined in the neutron transport simulations which where used to subsequently derive

the UTS. θ_{total} describes the total water content comprising the sum of all below-ground hydrogen pools, namely the soil moisture content θ_{UTS}, θ_{SM} and θ_{LW} which is then scaled by ratio of the soil bulk used in the neutron transport simulations to derive the UTS (1.43 g cm^{-3}) and the local soil bulk density at the study site ρ_{soil} [Köhli et al., 2021]. Different sets of shape-giving parameters $p_1 - p_{10}$ are available for the UTS in Köhli et al. [2021] and originate from the different neutron transport models used and whether a simple energy window threshold (thl) was used (parameter sets: URANOS thl, MCNP thl) to evaluate the neutron transport simulations or a more complex detector response function was applied (parameter sets: URANOS drf, MCNP drf). The latter mimics the response of a real neutron detector and is therefore expected to provide more accurate results. In the scope of this study, we investigate which of the two transfer functions and which parameter set of the UTS performs best in estimating surface soil moisture.

The CRNS footprint diameter as well as the integration depth decrease with i.e. increasing soil water content. The radius ranges between 130 and 240 m and the integration depth ranges between 15 and 83 cm during wet and dry conditions, respectively [Köhli et al., 2015]. In addition, further factors may influence the footprint dimensions such as open water or topography [e.g. Köhli et al., 2015; Schattan et al., 2019; Mares et al., 2020]. Consequently, reference measurements need to be depth-distance weighted according to the sensitivity of the CRNS instrument in order to match field observations of reference measurements when calibrating the two different transfer functions and derive soil moisture information from observed neutron intensities. In this study, we adapt the weighting procedure proposed by Schrön et al. [2017] which takes the total water content, average bulk density, absolute air humidity and vegetation height (set to 20 m) into account. Reference soil moisture information from the soil sampling campaign in February 2019 was weighted accordingly and used for calibrating both transfer functions. In a second step, the CRNS-derived soil moisture time series are compared to an analogously weighted average of all available in situ soil moisture sensors in 10, 20 and 30 cm depth. In order to assess the impact of weighting procedure, the calibration is repeated using the arithmetic soil moisture average from soil samples and comparing the CRNS-derived soil moisture time series to the arithmetic average soil moisture time series from in situ sensors.

4.3.3 Depth-extrapolation of surface soil moisture time series from CRNS

Modification of the SMAR model

To estimate depth-extrapolated soil moisture time series for a second, deeper soil layer from CRNS-derived surface soil moisture time series, the SMAR model is used. Introduced by Manfreda et al. [2014], it allows for the physically-based estimation of soil moisture in an adjacent second, lower soil layer from soil moisture information in a first, upper soil layer. SMAR is based on the relative saturation in the first and second layer s_1 (-) and s_2 (-), respectively, the relative saturation at field capacity sc_1 (-) and wilting point sw_2 (-). In order to transform values from $\text{cm}^3\,\text{cm}^{-3}$ to relative saturation, the respective variables are divided by the porosity of the individual layer n_1 ($\text{cm}^3\,\text{cm}^{-3}$) and n_2 ($\text{cm}^3\,\text{cm}^{-3}$). After applying the SMAR model, the resulting relative saturation time series of the second layer s_2 (-) is transformed back

to volumetric soil moisture in $\mathrm{cm}^3\,\mathrm{cm}^{-3}$ by multiplication with n_2 ($\mathrm{cm}^3\,\mathrm{cm}^{-3}$) and resulting in the depth-extrapolated soil moisture time series $\theta_{Layer\ 2}$. Soil moisture in layer 2 at time t is calculated with

$$s_2(t_i) = s_{\mathrm{w}2} + (s_2(t_{i-1}) - s_{\mathrm{w}2}) \cdot e^{-a\cdot(t_i - t_{i-1})} + (1 - s_{\mathrm{w}2}) \cdot b \cdot y(t_i) \cdot (t_i - t_{i-1}) \quad (4.7)$$

where a and b depend on the vertical extent of the first layer (Zr_1 in mm) which begins at the soil surface, and the vertical extent of the second layer (Zr_2 in mm). Zr_2 is the difference between the maximum depth of the second soil layer and Zr_1. The water loss term V_2 (mm t^{-1}) comprises the bulk water losses from the second layer due to percolation and evapotranspiration per unit time:

$$a = \frac{V_2}{(1 - s_{\mathrm{w}2}) \cdot n_2 \cdot Zr_2}, \quad (4.8)$$

$$b = \frac{n_1 \cdot Zr_1}{(1 - s_{\mathrm{w}2}) \cdot n_2 \cdot Zr_2}. \quad (4.9)$$

The fraction of saturation of the first layer that instantaneously infiltrates into the second layer $y(t_i)$ (-) is described as [e.g. Manfreda et al., 2014; Patil and Ramsankaran, 2018]:

$$y(t_i) = \begin{cases} (s_1(t_i) - s_{\mathrm{c}1}), & s_1(t_i) \geq s_{\mathrm{c}1} \\ 0, & s_1(t_i) < s_{\mathrm{c}1} \end{cases} \quad (4.10)$$

The SMAR model can be applied using known soil physical and environmental variables. However, although the soil physical parameters may be estimated through pedotransferfunctions, using tabulated values or global soil databases (e.g. SoilGrids 2.0 [Poggio et al., 2021]), the bulk water loss from the second layer V_2 is more difficult to estimate. This hampers the use of SMAR without calibration against reference soil moisture information in the depth of interest, i.e., in the deeper soil layer. To overcome this issue we modified and extended the SMAR model in order to estimate the V_2 based on simple soil physical, environmental variables and the surface soil moisture time series. A modification of the SMAR model with an extended definition of the water loss term V_2 has been suggested by Faridani et al. [2017] leading to an improved performance compared to the original SMAR model. As any modification makes the SMAR model more complex and potentially less easy to apply, our aim was to keep the added complexity to the model low by only including 3 additional parameters. These are the relative saturation at field capacity in the second layer sc_2 (-) and the cumulative root fraction to the maximum depth of the first and second layer R_1 (-) and R_2 (-), respectively. The water loss term is then defined as the sum of evapotranspiration ET_2 (mm t^{-1}) and percolation P_2

(mm t^{-1}) from the second layer.

$$V_2 = ET_2 + P_2 \tag{4.11}$$

We adapt the suggestion of Manfreda et al. [2014] to make use of existing (surface) soil moisture time series to gain information about water loss from the soil by evapotranspiration at a study site. Here, we estimate the amount of evapotranspiration from the deeper layer ET_2 based on the difference between the current and past value of relative saturation of the first layer, by scaling the value to the dimension (i.e. extent) of second layer and by considering the difference in cumulative root fraction between both layers, assuming that root water uptake for ET is larger in the layer with more roots eq. (4.13). The required root fraction R (-) for maximum depth d (cm) of the first and second layer are derived from the empirical equation (eq. 4.12) for forest biomes presented in Jackson et al. [1996]:

$$R = 1 - 0.970^d \tag{4.12}$$

Using eq. 4.13, ET_2 can only be estimated from the change in relative saturation in the first layer when 1) the relative saturation of the first layer s_1 decreases, 2) no infiltration into the second layer occurs and 3) the relative saturation of the second layer exceeds the relative saturation at wilting point. This means that both, surface evaporation and transpiration losses are scaled from the first layer to the second layer. Although surface evaporation is hardly relevant for the second layer due to its missing connection with the surface, this is a reasonable yet simplified approach because surface evaporation is a comparatively small component of total evapotranspiration in forests, with transpiration dominating evapotranspiration [e.g. Li et al., 2019b; Paul-Limoges et al., 2020].

$$ET_2\left(t_i\right) = \begin{cases} \left(s_1\left(t_i-1\right) - s_1\left(t_i\right)\right) \cdot n_1 \cdot Zr_1 \cdot \frac{Zr_2}{Zr_1} \cdot \frac{\left(R_2 - R_1\right)}{R_1}, & s_1\left(t_i-1\right) \geq s_1\left(t_i\right);\ y\left(t_i\right) > 0;\ s_2\left(t_i-1\right) \leq s_{\mathrm{w}2} \\ 0, & otherwise. \end{cases} \tag{4.13}$$

The amount of percolation P_2 from the second layer is estimated in analogy to the infiltration into this layer as an instantaneous water loss when the relative saturation exceeds field capacity sc_2 (eq. 4.14).

$$P_2\left(t_i\right) = \begin{cases} \left(s_2\left(t_i-1\right) - s_{\mathrm{c}2}\right), & s_2\left(t_i-1\right) \geq s_{\mathrm{c}2} \\ 0, & s_2\left(t_i-1\right) < s_{\mathrm{c}2} \end{cases} \tag{4.14}$$

Application of the SMAR model

We applied the SMAR model in its original form by calibrating the V_2 water loss term as a constant value. The calibration and evaluation was performed against

an average soil moisture time series in the deeper layer derived from in situ soil moisture sensors. All available in situ sensor soil moisture time series per depth were averaged to derive average soil moisture time series per sensor depth. Subsequently, we calculated an average soil moisture time series for the second, deeper soil layer by weighting the averages per depth according to their representative layer extent (called reference time series in the following). For example, having soil moisture sensors installed in 30, 50 and 70 cm depth, the average soil moisture content per time step of all sensors installed in 50 cm is representative for the layer between 40 and 60 cm. The soil physical parameters assigned to the individual layers can be found in Tab, 4.1. The calibration is performed by minimising the root-mean square error (RMSE) between the depth-extrapolated soil moisture time series and the entire reference soil moisture time series in the second soil layer.

The original SMAR with calibrated V_2 and the modified SMAR model with estimated V_2 are applied to estimate a soil moisture time series in a second soil layer with a maximum depth below terrain surface of 70, 130, 200, 300 and 450 cm. In contrast, the modified SMAR model based on eq. 4.11–4.14 is applied using the same soil physical parameters but it does not require calibration of the V_2 water loss term.

In order to test if a better surface soil moisture time series translates to better extrapolated soil moisture values in the second layer, we apply the SMAR model using the CRNS-derived surface soil moisture estimated from the standard transfer function (eq. (4.1)) as well as using the UTS (eq. (4.5) – (4.6)) with the parameter set resulting in the highest goodness of fit expressed by the lowest RMSE.

The vertical extent of the first soil layer is defined according to the representative measurement depth of the CRNS-derived soil moisture time series. In first step, the model is tested using a depth of the first layer of 35 cm as the sensitive measurement depth of CRNS is often estimated to range between 30 and 40 cm. However, more accurate approaches exist to determine the sensitive measurement depth. In this study, we also calculate median CRNS measurement depth of the entire CRNS-soil moisture time series based on Schrön et al. [2017] and use it as the depth of the first soil layer in the SMAR model. According to Schrön et al. [2017], the sensitive measurement depth D_{86} is estimated using the calibrated CRNS-derived soil moisture time series for distances from 1 to 300 m around the instrument. Subsequent averaging allows for estimating the average measurement depth in the CRNS footprint for each time step of the time series. The time series median measurement depth D_{86} is then calculated for the soil moisture time series derived with the standard transfer function and the UTS. For both CRNS-derived soil moisture time series, the estimated median sensitive measurement depth is 20 cm and much smaller than the rough initial estimate of 35 cm. As a consequence, we decided to apply the original and modified SMAR model with a first layer depth of both 20 cm and 35 cm to investigate the effect on the resulting depth-extrapolated soil moisture time series.

In summary, for each maximum depth of the second soil layer, the SMAR model is applied in its original form based on calibration and in the modified version presented in this study which does not require calibration. This is done using the CRNS surface soil moisture time series based on the standard transfer function as well as on the UTS. Lastly, we test whether the estimation of the representative measurement depth of CRNS and thus, the depth of the first soil layer, has an influence on the resulting modelled soil moisture time series in the second layer. An

overview of the different applications of the SMAR model performed in this study is given in Fig. 4.2.

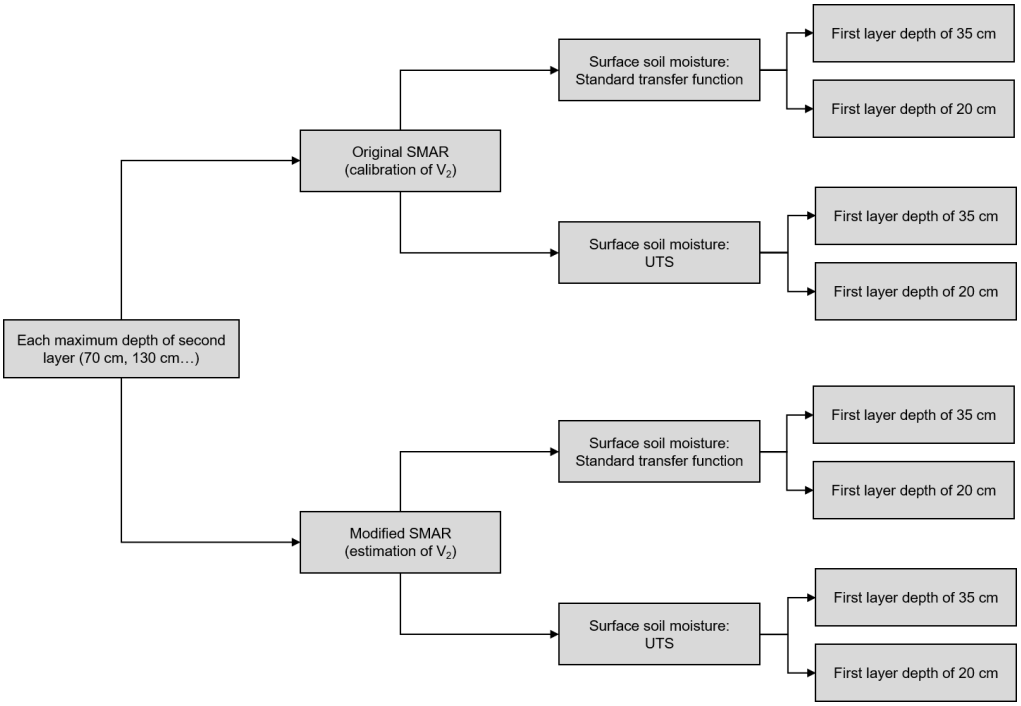

Figure 4.2: Overview of SMAR models set up in the scope of this study to compare the original SMAR based on the calibration of the water loss V_2 and the modified SMAR which does not require calibration.

To assess the robustness of the modified and uncalibrated SMAR model, we made a simple assessment of parameter uncertainty and its effect on the model results. We set up an ensemble of 50 realisations of the modified SMAR by randomly varying the values for n_1, n_2, sc_1, sc_2, sw_2 and R_1 in a range of ± 10 %. These sensitivity runs of the modified, uncalibrated SMAR are then assessed using the minimum to maximum range of calculated root mean square error (RMSE) between the simulated soil moisture time series in the second soil layer and the reference from in situ sensors. In satellite soil moisture estimations, a threshold of 0.06 $cm^3\,cm^{-3}$ has been used [Jackson et al., 2010] to evaluate the original SMAR performance for root-zone soil moisture estimates based on satellite-derived surface soil moisture information [Baldwin et al., 2019]. We adopt this benchmark for evaluating the performance of the uncalibrated, modified SMAR in this study.

Lastly, we performed a full calibration of the original and modified SMAR models in order to estimate the best possible simulation results within a physically acceptable range of the model parameters. This was done by randomly varying the values for n_1, n_2, sc_1, sc_2, sw_2 and R_1 in a range of ± 20 %. For the original SMAR model, the water loss term V_2 was calibrated instead of the R_1 with values in the range between 1 and a maximum of 500 mm. The calibration was performed by selecting the parameter combination that resulted in the lowest RMSE among a total of 10,000 random parameter sets. For the full calibration scenarios, we defined the year 2017 as the calibration period, while the entire study period (2016-2022) is used to evaluate the depth-extrapolated soil moisture time series. Except for the fact that several parameters were calibrated, the different scenarios are identical to

those where just the V_2 parameter was calibrated (see Fig. 4.2). In all SMAR applications in this study, the initial soil moisture content of the second layer was set to the first CRNS-derived soil moisture record of the first layer. The SMAR model with physically reasonable environmental value ranges showed generally low performance as described in the results section and led to some additional calibration tests of the model. Experimental calibration runs indicated that calibration parameters in a non-physical value range could produce better model results. Therefore, a second full calibration was performed where the values of the parameters sc_1, sc_2 and sw_2 where allowed to range from -1 to their initial, literature-based value while the range for other model parameters remained unchanged.

The SMAR model was originally designed to depth-extrapolate surface soil moisture time series on a daily resolution, as it assumes that all water above field capacity sc_1 infiltrates into the second layer within one day [Manfreda et al., 2014]. Consequently, the SMAR model has been applied on a daily resolution in previous studies [e.g. Baldwin et al., 2017, 2019]. In CRNS research, an hourly temporal resolution is the community standard and therefore, we test whether the SMAR models in their original and modified forms can also be applied at hourly resolution with a reasonable goodness of fit. All analyses described in this chapter are therefore carried out on both a daily and hourly basis.

All calculations were performed in R statistical software [R Core Team, 2018, 2023] using the hydroGOF package [Zambrano-Bigiarini, 2017, 2020] for calculating goodness-of-fit measures which evaluate absolute values and time series dynamics, namely the RMSE, the Kling-Gupta Efficiency (KGE) [Gupta et al., 2009] as well as the Pearson correlation coefficient.

4.4 Results and discussion

4.4.1 CRNS-derived surface soil moisture time series

The goodness of fit of the calibrated CRNS-based soil moisture time series to the time series derived from in situ point observations is shown for the two transfer functions Tab. 4.2. When the different transfer functions are calibrated against an arithmetic average soil moisture from soil samples and compared to an arithmetic average of soil moisture time series in 10-30 cm depth, the Pearson correlation coefficient and the KGE are lower than when using a weighted average of soil moisture observations for calibration as proposed by Köhli et al. [2015] and Schrön et al. [2017]. However, the RMSE is slightly higher for the calibration against the weighted observations. This might be linked to differences between the laboratory measurements of soil moisture in the soil samples (which were used for calibration) and the continuous soil moisture data obtained from the in situ sensors. Overall, however, in view of the much better KGE and correlation values, the results underline the importance of the weighting procedures when calibrating the CRNS observations to derive soil moisture estimates or comparing them to observations from in situ soil moisture sensors.

The goodness of fit of the CRNS-derived soil moisture time series that are based on the revised standard transfer function is always lower than for those that are derived with the UTS all parameters sets, especially when the KGE is considered, showing the improved soil moisture estimation with the UTS. However, the param-

Table 4.2: goodness of fit between the CRNS-derived soil moisture time series and the arithmetic and weighted average soil moisture time series from the local in situ point-sale soil moisture sensors in 10-30 cm depth. The different neutron to soil moisture transfer functions are independently calibrated against soil moisture from soil samples taken in February 2019. The UTS transfer function can be used with different parameter sets originating from different neutron transport models which are either based on an energy level threshold (thl) or a more realistic detector response functions (drf).

Transfer function	in situ soil moisture	Calibration parameter (cph)	KGE (-)	RMSE ($cm^3\,cm^{-3}$)	Pearson correlation (-)
Revised standard		777	0.08	0.030	0.88
UTS URANOS drf		1245	0.14	0.029	0.86
UTS URANOS thl	Arithmetic average	1596	0.59	0.020	0.87
UTS MCNP drf		1294	0.33	0.025	0.87
UTS MCNP thl		1645	0.59	0.021	0.87
Revised standard		809	0.46	0.030	0.91
UTS URANOS drf		1302	0.49	0.029	0.89
UTS URANOS thl	Weighted average	1693	0.81	0.022	0.90
UTS MCNP drf		1357	0.60	0.027	0.90
UTS MCNP thl		1741	0.77	0.023	0.90

eters sets of the UTS mimicking the varying sensitivity of a real neutron detector to neutrons of different energies (URANOS drf, MCNP drf) perform worse than those which rely on a simple energy range threshold (URANOS thl, MCNP thl). This counter-intuitive result has been previously described by Köhli et al. [2021] and could be related to the high sensitivity of the CRNS method to the soil moisture dynamics in the first few centimetres of the soil where unfortunately no in situ sensors are installed (the uppermost sensors are installed in 10 cm depth). Therefore, the better performance of the energy threshold parameters sets of the UTS can be related to insufficient reference soil moisture information from the in situ sensor network. Generally, the UTS with the parameter sets representing the response of a real neutron detector can be expected to be provide more accurate results. Here, the UTS with parameter set MNCP drf reveals a higher statistical goodness of fit compared to the URANOS drf parameter set which is in line with the findings presented in Köhli et al. [2021]. The improved performance of the UTS with the parameter set MNCP drf compared to the standard transfer function is shown in Fig. 4.3, revealing that the latter tends to overestimate soil moisture under the wet winter conditions and underestimate soil moisture under dry summer conditions.

Different from the study of Köhli et al. [2021] which introduced the UTS, we apply UTS to derive soil moisture from neutron observations at a forest site. The UTS calibration parameter N_D represents the average count rate under boundary conditions of the neutron transport simulations conducted to the derive the UTS. Therefore, N_D can be expected to be close to the average corrected neutron intensity observed at a study site with little or without vegetation or other above-ground hydrogen pools influencing the observed neutron intensity. At our study site, the calibrated N_D is much higher than the observed average corrected neutron intensity N_{pi} (557 cph). This is probably caused by the influence of the forest vegetation on observed neutron intensities and the calibration parameter of the transfer function and has been similarly described for the standard transfer function by Baatz et al. [2015]. As hydrogen stored in air humidity influences the functional relationship between neutron intensities and soil moisture, hydrogen stored in vegetation might

have a similar effect. Therefore, a correction or inclusion approach for other aboveground hydrogen pools such as vegetation may yield an even better performance of the UTS and may be investigated in future studies.

Our analyses confirm the improved performance of the UTS compared to the standard transfer function. In order to test whether the improved performance in deriving surface soil moisture translates into a better estimation of soil moisture in deeper layers, we apply the SMAR model using the surface soil moisture time series based on both the revised standard transfer function and the UTS with the MCNP drf parameter set (Fig. 4.3).

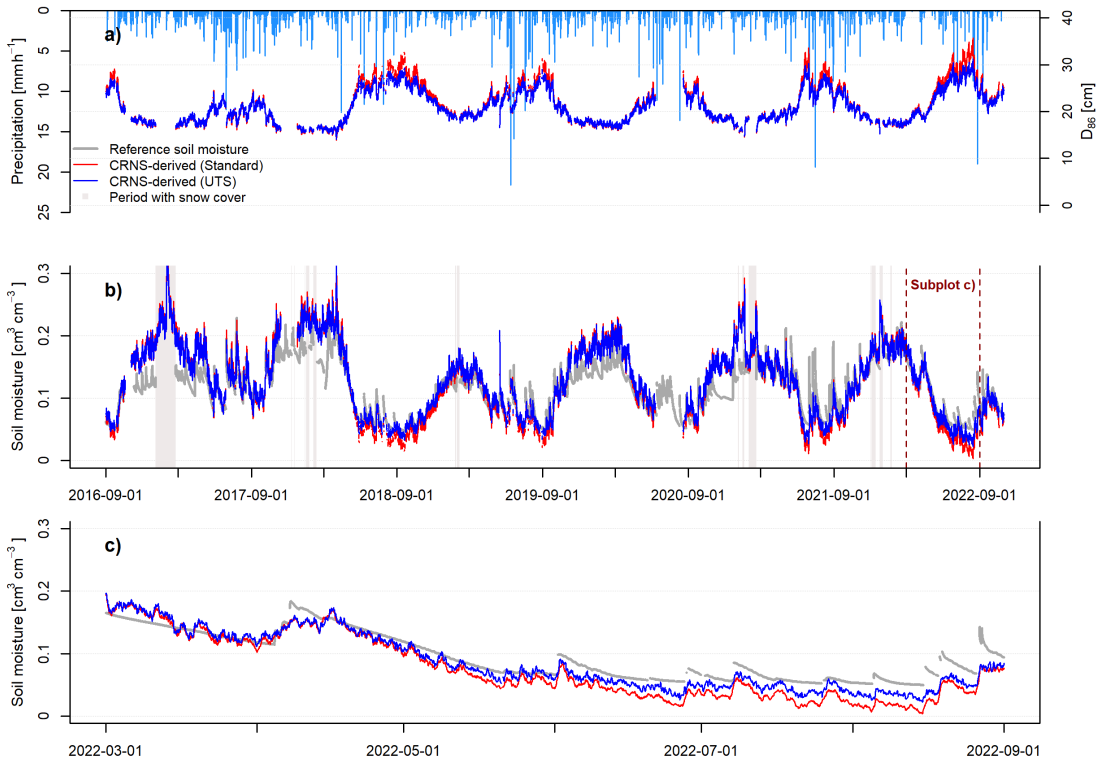

Figure 4.3: Soil moisture estimates with CRNS. (a) estimated time-variable sensitive measurement depth D_{86} of the CRNS-approach and precipitation time series (light blue bars); (b) soil moisture time series derived with the revised standard transfer function and the UTS with parameter set MCNP drf and (c) a period in 2022 illustrating the differences between the two CRNS-derived soil moisture time series.

4.4.2 Depth-extrapolation of CRNS-derived soil moisture time series

Original SMAR with calibrated water loss and uncalibrated, modified SMAR

The performance measures and the corresponding values for the depth-extrapolated soil moisture time series based on the calibrated original SMAR (calibrated water loss only) and the uncalibrated modified SMAR (estimated water loss based on eq. (4.11-4.14)) are listed in Tab. 4.3 as well as Tab. 4.4 and exemplary time series for a second layer depth of 130 cm are shown in Fig. 4.4 and Fig. 4.5 for a hourly and daily resolution, respectively. The standard transfer function and the UTS produce similar results with RMSE values ranging between 0.055 and and 0.015 $cm^3\,cm^{-3}$ for hourly values and between 0.054 and and 0.014 $cm^3\,cm^{-3}$ for daily values over all simulated scenarios. The SMAR model with daily resolution generally results in a higher goodness of fit. The correlation coefficients tend to be lower for the scenarios using the uncalibrated, modified SMAR and higher for the original SMAR with calibrated water loss. For KGE, the results are the opposite.

The better performance at a daily time step (irrespective of the depth-extrapolation method) can be attributed to the fact that it is generally assumed that all water above field capacity infiltrates from the first into the second layer within one time step. While this may be a reasonable assumption on a daily time step for which the SMAR model was designed for [Manfreda et al., 2014], this perquisite is likely to be violated at the hourly time step. Nevertheless, for our study site, the differences in terms of the RMSE are rather small, indicating that the SMAR model may also be used with an hourly resolution.

Following the RMSE threshold of $\leq 0.06\ cm^3\,cm^{-3}$ which has been used to evaluate the original SMAR performance [Baldwin et al., 2019; Guo et al., 2023], all simulations with the original and with the modified SMAR and both with an hourly and daily resolution lie below this threshold. This indicates that all SMAR models result in acceptable soil moisture time series for the second soil layer down to 450 cm depth according to RMSE performance. However, taking the dynamic goodness-of-fit parameters KGE and correlation coefficient into account, the performance with regard to the temporal dynamics is not satisfactory. This can also be visually identified from Fig. 4.4 and Fig. 4.5 for a second layer depth of 130 cm. The original SMAR with calibrated constant water loss reaches the wilting point of the second soil layer over large parts of the study period, indicating that the water loss calibrated by minimising RMSE, results in a high constant water loss to match the reference average water content of the second layer but thereby causing too strong and rapid decreases of soil moisture in dry summer periods. Here, the uncalibrated, modified SMAR model provides more realistic gradual decreases of soil moisture, leading to a better performance when visually assessing the time series. This is also true for the maximum second layer depth of 450 cm investigated in this study (Fig. 4.8 and Fig. 4.9) and illustrates that care should be taken when relying on statistical goodness-of-fit measures and that a visual assessment and interpretation of the simulation results should be undertaken. Nevertheless, it should be noted that the simulated soil moisture time series both for the original and for the modified SMAR do not represent intermediate pulses of increased soil moisture seen in the reference data even during the drier summer period.

For large maximum depths of the second layer such as 450 cm, the original SMAR with calibrated water loss better simulates the amplitudes of soil moisture in the second layer for a temporal resolution of both hours and days. This indicates that the water loss estimated with the modified SMAR is too low for large depths. The condition of eq. (4.13), imposing that no evapotranspiration losses occur when water percolates from the first to the second layer, could be one reason. Another reason could be uncertainties of the relative root fraction that is required to scale the water losses from the the first to the second layer. The use of an exponential model to describe the cumulative root distribution, as done in this study, is highly simplistic and such models generally remain under debate [e.g. Pierret et al., 2016]. Furthermore, too much water percolating from the first into the second soil layer may be compensated through the calibration of the water loss parameter in the original SMAR model, but this cannot be done when the uncalibrated, modified SMAR is applied.

Another major reason for the generally poor performance of both the original and the modified SMAR can be the literature-based soil physical parameters used here in order to apply the SMAR model without calibration against in situ reference measurements. In ensemble simulations with the modified SMAR, the soil physical parameters were varied in a range of $\pm$ 10 %. The minimum and maximum RMSE values derived from the 50 hourly and daily ensemble runs are shown in Tab. 4.7. It can be seen that smaller RMSE values can be achieved with parameter values that are different from the initial ones (Tab. 4.3). The maximum RMSE for all depths except for 70 cm still meet the RMSE benchmark criterion, indicating a certain robustness of the uncalibrated, modified SMAR model presented in this study if the soil physical parameters can be reasonable well estimated.

We also tested the impact of the input surface soil moisture time series to both the original SMAR with calibrated water loss and the uncalibrated, modified SMAR. Using either the CRNS-derived soil moisture time series based on the UTS equation or the revised standard equation for the first layer results in visually similar results with similar RMSE values, slightly higher correlation coefficients for the second case, and slightly better KGE values for the first case (Tab. 4.3, Tab. 4.4). Overall, in this study, a better estimated surface soil moisture time series from CRNS does not necessarily translate into a distinct improvement of the depth-extrapolated time series. This may be explained by the considerable overall deficiencies of the SMAR models to represent the soil moisture dynamics at our study site which are larger than the differences between the surface soil moisture time series derived with the different neutron-to-soil moisture transfer functions.

In contrast, improvements of the depth-extrapolated soil moisture times series in the second layer can be seen when the depth of the top soil layer in the SMAR model is taken to be the median calculated sensitive measurement depth (D_{86}, Schrön et al. [2017]) of the CRNS technique. Here, the statistical goodness of fit is generally higher compared to using an assumed sensitive depth of 35 cm for the top soil layer. This is the case for both the standard and the modified SMAR model and independent of the transfer function used for the CRNS soil moisture in the top layer (standard or UTS) with hourly and daily resolution. The better matching time series compared to the reference time series is also visible in Fig. 4.4 and Fig. 4.5 and is expressed through the RMSE values in Tab. 4.3 and Tab. 4.4. The nature of the SMAR model as a water balance approach implies that the correct estimation of the

volume of the upper soil layer and its storage is directly related to the accuracy of the depth-extrapolated time series of the second soil layer. Consequently, an accurate assessment of the sensitive measurement depth of CRNS is also highly important when using CRNS-derived soil moisture time series in e.g. (soil) hydrological model applications.

Table 4.3: Statistical goodness of fit between the depth-extrapolated *hourly* soil moisture time series from CRNS surface observations and the average soil moisture time series in the second layer calculated from the available in situ point-scale soil moisture sensors. The water loss parameter is either a calibrated static value (original SMAR model) or estimated based on the procedure described for the modified SMAR model, see chapter 2.

Layer 2 depth (cm)	Layer 1 depth (cm)	Transfer function	SMAR	Water loss	V_2 ($mm\,h^{-1}$)	RMSE ($cm^3\,cm^{-3}$)	Pearson correlation	KGE (-)
70	35	Revised standard	Modified	Estimated	-	0.055	0.735	-1.74
			Original	Calibrated	156	0.040	0.589	0.13
		UTS MCNP drf	Modified	Estimated	-	0.053	0.733	-1.64
			Original	Calibrated	132	0.041	0.577	0.14
	20	Revised standard	Modified	Estimated	-	0.041	0.803	-1.54
			Original	Calibrated	64	0.035	0.661	0.24
		UTS MCNP drf	Modified	Estimated	-	0.040	0.795	-1.44
			Original	Calibrated	58	0.035	0.654	-0.24
130	35	Revised standard	Modified	Estimated	-	0.036	0.711	-0.85
			Original	Calibrated	104	0.041	0.537	0.12
		UTS MCNP drf	Modified	Estimated	-	0.035	0.714	-0.83
			Original	Calibrated	94	0.041	0.529	0.13
	20	Revised standard	Modified	Estimated	-	0.033	0.773	-0.81
			Original	Calibrated	58	0.038	0.608	0.16
		UTS MCNP drf	Modified	Estimated	-	0.033	0.768	-0.79
			Original	Calibrated	52	0.038	0.604	0.17
200	35	Revised standard	Modified	Estimated	-	0.033	0.698	-0.82
			Original	Calibrated	113	0.036	0.492	0.15
		UTS MCNP drf	Modified	Estimated	-	0.032	0.704	-0.81
			Original	Calibrated	102	0.036	0.489	0.15
	20	Revised standard	Modified	Estimated	-	0.032	0.743	-0.78
			Original	Calibrated	63	0.034	0.557	0.18
		UTS MCNP drf	Modified	Estimated	-	0.031	0.741	-0.77
			Original	Calibrated	57	0.034	0.556	0.19
300	35	Revised standard	Modified	Estimated	-	0.036	0.676	-1.36
			Original	Calibrated	157	0.026	0.450	0.25
		UTS MCNP drf	Modified	Estimated	-	0.035	0.681	-1.33
			Original	Calibrated	142	0.026	0.449	0.25
	20	Revised standard	Modified	Estimated	-	0.034	0698	-1.27
			Original	Calibrated	87	0.025	0.511	0.29
		UTS MCNP drf	Modified	Estimated	-	0.033	0.694	-1.24
			Original	Calibrated	79	0.025	0.512	0.29
450	35	Revised standard	Modified	Estimated	-	0.044	0.545	-2.02
			Original	Calibrated	300	0.015	0.333	0.30
		UTS MCNP drf	Modified	Estimated	-	0.043	0.556	-1.98
			Original	Calibrated	269	0.015	0.336	0.31
	20	Revised standard	Modified	Estimated	-	0.040	0.558	-1.91
			Original	Calibrated	158	0.015	0.392	0.33
		UTS MCNP drf	Modified	Estimated	-	0.039	0.566	-1.88
			Original	Calibrated	143	0.015	0.396	0.33

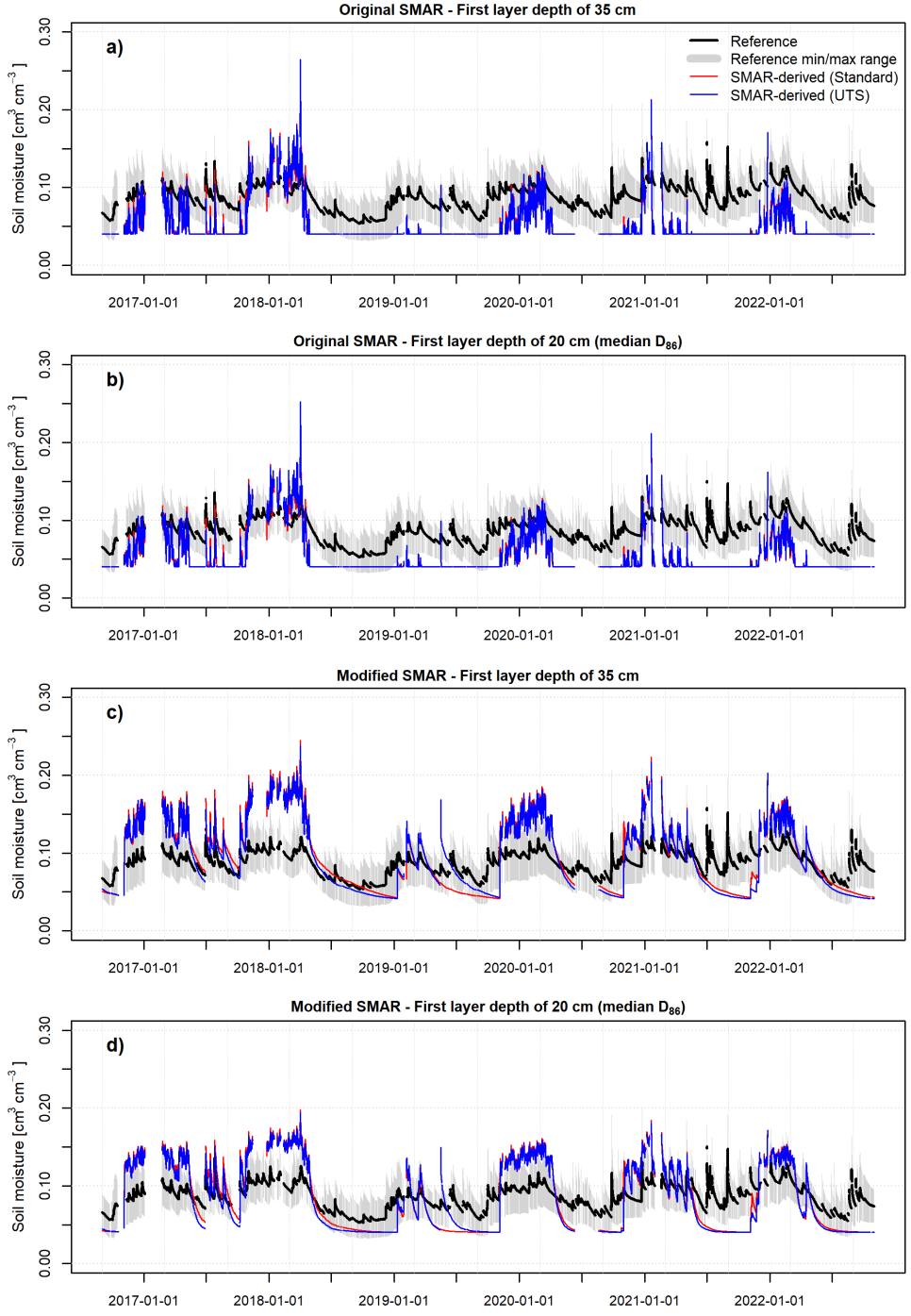

Figure 4.4: *Hourly* depth-extrapolated soil moisture time series for a depth of 130 cm using the calibrated standard SMAR model (calibrated water loss V_2) with a top layer depth of 35 cm (a), and 20 cm (b) as well as the depth-extrapolated soil moisture time series based on the uncalibrated modified SMAR (estimated water loss) model presented in this study (top layer depth of 35 cm (c) and 20 cm (d)) based on the CRNS-derived surface soil moisture time series from the standard transfer function and the UTS.

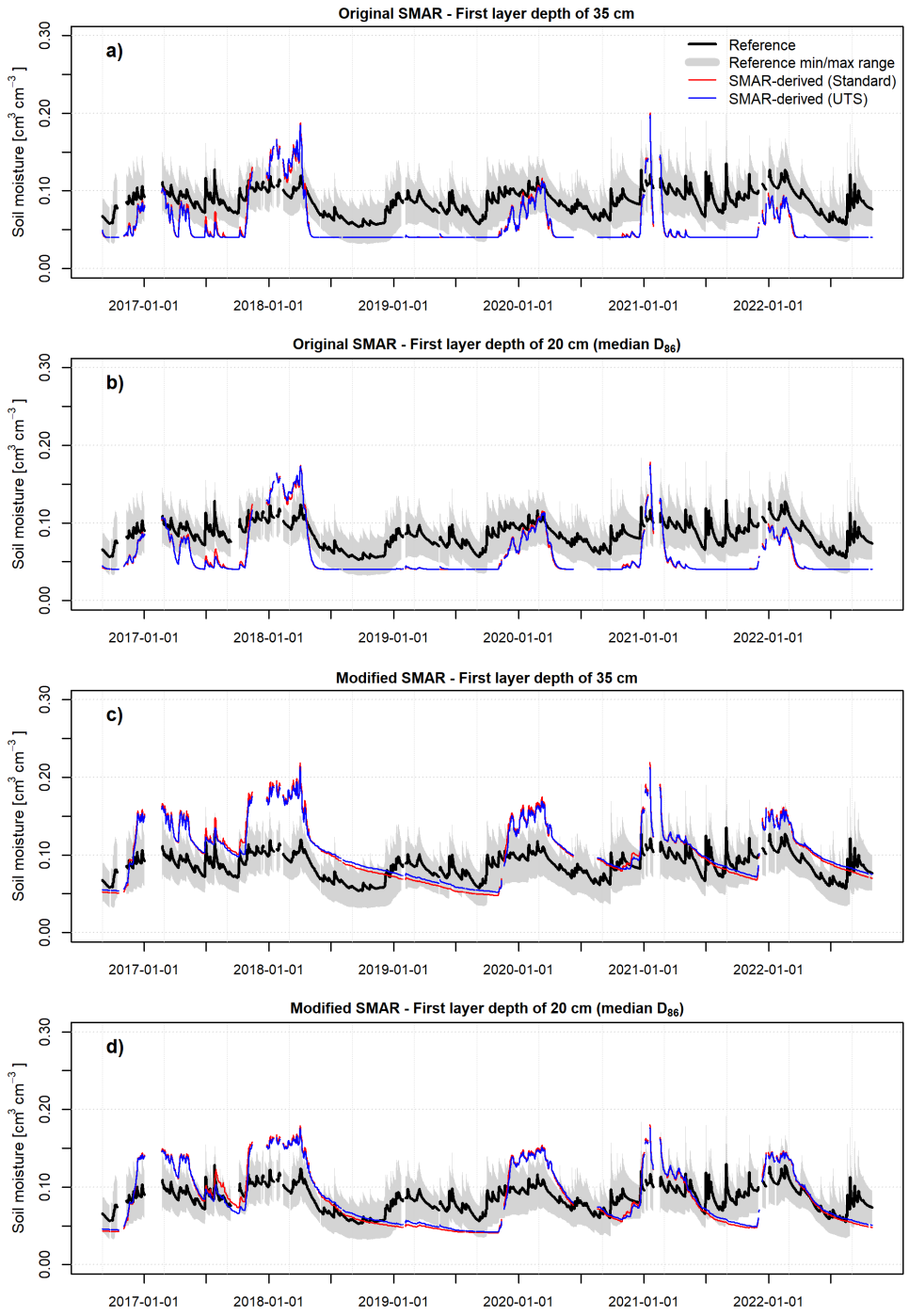

Figure 4.5: *Daily* depth-extrapolated soil moisture time series for a depth of 130 cm using the calibrated standard SMAR model (calibrated water loss V_2) with a top layer depth of 35 cm (a), and 20 cm (b) as well as the depth-extrapolated soil moisture time series based on the uncalibrated modified SMAR (estimated water loss) model presented in this study (top layer depth of 35 cm (c) and 20 cm (d)) based on the CRNS-derived surface soil moisture time series from the standard transfer function and the UTS.

Table 4.4: Statistical goodness of fit between the depth-extrapolated *daily* surface soil moisture time from CRNS and the average soil moisture time series in the second layer calculated from the available in situ point-scale soil moisture sensors. The water loss parameter is either as a calibrated static value (original SMAR model) or estimated based on the procedure described in the methods section (modified SMAR model, see chapter 2).

Layer 2 depth (cm)	Layer 1 depth (cm)	Transfer function	SMAR	Water loss	V_2 (mm h^{-1})	RMSE (cm^3 cm^{-3})	Pearson correlation	KGE (-)
70	35	Revised standard	Modified	Estimated	-	0.054	0.685	-1.18
			Original	Calibrated	131	0.040	0.602	0.10
		UTS MCNP drf	Modified	Estimated	-	0.051	0.675	-0.92
			Original	Calibrated	113	0.040	0.59	0.11
	20	Revised standard	Modified	Estimated	-	0.037	0.760	-1.03
			Original	Calibrated	56	0.034	0.688	0.20
		UTS MCNP drf	Modified	Estimated	-	0.035	0.752	-0.78
			Original	Calibrated	51	0.034	0.678	0.22
130	35	Revised standard	Modified	Estimated	-	0.034	0.626	-0.38
			Original	Calibrated	87	0.039	0.575	0.08
		UTS MCNP drf	Modified	Estimated	-	0.032	0.614	-0.22
			Original	Calibrated	79	0.040	0.564	0.09
	20	Revised standard	Modified	Estimated	-	0.029	0.697	-0.35
			Original	Calibrated	48	0.036	0.644	0.12
		UTS MCNP drf	Modified	Estimated	-	0.028	0.680	-0.19
			Original	Calibrated	44	0.036	0.635	0.13
200	35	Revised standard	Modified	Estimated	-	0.031	0.619	-0.34
			Original	Calibrated	91	0.035	0.546	0.09
		UTS MCNP drf	Modified	Estimated	-	0.030	0.608	-0.19
			Original	Calibrated	83	0.035	0.538	0.10
	20	Revised standard	Modified	Estimated	-	0.027	0.685	-0.30
			Original	Calibrated	51	0.032	0.611	0.13
		UTS MCNP drf	Modified	Estimated	-	0.026	0.668	-0.16
			Original	Calibrated	47	0.032	0.605	0.13
300	35	Revised standard	Modified	Estimated	-	0.035	0.633	-0.72
			Original	Calibrated	124	0.024	0.515	0.20
		UTS MCNP drf	Modified	Estimated	-	0.034	0.625	-0.56
			Original	Calibrated	113	0.025	0.511	0.20
	20	Revised standard	Modified	Estimated	-	0.027	0.688	-0.64
			Original	Calibrated	67	0.023	0.587	0.25
		UTS MCNP drf	Modified	Estimated	-	0.027	0.673	-0.48
			Original	Calibrated	62	0.023	0.583	0.25
450	35	Revised standard	Modified	Estimated	-	0.043	0.551	-1.18
			Original	Calibrated	237	0.014	0.392	0.37
		UTS MCNP drf	Modified	Estimated	-	0.043	0.549	-1.03
			Original	Calibrated	215	0.014	0.392	0.37
	20	Revised standard	Modified	Estimated	-	0.032	0.594	-1.10
			Original	Calibrated	122	0.014	0.470	0.39
		UTS MCNP drf	Modified	Estimated	-	0.032	0.581	-0.95
			Original	Calibrated	112	0.014	0.470	0.39

Full calibration of the original and modified SMAR

To further assess the performance of the original and modified SMAR at the study site, we performed a full (all parameter) calibration of the two SMAR models with 10,000 random combinations of the soil physical parameters. The initially assigned soil physical parameters were altered in the range of ± 20 % to assign values in a physically acceptable range for the sandy soils at the study site. Additionally to the soil physical parameters, the bulk water loss V_2 in the original SMAR was calibrated with random values in the range from 1 to 500 mm. For the modified SMAR model, the relative root fraction in the first layer R_1 was varied in the range of ± 20 % instead.

The results of the full calibration can be found in Tab. 4.5 and Tab. 4.6 and exemplary time series for a second layer depth of 130 cm are shown in Fig. 4.6 and Fig. 4.7 for a hourly and daily resolution, respectively. The results for the maximum depth of 450 cm can be found in the appendix. As expected, minimizing the RMSE in the calibration period 2017 leads to a decrease of the RMSE for the entire study period compared to the uncalibrated modified SMAR or when calibrating the water loss term in the original SMAR only. This is the case for both the hourly and daily time step, with generally better performance for the latter in terms of RMSE and KGE. Using a first layer depth of 20 cm instead of 35 cm leads to better soil moisture dynamics in the deeper layers. This is in line with results presented in the previous chapters when comparing the uncalibrated, modified SMAR and the original SMAR with calibrated water loss.

Following the statistical goodness-of-fit parameters in Tab. 4.5 and Tab. 4.6, the modified SMAR performs worse than the calibrated original SMAR in different depths after all parameters have been calibrated. This may be attributed to using a single-objective optimisation for minimising the RMSE, only. Furthermore, in the original SMAR, the bulk water loss from the second layer was optimised while for the modified SMAR, only the cumulative root fraction in the first layer was adjusted. This leads to more restricted conditions for the modified SMAR model. For example, calibrating the estimated complete water loss in the latter eq. 4.11 based on a calibration factor could lead to improved the results of the fully calibrated, modified SMAR and more close to those derived for the fully calibrated original SMAR. Nevertheless, the generally higher process restrictions due to the defined estimation of ET_2 and P_2 in eq. 4.13–4.14 of the modified SMAR remain.

In summary, the full calibration of the original and modified SMAR model with soil model parameters in physically reasonable value range show similar characteristics to those scenarios described in the previous chapter where literature-based values where assigned for soil physical parameters and only the bulk water loss V_2 was calibrated. Although the overall visual performance improved and a higher statistical goodness of fit can be achieved when all environmental model parameters are calibrated, the original and modified SMAR model tested in this study do not show satisfying results with respect to the temporal dynamics of the soil moisture time series of the second layer. Many intermediate rainfall events are not captured and thus, the reference soil moisture time series show a more dynamic behaviour than those simulated by the original and modified SMAR.

Calibration experiments revealed that assigning values in a non-physical parameter range, e.g. negative values, for soil physical model parameters could lead to an improved performance of SMAR. When allowing a non-physical value range for the

model parameters sc_1, sc_2 and sw_2, the visual and statistical performance of both, the original and modified SMAR improve dramatically with the exception of the depth of 70 cm. Again exemplary shown for a maximum depth of 130 and 450c̆m depth and both temporal resolutions, Fig. 4.12 – 4.15 as well as Tab. 4.8 – 4.9 illustrate the improved performance of both SMAR models. The poor and even worse performance in the depth of 70 cm compared to the full calibration with physically reasonable values could be related to a non-sufficient value range for the calibrated parameters when values in a non-physically based value range are assigned. Even better results may also be derived for other depths with a different value range or by also calibrating the remaining parameters n_1, n_2, V_2 and R_1 in a non-physically reasonable value range. These results show that satisfactory results with the original and the modified SMAR can be obtained at our study site at the expense of physical realism of the model, and only if in situ soil moisture measurements in the depth of interest are available for calibration.

General discussion

The evaluation of the original SMAR model against in situ observations in previous studies showed a range of RMSE values and correlation coefficients [e.g. Manfreda et al., 2014; Faridani et al., 2017], indicating that the performance of the SMAR model varies between study sites.

The particular water flow dynamics at our study site located in a mixed forest with sandy soils may explain the overall unsatisfactory representation of soil moisture dynamics of the SMAR model when model parameters are assigned in a physically reasonable range. Preferential flow in macropores including bypass flow along roots [e.g. Nimmo, 2021] can result in highly conductive forest soils with infiltrating water being quickly transported from the surface to deeper layers. For example, Chandler et al. [2018] and Alaoui et al. [2011] found that forest soils can have higher saturated hydraulic conductivity compared to other land cover types and combined with differing preferential flow processes this may lead to increased infiltration and percolation into lower layers of forest soils [e.g. Alaoui et al., 2011]. Complex preferential flow and infiltration processes are unlikely to be properly captured by the SMAR as it allows water movement only for soil moisture conditions above field capacity. A more complex root distribution than the exponential one assumed in this study and related temporally varying transpiration water losses from different depths adds for complexity that is not captured by the SMAR model. Maysonnave et al. [2022], for instance, found that root water uptake in forests can vary with time and depth depending on the water availability in different layers. These features can neither be reproduced by the original nor modified SMAR and makes forest sites generally challenging, in particular for simplified models. However, this may be partly compensated for when model-specific effective parameters are used. In this case, calibration against in situ reference soil moisture information is required and the parameters lose their physical meaning and interpretability but may account for the particular soil hydraulic processes of the study site.

In addition to the simplicity of the model, the field-scale approach of this study adds further difficulties when evaluating the simulated soil moisture time series against point-scale soil moisture observations. The reason is their high spatio-temporal variability, especially in forests caused by e.g. heterogeneous evapotranspiration, interception, [e.g. Schume et al., 2003] and root distribution patterns [e.g.

Jost et al., 2012]. Even more, the decreasing number of reference in situ soil moisture sensors with increasing soil depth may lead to a lower representativeness of the reference soil moisture time series at larger depths, lowering comparability to the model results. Nevertheless, with point sensors down to 450 cm, this study allows for exploring the potential of SMAR for larger depths than usually feasible. Even when depths down to 450 cm are considered, the original and modified SMAR meet the benchmark RMSE of ≤ 0.06 $cm^3\,cm^{-3}$ in scenarios with literature-based and with calibrated model parameters. This underlines the usefulness of SMAR to derive a first estimate of soil moisture in a second, deeper soil layer.

The largest limitation of the present study for evaluating the standard and the introduced modified SMAR models is its application to a single observation site. A comparison with other simple depth-extrapolation approaches including the soil water index [e.g. Wagner et al., 1999; Albergel et al., 2008], empirical approaches such as regression models [e.g. Zhang et al., 2017] and cumulative distribution function matching [e.g. Gao et al., 2018] as well as other versions of the SMAR model [e.g. Faridani et al., 2017] would allow for an improved evaluation of the presented modification of the SMAR model and should be assessed in future studies at sites with a broader range of climatic conditions, vegetation covers and soils.

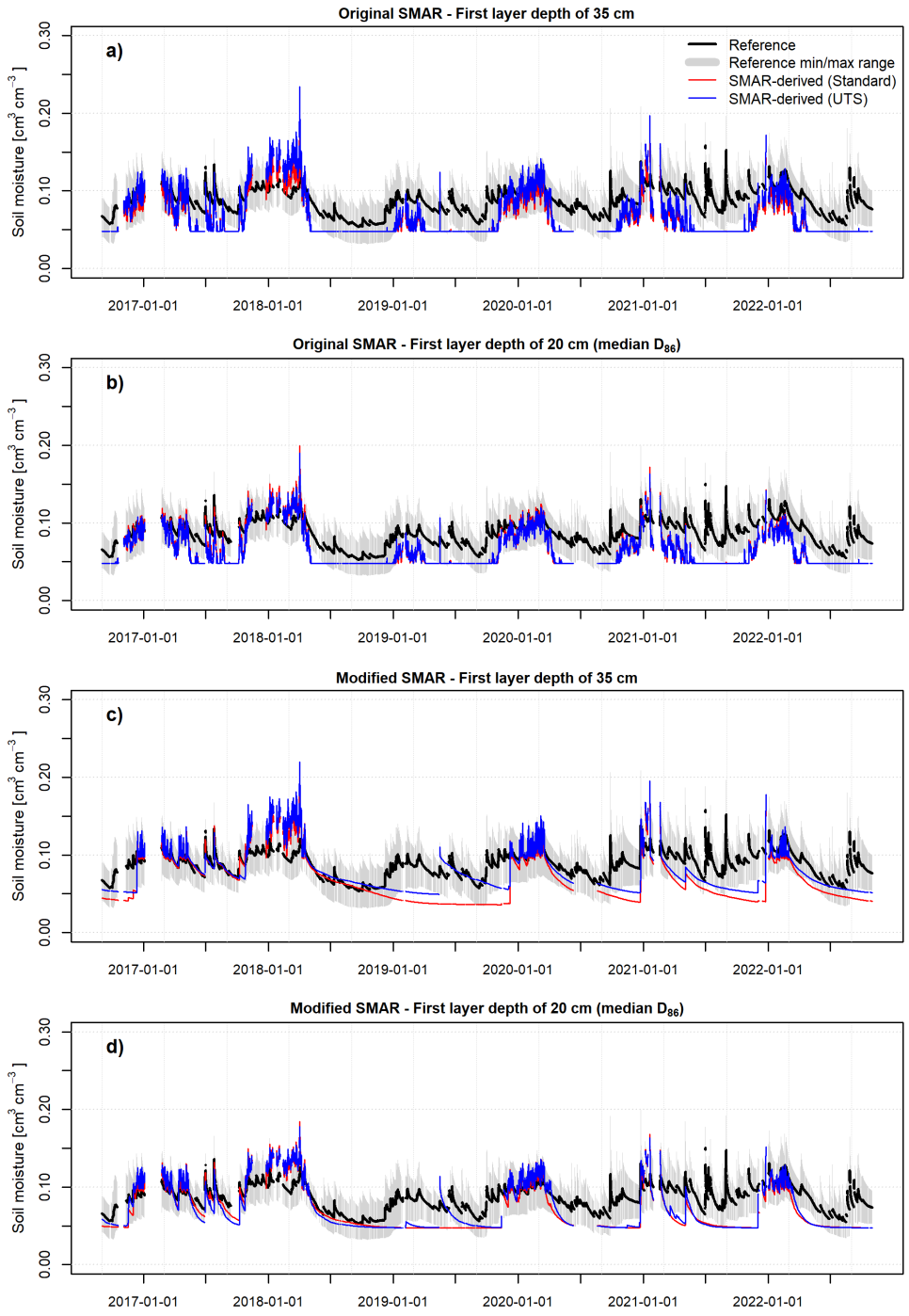

Figure 4.6: *Hourly* depth-extrapolated soil moisture time series for a depth of 130 cm using the standard SMAR model with a top layer depth of 35 cm (a), and 20 cm (b) as well as the depth-extrapolated soil moisture time series based on the modified SMAR model presented in this study (top layer depth of 35 cm (c) and 20 cm (d)) based on the CRNS-derived surface soil moisture time series from the standard transfer function and the UTS. The soil physical parameters n_1, n_2, sc_1, sc_2, sw_2 and R_1 were optimised by reducing the RMSE against reference soil moisture values in the year 2017. For the original SMAR model, the water loss term V_2 was calibrated instead of R_1.

Table 4.5: Statistical goodness of fit between the depth-extrapolated *hourly* surface soil moisture time series from CRNS and the average soil moisture time series in the second layer calculated from the available in situ point-scale soil moisture sensors with the fully calibrated SMAR in a physically acceptable parameter range. The calibrated model parameters and goodness-of-fit indicators for the original and modified SMAR model are shown.

Layer 2 depth (cm)	Layer 1 depth (cm)	Transfer function	SMAR	n_1 (-)	n_2 (-)	sc_1 ($cm^3\,cm^{-3}$)	sc_2 ($cm^3\,cm^{-3}$)	sw_2 ($cm^3\,cm^{-3}$)	V_2 ($mm\,h^{-1}$)	R_1 (-)	RMSE ($cm^3\,cm^{-3}$)	Pearson correlation	KGE (-)
70	35	Revised standard	Modified	0.56	0.34	0.19	0.10	0.04	-	0.77	0.030	0.584	-0.286
			Original	0.50	0.36	0.13	0.11	0.05	377	-	0.029	0.709	-0.029
		UTS MCNP drf	Modified	0.59	0.33	0.19	0.10	0.04	-	0.78	0.027	0.587	-0.148
			Original	0.50	0.36	0.13	0.11	0.05	377	-	0.028	0.707	0.072
	20	Revised standard	Modified	0.68	0.41	0.19	0.10	0.04	-	0.54	0.028	0.748	-0.062
			Original	0.64	0.45	0.12	0.13	0.05	123	-	0.024	0.754	0.263
		UTS MCNP drf	Modified	0.67	0.42	0.18	0.10	0.05	-	0.54	0.025	0.736	0.041
			Original	0.64	0.45	0.12	0.13	0.05	123	-	0.024	0.753	0.342
130	35	Revised standard	Modified	0.55	0.35	0.19	0.10	0.04	-	0.77	0.031	0.565	-0.014
			Original	0.51	0.41	0.13	0.13	0.05	226	-	0.028	0.678	0.364
		UTS MCNP drf	Modified	0.56	0.42	0.19	0.10	0.05	-	0.78	0.024	0.557	0.169
			Original	0.57	0.36	0.13	0.10	0.05	136	-	0.028	0.681	0.093
	20	Revised standard	Modified	0.63	0.45	0.18	0.10	0.05	-	0.53	0.026	0.692	0.175
			Original	0.64	0.45	0.12	0.13	0.05	123	-	0.026	0.724	0.372
		UTS MCNP drf	Modified	0.51	0.41	0.17	0.10	0.05	-	0.53	0.025	0.707	0.145
			Original	0.64	0.45	0.12	0.13	0.05	123	-	0.026	0.727	0.438
200	35	Revised standard	Modified	0.54	0.33	0.19	0.10	0.04	-	0.74	0.026	0.576	0.113
			Original	0.51	0.41	0.13	0.13	0.05	226	-	0.025	0.634	0.378
		UTS MCNP drf	Modified	0.60	0.40	0.19	0.10	0.04	-	0.77	0.023	0.574	0.164
			Original	0.51	0.41	0.13	0.13	0.05	226	-	0.024	0.642	0.436
	20	Revised standard	Modified	0.63	0.45	0.18	0.10	0.05	-	0.53	0.023	0.661	0.175
			Original	0.64	0.45	0.12	0.13	0.05	123	-	0.023	0.676	0.301
		UTS MCNP drf	Modified	0.51	0.41	0.17	0.10	0.05	-	0.52	0.023	0.682	0.135
			Original	0.64	0.45	0.12	0.13	0.05	123	-	0.023	0.684	0.375
300	35	Revised standard	Modified	0.52	0.31	0.19	0.10	0.05	-	0.61	0.019	0.575	-0.047
			Original	0.50	0.36	0.13	0.11	0.05	377	-	0.017	0.576	0.533
		UTS MCNP drf	Modified	0.52	0.31	0.19	0.10	0.05	-	0.61	0.019	0.561	0.062
			Original	0.51	0.45	0.13	0.14	0.05	370	-	0.016	0.585	0.523
	20	Revised standard	Modified	0.63	0.31	0.19	0.10	0.05	-	0.43	0.020	0.591	0.059
			Original	0.76	0.42	0.13	0.14	0.05	230	-	0.016	0.617	0.576
		UTS MCNP drf	Modified	0.59	0.31	0.18	0.10	0.05	-	0.48	0.019	0.592	0.108
			Original	0.68	0.36	0.12	0.10	0.05	136	-	0.015	0.629	0.512
450	35	Revised standard	Modified	0.51	0.32	0.19	0.10	0.04	-	0.59	0.023	0.425	-0.851
			Original	0.52	0.31	0.17	0.11	0.05	482	-	0.011	0.287	0.075
		UTS MCNP drf	Modified	0.52	0.31	0.19	0.10	0.05	-	0.61	0.018	0.451	-0.234
			Original	0.63	0.31	0.16	0.12	0.05	485	-	0.010	0.328	0.120
	20	Revised standard	Modified	0.63	0.31	0.19	0.14	0.05	-	0.43	0.018	0.466	-0.268
			Original	0.66	0.34	0.13	0.14	0.05	484	-	0.009	0.484	0.272
		UTS MCNP drf	Modified	0.63	0.31	0.19	0.10	0.05	-	0.43	0.017	0.461	-0.145
			Original	0.66	0.34	0.13	0.14	0.05	484	-	0.009	0.496	0.261

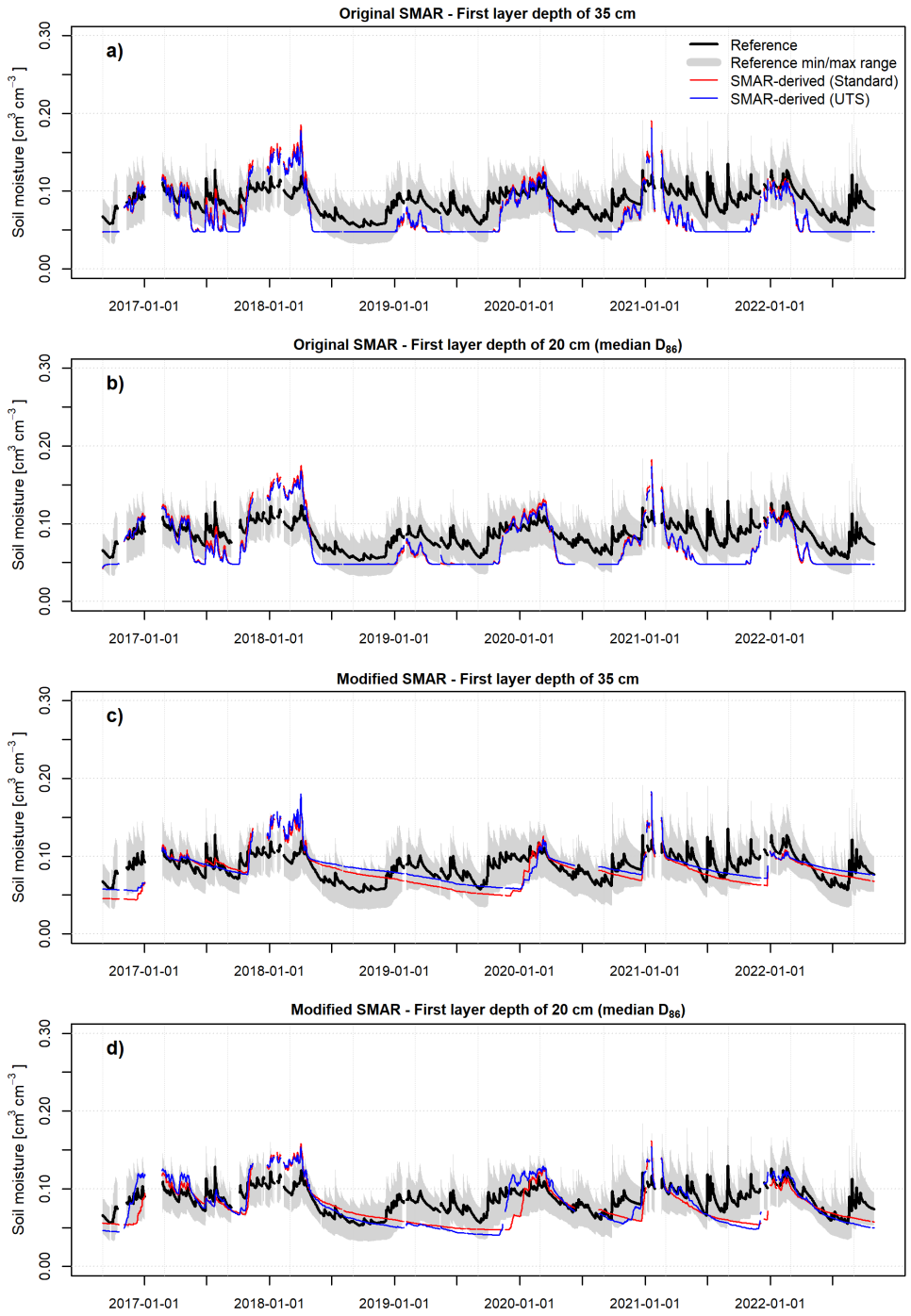

Figure 4.7: *Daily* depth-extrapolated soil moisture time series for a depth of 130 cm using the standard SMAR model with a top layer depth of 35 cm (a), and 20 cm (b) as well as the depth-extrapolated soil moisture time series based on the modified SMAR model presented in this study (top layer depth of 35 cm (c) and 20 cm (d)) based on the CRNS-derived surface soil moisture time series from the standard transfer function and the UTS. The soil physical parameters n_1, n_2, sc_1, sc_2, sw_2 and R_1 were optimised by reducing the RMSE against reference soil moisture values in the year 2017. For the original SMAR model, the water loss term V_2 was calibrated instead of R_1.

4.5 Conclusions

In the present study we investigated the feasibility of depth-extrapolating surface soil moisture time series derived from CRNS to deeper soil layers without additional in situ soil moisture information for calibration. We furthermore evaluated the Universal Transport Solution (UTS) for the estimation of field scale soil moisture from CRNS neutron counts.

Being among the first who evaluate the UTS as a new transfer function to estimate field-scale surface soil moisture information from CRNS, we confirm its improved performance compared to the standard approach. The UTS accounts for the interdependence of soil moisture and air humidity on the observed neutron intensity, being most important for dry soil conditions. Although applied at a forested site with rather dry soils but with large amounts of above-ground hydrogen stored in the local biomass and influencing the neutron signal, CRNS-derived soil moisture estimates can be improved compared to using established transfer functions. Thus, our results suggest hat the UTS should be used for an improved estimation of surface soil moisture in future CRNS research and applications.

We modified SMAR for estimating soil moisture times series in a second, deeper layer in a way that it can be applied without calibration against in situ sensors and with soil physical properties and the cumulative root fraction as a vegetation parameter only. Our analyses show that for a benchmark RMSE of ≤ 0.06 cm^3 cm^{-3}, the uncalibrated modified SMAR can compete with the original SMAR model down to a maximum depth of the second soil layer of 450 cm when the same soil physical properties are assigned and only the water loss term is calibrated. A certain robustness of the uncalibrated, modified SMAR in terms of the RMSE was shown by sensitivity runs of the model. However, major temporal dynamics of the reference in situ soil moisture in the second soil layer are neither captured by original nor by the modified SMAR. This is likely linked to the location of the study site in a mixed forest site with sandy soils, accompanied with preferential flow and root water uptake processes that are difficult to simulate, especially with rather simple modelling approaches. Only the use of SMAR with calibrated effective albeit non-physical parameters partly accommodates to the specific soil hydraulic processes at the study site, showing an improved simulation of soil moisture dynamics in a second soil layer. Under these circumstances, deeper soil moisture time series may be more satisfactorily simulated even with simple modeling approaches such as SMAR.

Although our study suggests that improved surface soil moisture estimates from CRNS do not translate to distinctly improved soil moisture estimates in greater depths, a more accurate estimation of the representative measurement depth of CRNS leads to better results of the SMAR model. This indicates that an accurate estimation of the representative measurement depth of CRNS is especially important when using CRNS data as input for hydrological models.

Given the overall performance of the SMAR model at our single study site, further research and testing of the presented modified version of the SMAR model with and without calibration at sites with varying climatic conditions, vegetation cover and soil properties is necessary and encouraged for future studies. Despite the overall unsatisfactory performance of the SMAR model with respect to accurately capturing soil moisture dynamics at our study site, meeting the defined RMSE benchmark, the simple modification of the SMAR algorithm may serve as a valuable first estimate

of soil moisture from a second, deeper soil layer, when in situ reference soil moisture information for calibration are not available and the soil physical parameters can be reasonably well estimated.

In CRNS research, this modified SMAR approach opens up potential for roving CRNS, i.e., by mounting CRNS instruments on cars [e.g. Schrön et al., 2018a] or trains [e.g. Schrön et al., 2021; Altdorff et al., 2023] moving beyond the field scale of stationary CRNS applications, thereby providing valuable information for landscape water balancing or hydrological catchment models on larger scales. Moreover, the modified SMAR approach introduced in this study is not limited to CRNS applications. It may also be used in estimating root-zone soil moisture in greater depths from satellite derived surface soil moisture in which the original SMAR already proved useful [e.g. Baldwin et al., 2017, 2019; Gheybi et al., 2019].

Table 4.6: Statistical goodness of fit between the depth-extrapolated *daily* surface soil moisture time from CRNS and the average soil moisture time series in the second layer calculated from the available in situ point-scale soil moisture sensors with the fully calibrated SMAR in a physically acceptable parameter range. The calibrated model parameters and goodness-of-fit indicators for the original and modified SMAR model are shown.

Layer 2 depth (cm)	Layer 1 depth (cm)	Transfer function	SMAR	n_1 (-)	n_2 (-)	sc_1 ($cm^3\,cm^{-3}$)	sc_2 ($cm^3\,cm^{-3}$)	sw_2 ($cm^3\,cm^{-3}$)	V_2 ($mm\,h^{-1}$)	R_1 (-)	RMSE ($cm^3\,cm^{-3}$)	Pearson correlation	KGE (-)
70	35	Revised standard	Modified	0.54	0.33	0.19	0.10	0.04	-	0.74	0.024	0.518	0.119
			Original	0.50	0.36	0.13	0.11	0.05	377	-	0.029	0.710	0.011
		UTS MCNP drf	Modified	0.47	0.35	0.19	0.10	0.03	-	0.78	0.022	0.490	0.252
			Original	0.50	0.36	0.13	0.11	0.05	377	-	0.028	0.707	0.111
	20	Revised standard	Modified	0.72	0.40	0.18	0.1	0.04	-	0.54	0.021	0.681	0.228
			Original	0.64	0.45	0.12	0.13	0.05	123	-	0.024	0.766	0.316
		UTS MCNP drf	Modified	0.59	0.45	0.18	0.10	0.05	-	0.55	0.020	0.655	0.307
			Original	0.64	0.45	0.12	0.13	0.05	123	-	0.023	0.763	0.389
130	35	Revised standard	Modified	0.55	0.35	0.19	0.10	0.04	-	0.77	0.021	0.441	0.321
			Original	0.57	0.36	0.13	0.10	0.05	136	-	0.028	0.694	0.086
		UTS MCNP drf	Modified	0.58	0.44	0.19	0.10	0.04	-	0.78	0.019	0.390	0.358
			Original	0.57	0.36	0.13	0.10	0.05	136	-	0.028	0.694	0.176
	20	Revised standard	Modified	0.59	0.45	0.18	0.10	0.05	-	0.55	0.021	0.585	0.351
			Original	0.63	0.34	0.12	0.12	0.05	63	-	0.026	0.741	0.031
		UTS MCNP drf	Modified	0.55	0.33	0.15	0.10	0.04	-	0.54	0.022	0.689	0.165
			Original	0.63	0.34	0.12	0.12	0.05	163	-	0.025	0.741	0.121
200	35	Revised standard	Modified	0.54	0.33	0.19	0.10	0.04	-	0.74	0.019	0.425	0.334
			Original	0.51	0.41	0.13	0.13	0.05	226	-	0.024	0.657	0.437
		UTS MCNP drf	Modified	0.45	0.44	0.19	0.10	0.04	-	0.75	0.018	0.321	0.304
			Original	0.57	0.36	0.13	0.10	0.05	136	-	0.024	0.665	0.162
	20	Revised standard	Modified	0.59	0.45	0.18	0.10	0.05	-	0.55	0.019	0.554	0.352
			Original	0.64	0.45	0.12	0.13	0.05	123	-	0.022	0.705	0.390
		UTS MCNP drf	Modified	0.59	0.45	0.18	0.10	0.05	-	0.55	0.019	0.503	0.383
			Original	0.64	0.45	0.12	0.13	0.05	123	-	0.022	0.708	0.448
300	35	Revised standard	Modified	0.56	0.34	0.19	0.10	0.04	-	0.77	0.017	0.377	0.141
			Original	0.53	0.44	0.13	0.11	0.05	323	-	0.016	0.605	0.504
		UTS MCNP drf	Modified	0.52	0.41	0.19	0.10	0.04	-	0.75	0.017	0.310	0.223
			Original	0.53	0.44	0.13	0.11	0.05	323	-	0.016	0.610	0.538
	20	Revised standard	Modified	0.68	0.41	0.19	0.10	0.04	-	0.54	0.018	0.446	0.171
			Original	0.68	0.36	0.12	0.10	0.05	136	-	0.015	0.665	0.536
		UTS MCNP drf	Modified	0.52	0.41	0.18	0.11	0.05	-	0.54	0.017	0.376	0.178
			Original	0.68	0.36	0.13	0.10	0.05	136	-	0.015	0.669	0.574
450	35	Revised standard	Modified	0.52	0.31	0.19	0.10	0.05	-	0.61	0.016	0.362	0.050
			Original	0.63	0.31	0.16	0.12	0.05	485	-	0.010	0.365	0.156
		UTS MCNP drf	Modified	0.52	0.31	0.19	0.10	0.05	-	0.61	0.016	0.291	0.028
			Original	0.62	0.34	0.16	0.10	0.05	492	-	0.010	0.363	0.170
	20	Revised standard	Modified	0.63	0.31	0.19	0.10	0.05	-	0.43	0.013	0.416	0.189
			Original	0.66	0.34	0.13	0.14	0.05	484	-	0.009	0.517	0.283
		UTS MCNP drf	Modified	0.63	0.31	0.19	0.10	0.05	-	0.43	0.013	0.384	0.217
			Original	0.66	0.34	0.13	0.14	0.05	484	-	0.009	0.527	0.270

4.6 Appendix

Table 4.7: Minimum and maximum RMSE values between the depth-extrapolated soil moisture time from CRNS using the modified SMAR model of the 50 ensemble runs and the reference soil moisture time series in the second layer calculated from the available in situ point-scale soil moisture sensors for the simulations with hourly and daily resolution.

			Hourly resolution		Daily resolution	
Transfer function	**Layer 1 depth (cm)**	**Layer 2 depth (cm)**	**RMSE$_{min}$ (cm^3 cm^{-3})**	**RMSE$_{max}$ (cm^3 cm^{-3})**	**RMSE$_{min}$ (cm^3 cm^{-3})**	**RMSE$_{max}$ (cm^3 cm^{-3})**
Revised standard	35	70	0.040	0.073	0.037	0.072
		130	0.029	0.049	0.025	0.049
		200	0.027	0.044	0.023	0.045
		300	0.026	0.047	0.025	0.047
		450	0.034	0.057	0.032	0.058
	20	70	0.032	0.052	0.027	0.049
		130	0.027	0.042	0.024	0.038
		200	0.026	0.040	0.023	0.034
		300	0.025	0.043	0.020	0.035
		450	0.031	0.052	0.023	0.043
UTS MCNP drf	35	70	0.037	0.070	0.035	0.070
		130	0.028	0.048	0.024	0.049
		200	0.027	0.043	0.022	0.045
		300	0.024	0.047	0.024	0.047
		450	0.032	0.057	0.032	0.059
	20	70	0.031	0.051	0.026	0.049
		130	0.027	0.041	0.023	0.037
		200	0.026	0.040	0.022	0.033
		300	0.024	0.043	0.019	0.035
		450	0.030	0.051	0.023	0.044

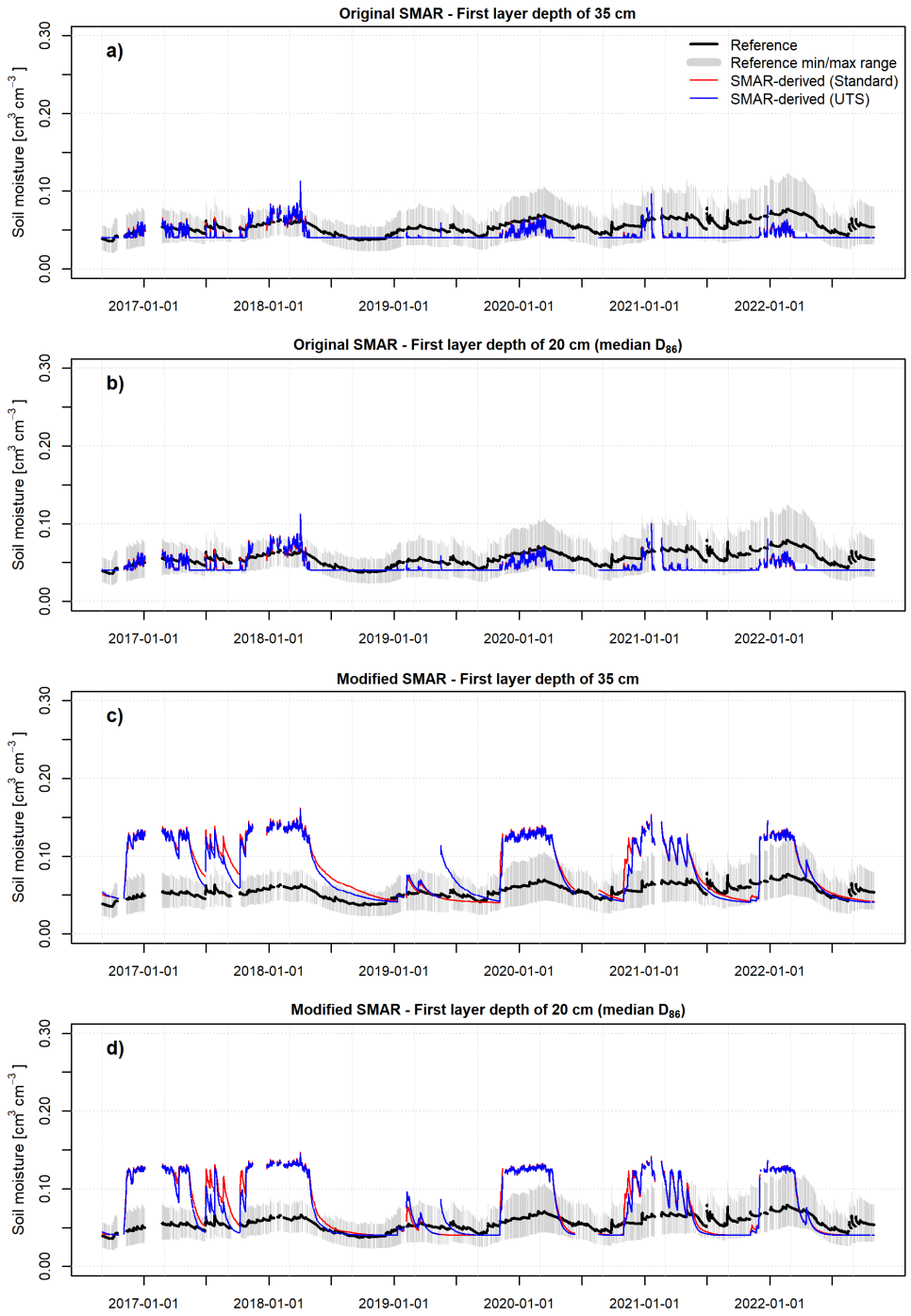

Figure 4.8: *Hourly* depth-extrapolated soil moisture time series for a depth of 450 cm using the calibrated standard SMAR model (calibrated water loss V_2) with a top layer depth of 35 cm (a), and 20 cm (b) as well as the depth-extrapolated soil moisture time series based on the uncalibrated modified SMAR (estimated water loss) model presented in this study (top layer depth of 35 cm (c) and 20 cm (d)) based on the CRNS-derived surface soil moisture time series from the standard transfer function and the UTS.

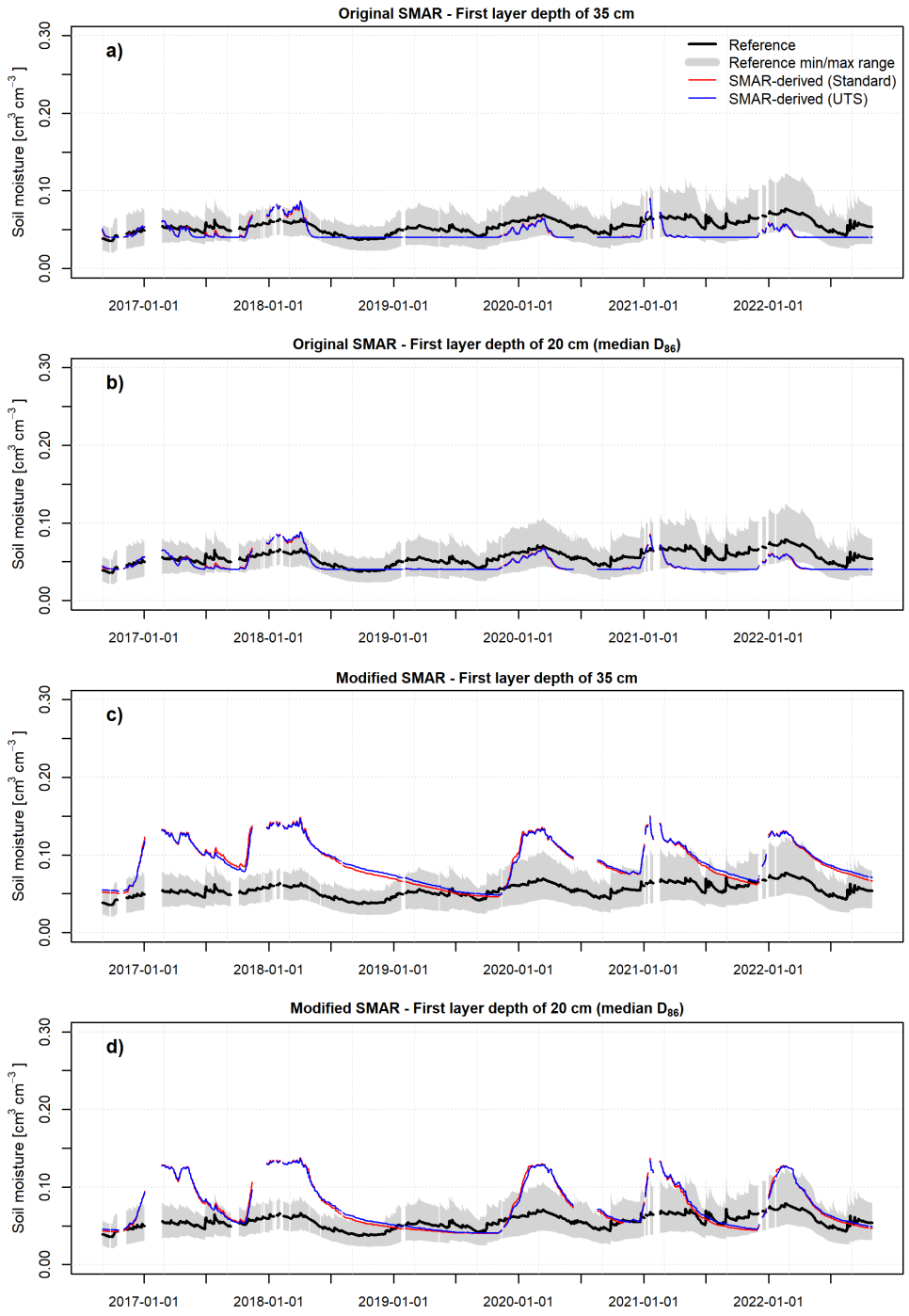

Figure 4.9: *Daily* depth-extrapolated soil moisture time series for a depth of 450 cm using the calibrated standard SMAR model (calibrated water loss V_2) with a top layer depth of 35 cm (a), and 20 cm (b) as well as the depth-extrapolated soil moisture time series based on the uncalibrated modified SMAR (estimated water loss) model presented in this study (top layer depth of 35 cm (c) and 20 cm (d)) based on the CRNS-derived surface soil moisture time series from the standard transfer function and the UTS.

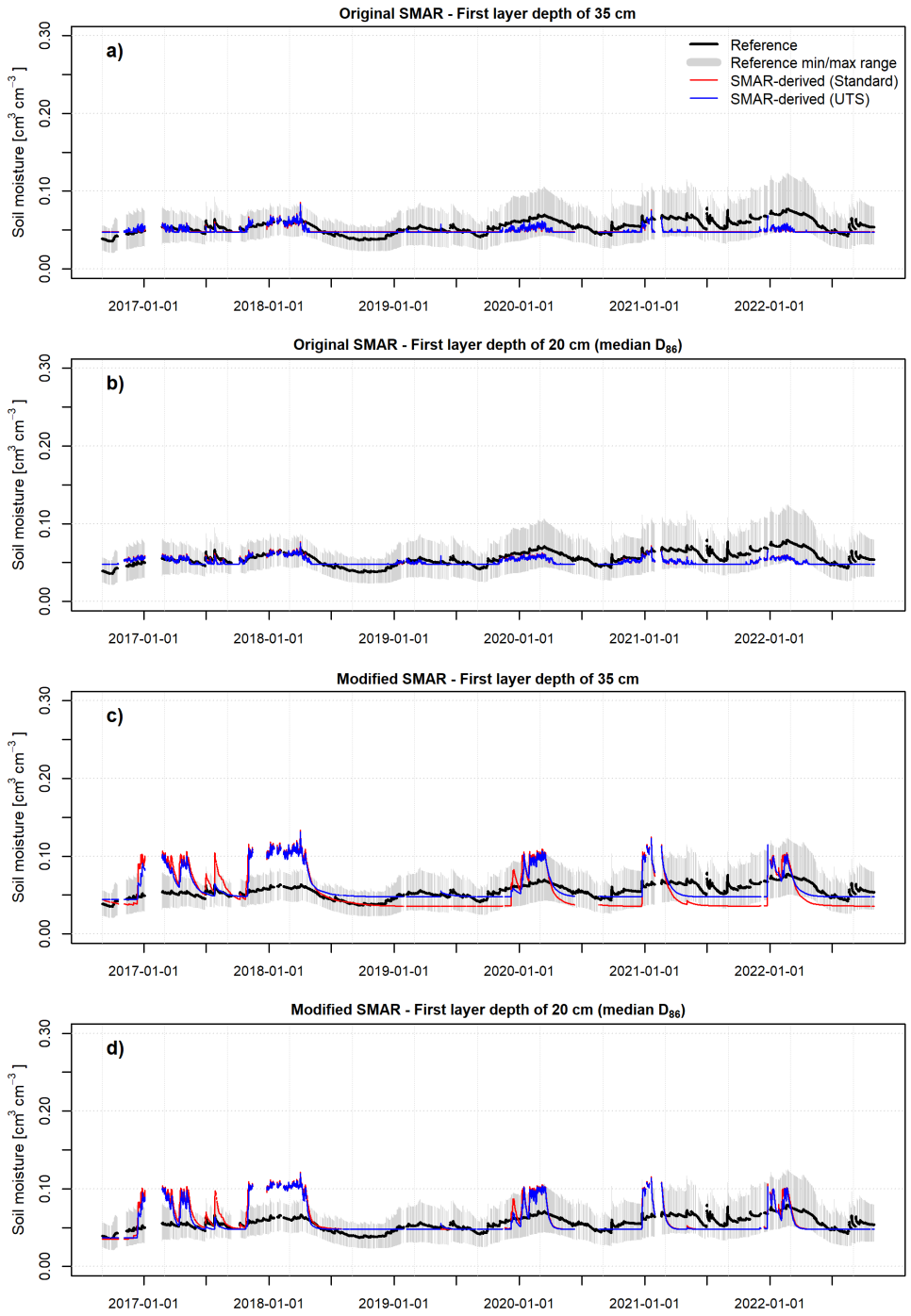

Figure 4.10: *Hourly* depth-extrapolated soil moisture time series for a depth of 450 cm using the standard SMAR model with a top layer depth of 35 cm (a), and 20 cm (b) as well as the depth-extrapolated soil moisture time series based on the modified SMAR model presented in this study (top layer depth of 35 cm (c) and 20 cm (d)) based on the CRNS-derived surface soil moisture time series from the standard transfer function and the UTS. The soil physical parameters n_1, n_2, sc_1, sc_2, sw_2 and R_1 were optimised by reducing the RMSE against reference soil moisture values in the year 2017. For the original SMAR model, the water loss term V_2 was calibrated instead of R_1.

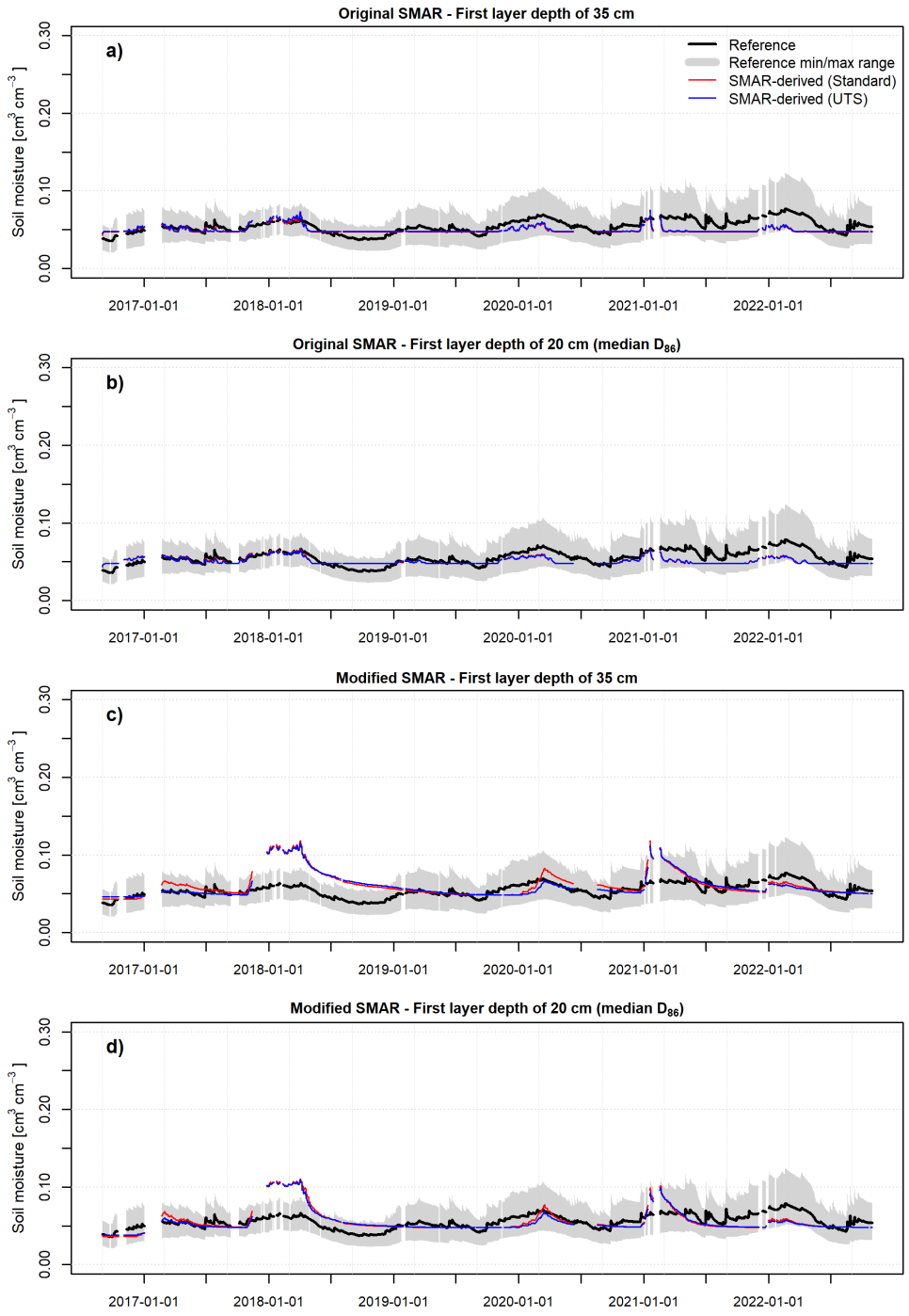

Figure 4.11: *Daily* depth-extrapolated soil moisture time series for a depth of 450 cm using the standard SMAR model with a top layer depth of 35 cm (a), and 20 cm (b) as well as the depth-extrapolated soil moisture time series based on the modified SMAR model presented in this study (top layer depth of 35 cm (c) and 20 cm (d)) based on the CRNS-derived surface soil moisture time series from the standard transfer function and the UTS. The soil physical parameters n_1, n_2, sc_1, sc_2, sw_2 and R_1 were optimised by reducing the RMSE against reference soil moisture values in the year 2017. For the original SMAR model, the water loss term V_2 was calibrated instead of R_1.

Table 4.8: Statistical goodness of fit between the depth-extrapolated *hourly* surface soil moisture time series from CRNS and the average soil moisture time series in the second layer calculated from the available in situ point-scale soil moisture sensors with the fully calibrated SMAR and effective parameters in a non-physically based value range. The calibrated model parameters and goodness-of-fit indicators for the original and modified SMAR model are shown.

Layer 2 depth (cm)	Layer 1 depth (cm)	Transfer function	SMAR	n_1 (-)	n_2 (-)	sc_1 ($cm^3\,cm^{-3}$)	sc_2 ($cm^3\,cm^{-3}$)	sw_2 ($cm^3\,cm^{-3}$)	V_2 ($mm\,h^{-1}$)	R_1 (-)	RMSE ($cm^3\,cm^{-3}$)	Pearson correlation	KGE (-)
70	35	Revised standard	Modified	0.44	0.33	-0.25	-0.96	-0.45	-	0.77	0.057	0.847	-2.014
			Original	0.55	0.35	-0.03	-0.25	-0.10	393	-	0.054	0.846	-1.948
		UTS MCNP drf	Modified	0.44	0.37	0.04	-0.88	-0.02	-	0.65	0.045	0.836	-1.488
			Original	0.55	0.35	-0.03	-0.25	-0.10	393	-	0.047	0.836	-1.552
	20	Revised standard	Modified	0.73	0.36	-0.72	-0.88	-0.38	-	0.51	0.015	0.849	0.458
			Original	0.59	0.46	0.02	-0.30	0.03	452	-	0.016	0.849	0.423
		UTS MCNP drf	Modified	0.73	0.36	-0.72	-0.88	-0.38	-	0.51	0.013	0.841	0.602
			Original	0.64	0.31	0	-0.07	0.03	353	-	0.012	0.841	0.627
130	35	Revised standard	Modified	0.42	0.38	-0.96	-0.87	-0.54	-	0.73	0.016	0.839	0.447
			Original	0.54	0.34	0.01	-0.22	0.01	358	-	0.025	0.838	0.007
		UTS MCNP drf	Modified	0.42	0.38	-0.96	-0.87	-0.54	-	0.73	0.014	0.829	0.558
			Original	0.54	0.34	0.01	-0.22	0.01	358	-	0.022	0.829	0.199
	20	Revised standard	Modified	0.66	0.38	-0.53	-0.09	-0.75	-	0.45	0.008	0.855	0.790
			Original	0.64	0.37	-0.23	-0.48	-0.01	497	-	0.009	0.855	0.839
		UTS MCNP drf	Modified	0.66	0.38	-0.53	-0.09	-0.75	-	0.45	0.009	0.847	0.717
			Original	0.64	0.37	-0.23	-0.48	-0.01	497	-	0.009	0.846	0.781
200	35	Revised standard	Modified	0.45	0.31	-0.79	-0.58	-0.19	-	0.68	0.011	0.794	0.782
			Original	0.53	0.31	0	-0.07	0.03	353	-	0.015	0.794	0.366
		UTS MCNP drf	Modified	0.45	0.31	-0.79	-0.58	-0.19	-	0.68	0.010	0.788	0.750
			Original	0.53	0.31	0	-0.07	0.03	353	-	0.013	0.512	0.787
	20	Revised standard	Modified	0.71	0.38	-0.68	-0.33	-0.07	-	0.51	0.009	0.811	0.563
			Original	0.54	0.32	-0.90	-0.75	-0.22	479	-	0.014	0.811	0.739
		UTS MCNP drf	Modified	0.71	0.38	-0.68	-0.33	-0.07	-	0.51	0.009	0.805	0.504
			Original	0.75	0.37	-0.96	-0.53	-0.27	498	-	0.012	0.805	0.749
300	35	Revised standard	Modified	0.49	0.36	-0.93	-0.60	-0.12	-	0.71	0.009	0.733	0.658
			Original	0.54	0.34	0.01	-0.22	0.01	358	-	0.022	0.734	-0.042
		UTS MCNP drf	Modified	0.49	0.36	-0.93	-0.60	-0.12	-	0.71	0.009	0.728	0.602
			Original	0.54	0.34	0.01	-0.22	0.01	358	-	0.019	0.729	0.147
	20	Revised standard	Modified	0.61	0.33	-0.79	-0.02	-0.85	-	0.49	0.009	0.751	0.393
			Original	0.70	0.35	-0.09	-0.73	0.02	374	-	0.009	0.751	0.739
		UTS MCNP drf	Modified	0.61	0.33	-0.79	-0.02	-0.85	-	0.49	0.009	0.746	0.350
			Original	0.70	0.35	-0.09	-0.73	0.02	374	-	0.009	0.747	0.738
450	35	Revised standard	Modified	0.55	0.32	-0.24	-0.44	0.01	-	0.65	0.010	0.593	0.448
			Original	0.54	0.37	0.06	-0.42	0.02	448	-	0.019	0.577	0.045
		UTS MCNP drf	Modified	0.55	0.32	-0.24	-0.44	0.01	-	0.65	0.010	0.592	0.404
			Original	0.54	0.37	0.06	-0.42	0.02	448	-	0.018	0.586	0.139
	20	Revised standard	Modified	0.54	0.44	-0.27	-0.70	0.03	-	0.46	0.009	0.619	0.232
			Original	0.64	0.37	-0.23	-0.48	-0.01	497	-	0.009	0.618	0.609
		UTS MCNP drf	Modified	0.54	0.44	-0.27	-0.70	0.03	-	0.46	0.009	0.618	0.202
			Original	0.64	0.37	-0.23	-0.48	-0.01	497	-	0.008	0.619	0.616

Table 4.9: Statistical goodness of fit between the depth-extrapolated *daily* surface soil moisture time from CRNS and the average soil moisture time series in the second layer calculated from the available in situ point-scale soil moisture sensors with the fully calibrated SMAR and effective parameters in a non-physically based value range. The calibrated model parameters and goodness-of-fit indicators for the original and modified SMAR model are shown.

Layer 2 depth (cm)	Layer 1 depth (cm)	Transfer function	SMAR	n_1 (-)	n_2 (-)	sc_1 ($cm^3\,cm^{-3}$)	sc_2 ($cm^3\,cm^{-3}$)	sw_2 ($cm^3\,cm^{-3}$)	V_2 ($mm\,h^{-1}$)	R_1 (-)	RMSE ($cm^3\,cm^{-3}$)	Pearson correlation	KGE (-)
70	35	Revised standard	Modified	0.42	0.43	0.11	-0.82	0.04	-	0.61	0.033	0.764	-0.555
			Original	0.45	0.37	0.01	0.340	-0.05	488	-	0.052	0.854	-1.806
		UTS MCNP drf	Modified	0.48	0.31	0.09	-0.76	0.04	-	0.64	0.032	0.804	-0.743
			Original	0.45	0.37	0.01	-0.34	-0.05	488	-	0.046	0.844	-1.420
	20	Revised standard	Modified	0.74	0.33	0	-0.77	0.03	-	0.54	0.013	0.856	0.521
			Original	0.74	0.34	-0.06	-0.69	0	452	-	0.015	0.856	0.482
		UTS MCNP drf	Modified	0.74	0.33	0	-0.77	0.03	-	0.54	0.012	0.848	0.658
			Original	0.68	0.33	-0.02	-0.03	0.02	391	-	0.012	0.848	0.619
130	35	Revised standard	Modified	0.61	0.33	0	-0.77	0.03	-	0.78	0.016	0.843	0.536
			Original	0.48	0.32	0.04	-0.86	0.04	477	-	0.013	0.840	0.378
		UTS MCNP drf	Modified	0.60	0.31	-0.43	-0.80	-0.16	-	0.63	0.013	0.835	0.641
			Original	0.48	0.32	0.04	-0.86	0.04	477	-	0.016	0.835	0.502
	20	Revised standard	Modified	0.55	0.39	-0.68	-0.14	-0.70	-	0.46	0.008	0.862	0.798
			Original	0.64	0.37	-0.23	-0.48	-0.01	497	-	0.009	0.846	0.846
		UTS MCNP drf	Modified	0.73	0.43	-0.29	-0.03	-0.69	-	0.46	0.008	0.854	0.769
			Original	0.65	0.38	-0.04	-0.64	0.04	423	-	0.008	0.854	0.808
200	35	Revised standard	Modified	0.47	0.31	-0.33	-0.71	-0.03	-	0.73	0.01	0.798	0.775
			Original	0.61	0.34	-0.06	-0.69	0	452	-	0.018	0.804	0.383
		UTS MCNP drf	Modified	0.47	0.31	-0.33	-0.71	-0.03	-	0.73	0.010	0.792	0.727
			Original	0.61	0.34	-0.06	-0.69	0	452	-	0.016	0.797	0.527
	20	Revised standard	Modified	0.72	0.42	-0.93	-0.19	-0.29	-	0.43	0.009	0.820	0.617
			Original	0.73	0.33	-0.19	-0.13	0.01	421	-	0.009	0.822	0.769
		UTS MCNP drf	Modified	0.59	0.45	-0.39	-0.03	-0.39	-	0.39	0.009	0.814	0.608
			Original	0.61	0.31	-0.08	-0.23	0.04	409	-	0.009	0.814	0.644
300	35	Revised standard	Modified	0.55	0.40	-0.54	-1	-0.03	-	0.56	0.008	0.741	0.626
			Original	0.48	0.32	0.04	-0.86	0.04	477	-	0.012	0.747	0.502
		UTS MCNP drf	Modified	0.55	0.40	-0.54	-1	-0.03	-	0.56	0.008	0.736	0.567
			Original	0.48	0.32	0.04	-0.86	0.04	477	-	0.011	0.744	0.597
	20	Revised standard	Modified	0.57	0.46	-0.28	0.02	-0.57	-	0.40	0.008	0.764	0.504
			Original	0.67	0.33	-0.39	-0.49	-0.04	442	-	0.009	0.771	0.760
		UTS MCNP drf	Modified	0.66	0.39	0.06	0.06	-0.39	-	0.50	0.024	0.666	-0.429
			Original	0.67	0.33	-0.39	-0.49	-0.04	442	-	0.008	0.766	0.747
450	35	Revised standard	Modified	0.55	0.34	-0.20	-0.91	0.02	-	0.74	0.009	0.604	0.405
			Original	0.42	0.35	0	-0.17	0.01	487	-	0.016	0.619	0.067
		UTS MCNP drf	Modified	0.44	0.37	-0.82	-0.83	-0.04	-	0.54	0.008	0.604	0.387
			Original	0.42	0.35	0	-0.17	0.01	487	-	0.015	0.617	0.230
	20	Revised standard	Modified	0.71	0.39	-1	-0.04	-0.47	-	0.41	0.008	0.637	0.339
			Original	0.64	0.31	-0.33	-0.13	-0.03	456	-	0.011	0.649	0.618
		UTS MCNP drf	Modified	0.54	0.34	-0.65	0	-0.66	-	0.41	0.008	0.633	0.260
			Original	0.64	0.31	-0.33	-0.13	-0.03	456	-	0.010	0.647	0.627

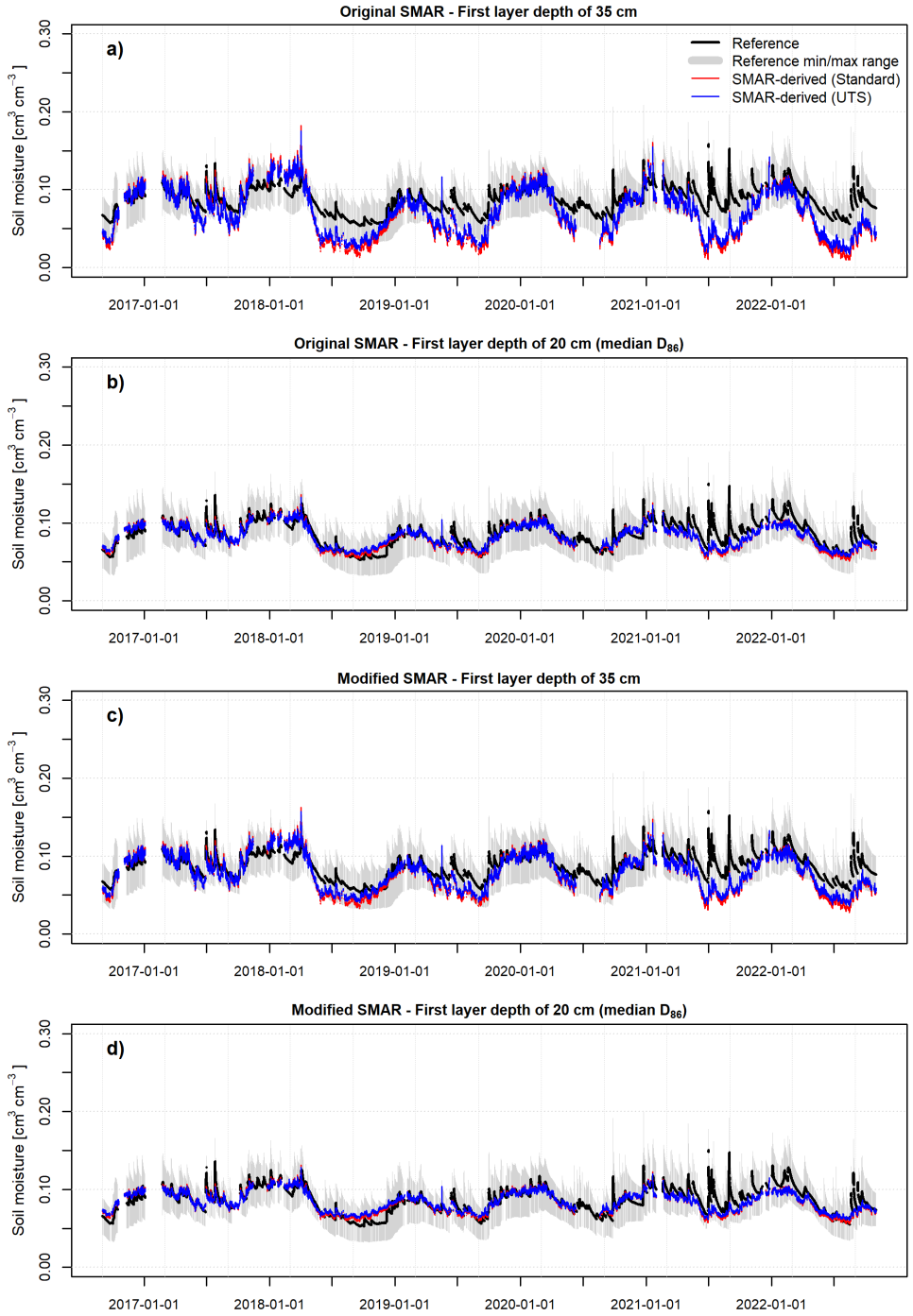

Figure 4.12: *Hourly* depth-extrapolated soil moisture time series for a depth of 130 cm using the standard SMAR model with a top layer depth of 35 cm (a), and 20 cm (b) as well as the depth-extrapolated soil moisture time series based on the modified SMAR model presented in this study (top layer depth of 35 cm (c) and 20 cm (d)) based on the CRNS-derived surface soil moisture time series from the standard transfer function and the UTS. The soil physical parameters n_1, n_2, sc_1, sc_2, sw_2 and R_1 were optimised by reducing the RMSE against reference soil moisture values in the year 2017. Here, the parameters sc_1, sc_2 and sw_2 were calibrated as effective parameters in a non-physically based value range. For the original SMAR model, the water loss term V_2 was calibrated instead of R_1.

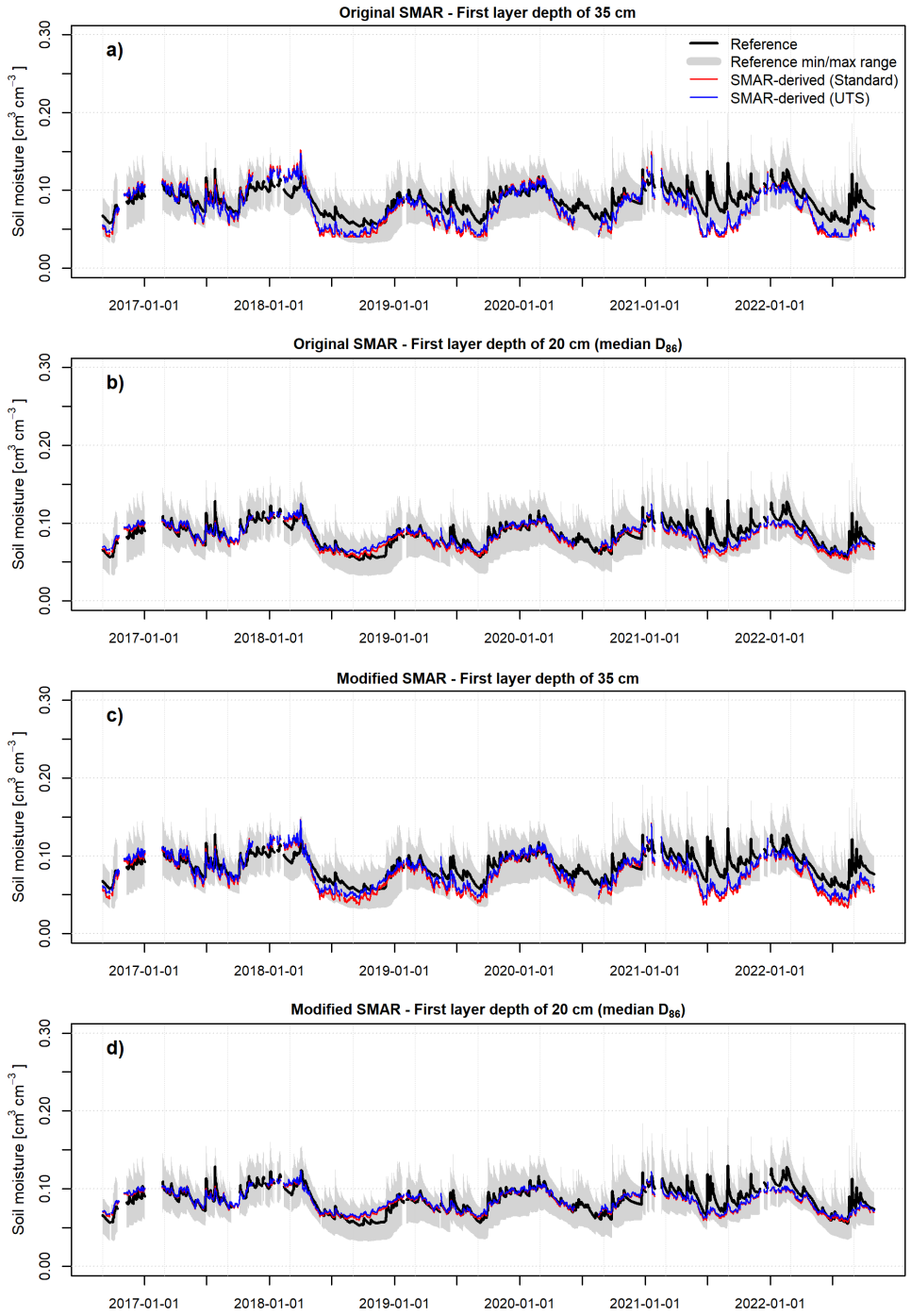

Figure 4.13: *Daily* depth-extrapolated soil moisture time series for a depth of 130 cm using the standard SMAR model with a top layer depth of 35 cm (a), and 20 cm (b) as well as the depth-extrapolated soil moisture time series based on the modified SMAR model presented in this study (top layer depth of 35 cm (c) and 20 cm (d)) based on the CRNS-derived surface soil moisture time series from the standard transfer function and the UTS. The soil physical parameters n_1, n_2, sc_1, sc_2, sw_2 and R_1 were optimised by reducing the RMSE against reference soil moisture values in the year 2017. Here, the parameters sc_1, sc_2 and sw_2 were calibrated as effective parameters in a non-physically based value range. For the original SMAR model, the water loss term V_2 was calibrated instead of R_1.

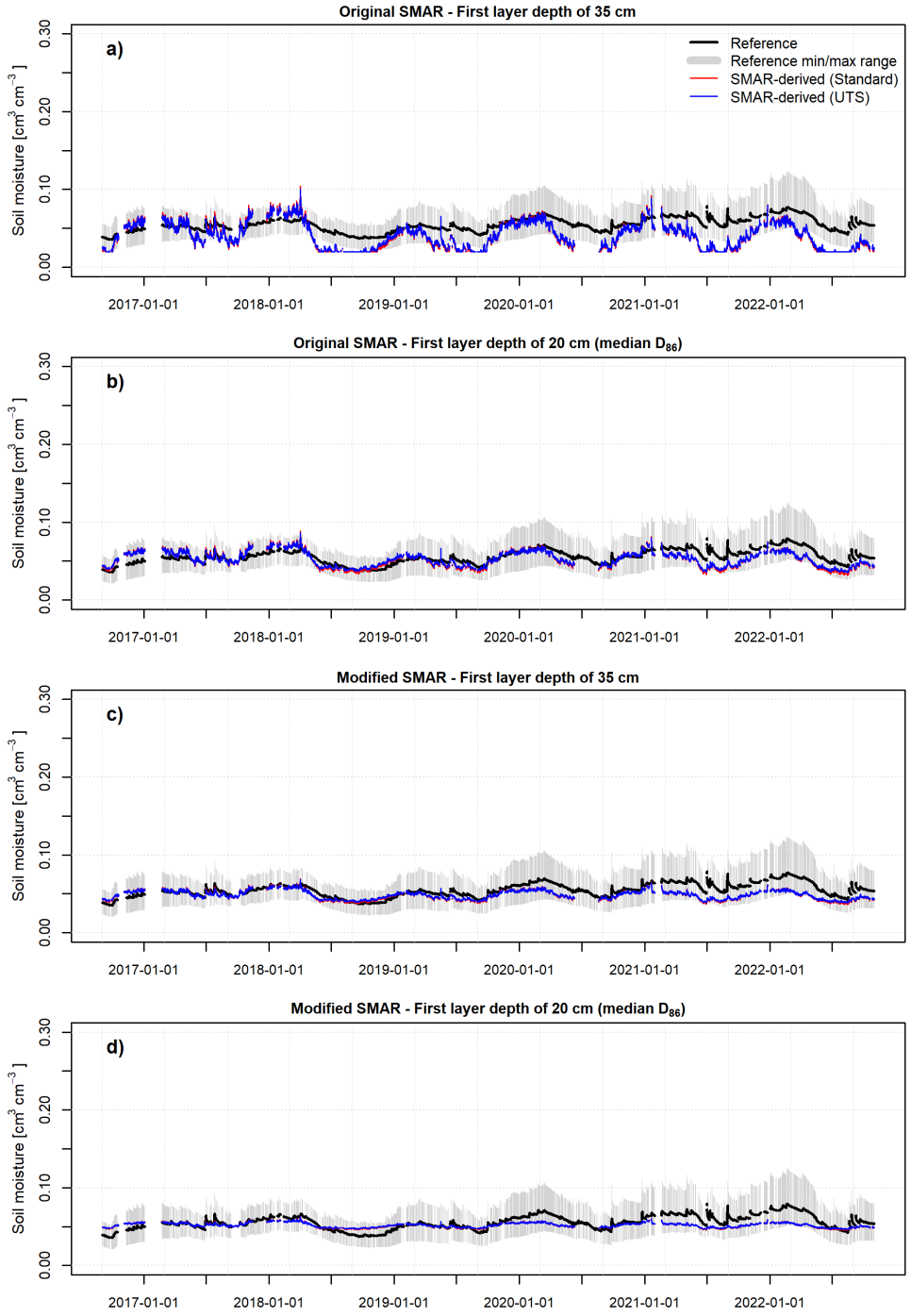

Figure 4.14: *Hourly* depth-extrapolated soil moisture time series for a depth of 450 cm using the standard SMAR model with a top layer depth of 35 cm (a), and 20 cm (b) as well as the depth-extrapolated soil moisture time series based on the modified SMAR model presented in this study (top layer depth of 35 cm (c) and 20 cm (d)) based on the CRNS-derived surface soil moisture time series from the standard transfer function and the UTS. The soil physical parameters n_1, n_2, sc_1, sc_2, sw_2 and R_1 were optimised by reducing the RMSE against reference soil moisture values in the year 2017. Here, the parameters sc_1, sc_2 and sw_2 were calibrated as effective parameters in a non-physically based value range. For the original SMAR model, the water loss term V_2 was calibrated instead of R_1.

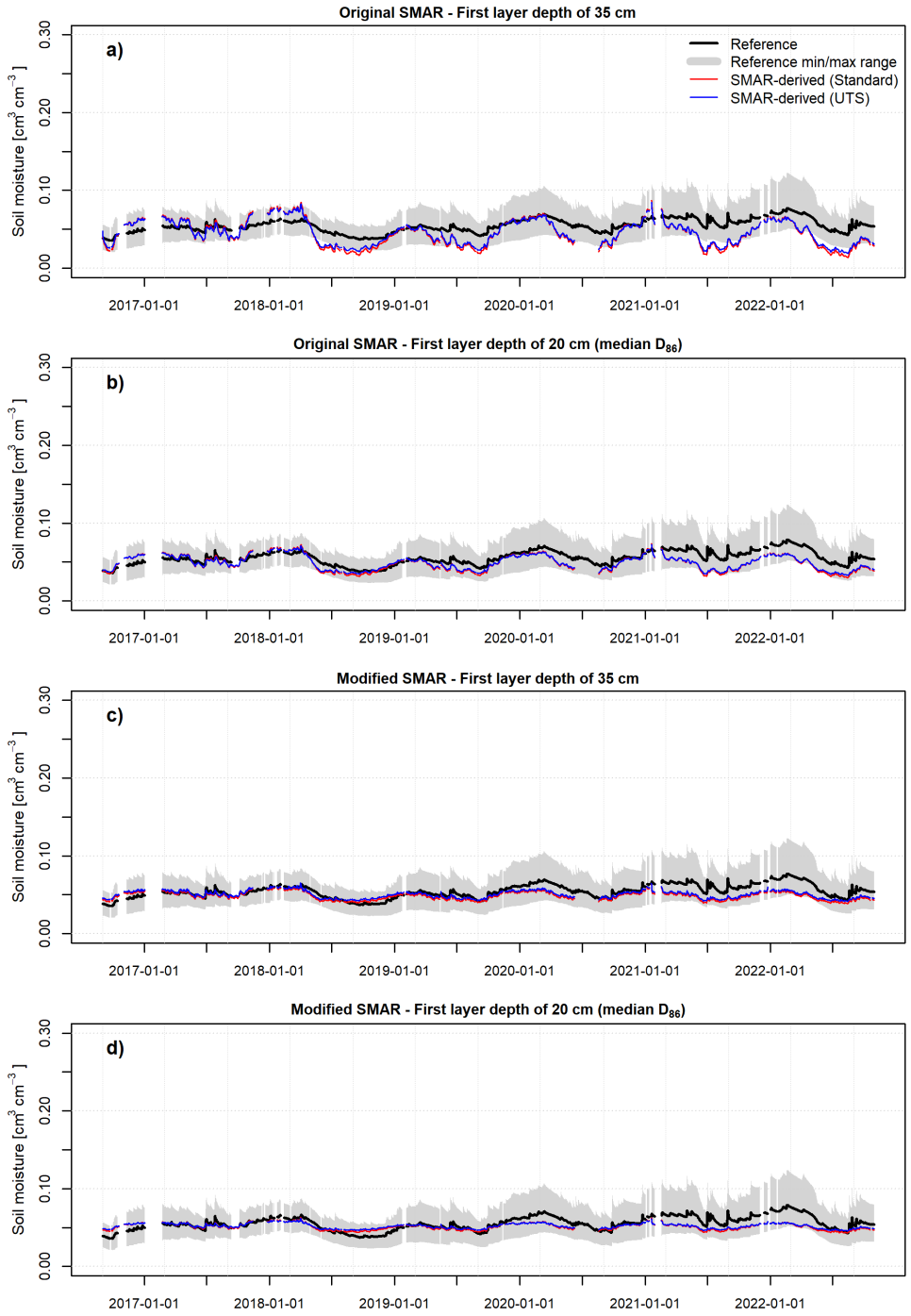

Figure 4.15: *Daily* depth-extrapolated soil moisture time series for a depth of 450 cm using the standard SMAR model with a top layer depth of 35 cm (a), and 20 cm (b) as well as the depth-extrapolated soil moisture time series based on the modified SMAR model presented in this study (top layer depth of 35 cm (c) and 20 cm (d)) based on the CRNS-derived surface soil moisture time series from the standard transfer function and the UTS. The soil physical parameters n_1, n_2, sc_1, sc_2, sw_2 and R_1 were optimised by reducing the RMSE against reference soil moisture values in the year 2017. Here, the parameters sc_1, sc_2 and sw_2 were calibrated as effective parameters in a non-physically based value range. For the original SMAR model, the water loss term V_2 was calibrated instead of R_1.

Chapter 5

Estimating soil moisture in larger depths with downhole CRNS

A version of this chapter has been published as:

A change in perspective: downhole cosmic-ray neutron sensing for the estimation of soil moisture

Daniel Rasche, Jannis Weimar, Martin Schrön, Markus Köhli, Markus Morgner, Andreas Güntner, and Theresa Blume

Hydrology and Earth System Sciences, 27(16):3059–3082. doi: 10.5194/hess-27-3059-2023. 2023.

5.1 Abstract

Above-ground Cosmic-Ray Neutron Sensing (CRNS) allows for the non-invasive estimation of the field-scale soil moisture content in the upper decimetres of the soil. However, large parts of the deeper vadose zone remain outside of its observational window. Retrieving soil moisture information from these deeper layers requires extrapolation, modelling or other methods, all of which come with methodological challenges. Against this background, we investigate CRNS for downhole soil moisture measurements in deeper layers of the vadose zone. To render calibration with in situ soil moisture measurements unnecessary, we rescaled neutron intensities observed below the terrain surface with intensities measured above a waterbody.

An experimental set-up with a CRNS sensor deployed at different depths of up to 10 m below the surface in a groundwater observation well combined with particle transport simulations revealed the response of downhole thermal neutron intensities to changes in the soil moisture content at the depth of the downhole neutron detector as well as in the layers above it. The simulation results suggest that the sensitive measurement radius of several decimetres, which depends on soil moisture and soil bulk density, exceeds that of a standard active neutron probe which is only about 30 cm. We derived transfer functions to estimate downhole neutron signals from soil moisture information and we describe approaches for using these transfer functions in an inverse way to derive soil moisture from the observed neutron signals. The in situ neutron and soil moisture observations confirm the applicability of these functions and prove the concept of passive downhole soil moisture estimation even at larger depths using Cosmic-Ray Neutron Sensing.

5.2 Introduction

Soil moisture is a key variable in the hydrological cycle [Vereecken et al., 2008, 2014; Seneviratne et al., 2010], as it drives energy and water fluxes, thereby influencing groundwater recharge, runoff generation processes and, subsequently, the local water balance. It influences vegetation growth and vegetation communities which, in turn, influence the local soil moisture and microclimate [e.g. see, Daly and Porporato, 2005; Seneviratne et al., 2010; Wang et al., 2018]. Averaged over several ecosystems, approximately 75 % of roots can be found in the upper 40 cm of the soil [Jackson et al., 1996]. As a result, soil moisture in these upper decimetres of the root zone exerts an important control on the hydrological cycle. However, the maximum rooting depth largely exceeds the upper decimetres of the soil, depends on the plant species [Canadell et al., 1996] and is driven by local hydrological conditions [e.g. Fan et al., 2017]. These deep roots can be of high importance for the water supply of other, more shallow rooting plants through processes such as hydraulic lift [e.g. Neumann and Cardon, 2012; Pierret et al., 2016], especially during dry periods. Additionally, infiltrating water can be diverted along deep roots to greater depths as preferential flow [e.g. see, Nimmo, 2021], potentially leading to increased water storage in deeper layers of the unsaturated zone. Among others, these processes make deeper layers similarly important for the local water balance and the local hydrological processes.

As soil moisture is highly variable, even on small horizontal scales [Vereecken et al., 2014], a large number of point-scale measurements (e.g. in situ sensors) are

required to overcome the small-scale variability and derive representative averages. One method to directly measure representative soil moisture averages over several hectares and is Cosmic-Ray Neutron Sensing [CRNS; Schrön et al., 2018b]. This techniques was introduced by Zreda et al. [2008] and Desilets et al. [2010] about a decade ago and uses secondary neutrons produced from cosmic rays which are inversely correlated with the amount of hydrogen in the surrounding area. It allows for the non-invasive estimation of average soil moisture contents up to depths of 15–83 cm [Köhli et al., 2015] and, thus, largely covers the shallow soil layers with high root densities.

Despite the large horizontal measurement footprint radius of 130–240 m [Köhli et al., 2015], CRNS lacks an integration depth large enough to cover greater parts of the deeper root zone. Other geophysical methods with a large (hectometre-scale) horizontal measurement area such as geoelectric approaches [Cimpoiaşu et al., 2020; de Jong et al., 2020] and the observation of integral mass changes by terrestrial gravimetry [Van Camp et al., 2017; Reich et al., 2021], may allow one to infer soil moisture dynamics at larger depths of the vadose zone. However, the separation of the integral gravity signal into different hydrological signatures can be challenging [Van Camp et al., 2017]. In addition, depending on the geophysical method chosen, continuous measurements may not be feasible, which would hamper the monitoring of the soil moisture dynamics in the deeper vadose zone.

Another soil moisture measurement technique with a measurement volume smaller than other geophysical methods but larger than that of point-scale sensors is the active neutron probe. Invented in the middle of the previous century [Gardner and Kirkham, 1952], the active neutron probe allows for the estimation of soil moisture at a depth of interest via access tubes. Instead of passively observing the flux of naturally occurring epithermal (0.25 eV–100 keV) neutrons, as is the case for above-ground CRNS, an active neutron source produces fast neutrons (100 keV–10 MeV) and a co-located neutron detector observes the intensity of backscattered slowed-down thermal (below 0.25 eV) neutrons. The intensity of thermal neutrons measured under radiation of a fast-neutron source largely depends on the hydrogen content of the soil due to the decelerating power of hydrogen through elastic collisions and removal of thermal neutrons by absorption [see e.g. IAEA - International Atomic Energy Agency, 1970; Gardner, 1986; Kramer et al., 1992; Ferronsky, 2015, for a detailed review].

An important advantage of downhole soil moisture estimation using active neutron probes is their decimetre-scale measurement volume around the probe in the soil. The Ølgaard (1965) equation in Kristensen [1973] and Gardner [1986] defines the measurement radius in a surrounding soil volume as the radius R_{95} within which 95 % of the detected thermal neutron signal originates. Accordingly, the radius inversely depends on the soil water content, described as $R_{95} \approx 53\,\mathrm{cm}$ for $\theta = 0.05\,\mathrm{cm^3\,cm^{-3}}$, or as $R_{95} \approx 20\,\mathrm{cm}$ for $\theta = 0.35\,\mathrm{cm^3\,cm^{-3}}$. As a consequence, the measurement volume of the active neutron probe exceeds the integration volume of standard in situ point-scale sensors and allows for a more representative average soil moisture value at the depth of interest. However, a disadvantage of this method is the precautions that need to be taken when handling active radiation sources [e.g. IAEA - International Atomic Energy Agency, 1970; Gardner, 1986] as well as the typically non-continuous nature of snapshot measurement campaigns with active neutron probes.

Kodama et al. [1985] observed the response of cosmic-ray neutrons to changes in soil moisture at depths down to 40 cm, largely covering the sensitive measurement depth of above-ground CRNS. Against this background, we investigate the possibility of using CRNS as a passive downhole technique (d-CRNS) to estimate soil moisture at different depths below 40 cm, also including the deeper unsaturated zone. For this, we installed CRNS neutron detectors in a standard groundwater observation well, thereby using the well casing above the groundwater level as an access tube.

We hypothesise that a sufficient neutron intensity can be observed by a downhole neutron detector to measure neutron intensity changes caused by soil moisture dynamics at discrete soil depths, thereby, taking advantage of both the passive, non-invasive characteristics and continuous monitoring capabilities of CRNS as well as the decimetre-scale measurement volume of sub-surface active neutron probes. Using existing standard groundwater observation wells allows for the a multi-purpose use of existing observational infrastructure, as simultaneous groundwater level measurements remain undisturbed.

To test our hypotheses, we first conducted particle transport simulations using the Monte Carlo N-Particle (MCNP) particle transport code commonly employed in CRNS research [e.g. Zreda et al., 2008; Franz et al., 2012a; Andreasen et al., 2016, 2017b; Weimar et al., 2020; Köhli et al., 2021, among others] to investigate the neutron flux at different soil depths. As we expect the neutron response to changes in moisture in the surrounding soil to be different compared with above-ground CRNS or the active neutron probe, we use the particle transport simulations to obtain information on the integration volume and to derive a transfer function from soil moisture to neutron intensities. In a second step, we compare the estimated neutron intensities calculated from reference soil moisture observations based on the derived transfer function with measurements of downhole neutron intensities at different depths. Finally, we illustrate the potential of passive downhole Cosmic-Ray Neutron Sensing for the estimation of soil moisture in the vadose zone.

5.3 Material and methods

5.3.1 Study site

The study site comprises the permanent CRNS observation site „Serrahn“ [Bogena et al., 2022], located in the Müritz National Park in the lowlands of north-eastern Germany (Fig. 5.1). The site is of one of three permanently operating CRNS stations [Heidbüchel et al., 2016; Rasche et al., 2021] in the Terrestrial Environmental Observatories TERENO-NE [Zacharias et al., 2011; Heinrich et al., 2018]. The observatory is located in the cfb climatic zone following the Köppen-Geiger classification [Bogena et al., 2022], with an average annual temperature of 8.8°C and a precipitation sum of 591 mm yr^{-1} at the closest long-term weather station in Waren (at a distance of approximately 35 km) operated by the German Weather Service [station ID: 5349; period 1981–2010; DWD - German Weather Service, 2020a,b].

The study site is located on a glacial terminal moraine formed during the Pomeranian phase of the Weichselian glaciation in the Pleistocene [Börner, 2015]. The sedimentological profile obtained during the drilling of an on-site groundwater observation well (Fig. 5.2) with a total depth of 24 m revealed an uppermost layer of

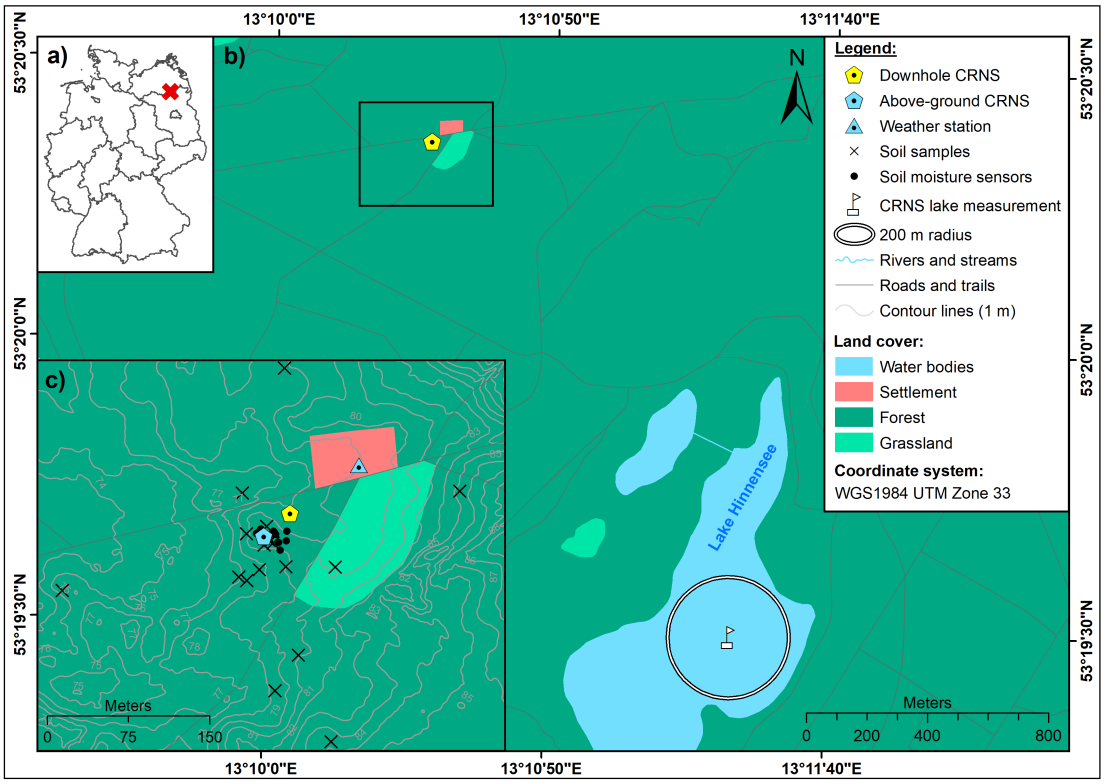

Figure 5.1: Panel (a) presents the location of the study area within Germany, panel (b) shows the location of the study site in relation to the reference lake measurement site and panel (c) displays the details of the CRNS observation site „Serrahn“ where the field experiment took place. The digital elevation model was sourced from LAIV-MV - State Agency for Interior Administration Mecklenburg-Western Pomerania [2011], and land cover was taken from BKG - German Federal Agency for Cartography and Geodesy [2018a]).

aeolian sands deposited during the Holocene reaching a depth of 450 cm followed by a 400 cm thick layer of glacial till which can be attributed to the geological unit of the terminal moraine. From a depth of 850 cm, a layer of glacio-fluvial coarse sands containing fine gravel components extend downward until they reach the glacial till deposited during an earlier phase of the Weichselian glaciation. Regular measurements show a variation in the groundwater level of between 13 and 14 m below the surface. Soil samples collected in the scope of the calibration of the permanent CRNS sensor Serrahn in February 2019 were taken in order to determine the soil physical characteristics, such as average grain size distributions, soil organic matter and lattice water, via laboratory analyses, as shown in Tab. 5.1. Soil organic matter and lattice water contents were obtained from subsamples of bulk samples from all sample locations per depth using 24 h loss-on-ignition analyses at 550 and 1000°C, respectively. Based on the average bulk density at 0–35 cm in the upper soil layer and at 35 cm depth as the representative value for greater depths, soil water contents at field capacity and wilting point were derived for medium fine sand from tabulated values [Sponagel et al., 2005]. Accordingly, 0.16 and 0.06 $cm^3\,cm^{-3}$ for the upper layer and 0.12 and 0.04 $cm^3\,cm^{-3}$ for greater depths were derived for the soil water content at field capacity and wilting point, respectively. Similarly, the soil porosity

was estimated based on the material density of quartz ($2.65\,\mathrm{g\,cm^{-3}}$) and corrected for the amount of soil organic matter based on the density of cellulose ($1.5\,\mathrm{g\,cm^{-3}}$). Consequently, we derived a porosity of 0.52 and $0.38\,\mathrm{cm^3\,cm^{-3}}$ for the upper soil layer and below depths of 35 cm, respectively.

Table 5.1: Soil physical characteristics obtained from laboratory analyses of soil samples taken in February 2019. Soil bulk densities per depth were obtained from oven-drying soil core samples at 105°C for 12 h and subsequent averaging.

Depth (cm)	Grain size (weight %)					Bulk density ($\mathrm{g\,cm^{-3}}$)	Organic matter ($\mathrm{g\,g^{-1}}$)	Lattice water ($\mathrm{g\,g^{-1}}$)
	> 2 mm	2 - 0.63 mm	0.63 - 0.2 mm	0.2 - 0.063 mm	< 0.063 mm			
0–5	2.7	19.7	42.2	33.7	2.1	0.24	0.32	0.003
5–10	1.1	8.7	43.5	45.7	2.4	0.77	0.10	0.002
10–15	0.7	7.2	41.5	47.9	2.8	1.25	0.05	0.002
15–20	1.2	7.8	38.7	44.3	2.2	1.43	0.02	0.002
20–25	1.7	7.7	42.2	46.5	2.2	1.55	0.02	0.002
25–30	1.7	8.5	43.5	45.4	1.2	1.59	0.01	0.002
30–35	1.1	8.0	42.8	46.8	1.5	1.63	0.01	0.002

The land cover at the site is mainly a mixed forest dominated by European beech (*Fagus sylvatica*) and Scots pine (*Pinus sylvestris*) with a clearing covered by grassy vegetation located a few decametres from the neutron detector. A vegetation survey was conducted in July 2021 in order estimate the total above-ground biomass at the site. Using allometric regressions for *Pinus sylvestris* [Urban et al., 2014] and *Fagus sylvatica* [Chakraborty et al., 2016] revealed a total wet above-ground biomass estimate of $3.73\,\mathrm{g\,cm^{-2}}$, assuming that other sources of biomass can be neglected.

Along with the stationary CRNS instruments and the groundwater observation well, the study site is equipped with a weather station and a network of in situ point-scale soil moisture sensor profiles (type SMT100; Truebner GmbH, Germany). The soil moisture sensors are installed at depths down to 450 cm along the profiles displayed in Tab. 5.3 and continuously monitor the volumetric soil moisture based on the manufacturer's calibration function. The measurement interval is 10 minutes. The soil moisture profiles are located close to the CRNS instruments and at a distance of 20–40 m from the groundwater observation well (Fig. 5.1).

5.3.2 Experimental design

In the scope of this study, we deployed a gaseous proportional neutron detector of the type CRS1000 (Hydroinnova LCC, USA) inside the on-site groundwater observation well. The detector uses ^{3}He as the converter gas [see Zreda et al., 2012; Schrön et al., 2018b, for details]. We disassembled the original set-up and placed two unshielded counter tubes into 50 cm long polypropylene pipes with a wall thickness of 1.9 mm. The relative air humidity in closed groundwater observation wells is constantly close to saturation, making such additional protection of the counter tubes necessary. For the downhole measurements, the CRS1000 counter tubes as well as their readout electronics were lowered into the well to the desired measurement depths by steel ropes. The data logger with its direct-current (DC) power supply remains above the surface.

As shown in the schematic illustration in Fig. 5.2, the groundwater well itself is composed of an aluminium tube above the surface that is mounted to a small concrete foundation, whereas the below-ground tube is made of 7.5 mm thick PVC (polyvinyl chloride) with an inner diameter of 11 mm. An approximately 100 mm

wide gap between the surrounding undisturbed sediment and the well tube was filled with sand and clay (see Fig. 5.2), depending on the surrounding material, during the installation of the groundwater well in 2014. The presence of filling material as well as the PVC tube material may reduce the response of the sensor to changes in the soil moisture of the surrounding undisturbed soil due to, for example, the high absorption cross section of chlorine and scattering cross section of hydrogen contained in the PVC material. Although some influence on the neutron signal has been described for the active neutron probe [e.g. Keller et al., 1990], the precise influence of both remains unknown for the d-CRNS approach. Following the assumption that the soil moisture dynamics in the porous filling material are similar to those in the surrounding undisturbed material and the sphere of influence largely exceeds the volume of the filling material, we expect the soil moisture signal to dominate the dynamics in the downhole neutron intensity.

Above-ground CRNS relies on epithermal neutrons counted by moderated detector tubes shielded with a 2.5 cm layer of high-density polyethylene (HDPE). In the scope of d-CRNS, we use thermal neutrons counted from unshielded detectors. This is done for different reasons. Firstly, thermal neutrons respond to changes in environmental hydrogen content and, thus, soil moisture [e.g. Hubert et al., 2016; Weimar et al., 2020; Rasche et al., 2021]. Secondly, we expect the neutron intensity (i.e. count rate) to decrease strongly with soil depth. A bare counter tube is then more effective, as the HDPE shielding of a moderated tube would not only slow down but would also reflect a certain percentage of potentially countable neutrons away from the instrument and would, thus, reduce the observed intensity. Furthermore, it has been shown that thermal neutrons can potentially be used to obtain soil moisture information from larger depths compared with epithermal neutrons [Rasche et al., 2021]. This may be especially useful for downhole measurements in order to increase the potential measurement radius. Lastly, using unshielded detector tubes is of a practical nature, as the removal of the 2.5 cm HDPE shielding reduces the weight and dimensions of the CRS1000 counter tubes, allowing them to fit into standard groundwater well tubes with an inner diameter of 11 cm.

5.3.3 Neutron measurements and processing

The counter tubes simultaneously measured neutron intensities at 100 cm (tube no. 2) and 200 cm (tube no. 1) depths from July 2021 to November 2021 from January 2022 to May 2022. In between these two periods, the detectors were placed at 500 cm (tube no. 2) and 1000 cm (tube no. 1) depths.

Following conventional approaches, the observed above-ground epithermal neutron intensities were corrected for variations in atmospheric shielding depth, absolute air humidity and primary neutron flux [Zreda et al., 2012; Rosolem et al., 2013] before being smoothed by a 25 h and 49 h moving average in order to reduce the uncertainty in the time series [Schrön et al., 2018b]. For downhole CRNS applications measuring thermal neutrons, an adjusted correction algorithm for the neutron signal is required. Thermal neutrons detected by a downhole CRNS have not interacted with the atmosphere from the point where they reach water-sensitive energies in the soil to eventually reaching the detector. As a consequence, downhole thermal neutron intensities will be corrected for variations in atmospheric shielding depth and primary neutron influx only. In accordance with Heidbüchel et al. [2016], the

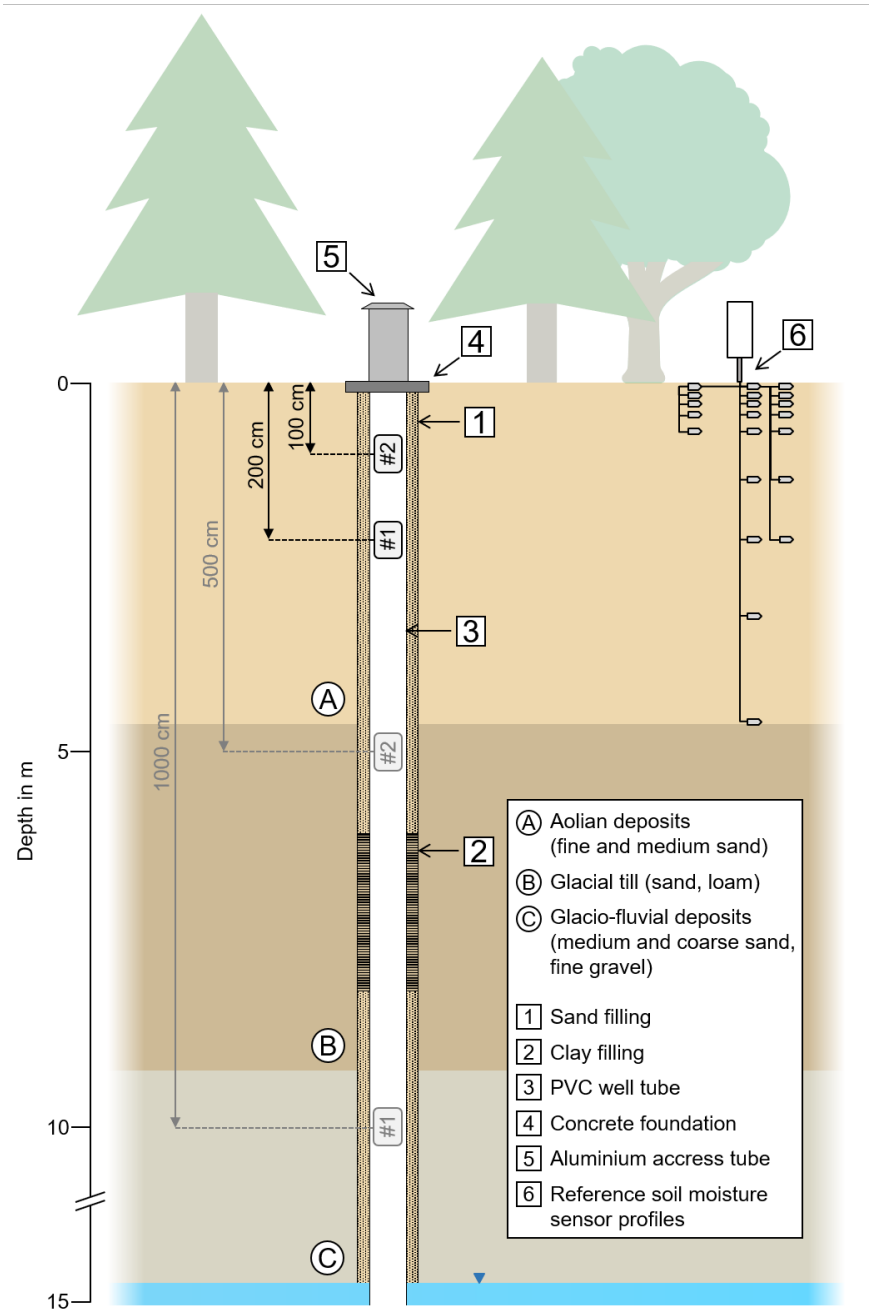

Figure 5.2: Schematic illustration of the experimental set-up at the study site. The thermal (unshielded) neutron detectors no. 1 and no. 2 were simultaneously installed at respective depths of 200 and 100 cm from July to November 2021 and from January to May 2022 and at respective depths of 1000 and 500 cm for the time period in between.

required neutron attenuation length was set to 135.9 g cm^{-2} for the study site. The neutron monitor database (`www.nmdb.eu`, station: JUNG - Jungfraujoch) was used to obtain data for the primary neutron flux.

To convert above-ground neutron intensities to soil moisture estimates, a calibration against soil moisture reference measurements is necessary in order to scale the transfer function to possible site-specific characteristics. This is the case for the N0

method [Desilets et al., 2010], as well as for the recently introduced universal transport solution (UTS) [Köhli et al., 2021]. Reference soil moisture measurements can be obtained at shallow depths from soil sampling and subsequent laboratory analysis or from point-scale in situ soil moisture sensors. However, using a CRNS detector as a downhole instrument would require reference measurements from greater depths, which are more difficult to acquire. For this reason, we decided to adapt an approach proposed by Franz et al. [2013b] for above-ground CRNS applications using epithermal neutrons. It comprises scaling the transfer function by the neutron intensity measured above water instead of above dry soil, as is the case for the N0 method. The count rate above dry soil can be calibrated with reference soil moisture information; however, without this reference information the count rate above dry soil needs to be measured in order to transfer observed neutron count rates to soil moisture. Measuring neutrons above an (ideal) hydrogen-free soil is practically impossible, whereas the intensity above water can be measured directly and, thus, does not require additional calibration. This approach has been applied in previous studies related to above-ground epithermal CRNS [e.g. McJannet et al., 2014; Andreasen et al., 2016, 2020]. We adjusted the approach of above-water measurements for the scaling of thermal neutrons. Therefore, a measurement at 25 cm (detector bottom) above the water surface and of 1.5 h duration was conducted with the two detector tubes on Lake Hinnensee prior to their installation below the ground (Fig. 5.1). By scaling the downhole neutron intensities with the detector-specific neutron intensity above water by calculating the neutron ratios, Eq. (5.1) allows for the comparison of observed neutron ratios with simulated neutron ratios. Furthermore, it enables the development of a transfer function from simulations that may be applied without additional calibration against reference soil moisture measurements.

Unlike the measurements below the ground, the neutron intensity above water needs to be corrected for variations in absolute air humidity. A specific humidity correction function has been developed for epithermal neutrons only [Rosolem et al., 2013; Köhli et al., 2021] and may not be valid for thermal neutrons. For this reason, we developed a first equation to correct thermal neutron intensities observed above water to variations in absolute humidity. The observed neutron ratio N_r,

$$N_\mathrm{r} = \frac{N_\mathrm{s}}{N_\mathrm{w}} \tag{5.1}$$

can then be calculated from the downhole thermal neutron intensity N_s corrected for variations in atmospheric shielding depth and primary neutron influx only as well as the thermal neutron intensity above water N_w corrected for variations in atmospheric shielding depth, primary neutron influx and absolute humidity.

5.3.4 Particle transport simulations

Several different Monte Carlo-based particle transport simulation toolkits have previously been used for the investigation of secondary cosmic-ray neutrons at the soil-atmosphere interface in the context of CRNS, including GEANT4 [Hubert et al., 2016; Brall et al., 2021], MCNP [Zreda et al., 2008; Franz et al., 2012a; Andreasen et al., 2016, 2017b; Weimar et al., 2020; Köhli et al., 2021] and URANOS [Köhli et al., 2015, 2021; Li et al., 2019a; Rasche et al., 2021], the latter of which only simulates neutrons of different energies. Although simulating only neutrons (and

not including protons and muons) might be sufficient at the soil-atmosphere interface with a detector placed above the surface, the simulation of the neutron flux at different depths of the soil requires the inclusion of several other types of particles that may induce neutron production in the deeper soil volume. As the atmospheric neutron flux is attenuated strongly within the soil volume, the in-soil neutron production dominates the thermal neutron flux below soil depths several decimetres. In-soil neutrons are generated by different cosmic-ray particle species depending on the soil depth. Within the first few metres, the inelastic collisions of high-energy protons and neutrons with atomic nuclei lead to particle production in hadronic showers [e.g. Mollerach and Roulet, 2018]. During the collision, neutrons are ejected from the nucleus with energies peaking at few hundred megaelectron volts [e.g. Gudima et al., 1983]. The target nucleus remains in an excited state after the impact and deexcites via the emission of lower-energy neutrons with few megaelectron volts. This process is called evaporation. The hadrogenic neutron production falls off rapidly with soil depth due to the short penetration length of high-energy neutrons and protons. Below that and down to several tens of metres, hadrogenic neutron production is significantly lower and is dominated by muons [Heusser, 1996] via capture processes that release neutrons with few megaelectron volts. Consequently, we used the MCNP v6.2 model [Werner et al., 2018] to simulate the neutron ratios for different soil depths and soil bulk densities, as this model includes, for example, protons, muons and neutrons as source particles within the model domain. Energy spectra and angular distributions of the particle species were set according to Sato [2015] and Sato [2016]. The starting particles are released 450 m above the soil surface embedded in a cylindrical simulation domain with 6 m radius and reflecting boundaries.

All simulation scenarios described in the following comprise a cutoff rigidity of 2.6 GV, an absolute humidity of $10\,\mathrm{g\,m^{-3}}$ and an atmospheric pressure of 1013.25 hPa. The detector has a length of 50 cm and diameter of 5.5 cm. The tube volume is filled with ^{3}He at 1.5 bar, and all neutrons are counted that undergo an absorption process in the simulated detector volume. Thus, the behaviour of an unshielded (bare) proportional neutron detector tube is modelled.

In a first step, the detector was placed 50 cm above an infinite water surface, with the 50 cm being measured from the detector tube centre. The detector volume is slightly larger than the real CRS1000 detector tubes in order to enhance the counting statistics in low-count environments. To estimate the influence of variations in absolute humidity on the thermal neutron intensity above water and in order to develop a correction function, the simulation scenario was repeated with air humidity values of 1, 6, 11, 16, 21 and $26\,\mathrm{g\,m^{-3}}$.

Neutron responses at different soil depths were modelled with a soil bulk density of $1.43\,\mathrm{g\,cm^{-3}}$ where the soil material is composed of 75 % SiO_2 and 25 % Al_2O_3. The detector was placed at shielding depths of 75, 100, 150, 200, 250, 300, 350, 400, 500, 750, 1000 and $1500\,\mathrm{g\,cm^{-2}}$ with 10 different soil moisture contents ranging from 0.005 to $0.5\,\mathrm{cm^3\,cm^{-3}}$. The shielding depth describes the total amount of matter that a particle has to travel trough. It is influenced by the material dry bulk density, the absolute depth in centimetres and the soil water content (Eq. (5.10)). In the simulation scenarios, the absolute depth of the detector was changed for the different soil moisture states in order to maintain the same simulated shielding depth at the detector centre. In accordance with the set-up of the real groundwater observation

well, the virtual detector was placed in a PVC cylinder of the same dimensions. To investigate the influence of the local soil bulk density on the simulated neutron response, a smaller subset of scenarios for all soil moisture states with the shielding depths of 75, 100, 200, 350, and 500 g cm^{-2} were additionally modelled with soil bulk densities of 1.1 and 1.8 g cm^{-3}.

In order to assess the sphere of influence for the downhole neutron detector, particle tracking simulations for a single shielding depth of 300 g cm^{-2} and all soil moisture conditions listed above were run. The trajectory of all detected neutrons is traced backwards in order to determine the locations where they probed the soil via scattering. Above 150–200 g cm^{-2} an increase in the measurement volume can be expected due to an increased contribution from neutrons that previously scattered in the atmospheric layer before entering the soil and eventually being detected. Using the simulations with 300 g cm^{-2} allows for the isolated characterisation of the measurement volume without the influence of neutrons that previously interacted with the atmosphere. In the scope of this study, the dimensions of the measurement volume are estimated based on the locations of all elastic scattering processes above the thermal energy regime and, thus, the entire moderation process from the point where a detected neutron was generated.

To assess the influence of the well tube material on the neutron ratio as well as on the dimensions of the sphere of influence, we not only simulated a PVC well tube with a wall thickness of 7.5 mm but also a well tube composed of stainless steel of equal wall thickness and a well tube composed of thinner PVC. The additionally simulated PVC material had wall thickness of 5 mm and a density of 1.44 g cm^{-3}, and the steel tube (type X5CrNi18-10) had a wall thickness of 7.5 mm, a density of 7.85 g cm^{-3}, and contained 18 % chromium and 10 % nickel. Particle transport simulations with a shielding depth of 300 g cm^{-2} were run to investigate the size of the measurement volume for stainless steel, and the neutron ratios were simulated for a soil bulk density of 1.43 g cm^{-3} and shielding depths from 100 to 400 g cm^{-2}.

5.4 Results

5.4.1 MCNP simulations

Neutron ratio response and sphere of influence

We simulated the detector-specific neutron intensity above water to aid with processing the downhole neutron intensities without the need for calibration based on in situ soil moisture information. The simulation revealed a dependence of thermal neutrons detected above water on absolute air humidity. The thermal neutron intensity decreased approximately linearly by 0.21 % per 1 g m^{-3} absolute humidity ($R^2 = 0.93$), which is less than half of what has been reported for epithermal neutrons [Rosolem et al., 2013]. The correction function developed by Rosolem et al. [2013] for epithermal neutrons can, thus, be adjusted to correcting observed thermal neutron intensities above water by changing the correction factor from the original 0.0054 to the derived 0.0021. It should be noted that the reference absolute humidity for the simulations and the transfer functions was set to an arbitrary 10 g cm^{-3}.

Neutron ratios were calculated for all neutron transport simulations using the reference simulation scenario with the detector placed above a water surface. The

simulation results for the first set of scenarios conducted with a soil bulk density of 1.43 g cm^{-3} are shown in Fig. 5.3. The response of the simulated neutron ratios observed by the virtual downhole neutron detector to changes in soil moisture differ between the different simulated shielding depths, with generally lower neutron ratios at larger depths. For each simulated shielding depth, the neutron ratio decreases with increasing soil moisture, although a specific behaviour can be observed for shallow shielding depths. From the 75 to the 100 g cm^{-2} shielding depth scenario, the simulated neutron ratio increases, i.e. the neutron intensity observed by the downhole neutron detector increases, when the soil moisture content is below 0.045 cm^3 cm^{-3}. This reveals a peak neutron intensity in shallow soil layers under low-soil-moisture conditions. At higher soil moisture contents, this peak ratio disappears and a continuous decrease in the neutron ratio with increasing shielding depth per simulated soil moisture content can be observed. The simulation sets conducted with lower (1.1 g cm^{-3}) and higher (1.8 g cm^{-3}) soil bulk densities show a similar behaviour, although the absolute values of the neutron ratios change. Higher soil bulk densities result in lower neutron intensities and, thus, lower neutron ratios observed by the virtual downhole neutron detector and vice versa (see section 5.4.1 for details). We also investigated the possible influences of the groundwater observation well tube material by simulating a 5 mm PVC and 7.5 mm stainless-steel tubing. The additional subset of simulations revealed that neutron ratios for a well tube composed of stainless steel are on average 60 % higher compared with a PVC tube with equal wall thickness but the two materials respond similarly to changes in soil moisture. In addition, a thinner PVC material with a thickness of only 5 mm produces neutron ratios which are on average 28 % higher compared with a PVC tubing with a wall thickness of 7.5 mm.

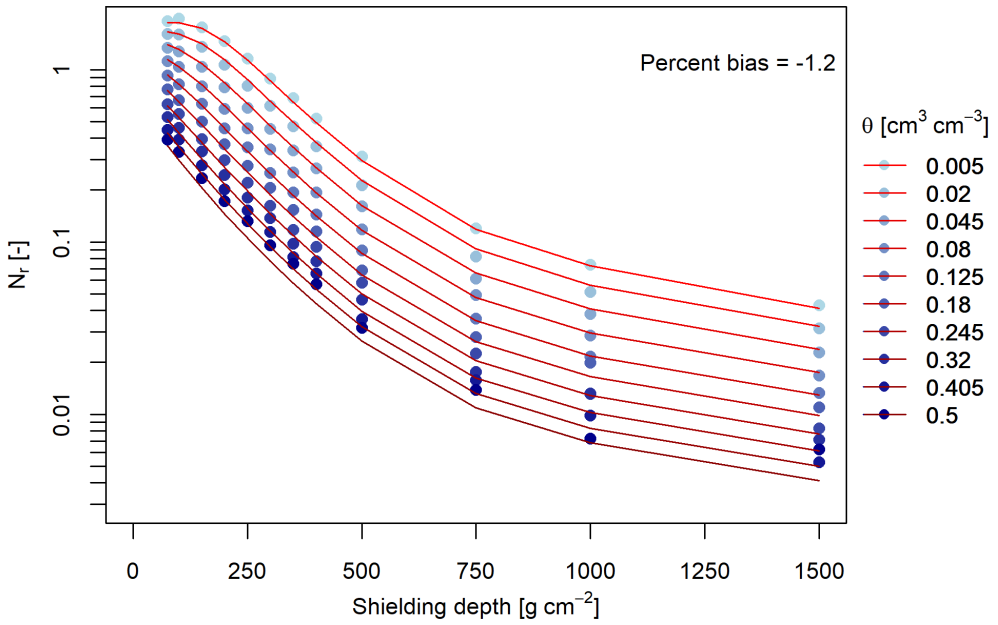

Figure 5.3: Simulated values of N_r from neutron transport modelling with the predicted values (red lines) from Eq. (5.5-5.10) for a soil bulk density of 1.43 g cm^{-3}, different soil moisture conditions and different shielding depths.

In this study, the sphere of influence, i.e. the measurement volume around the downhole neutron detector, is calculated as the 86 % quantile and 95 % quantile of all locations of elastic collision processes of a detected neutron in the soil. The definition based on the 86 % quantile relies on the convention established for describing the horizontal integration radius and integration depth of above-ground CRNS applications, whereas the 95 % quantile is common for active neutron probe applications. In order to better compare d-CRNS with above-ground CRNS and the traditional active neutron probe, the results of both definitions are shown in Fig. 5.4.

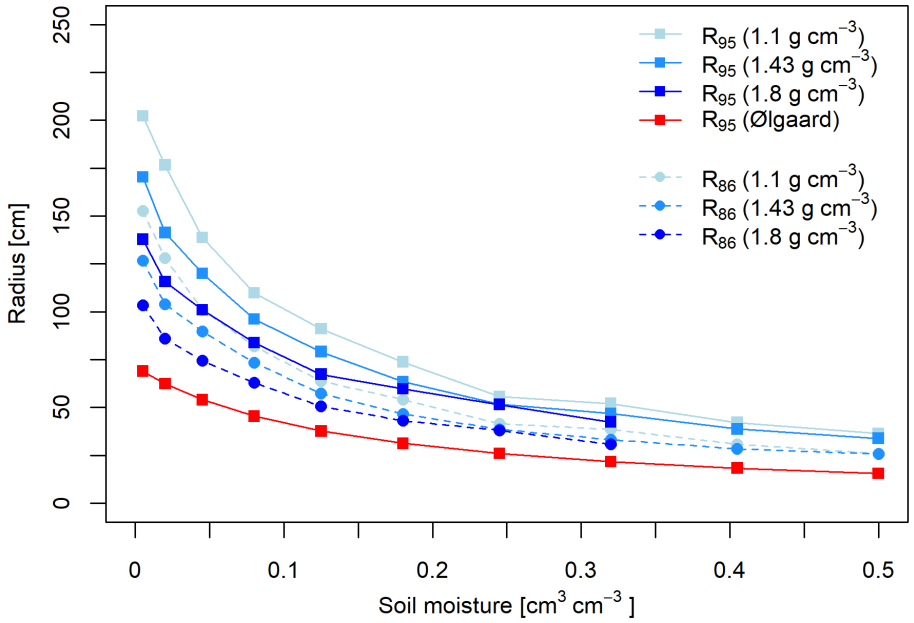

Figure 5.4: Simulated horizontal radii of the sphere of influence defined as the R_{86} and R_{95} for different local (at the depth of measurement) soil moisture values θ (see Eq. (5.9)) and soil bulk densities. In addition, the R_{95} values based on the equation of Ølgaard (1965) in Gardner [1986] for an active neutron probe are displayed for comparison.

In line with above-ground CRNS, only the 86 % quantile is used for a mathematical description of the sphere of influence and its dimensions. The shape of the sphere of influence simulated for a neutron detector with a height of 50 cm and diameter of 5.5 cm and for different soil moisture contents at a shielding depth of 300 g cm^{-2} measured at the detector centre can be described by the following equations. The horizontal sensitive radius of the sphere R_{86} can be described by the local soil moisture content θ (cm^3 cm^{-3}; see Eq. (5.9)) as well as the local soil bulk density ρ (g cm^{-3}) and the fitted parameters p_1 to p_3 (Tab. 5.2) at the depth of the neutron detector via

$$R_{86} = \frac{p_1}{(\rho/\,(\mathrm{g\,cm^{-3}})) \cdot (1 + p_2 \cdot \theta \cdot 100)} + p_3 \cdot \left(\rho/\left(\mathrm{g\,cm^{-3}}\right)\right)^{p_4}. \qquad (5.2)$$

The simulated horizontal radii of the sphere of influence defined as the R_{86} and R_{95},

are shown in Fig. 5.4 for different soil moisture values and soil bulk densities. Both R_{86} and R_{95} decrease with increasing soil moisture and show generally lower values when the soil bulk density is higher. For instance, a bulk density of $1.43\,\mathrm{g\,cm^{-3}}$ leads to an R_{95} of 170 cm at $0.005\,\mathrm{cm^3\,cm^{-3}}$ and to an R_{95} of 34 cm at $0.5\,\mathrm{cm^3\,cm^{-3}}$. At the same bulk density and for the same soil moisture values, R_{86} is generally smaller and decreases from 127 to 26 cm. The values derived from the Ølgaard (1965) equation in Gardner [1986] for the R_{95} of an active neutron probe reveal 69 and 16 cm at 0.005 and $0.5\,\mathrm{cm^3\,cm^{-3}}$ and, hence, smaller radii of the sphere of influence than for a downhole neutron detector for all simulated soil bulk densities and both R_{95} and R_{86}. Consequently, even for a high bulk density of $1.8\,\mathrm{g\,cm^{-3}}$, the generally smaller R_{86} of d-CRNS is approximately 40 % larger than the R_{95} of an active neutron probe.

The average vertical sensitive radius of the sphere of influence V_{86} can be described by Eq. (5.3) and has a size range of 89–24 cm from the lowest (0.005 $\mathrm{cm^3\,cm^{-3}}$) to the highest (0.5 $\mathrm{cm^3\,cm^{-3}}$) simulated soil moisture content at a $1.43\,\mathrm{g\,cm^{-3}}$ bulk density. In combination with the simulated horizontal radii, an ellipsoidal shape of the sphere of influence can be derived for a downhole neutron detector in d-CRNS applications, with R_{86} and V_{86} describing the ellipsoid's semi-axes from the detector centre. However, a vertical shift in the most sensitive area, i.e. the location of the largest horizontal radius relative to the detector centre with varying soil moisture, can be observed. This dimension is described by Eq. (5.4) and shown in Fig. 5.5. The vertical sensitive radius V_{86} increases with decreasing soil moisture, while the most sensitive region Vc_{86} is always located slightly above the detector centre and shifts upwards with lower soil water contents. For example, for a soil bulk density of $1.43\,\mathrm{g\,cm^{-3}}$, the most sensitive region of the downhole neutron detector Vc_{86} is located 5–20 cm (for 0.5–$0.005\,\mathrm{cm^3\,cm^{-3}}$ soil moisture content) above the detector centre. The fitted parameters p_1–p_5 required in Eq. (5.2), Eq. (5.3) and Eq. (5.4) can be found in Tab. 5.2, and a schematic illustration of the sphere of influence for different soil moisture contents can be found in Fig. 5.6. We define the vertical footprint size as

$$V_{86} = \frac{p_1}{(\rho/\,(\mathrm{g\,cm^{-3}}))^{p_2} \cdot (1 + p_3 \cdot \theta \cdot 100)} + p_4 \cdot \left(\rho/\left(\mathrm{g\,cm^{-3}}\right)\right)^{p_5}, \tag{5.3}$$

and the location of the most sensitive region above the detector centre as

$$Vc_{86} = \frac{p_1 \cdot \exp\left((-\theta \cdot 100)/p_2\right)}{(\rho/\,(\mathrm{g\,cm^{-3}}))} + p_3 \cdot \left(\rho/\left(\mathrm{g\,cm^{-3}}\right)\right)^{p_4}. \tag{5.4}$$

The simulation results for a well tube made from stainless steel with a wall thickness of 7.5 mm revealed similar dimensions of the sphere of influence to those derived for PVC with equal wall thickness. Averaged over the range of simulated soil moisture values and for a soil bulk density of $1.43\,\mathrm{g\,cm^{-3}}$, R_{86} is approximately 1.2 cm larger for a well tube made from PVC compared to the steel tube, whereas Vc_{86} and V_{86} are 8.2 cm and 4.5 cm smaller, respectively. The fitted parameters for a well tubing made from stainless steel can be found in Tab. 5.4.

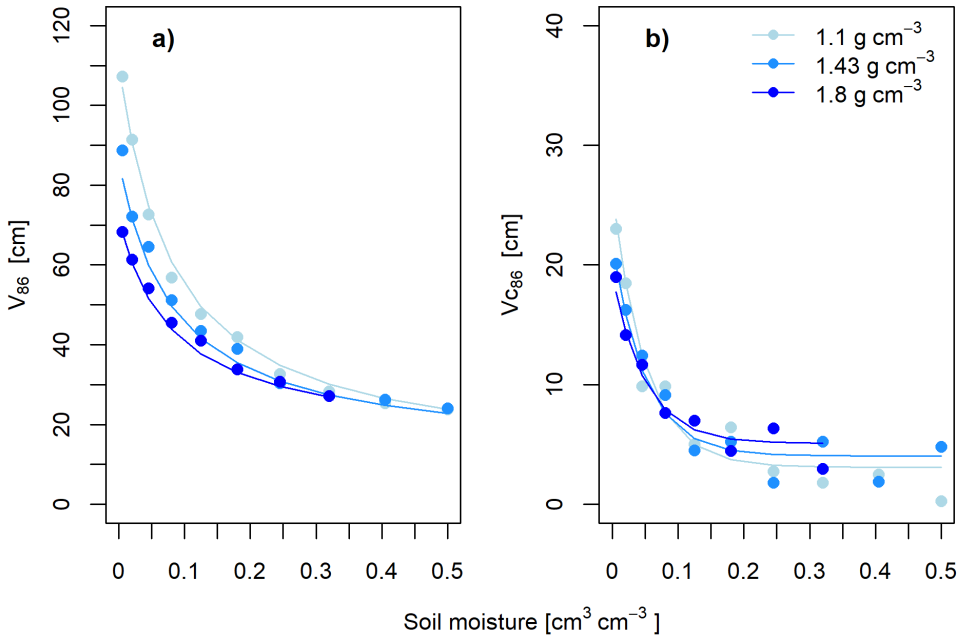

Figure 5.5: (a) Simulated values of the vertical sensitive radius V_{86} from the detector centre and (b) the position of the most sensitive area relative to the detector centre Vc_{86} for different local soil moisture values θ (see Eq. (5.9)) and soil bulk densities.

Predicting neutron ratios

Our neutron transport simulations revealed a change of the hyperbolic relationship between the neutron ratio N_r and the simulated soil moisture content depending on the shielding depth D measured at the centre of the detector tube (Fig. 5.3). Therefore, we derived a hyperbolic fit model with the analytical form of Eq. (5.5) for each shielding depth and subsequently predicted the shape-defining parameters F_1 and F_2 by shielding depth. A third-order and second-order exponential model resulted in a high goodness of fit for parameters F_1 and F_2, which lead to the following equations, allowing for the estimation of N_r:

$$N_\mathrm{r} = \frac{F_1}{F_2 + \theta}, \tag{5.5}$$

where (5.6)

$$F_1 = (p_1 \cdot \exp(p_2 \cdot \ D) + p_3 \cdot \exp(p_4 \cdot \ D) + p_5 \cdot \exp(p_6 \cdot \ D)) \cdot \frac{\rho}{1.43\,\mathrm{g\,cm^{-3}}}, \tag{5.7}$$

$$F_2 = (p_7 \cdot \exp(p_8 \cdot \ D) + p_9 \cdot \exp(p_{10} \cdot \ D)) \cdot \frac{\rho}{1.43\,\mathrm{g\,cm^{-3}}}. \tag{5.8}$$

The equation makes use of two key quantities, the local soil water content at the depth of measurement

$$\theta = \theta_\mathrm{SM} + \theta_\mathrm{SOM} + \theta_\mathrm{LW} \tag{5.9}$$

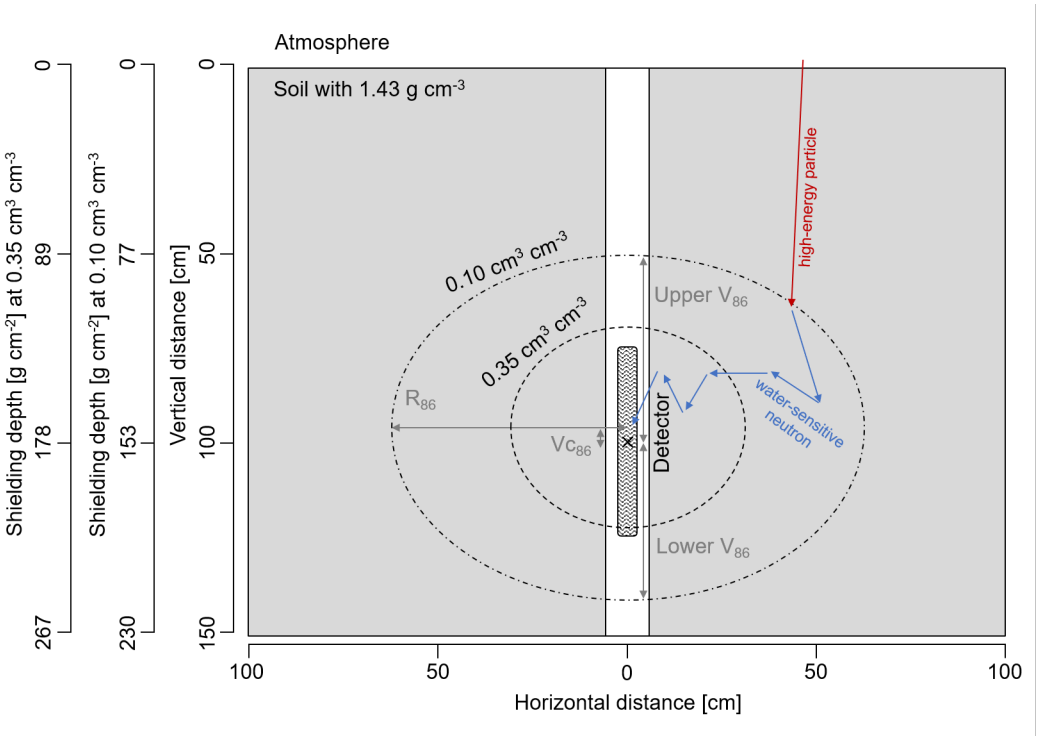

Figure 5.6: Schematic illustration of the sphere of influence described by R_{86}, Vc_{86} and V_{86} for a soil with a bulk density of 1.43 g cm^{-3} and a soil moisture content of 0.10 and 0.35 cm^3 cm^{-3} in the entire soil column. The V_{86} is different above (upper V_{86}) and below (lower V_{86}) the neutron detector (its centre is marked by an "here); thus, V_{86} represents the average vertical extent. A schematic neutron transport path is displayed with a high-energy particle producing a hydrogen-sensitive and, thus, water-sensitive neutron in the soil which is slowed down to thermal energies by multiple elastic scattering interactions before eventually being detected.

and the shielding depth

$$D = d \cdot \left(\hat{\rho} + \hat{\theta}_{\mathrm{SM}} \cdot \rho_{\mathrm{water}}\right) + D_{\mathrm{AGM}}. \tag{5.10}$$

The parameters and variables used in Equations (5.5)–(5.10) are explained in the following. The fitted parameters p_1–p_{10} can be found in Tab. 5.2 for a PVC well tube with a wall thickness of 7.5 mm, in Tab. 5.4 for a well tube composed of stainless steel of equal thickness and in Tab. 5.5 for a PVC well tube with a thickness of only 5 mm, while the following remaining variables depend on the conditions of the study site. The variable θ describes the total local water content comprising soil moisture θ_{SM}, lattice water θ_{LW} and the water equivalent of soil organic matter θ_{SOM} in (cm^3 cm^{-3}) at the depth of neutron observation measured as the distance from the soil surface to the centre of the detector tube d (in cm). Based on the subset of neutron transport simulations with different soil bulk densities, we found F_1 and F_2 to be dependent on the ratio between the density ρ at the depth of measurement and the soil density of 1.43 g cm^{-3} used in the simulations from which the equations were derived.

The second required variable is the shielding depth D, describing the total mass neutrons, protons and muons need to travel through before reaching the depth of the centre of the detector tube. The shielding depth represents the integral mass from the surface to the detector centre. Thus, it depends on the measurement depth d (in cm) as well as on the average soil bulk density $\hat{\rho}$ ($\mathrm{g\,cm^{-3}}$) from the soil surface to the measurement depth. Likewise, the average soil water content $\hat{\theta}_{\mathrm{SM}}$ ($\mathrm{cm^3\,cm^{-3}}$) is required, assuming a constant water density ρ_{water} of $1\,\mathrm{g\,cm^{-3}}$. It should be noted that for the calculation of the shielding depth, the total mass of material above the centre of the detector tube is required, regardless of its elemental composition. Thus, the mass of soil organic matter and lattice water is already accounted for by the integral soil bulk density. Additionally, as the study site of the present work is located in a mixed forest, the total above-ground mass (D_{AGM}) associated with vegetation needs to be added. Above-ground mass from other sources, such as snow, may also be considered and included in D_{AGM}. Furthermore, it should be noted that, in Eq. (5.5–5.8), the parameters p_2, p_4, p_6, p_8 and p_{10} are in square centimetres per gram (inverse shielding depth), whereas the remaining parameters p_1, p_3, p_5, p_7 and p_9 are dimensionless.

Applying the above equations (Eq. (5.5-5.10)) to the input variables of the neutron transport simulation and comparing this prediction with the simulated N_{r} shows a good overall fit, with a percent bias between the predicted and simulated values of -1.2 % for a bulk density of $1.43\,\mathrm{g\,cm^{-3}}$ (Fig. 5.3) and 0.8 % for all modelled densities.

Table 5.2: Fitted parameters for Eq. (5.2-5.8) derived from particle transport simulation scenarios for a PVC well tube with a wall thickness of 7.5 mm.

Eq. no.	Variable	p_1	p_2	p_3	p_4	p_5	p_6	p_7	p_8	p_9	p_{10}
(5.2)	R_{86}	173 cm	0.214	4.05 cm	2						
(5.3)	V_{86}	113 cm	1.2	0.121	8.61 cm	1					
(5.4)	Vc_{86}	25.2 cm	5	2.82 cm	1						
(5.7)	F_1	0.252	-0.0206 $\mathrm{cm^2\,g^{-1}}$	0.00794	-0.000839 $\mathrm{cm^2\,g^{-1}}$	0.267	-0.00674 $\mathrm{cm^2\,g^{-1}}$				
(5.8)	F_2							0.0406	0.000139 $\mathrm{cm^2\,g^{-1}}$	0.265	-0.0172 $\mathrm{cm^2\,g^{-1}}$

Estimating soil moisture

A key motivation of this study is to derive soil moisture time series by d-CRNS at depths larger than those accessible by surface CRNS. The equations above describe the physical relationships that influence the neutron intensity, and thus N_{r}, inside the shaft of the groundwater observation well or access tube. They illustrate that both the soil moisture at the local depth of the detector as well as the average soil moisture in the vadose zone above the detector have an effect on the N_{r} observed at a certain measurement depth. However, estimating two unknown variables, namely θ_{SM} and $\hat{\theta}_{\mathrm{SM}}$, from N_{r} (the single known variable) is only possible with further assumptions. One option would be the use of Eqs. (5.5-5.10) as a forward operator in combination with soil hydraulic models [e.g. HYDRUS-1D; Šimůnek et al., 2008] to model soil moisture time series at different soil depths. The model can then be calibrated by applying Eq. (5.5-5.10) with the modelled soil moisture time series and optimising the goodness of fit between the observed and predicted N_{r} by adjusting the parameters in the soil hydraulic model. However, soil hydraulic models may require further variables, such as rainfall, evapotranspiration and root distributions, which are not always available.

We propose an alternative and more simple approach to estimate the soil moisture time series at the depth of measurement from the observed neutron ratios by using Eq. (5.5-5.10). This approach is exemplary in that, while reasonable for the conditions of our study site, the assumed range of soil moisture between the wilting point and field capacity in Eq. (5.5-5.10) may need to be modified for other sites. Following these equations, the approach is based on the fact that the influence of θ_{SM} on N_r is considerably larger than that of $\hat{\theta}_{SM}$. For example, at a θ_{SM} of 0.1 $cm^3\,cm^{-3}$, a change in $\hat{\theta}_{SM}$ from 0.05 to 0.15 $cm^3\,cm^{-3}$ results in a 6 % change in N_r (at a measurement depth of 100 cm). In contrast, changing θ_{SM} from 0.05 to 0.15 $cm^3\,cm^{-3}$ at a value of 0.1 $cm^3\,cm^{-3}$ for $\hat{\theta}_{SM}$ leads to a 47 % change in N_r. The higher sensitivity of N_r to changes in the soil moisture content at depth of measurement allows for its estimation as described in appendix A.

5.4.2 Experimental evidence

Observed neutron response

The reference measurement at Lake Hinnensee was conducted in order to the derive the detector-specific raw count rate above water and resulted in values of 315 and 155 counts per hour (cph) for detector tube no. 1 and 2, respectively. The measurement duration of 1.5 h and measurement intervals of 1 min led to a Poisson standard deviation of 14 and 10 cph or a coefficient of variation of 4.6 and 6.6 %, respectively. The average uncorrected downhole neutron count rate was 101 cph for 100 cm (tube no. 2) and 70 cph for 200 cm (tube no. 1), covering the entire measurement period. During about two months of measurements at larger depths, the average count rate was significantly lower, with tube no. 2 observing 6 cph for 500 cm and tube no. 1 observing 11 cph for 1000 cm. As a result, the measurement uncertainty increased sharply. For instance, for an observed count rate of 10 cph, the coefficient of variation was 32 %.

N_r calculated based on the corrected neutron count rates decreases with increasing measurement and shielding depth (Fig. 5.7). The average N_r decreases from 0.63 for 100 cm and 0.22 for 200 cm to 0.039 for 500 cm and 0.034 for 1000 cm.

Figure 5.8 shows the comparison of the observed neutron intensity corrected for variations in air pressure and primary neutron influx N_s and the local in situ reference soil moisture at depths of 100 and 200 cm. Due to the location of all reference sensors outside the expected sphere of influence of the downhole neutron detector, a comparison with the soil moisture sensor at the respective depth showing the highest Pearson correlation coefficient between the observed and predicted values from a hyperbolic, non-linear least-squares-fit model in the form of Eq. (5.5) is shown. In case of the downhole neutron detector installed at 100 cm depth, the reference sensors with the highest and lowest goodness of fit in 70 and 130 cm are considered (due to the lack of sensors at 100cm depth), whereas reference soil moisture sensors at the same depth are available for the neutron detector at 200 cm depth. Figure 5.8 illustrates that a distinct neutron intensity response to changes in the local soil moisture following a hyperbolic relationship can be observed at both measurement depths. However, differences occur between the individual in situ reference sensors including distinct different slopes of the fitted hyperbolic regression model as well as larger deviations from the model fit, indicating different soil moisture dynamics

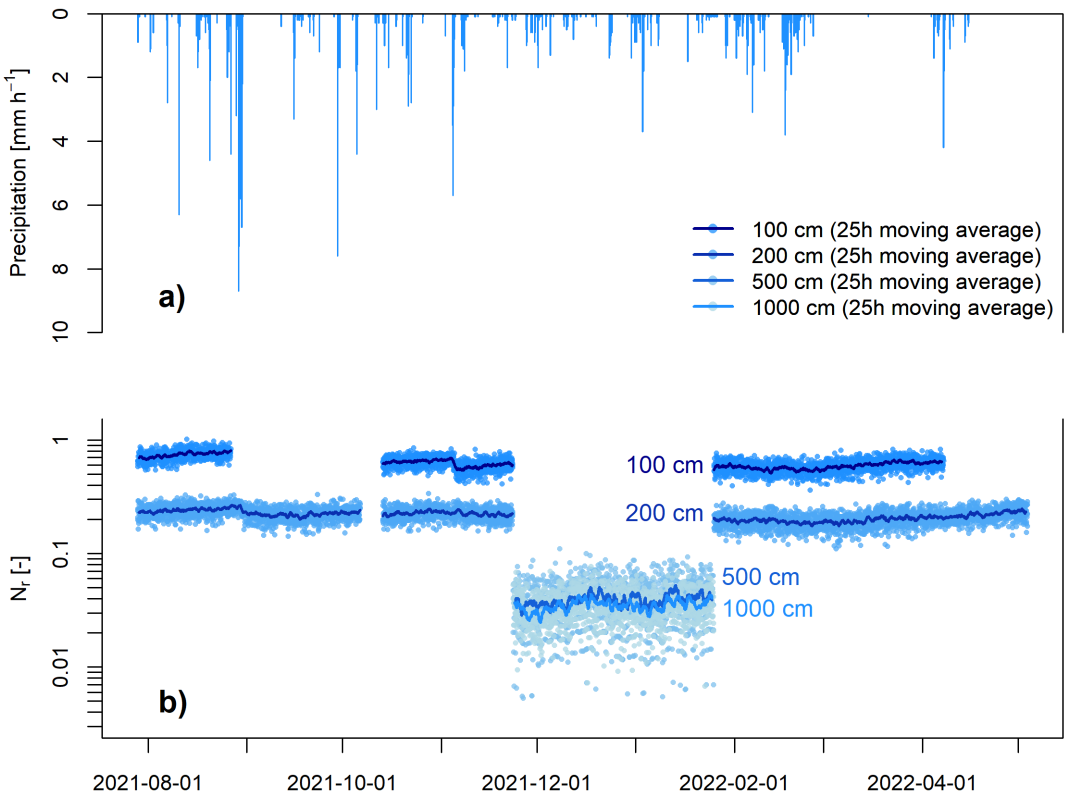

Figure 5.7: Panel (a) presents the hourly precipitation observed at the study site during the experimental period. Panel (b) shows observed time series of N_r in the different measurement depths of 100, 200, 500 and 1000 cm. Points represent the original (not smoothed) neutron ratios from corrected neutron intensities and lines represent the 25 h moving average calculated from corrected neutron intensities.

at the individual reference sensor locations.

Predicting neutron ratios from reference soil moisture observations

In order to provide experimental proof of the proposed downhole application of cosmic-ray thermal neutron sensing (d-CRNS), in a first step, observed soil moisture time series along the different reference sensor profiles are used to predict N_r based on Eqs. 5.5–5.10. Again, for the measurement depth of 100 cm, we include the sensor profiles with sensors down to depths of 70 and 130 cm, as there are no reference sensors available at the same measurement depth. For each sensor profile, the average soil moisture content is calculated from all sensors along the profile weighted by the depth range covered by each sensor down to the maximum depth of the respective sensor profile (70 and 130 cm) to calculate $\hat{\theta}_{SM}$. Additionally, the soil moisture time series from the sensors installed at depths of 70 and 130 cm are defined as θ_{SM} for each individual profile depending on the maximum profile depth. This leads to the set of predicted N_r time series shown in Fig. 5.9. The observed time series of N_r for the CRNS lies within the range of predicted N_r time series although the values observed at 100 cm depth are slightly shifted towards the range of the neutron ratios predicted from reference sensor profiles with a depth of 130 cm. Furthermore, the dynamics of the predicted neutron ratios from reference soil moisture

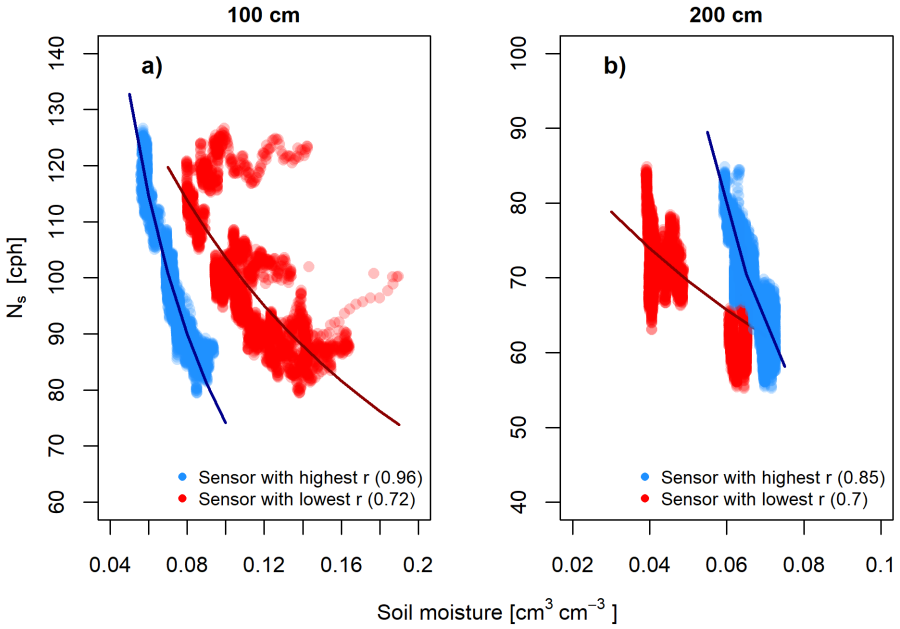

Figure 5.8: Comparison of the hourly corrected neutron intensity N_s smoothed with a 25 h moving average and values from the reference soil moisture sensors with the highest and lowest Pearson correlation coefficient (r) between the observed data and predicted data from a hyperbolic, non-linear least-squares-fit model in the form of Eq. (5.5). Panel (a) shows 100 cm depth and reference sensors at 70 and 130 cm depths, whereas panel (b) shows 200 cm depth with the corresponding reference soil moisture sensors also at 200 cm depth.

sensors match the dynamics of the CRNS-based values, which becomes especially visible during the rainfall event at the beginning of November 2021 (Fig. 5.11) as well as during the period in March 2022 when very little rainfall was observed. The latter led to a decrease in soil moisture and, hence, an increase in the observed N_r. Additionally, the short-term neutron ratio variations in the observed time series N_r are strongly reduced when the time series is smoothed with a 49 h moving average compared with a 25 h moving average that better corresponds to the N_r time series calculated from reference soil moisture sensors.

Similarly, a set of N_r time series is calculated from the available reference soil moisture sensor profiles with sensors at depths down to 200 cm and 450 cm. At a measurement depth of 200 cm reference measurements are available at the exact depth of the detector tube location, whereas the neutron ratios observed at 500 cm are compared to those predicted from sensor profiles with a maximum sensor depth of 450 cm. Fig. 5.9c shows the observed and predicted time series of N_r at 200 cm. The temporal dynamics of the predicted N_r time series are smaller than those predicted from soil moisture sensors at shallower depths. This matches the dynamics of the observed N_r; however, stronger short-term fluctuations become more visible here. Although the dynamics are dampened in both the observed and the different predicted N_r time series, the soil moisture increase caused by the intense rainfall event in late August 2021 is clearly visible (Fig. 5.12). In contrast, the predicted N_r time series from soil moisture sensors down to 450 cm depth do not show any

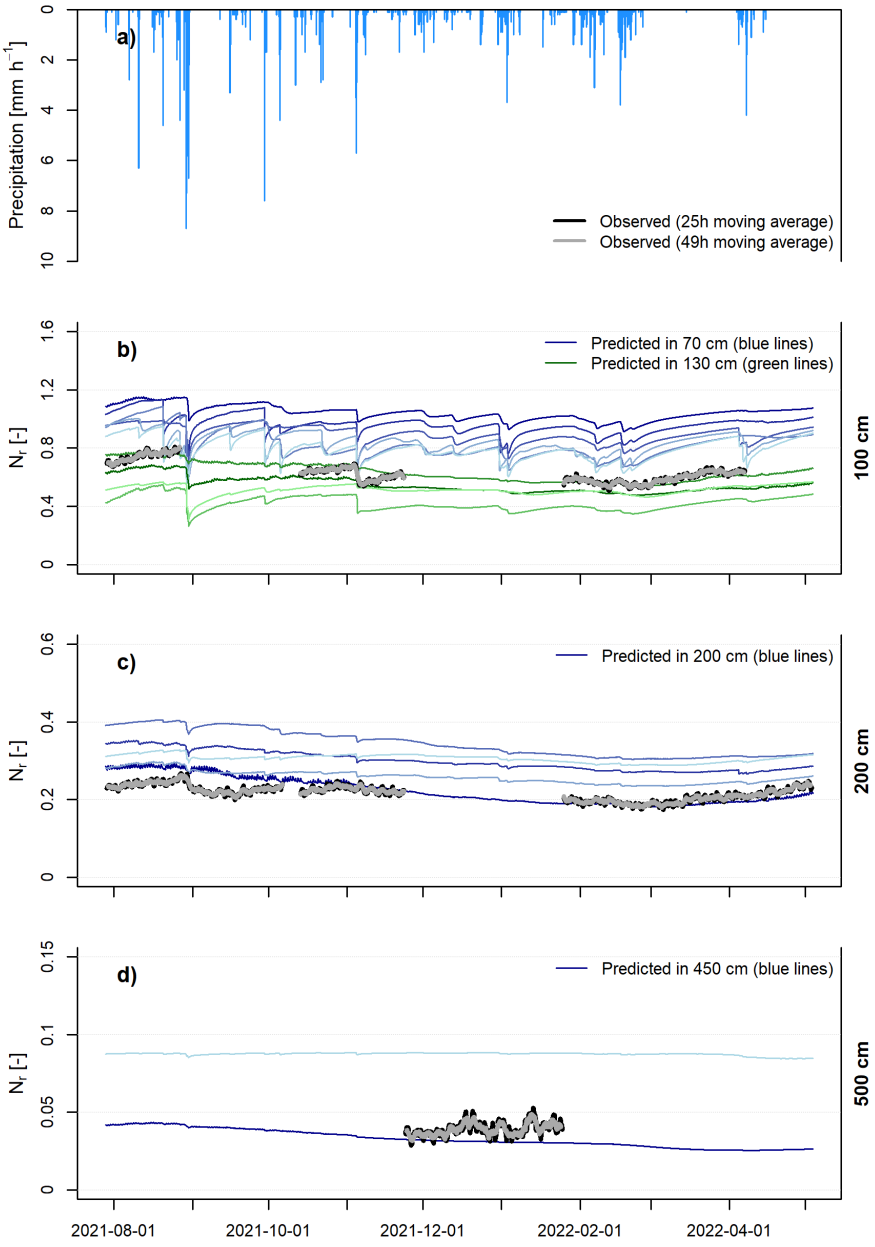

Figure 5.9: Panel (a) shows the hourly precipitation observed at the study site during the experiment. Panels (b)-(d) present the observed (by CRNS detector at 100, 200 and 500 cm depth) and predicted (based on reference soil moisture measurements at similar depths) time series of N_r. The different times series of the predicted N_r at each depth represent the results for every individual soil moisture sensor at that depth (θ_{SM}) and the average from the associated sensor profile from the soil surface to the depth of the CRNS ($\hat{\theta}_{SM}$).

dynamics over the measurement period (Fig. 5.9d). However, despite the short-term fluctuations visible in the observed neutron ratio, no trend can be observed, which is in line with the predicted values of N_r. In both measurement depths of 200 cm and 500 cm, the observed time series of N_r largely lie within the set of time series predicted with different reference soil moisture sensor profiles.

Estimating soil moisture from neutron ratio observations

The soil moisture time series of θ_{SM} derived from the observed N_r at depths of 100 and 200 cm are shown in Fig. 5.10. The estimated soil moisture time series follow the general dynamics of the reference values of θ_{SM} at both depths. During the observed intense precipitation events in August and November 2021, θ_{SM} at both 100 and 200 cm depth shows a distinct increase, which can also be seen in the soil moisture time series observed by the reference sensors. Similarly, the dry period in March 2022 results in a decrease in soil moisture, as indicated by θ_{SM} estimated from N_r at depths of 100 and 200 cm as well as by the in situ reference sensors at the respective depths. While the absolute values of θ_{SM} at 100 cm depth lie in the range of observed soil moisture values from the different in situ reference sensors available, the values of θ_{SM} at 200 cm depth are at the upper end of the set of time series of reference sensors.

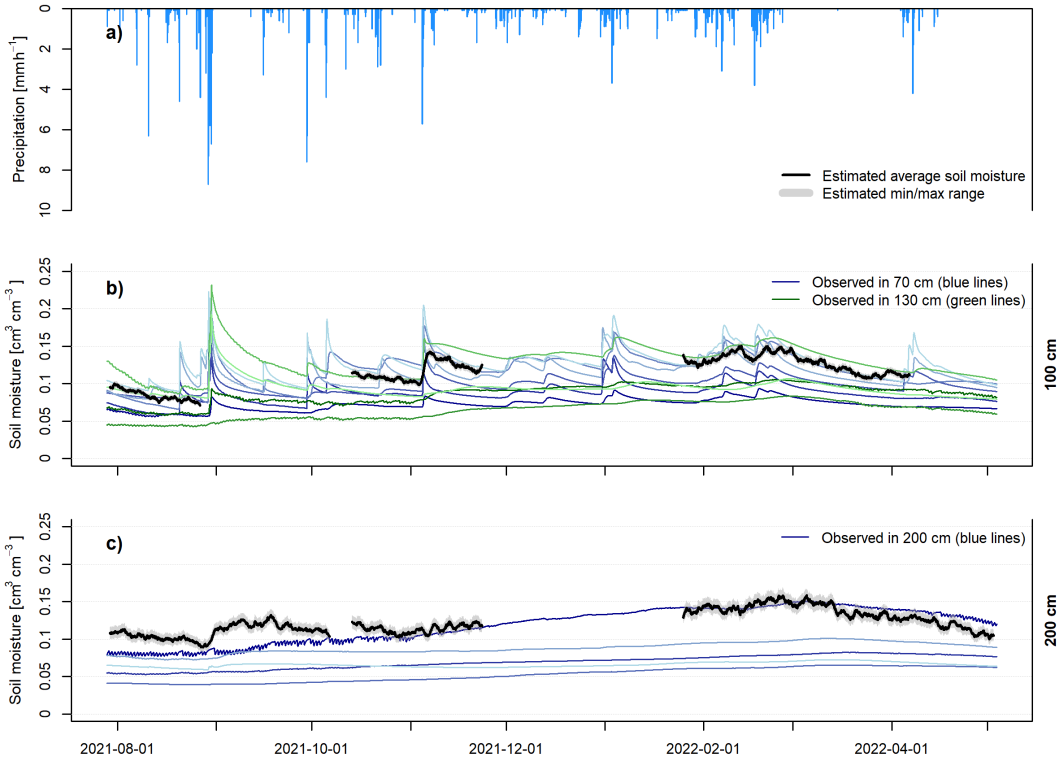

Figure 5.10: The observed time series of θ_{SM} from reference soil moisture sensor profiles and estimated time series of θ_{SM} from N_r. The different colours indicate the observed time series from individual reference sensors at the respective depths. At both depths, corrected neutron intensities were smoothed with a 49 h moving average prior to calculating N_r and subsequently estimating soil moisture. Panel (a) shows th hourly precipitation observed at the study site during the experiment. Panel (b) presents θ_{SM} from reference soil moisture sensors at 70 and 130 cm depth and estimated time series of θ_{SM} at 100 cm depth. Panel (c) displays θ_{SM} from reference soil moisture sensors and estimated time series of θ_{SM} from N_r at 200 cm depth.

5.5 Discussion

5.5.1 Feasibility assessment

The particle transport simulations conducted within the scope of this study revealed a distinct relationship of the neutron ratio (N_r) with the local soil moisture content as well as with the shielding depth. As a consequence, changes in both the local soil moisture content at the depth of measurement and in the average soil moisture content above the detector (due to its contribution to the shielding depth) alter the neutron intensity and, thus, N_r observed by a downhole neutron detector. This illustrates the general possibility of deriving soil moisture information from N_r observed in the scope of d-CRNS.

Before neutron ratios can be calculated from downhole neutron intensities and from neutron intensities observed with the same detector above a water surface, the latter need to be corrected for variations in absolute humidity. The response of thermal neutrons to changes in absolute air humidity found here is less than half of the value that was reported by Rosolem et al. [2013] and may be explained by the generally smaller response of thermal neutrons to changes in hydrogen [e.g. Weimar et al., 2020]. The rate of change between the thermal neutron intensity and absolute humidity derived in our study can be used to adjust the correction approach described by Rosolem et al. [2013] for epithermal neutrons so that it can be used to correct thermal neutrons observed above water instead. Although this correction approach may also be used as a first approach to correct thermal neutron intensities measured above soils, it should be noted that the response of neutron intensity to absolute humidity may change with soil moisture content, as reported for epithermal neutrons by Köhli et al. [2021]. This illustrates the need to develop more sophisticated approaches to the correction thermal neutron intensities for variations in absolute air humidity.

A specific feature observed in the neutron transport simulations is that, although neutron intensities generally increase with decreasing shielding depths, we find a maximum of the neutron intensity and, hence, the neutron ratio for low soil moisture content at shielding depths between 75 and 100 $\mathrm{g\,cm^{-2}}$, with lower neutron intensities at shielding depths below 75 $\mathrm{g\,cm^{-2}}$. A maximum secondary neutron intensity at shallow depths below the surface has been simulated, for example, for surface of Earth's [Phillips et al., 2001; Zweck et al., 2013] or the surface of Mars [Zhang et al., 2022], and it is linked to production of neutrons in the upper soil layers through nuclear evaporation as well as moderation by elastic scattering and absorption processes. Based on the neutron transport simulations conducted for a soil bulk density of 1.43 $\mathrm{g\,cm^{-3}}$, an intensity maximum occurs in the soil up to a soil moisture content of 0.045 $\mathrm{cm^3\,cm^{-3}}$ at a shielding depth of 100 $\mathrm{g\,cm^{-2}}$ (Fig. 5.3). At higher soil moisture contents, the maximum disappears. This may be linked to a smaller leakage of neutrons to the atmosphere as more hydrogen causes more elastic scattering in the soil.

The tube and filling materials of the groundwater well noticeably influence the signal of the active neutron probe [e.g. Keller et al., 1990] due to, for example, an influence of material chemistry on thermal neutron intensities [e.g. Quinta-Ferreira et al., 2016]. The simulation results of the present study show that the dimensions of the sphere of influence can be comparable for a well tube made of PVC and stainless steel with equal material thickness. As the average difference between a stainless

steel and a PVC tube is approximately 1 cm for R_{86} and between 8 and 5 cm for Vc_{86} and V_{86}, a small effect of the material composition on the sphere of influence can be identified but may be regarded as negligible. However, a thinner or thicker wall of the tube is likely to have a stronger impact on the measurement volume. For instance, a thicker PVC wall can be expected to reduce the measurement volume.

In contrast, the neutron ratios differ between a well tube composed of stainless steel and PVC. Although the response to changes in soil moisture are similar, the absolute neutron ratios of a PVC well tube compared with a stainless-steel tube of equal thickness are noticeably lower. This may be attributed to the influence of the higher absorption probability of chlorine for thermal neutrons in the PVC material. For the same reason, a thinner PVC material reduces the absolute neutron ratios to a smaller degree compared with a thicker PVC wall tubing.

For similar reasons, the effect of the filling material surrounding the actual tube of the groundwater observation well might be of importance in the scope of d-CRNS and should be assessed in future research. However, at our study site the width of the filling material around the tube was only 10 cm, and the filling material was similar to the original material of the surrounding undisturbed soils: a sand filling for soil layers composed of sandy soils and clay for less conductive layers at greater depths. Therefore, similar soil moisture dynamics in the refilled material to those of the undisturbed material can be assumed for our test site.

The radius (R_{95}) of the sphere of influence of the d-CRNS approach, even at high soil bulk densities, is larger compared with active neutron probes. For the latter, neutrons have to traverse the soil volume twice: on the way into the soil and back to the detector. In contrast, for passive applications, the water-sensitive neutrons in the fast-energy range are directly generated in the soil by high-energy neutrons, protons and muons, and they only have to traverse the soil volume once. Consequently, secondary cosmic-ray neutrons can reach the downhole neutron detector from origins at greater distances.

According to the particle transport simulation, the most sensitive volume lies above the detector centre. This is related to the source of cosmic-ray neutrons from above the soil surface. Similarly to the measurement footprints of above-ground CRNS, the sphere of influence varies with soil water content and with bulk density, with a higher sensitivity close to the neutron detector. As a consequence, reference soil moisture measurements close to the detector are likely to be more important than those at greater distances of the integration volume when predicting neutron ratios from reference soil moisture observations. Thus, further research may be required in order to assess whether weighting schemes for reference soil moisture measurements similar to those developed for above-ground CRNS are necessary in order to improve predicted neutron ratios. It should be noted that the simulated footprint dimensions are only valid for the modelled detector geometry and may vary with detector size and well or access tube dimensions.

Thermal neutrons detected with an unshielded, bare neutron detector, as is used in the present study, are more sensitive to absorption processes compared with neutrons in the epithermal energy range, which are dominated by moderation processes. As a consequence, soil chemistry influences the observed neutron intensity in the soil and, hence, also the derived neutron ratios from thermal neutrons and the neutron ratio variations with changes in soil moisture contents due to differing nuclear absorption probabilities in soils with different chemical compositions [e.g. Zreda et al.,

2008; Quinta-Ferreira et al., 2016]. However, we purposely used a simple soil chemistry set-up, which has been used as a standard configuration in several simulation studies, in the particle transport simulations [e.g. Köhli et al., 2015, 2021]. This is done in order to derive a first set of equations describing the neutron ratio response and sphere of influence in the scope of the d-CRNS approach that can be applied over wide range of observation sites instead of tailoring the simulation set-up and, thus, the derived equations, specifically to the observation site of this study. Although a standard soil chemistry was used to derive the transfer functions, the observed neutron ratios match the dynamics and ranges of predicted neutron ratios from in situ reference sensors, indicating the suitability and applicability of the d-CRNS approach as well as the equations derived at this site. A different soil chemistry may only introduce an overall damping of the measured intensity [Köhli and Schmoldt, 2022]. Nonetheless, the conclusions are limited by the single site chosen for this study. Further research is required to test and validate the transferability of the approach and to investigate the influences of, for example, varying soil chemical compositions, access tube and filling materials, and suitable technical set-ups for practicable applications.

5.5.2 Uncertainties

The experimental set-up of field measurements conducted within the scope of this study comprised the measurement of thermal neutrons with an unshielded proportional detector at 100, 200, 500 and 1000 cm depth with co-located reference in situ soil moisture sensors installed down to 450 cm depth. Observed neutron intensities in the groundwater observation well show a distinct response with changing soil moisture contents at the depth of measurement, indicating the possibility of measuring soil moisture and supporting the results from the various particle transport simulation scenarios.

In line with the exponential decrease in the absolute neutron flux with increasing soil depth, the uncertainty in the neutron intensity as well as the neutron ratio (N_r) increases. In general, the observed downhole neutron intensities are lower than those observed above a water surface and thus, lower compared with the intensities expected for above-ground CRNS applications. As the uncertainty increases with decreasing neutron intensity, the hourly time series needs to be averaged over longer time intervals compared with time series of above-ground neutron detectors. While above-ground neutron time series are typically averaged with a moving average of 13–25 h [e.g. Bogena et al., 2013; Schrön et al., 2018b], longer moving average windows of 25–49 h are more suitable for d-CRNS. However, with respect to the passive, continuous nature of d-CRNS as well as the expected smaller soil moisture dynamics at greater depths where soil moisture responses are also more strongly dampened, larger averaging intervals are acceptable.

Additional improvements can be made to reduce the uncertainty in observed downhole neutron time series. For example, detector tube no. 2 showed significantly lower neutron intensities compared with tube no. 1, which can be related to the settings of the instrument electronics. As the detector system used in this study was reassembled from different CRS1000 neutron detector systems, the neutron pulse module settings of tube no. 2 did not match the ideal configuration of the proportional counter tube attached; thus, a large part of potentially countable thermal

neutrons were discarded, leading to the lower observed intensities.

In spite of these uncertainties, our study reveals that observed N_r values follow the temporal dynamics of predicted N_r values from Eqs. (5.5-5.10) and lie within the range of predicted N_r values from in situ reference soil moisture sensor profiles. Both intense rainfall events and gradual soil moisture changes during drying periods could be observed in the downhole measurements. The measurements at 100 cm depth exhibit stronger dynamics compared with those in 200 cm, which is in line with reference soil moisture time series and predicted neutron ratios. The observed N_r time series at 100 cm is closer to that predicted for 130 than for 70 cm depth; this may be explained by the fact that the predicted time series of N_r strongly differ between 70 and 130 cm depth as well as among the sensors within the two depth layers. This is due to markedly different values and dynamics of the individual soil moisture sensors. This marked variability in point-scale soil moisture hampers direct comparison to the results derived from d-CRNS. It should be noted that, especially at large depths of 500 cm, few soil moisture dynamics occur and the d-CRNS uncertainty is high, limiting the range of suitable application depths of d-CRNS. The results of this initial study revealed that the predicted hourly time series of N_r from reference soil moisture sensors at 70 and 130 cm have a coefficient of variation of 5–12 % for the study period. At 200 cm, the coefficients of variation are in a range between 3 and 16 %. The time series of the observed N_r need to be smoothed with a 49 h moving average to suppress noise and to result in coefficients of variation at the same order of magnitude, i.e., a value of 11 % at 100 cm and 9 % at 200 cm depth, respectively. In contrast, the coefficient of variation of the observed N_r at 500 cm depth with the same moving average applied is 4.3 times larger than the maximum coefficient of variation from the predicted N_r time series at 450 cm depth. According to these findings, the d-CRNS observations can be expected to be dominated by noise at the depth of 500 cm, rendering them unable to resolve the small soil moisture variations at this depth. However, the d-CRNS approach may be suitable for resolving the soil moisture dynamics at this site for shielding depths of up to at least 330 $g\,cm^{-2}$ which roughly corresponds to a soil depth of at least 200 cm, when a moving average interval of 49 h is applied.

The uncertainties in θ_{SM} that are caused by the simplified estimation method used here (section 5.4.1) are comparatively small. Although we allowed the assumed mean soil moisture in the unsaturated zone above the sensor to vary between the wilting point and field capacity when estimating the soil moisture at the sensor depth (which represents the upper bound of the possible uncertainty), the resulting uncertainty bounds of θ_{SM} are very small and hardly relevant for the depth of 100 cm, and they are still small for the depth of 200 cm (see Figure 5.10).

While it is a major advantage of this study that in situ point-scale soil moisture observations for evaluating the d-CRNS approach are available at the study site at 200 cm and even at 450 cm depth, all reference sensors are unfortunately located outside the sphere of influence of the downhole neutron detectors in the groundwater observation well (at distances between 20 and 40 m). However, the observed N_r lies within the set of predicted time series of N_r from in situ reference sensor profiles and follows the general temporal dynamics of the predicted time series of N_r, thereby supporting the applicability of d-CRNS.

A key motivation of this study is to provide a new methodological approach to derive soil moisture information from deeper layers of the vadose zone in a larger

integration volume compared with point-scale in situ sensors. However, deriving soil moisture from observed N_r is difficult, as two soil moisture variables influence the latter: the soil moisture content at the measurement depth (θ_{SM}) and the average soil moisture from the soil surface to the detector centre ($\hat{\theta}_{SM}$). A first option would be the use of Eq. (5.5-5.10)) as a forward operator in combination with a soil hydraulic model. Similar approaches have been conducted using techniques such as the COSMIC (COsmic-ray Soil Moisture Interaction Code) forward-operator model [Shuttleworth et al., 2013] for above-ground CRNS applications [e.g. Brunetti et al., 2019; Barbosa et al., 2021]. Although the application as a forward operator in combination with soil hydraulic modelling may produce more accurate results as the soil water transport is simulated at different depths, and also allows for the retrieval of soil moisture simulated in several soil layers, a large number of input parameters are required that may not be available at all sites. Furthermore, coupling the derived equations with a soil hydraulic model may introduce additional uncertainties due to the model assumptions and the propagation of uncertainties from input parameters.

In contrast, the simple approach to estimate the local soil moisture content at the depth of measurement (as the most sensitive variable) showed that the resulting soil moisture time series follow the dynamics and also lie in the range of expected values derived from in situ soil moisture sensors. However, it should be noted that this approach may be less accurate and only allows for an estimation of the local soil moisture time series.

As this study is restricted to a single observation site, further research is required to test both the soil hydraulic-model-based approach and the approach used here under different site-specific boundary conditions, set-ups and measurement depths. This also includes the consideration of uncertainties arising from soils with high vertical variability in bulk density (and possibly soil moisture), their impact on predicted neutron ratios, and their impact on the estimated soil moisture at the depth of measurement. For example, a lower bulk density and a lower soil water content would lead to more neutrons penetrating into greater depths and, hence, to increased count rates and footprint volumes. Nevertheless, the two mentioned approaches are available for soil moisture retrieval from d-CRNS and could be applied under different soil hydrological conditions in future studies.

5.6 Conclusions

In this study, we tested the feasibility of CRNS downhole applications to estimate soil moisture at greater depth by combining particle transport simulations with a first application in the field. Although we used an unshielded neutron detector that was most sensitive to thermal neutrons, a distinct response to changes in the soil moisture content at the observation depth as well as in the shielding depth above the neutron detector was found. This illustrates the possibility to observe soil moisture values at greater depth with d-CRNS without additional soil moisture information for calibration. This is achieved through the calculation of neutron ratios using a measurement above water. The sphere of influence has a unique shape differing from those expected for active neutron probes as the neutron source and detector are not co-located. As detected neutrons are produced directly in the soil, the sphere of influence is much larger compared with an active neutron probe; thus, d-CRNS allows one to derive representative average soil moisture information at different

depths of the root zone.

Our measurements of downhole neutron intensities and calculated neutron ratios from a groundwater observation well provide experimental evidence that downhole thermal neutron detectors are sensitive to changes in soil moisture contents at the measurement depth. Simultaneously, the results of this study illustrate the opportunityto use existing monitoring infrastructure to retrieve soil moisture information from deeper soil layers. The transfer functions developed from particle transport simulations in the scope of this study can be used as an forward operator to calculate neutron signals from soil moisture information. In combination with soil hydraulic models, the forward operator can then be used to derive soil moisture contents in future applications. When the use of complex models is hampered, for example, by scarce data, a simple approach can be used for a first estimation of the soil moisture at the measurement depth.

In conclusion, we provide both simulation-based and experimental evidence for the feasibility of using downhole secondary cosmic-ray neutrons for the continuous, non-invasive estimation of soil moisture from greater depth. This method has several advantages compared with traditional in situ soil moisture sensors: the larger integration volume of the measurement counteracts the usual problems caused by the high spatial variability in soil moisture, even at small scales as a result of the subsurface heterogeneity. Furthermore, it does not require demanding installation procedures, as it simply uses existing infrastructure (i.e. observation wells) which is readily available in many locations as part of standard monitoring networks. The mathematical relationships presented allow for the prediction of the neutron signal from soil moisture information, and approaches are available to derive soil moisture contents from downhole neutron observations. However, as this study poses several limitations and is only a first proof of concept, further testing and developments will be necessary. This effort is worthwhile, especially as deep soil moisture measurements are becoming increasingly important to monitor subsurface droughts or water stress in forests as well as to validate hydrological models and extrapolation efforts from remote-sensing products.

5.7 Appendix A

In order to derive soil moisture information at the depth of measurement from the observed neutron ratios, we propose the following exemplary approach:

1. For $\hat{\theta}_{\mathrm{SM}}$, we assign values ranging from the wilting point to the field capacity in steps of $0.001\,\mathrm{cm^3\,cm^{-3}}$.

2. For every value of $\hat{\theta}_{\mathrm{SM}}$, we apply Eqs. (5.5-5.10).

3. For each time step of the observed time series of N_{r}, values of N_{r} are calculated by assigning values from $0.01\,\mathrm{cm^3\,cm^{-3}}$ to the soil moisture content at saturation in steps of $0.0001\,\mathrm{cm^3\,cm^{-3}}$ to θ_{SM}.

4. The value of θ_{SM} that produces the smallest absolute difference between the observed and calculated N_{r} at each time step is chosen. This procedure results in a time series of θ_{SM} for each value of $\hat{\theta}_{\mathrm{SM}}$.

5. Based on this set of time series, we propose averaging the values for θ_{SM} for each time step in order to provide a single time series of estimated soil moisture values at the depth of measurement. The minimum and maximum time series can also be calculated to assess the range (uncertainty) of possible θ_{SM} values based on the observed N_{r}.

5.8 Appendix B

Table 5.3: Sensor distribution of the reference soil moisture sensor profiles at the study site located at a distance of about 20–30 m from the groundwater observation well.

	Profile no.						
Depth (cm)	**1**	**2**	**3**	**4**	**5**	**6**	**7**
10	✓	✓	✓	✓	✓	✓	✓
20	✓	✓		✓	✓	✓	✓
30	✓	✓	✓	✓	✓	✓	✓
50	✓	✓	✓	✓	✓	✓	✓
70	✓	✓		✓	✓	✓	✓
130		✓	✓			✓	✓
200	✓			✓	✓	✓	✓
300						✓	✓
450						✓	✓

Table 5.4: Fitted parameters for Eq. (5.2-5.8) derived from particle transport simulation scenarios for a stainless-steel well tube with a wall thickness of 7.5 mm.

Eq. no.	**Variable**	p_1	p_2	p_3	p_4	p_5	p_6	p_7	p_8	p_9	p_{10}
(5.2)	R_{86}	185 cm	0.164	4.51 cm	2						
(5.3)	V_{86}	115 cm	1.2	0.211	23.9 cm	0.5					
(5.4)	Vc_{86}	31.2 cm	4	6.7 cm	0.6						
(5.7)	F_1	0.502	-0.0206 $cm^2\,g^{-1}$	0.0158	-0.000839 $cm^2\,g^{-1}$	0.531	-0.00674 $cm^2\,g^{-1}$				
(5.8)	F_2							0.0667	0.000139 $cm^2\,g^{-1}$	0.435	-0.0172 $cm^2\,g^{-1}$

Table 5.5: Fitted parameters for Eq. (5.7-5.8) derived from particle transport simulation scenarios for a PVC well tube with a wall thickness of 5 mm.

Eq. no.	**Variable**	p_1	p_2	p_3	p_4	p_5	p_6	p_7	p_8	p_9	p_{10}
(5.7)	F_1	0.348	-0.0206 $cm^2\,g^{-1}$	0.011	-0.000839 $cm^2\,g^{-1}$	0.369	-0.00674 $cm^2\,g^{-1}$				
(5.8)	F_2							0.0482	0.000139 $cm^2\,g^{-1}$	0.314	-0.0172 $cm^2\,g^{-1}$

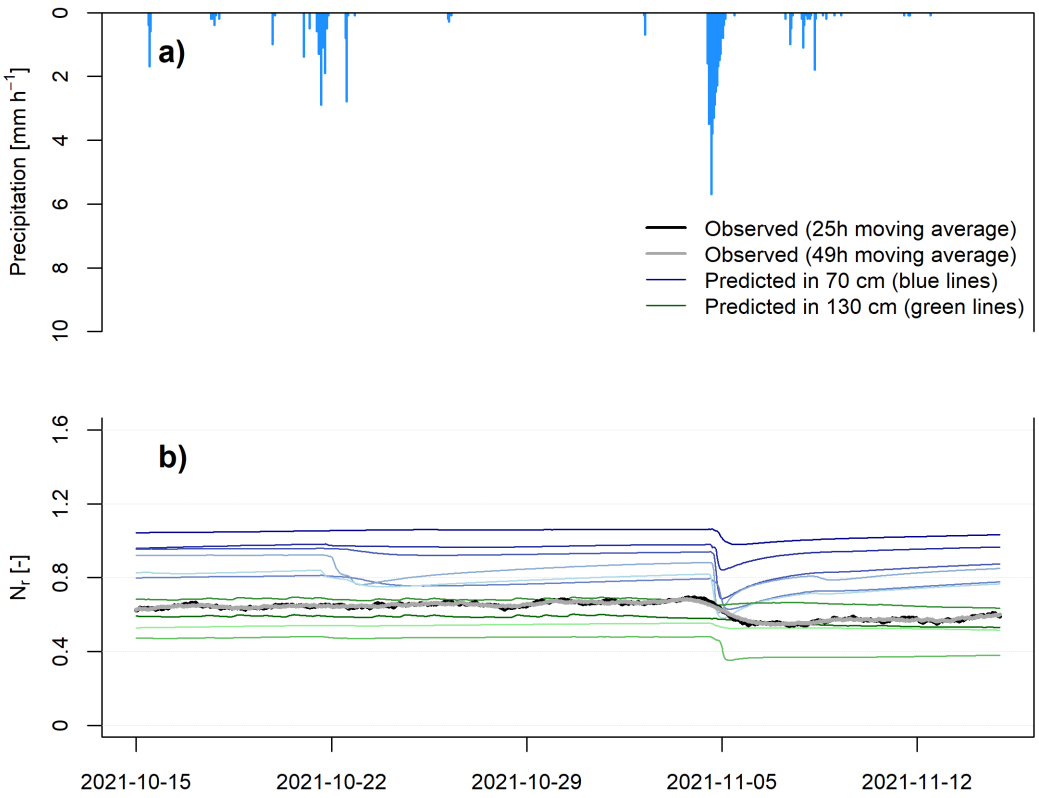

Figure 5.11: Panel (a) shows the hourly precipitation observed at the study site during a detailed period of the experiment in October-November 2021, and panel (b) presents the observed time series of N_r at 100 cm depth and the predicted time series of N_r from reference soil moisture sensor profiles at 70 and 130 cm depths. The different colours indicate the predictions from individual reference sensor profiles.

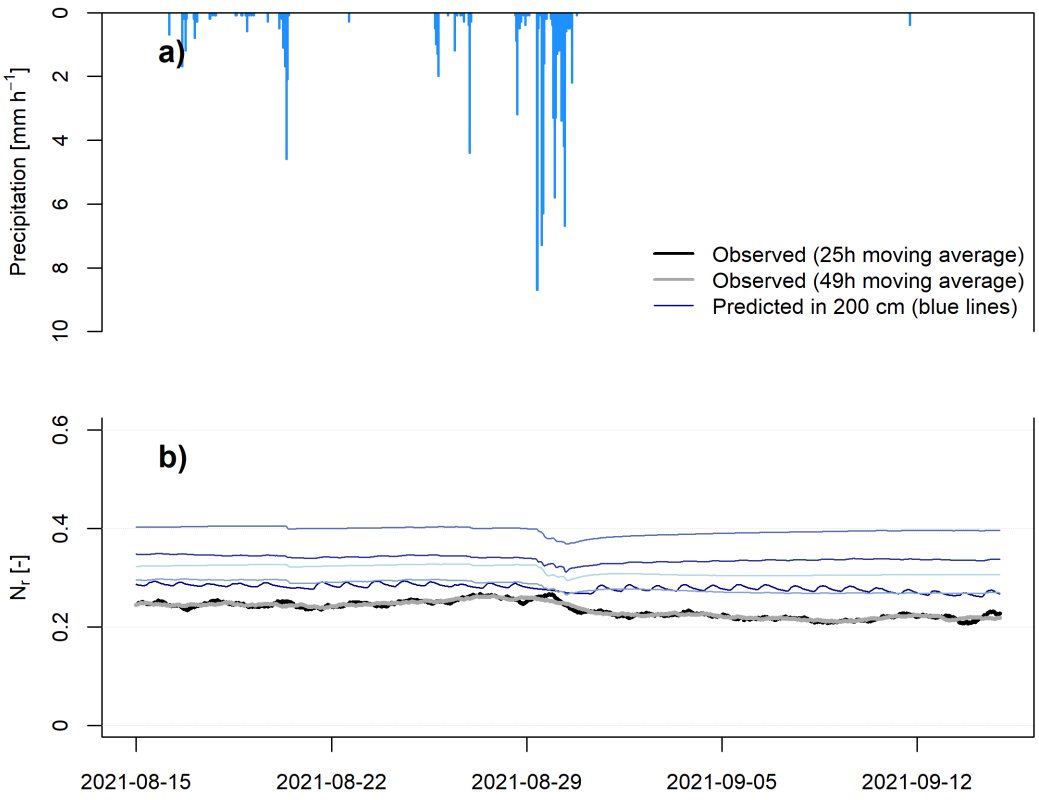

Figure 5.12: Panel (a) show the hourly precipitation observed at the study site during a detailed period of the experiment in October-November 2021, and panel (b) presents the observed time series of N_r at 200 cm depth and the predicted time series of N_r from reference soil moisture sensor profiles at 200 cm depth. The different colours indicate the predictions from individual reference sensor profiles.

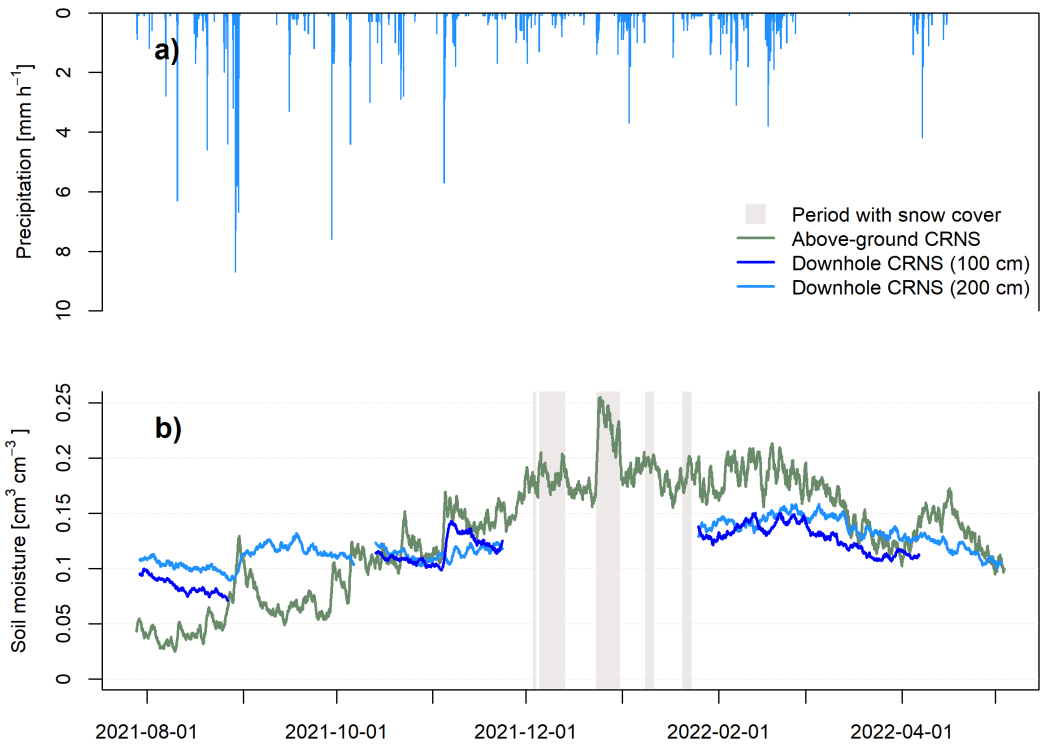

Figure 5.13: Panel (a) shows the hourly precipitation time series, and panel (b) presents the different soil moisture time series derived from CRNS. The neutron observations from above-ground CRNS were processed with standard correction and calibration procedures [site Serrahn; Bogena et al., 2022]. A 25h moving average was applied to the corrected neutron intensities prior to deriving soil moisture from above-ground CRNS observations with the standard transfer function [Desilets et al., 2010; Köhli et al., 2021]. Marked periods with snow cover represent periods with fractional to full snow cover and snow depths of up to 10-15 cm.

Chapter 6

Synthesis and conclusion

6.1 Synthesis

The four chapters of this thesis comprise individual studies which contribute to the advancement of the CRNS technique in respect to (i) atmospheric, geomagnetic and heliospheric variables influencing epithermal and thermal neutron observation and their correction, (ii) the possibilities to derive soil moisture from corrected neutron observations and to reduce the measurement footprint as well as (iii) to obtain CRNS-derived soil moisture information for greater soil depths.

6.1.1 On the correction of environmental influences on neutron observations

Alternatives for the correction of high-energy cosmic ray fluxes

Apart from variations of hydrogen in the ground, e.g. stored as soil organic matter, lattice water and most importantly soil moisture as well as above the ground as hydrogen stored in biomass, epithermal and thermal neutron signals are influenced by atmospheric variables and the intensity of primary high-energy cosmic radiation. Above land, the investigation of influencing factors beyond variations of hydrogen stored in and above the soil is inherently difficult. Given the high spatio-temporal variability of soil moisture, knowledge on its exact spatio-temporal variations would be required to separate observed neutron signals into the different components. In contrast, when CRNS instruments, i.e. neutron detectors, are placed above a large water body, the below and above-ground hydrogen pools can be assumed constant and the atmospheric influences as well as the influence of incoming primary radiation variations can be isolated.

The value of an above-water reference measurement of neutron intensities has been already proposed by Franz et al. [2013b] and applied by McJannet et al. [2014] for e.g. transforming neutron observations to soil moisture. Similarly, Andreasen et al. [2016] used above-water measurements of thermal and epithermal neutrons for a comparison with modelled neutron intensities. In chapter 5 of this thesis, above-water measurements are used to derive a detector-specific scaling parameter for a neutron-to-soil moisture transfer function, enabling a direct measurement of the required calibration parameter and to obviate the need for a calibration against in situ soil moisture measurements. While these measurements are usually of a comparably

short duration of a few days, continuous long-term measurements of epithermal and thermal neutron measurements may also serve as an alternative to neutron monitors for determining the variations incoming primary radiation and its subsequent use for the correction of neutron signals observed at CRNS sites on land [Schrön et al., 2017]. After correcting neutron signals observed above water for the effect of air pressure and absolute air humidity variations based on local measurements of air pressure, relative air humidity and air temperature, the remaining signal mainly consists of variations in incoming primary radiation and a noise component, only. In chapter 2, this remaining signal of an floating above-water detector is compared to neutron monitors around the globe covering different altitudes and geomagnetic cutoff rigidities. In general, the corrected neutron signal correlates well with the signals of the respective neutron monitors with better matching temporal dynamics for neutron monitors with similar cutoff rigidity and altitude. Advanced scaling approaches accounting for the difference in geomagnetic cutoff rigidity and altitude [Hawdon et al., 2014; McJannet and Desilets, 2023] improve the statistical goodness of fit with the different neutron monitors, especially for large difference in cutoff rigidity and altitude, with the most recent approach after McJannet and Desilets [2023] generally showing the best performance.

On the one hand, the findings from chapter 2 illustrate that newly developed scaling approaches can provide an improved incoming primary radiation correction of observed epithermal neutron intensities from CRNS with available neutron monitors. On the other hand, and more importantly, it is shown that floating CRNS instruments mounted on buoys or pontoons can serve as an alternative to neutron monitors for measuring variations incoming radiation and consequently, offer the possibility for correcting neutron signals at CRNS site on land. Given the uncertainty of the availability of high-quality and near-real time neutron monitor data in future and the dependency on the CRNS technique on the availability of data of incoming primary cosmic-ray variations, these findings are of high importance for advancing the CRNS technique and sustaining its applicability in future by becoming independent from external data sources as e.g. individual national CRNS networks could operate their own CRNS reference station observing neutron intensities above water. Yet, differences in altitude and geomagnetic cutoff rigidity between the above-water reference site and the CRNS instruments installed on land remain.

Therefore, muons observed by CRNS instruments with an additional muon detector could serve as an on-site reference for incoming primary radiation and its correction [Stevanato et al., 2019, 2022] which would allow for a site-specific correction for incoming radiation. Although muons have been shown to respond to solar events [e.g. Braun et al., 2009] and hence, variations in incoming primary radiation, their intensity observed at the ground level is influenced by air pressure and air temperature variations in different altitudes of the atmosphere [de Mendonça et al., 2016] which needs to be removed before using them in correction procedures for CRNS data. Previous studies used near-surface temperatures only [e.g. Stevanato et al., 2022], while correction approaches incorporating temperature information from the entire atmosphere profile provided the most accurate results in correcting the temperature effect from muon observations [de Mendonça et al., 2016]. The need for high altitude air temperature information for accurately correcting muon information may hamper their application in correcting low-energy cosmic-ray neutrons.

Furthermore, it has been shown that neutrons of different energies respond differently to solar events such as Forbush Decreases [Hubert et al., 2019]. This raises the question if a direct comparison between high-energy neutrons detected by neutron monitors and muons detected by local detectors is generally possible or if additional scaling and transfer functions are required to obtain most accurate correction results. Installing CRNS instruments above water which are identical to those used in CRNS applications would overcome this issue and allow for a more direct comparison and correction of variations in primary incoming radiation. Consequently, above-water CRNS instruments and locally observed muons yield potential to serve as alternatives for correcting variations in incoming primary cosmic radiations in the context of CRNS. Although chapter 2 underlines the potential of above-water measurements, the advantages, disadvantages and remaining challenges of either approach remain an important topic in CRNS research and further developments are required to enable and sustain the applicability of the CRNS technique, also in the absence of available high-energy neutron monitor data.

Differing influences on epithermal and thermal neutrons

The above-water neutron measurements described in chapter 2 also provide a first empirical analysis of the dependencies of epithermal neutrons, observed by the moderated neutron detector and thermal neutrons observed by the bare detector under conditions with a constant amount of hydrogen in the sensitive measurement footprint. It is shown that epithermal neutrons respond most intensely to changes in air pressure followed by incoming primary radiation and absolute air humidity. Thereby, empirical evidence for the air humidity correction factor determined by Rosolem et al. [2013] from neutron transport simulations is provided indicating its validity for hydrogen-rich environments. Some studies suggest that applying individual correction factors can improve the goodness of fit of CRNS-derived soil moisture estimates when compared against reference soil moisture measurements [e.g. Jeong et al., 2021]. However, the empirical findings of this thesis underline the impact of the three parameters on observed neutron intensities and the need for correcting their effect on the observed neutron signal. Empirical findings from studies which obtain better results when using only selected correction parameters may be related to the high-spatio temporal variability of the target variable, e.g. soil moisture, and its insufficient representation in reference measurements or the insufficient choice of correction data sets, e.g. a neutron monitor. This again highlights the usefulness of measurements above a water surface without variability in environmental hydrogen content in order to assess the impact of atmospheric variables and incoming radiation flux on neutron observation and to evaluate correction approaches. While the response of epithermal neutrons has been already shown in a preliminary analysis of the buoy experiment [Schrön et al., 2016; Schrön, 2017], the response of thermal neutrons remained unexplored.

In previous research investigating the response of thermal neutrons to environmental changes and their potential in, e.g., estimating snow water equivalents or above-ground biomass, thermal neutron intensities have been corrected differently for atmospheric variables such as air pressure and air humidity as well as variations in incoming primary cosmic radiation. Chapter 2 provides the first empirical evidence that thermal neutrons also respond to changes in atmospheric pressure, incoming primary cosmic radiation and absolute humidity. While the effect of air

pressure is similar on epithermal and thermal neutrons, first differences become visible when the incoming primary radiation is considered. This corresponds to findings from previous studies indicating a different response of different neutron energies to changes in primary cosmic radiation [e.g. Hubert et al., 2019]. On the one hand, this highlights the need for further research, but on the other hand, due to the similar response, an equal correction of epithermal and thermal neutrons as first approach may be justified rather than not applying any correction for variations of incoming primary radiation. Distinct differences are visible when the response to changes in absolute air humidity is considered, which is less than half of what can be observed for epithermal neutrons. This empirical finding is in line with results from neutron transport simulations conducted in chapter 5 and validates the first air humidity correction coefficient for thermal neutrons subsequently developed in this thesis.

As illustrated in chapter 2, applying correction procedures designed for epithermal neutrons to thermal neutron observations can lead to an over-correction, misleading results and biased interpretations. As a consequence, results from studies using and correcting thermal neutrons for not all influencing parameters [e.g. Tian et al., 2016] and with correction procedures designed for epithermal neutrons [e.g. Jakobi et al., 2018, 2022; Bogena et al., 2020] need to be assessed with extreme caution. When thermal neutrons are not corrected for absolute air humidity variations using the approach after Rosolem et al. [2013] for epithermal neutrons [e.g. Andreasen et al., 2016], conclusions on the observed neutron responses need to be drawn against the background of an air humidity effect still being present in the neutron signal. However, due to the relatively small effect of air humidity, this may be more feasible than interpreting the results in the light of all influencing factors and potential over-corrections.

6.1.2 From neutron observations to soil moisture estimates

Towards new transfer functions

Observing neutron intensities above water poses further potential for the comparison with neutron transport simulations, as above-water conditions are less complex than terrestrial field sites with e.g., heterogeneous soil moisture conditions, and hence, can be easier and more accurately represented in computational models [Andreasen et al., 2016]. This has been already demonstrated with the validation of the simulated air humidity correction factor for thermal neutrons (chapter 5) using the buoy-based neutron measurements above water (chapter 2) and is further exploited, evaluating newly developed neutron-to-soil moisture transfer functions. Köhli et al. [2021] provide an innovative transfer function relating epithermal neutron observations to changes in soil moisture and incorporating the change of the functional relationship with air humidity. The new transfer function is available with different fitted parameter sets originating from the simulations with different neutron transport models. As neutron transport models naturally produce deviating results depending on, for example how specific physical processes are mathematically implemented, it remains challenging which parameter set provides the most accurate results.

By using the above-water measurements from chapter 2, it was shown that the parameter sets from the MCNP neutron transport model are generally better than those from the URANOS neutron transport model, which is in line with Köhli et al.

[2021]. Contrasting results have been found regarding the use of complex detector response functions for evaluating the transport simulations. Using a detector response function mimicking the response and behaviour of a real neutron detector to derive the fitting parameters for the transfer function can be expected to match measured field data more closely. Applying the transfer function above water, where only air humidity influences the neutron signal dynamics, it was found that those parameter sets which are based on detector response function produce more accurate results. However, Köhli et al. [2021] found that the transfer function performs slightly worse in predicting neutron signals from local soil moisture measurements using these parameter sets. Köhli et al. [2021] suggested insufficient spatio-temporal soil moisture reference data as an explanation why the more realistic detector response function parameter sets performed worse. Further evidence for this hypothesis was found in chapter 4 where the new transfer function with all available parameter sets was tested against soil moisture measurement from a network of in situ point-scale soil moisture sensors. It was confirmed that the parameter sets from the MCNP model provide better results and that the detector response function parameter sets performed slightly worse. The number of reference soil moisture sensors is, however, limited with a minimum installation depth of 10 cm and therefore the first centimetres of the soil to which the CRNS method is most sensitive are not covered. This may lead to the better performance of the transfer functions with parameter sets not representing the response of a real neutron detector [Köhli et al., 2021] and again illustrates the advantages of above-water measurements of neutron signals in order to exclude the spatio-temporal variability of different soil moisture and other sources of hydrogen at terrestrial observation sites.

On the basis of chapter 2 and 4, the initial findings of Köhli et al. [2021] can be confirmed, that the new transfer function with the fitting parameter set derived from the MCNP model and evaluated with a detector response function provide the most accurate results. Furthermore, chapter 4 confirms the superior performance of the new transfer function compared to the standard transfer function after Desilets et al. [2010]. Although the standard transfer function is still commonly used for deriving soil moisture from CRNS in current research [e.g. Altdorff et al., 2023; Brogi et al., 2023; Jiang et al., 2023], the findings of this thesis underline the potential of new approaches and the need for a shift from using the standard transfer function to the universal transport solution introduced by Köhli et al. [2021], for retrieving most accurate soil moisture estimates.

Limiting the horizontal footprint

Some cases of application require a reduction of the epithermal neutron signal and especially, the subsequently derived soil moisture estimates to an area of interest smaller than the actual sensitive measurement footprint of CRNS. This could be the case if two distinct soil moisture regimes, e.g. caused by different soil physical properties or vegetation covers, occur within the CRNS measurement footprint with only one being of interest for a specific monitoring application or environmental modelling task.

In the case of a constant soil moisture value in one part of the footprint and a variable soil moisture content in the subfootprint area of interest, a correction of the neutron signal can be applied to account for the resulting dampening effect in the neutron signal [Schrön et al., 2018b]. However, difficulties arise when multiple soil

moisture regimes with varying and unknown soil moisture dynamics occur within the sensitive measurement footprint. Chapter 3 investigates possibilities to reduce the CRNS-derived soil moisture estimates at a study site with two distinct soil moisture regimes. On the one hand, the neutron signal of the bare, thermal neutron detector is used and on the other hand, the neutron-to-soil moisture transfer function is adjusted to compensate for the influence of soil moisture dynamics from areas outside the subfootprint area of interest.

Thermal neutrons observed by the unshielded, bare neutron detector have been thought to have a smaller measurement radius and thus, a smaller sensitive measurement footprint compared to epithermal neutrons observed by the moderated neutron detector of CRNS instruments. Bogena et al. [2020] were the first stating a measurement radius of 35 m for thermal neutrons, which is much smaller compared to the values above 150 m suggested by Köhli et al. [2015] as the lower bound for epithermal neutrons. A footprint radius in a similar range of 40-50 m was determined by Jakobi et al. [2021] from neutron transport simulations, suggesting that at the study site described in chapter 3, the thermal neutron signal should not be influenced by soil moisture dynamics occurring in areas of greater distance, i.e. those not of interest. Following these results, thermal neutrons could be used to derive soil moisture for the subfootprint area of interest. However, the neutron transport simulations conducted in chapter 3 show that also thermal neutrons respond to soil moisture changes in distances beyond the suggested 40-50 m. This indicates that the definition of the sensitive measurement radius used in previous studies is insufficient and should be adapted to the one used for determining the measurement radius of epithermal neutrons. In this case, the measurement footprint is likely to be much larger than 50 m, although it remains smaller than the footprint of epithermal neutrons. Supporting evidence for the larger footprint of the bare neutron detector derived in chapter 3 is given by Brogi et al. [2022], who simulated measurement footprint radii of above 120 m for a neutron detector shielded with 5 mm HDPE, which largely measures thermal neutrons and is hence, most comparable to an unshielded, bare detector.

Consequently, the neutron signal of the bare neutron detector cannot be used for estimating soil moisture in subfootprint areas around the CRNS instrument as small as investigated in chapter 3. However, the correlation between the two neutron signals may yield some information about the horizontal heterogeneity and should be investigated more closely in future studies. At some observation sites including the latter, the thermal neutron signal may still be considered as a proxy for a different response of neutrons to soil moisture changes in the subfootprint area of interest. An adjusted neutron signal for a better estimation of soil moisture with the standard neutron-to-soil moisture transfer function in subfootprint areas can be derived. Although the approach improved the soil moisture estimates in a subfootprint area at the study site considered in chapter 3, the transferability to study sites with other characteristics and soil moisture distributions is limited.

Instead, a more general approach successfully tested in chapter 3 includes the change of the neutron-to-soil moisture transfer function rather than changing the neutron signal by fitting the functional relationship to reference soil moisture information in the subfootprint area of interest. The adjusted transfer function may then be able to partly compensate for the influences of soil moisture changes in parts of the footprint which are outside the area of interest. Although this approach

strongly improved the estimation of soil moisture in a subfootprint area of interest and is generally applicable, it requires a sufficient amount of in situ reference soil moisture information for calibration of all parameters of the neutron-to-soil moisture transfer function. As multiple calibration campaigns have been suggested in previous studies for obtaining more accurate CRNS-derived soil moisture estimates [Iwema et al., 2015], enough reference data for adjusting may already be available at many CRNS observation sites due to existing sampling strategies. Even more data for an adjustment of the transfer function could be obtained from a small number of permanently installed point-scale in situ soil moisture sensors, which has been suggested in other studies [e.g. Scheiffele et al., 2020] to complement CRNS observation sites and allow for additional analyses and processing procedures.

The finding that adjusting the neutron-to-soil moisture transfer function can be used to improve the estimation of soil moisture in a subfootprint area of interest and thereby limiting the measurement footprint, sheds light on other studies which adjusted the functional relationship to improve CRNS-derived soil moisture estimates in the entire footprint such as Lv et al. [2014] and Heidbüchel et al. [2016]. Spatio-temporal heterogeneities of soil moisture could have led to the necessity of adjusting the neutron-to-soil moisture transfer function. Investigations by Schrön et al. [2023a] on the influence of soil moisture heterogeneities in the measurement footprint on the observed epithermal neutron signal confirm a change of the neutron response to soil moisture, if e.g. soil moisture changes are limited to a smaller subfootprint area close to the CRNS instrument. A subsequently provided correction approach may allow for the correction of the transfer function for areas with static soil moisture in the measurement footprint [Schrön et al., 2018b, 2023a] and serve as a more general approach than empirically deriving site-specific transfer functions by calibration against in situ reference soil moisture information. However, in case of non-static soil moisture conditions in both, the subfootprint area of interest and the remaining footprint area with generally unknown soil moisture content, it remains to be investigated whether the physically-based approach after Schrön et al. [2023a] can robustly improve the derived soil-moisture estimates in the subfootprint area of interest. Here, the empirical adjustment of the transfer function against reference soil moisture information in the subfootprint area of interest may serve as an efficient alternative. Due to its simplicity, the latter may be especially useful as the reduction of the CRNS-derived soil moisture estimates to a specific subfootprint soil moisture regime is a prerequisite for their subsequent incorporation in, e.g. soil water transport models.

Although chapter 3 contributes to the understanding of impact of subfootprint soil moisture heterogeneities in the scope of CRNS research, further research is required, especially with respect to differing and partly unknown soil moisture contents in the sensitive measurement footprint, their influence on epithermal and thermal neutron signals as well as potential correction approaches.

6.1.3 Deriving soil moisture in greater depths

Modelling deeper soil moisture

Soil moisture in deeper soil layers is of great importance for the water supply of plants and hence, the drought tolerance of ecosystems as well as the storage capacity available to retain water in the flood generation process. Despite its generally large

integration volume allowing for estimating representative areal soil moisture averages at the field scale, the measurement depth of CRNS is limited to the first decimetres of the soil.

Simple mathematical modelling approaches have been used to extrapolate surface soil moisture information from CRNS to greater depths [e.g. Peterson et al., 2016; Zhu et al., 2017; Nguyen et al., 2019; Franz et al., 2020]. However, all these approaches require reference soil moisture information in the depth of interest for calibrating or building empirical models or permanently installed reference sensors. In many cases, such reference in situ soil moisture information is not available, which raises the question of approaches that can be applied without calibration and relying on soil physical and environmental parameters.

Complex soil hydraulic models solving the Richards equation including HYDRUS-1D [Šimůnek et al., 2008] may be used when solely relying on soil physical and environmental variables and have been applied to simulate soil water fluxes in different aspects of CRNS research [Bogena et al., 2013; Lv et al., 2014; Brunetti et al., 2019; Barbosa et al., 2021]. Although physically-based, models with higher complexity decrease the ease of application and usually require a larger number of input parameters such as precipitation, which is not always available at CRNS observation sites.

Against this background, a simple but physically-based depth-extrapolation approach after Manfreda et al. [2014] is modified in chapter 4 in order to allow its application based on estimated soil physical and environmental parameters. Using literature-based values and estimating the remaining parameters based on the modification described in chapter 4, the depth-extrapolation approach provides soil moisture information in a second, deeper soil layer without the necessity of in situ reference soil moisture information in the depth of interest for calibration.

Under similar boundary conditions, the modified, uncalibrated modelling approach can compete with the original, calibrated approach introduced by Manfreda et al. [2014] by meeting a benchmark statistical goodness of fit threshold used to evaluate the modelling approach in previous studies [Baldwin et al., 2019]. However, at the forested study site with sandy soils considered in chapter 4, the modelling approach in its original and modified form is generally not able to capture the soil moisture dynamics in deeper soil layers to a sufficient degree.

Only a calibration against in situ reference soil moisture information and allowing soil physical parameters of the model in a non-physically reasonable range sufficiently captures the soil moisture dynamics observed by in situ reference sensors in the depth of interest. Likely caused by complex preferential flow processes in sandy forest soils, this illustrates the limitations of modelling approaches for deriving information on soil moisture in deeper soil layers.

On the one hand, the results presented in chapter 4 underline the value of simple depth-extrapolation approaches for simulating first estimates soil moisture in greater depths, even when no in situ reference soil moisture information for calibration are available. These approaches are not limited to CRNS-derived surface soil moisture estimates and may also be applied with surface soil moisture information derived from, for example, remote sensing applications, making them applicable on even larger spatial scales. On the other hand, complex soil hydraulic processes are difficult to capture, especially with simple modelling approaches highlighting the need for in situ measurements of soil moisture in greater depths.

Measuring deeper soil moisture

Obtaining the most accurate and reliable results in soil hydrological modelling applications requires the evaluation and calibration of the model against in situ reference information such as measured soil moisture values. Point-scale electromagnetic soil moisture sensors buried in the soil are commonly used to measure soil moisture at monitoring sites. However, a large number of sensors are required to obtain representative field-scale averages of soil moisture to make them most comparable with the process scales of many (soil) hydrological models.

Especially in larger depths, the installation of a larger amount of electromagnetic sensors is accompanied with higher work efforts and soil disturbance. Other geophysical methods such as ERT may overcome the need for sensor installations in the depth of interest and measure soil moisture on a larger spatial scale. However, these come with their own methodological challenges and limitations. Other geophysical methods also often rely on campaign-based snapshot measurements while continuous soil moisture information on a high temporal resolution are required for monitoring purposes and beneficial for model calibration and validation efforts.

The main advantage of CRNS in its standard application with instruments installed above the soil surface is the large integration volume allowing for estimating representative field-scale averages of soil moisture at a high, i.e. hourly temporal resolution. Therefore, chapter 5 investigates the possibility of using neutron detectors in access tubes to observe soil moisture in greater depths.

Used as an analogy to the active neutron probe for soil moisture measurements developed in the last century [Gardner and Kirkham, 1952] and equipped with an active neutron source and co-located neutron detector, the downhole CRNS approach described in chapter 5 is an entirely passive approach. Compared to the active neutron probe, its application is not restricted due to radiation hazards and can be operated in a continuous mode.

The methodological framework introduced in chapter 5 produced valuable estimates of soil moisture in greater depths and does not require calibration against in situ reference soil moisture information. Instead, the detector-specific neutron intensity above a large water-body is used as a calibration parameter, as previously suggested for above-ground CRNS applications [Franz et al., 2013b]. The detector-specific intensity above water can be measured by taking the CRNS instrument on a lake, making in situ soil moisture sensors or soil samples from the depth of interest not necessarily required. In contrast, soil physical properties including the soil bulk density need to be reasonably well estimated in order to obtain the most accurate results. Adding to the limitations of the approach, the impact of a soil profile comprising soil layers with different bulk densities and soil chemical compositions has not been assessed in chapter 5 and requires further research to investigate the applicability of the introduced methodological framework at sites with different environmental characteristics.

The integration volume of the downhole CRNS approach is much smaller compared to the CRNS applied above-ground. Nevertheless, chapter 5 suggests that it is almost twice as large as the estimated measurement volume of the active neutron probe, being another advantage of the passive downhole CRNS approach. Consequently, a downhole CRNS instrument may be as representative as a larger number of point-scale electromagnetic in situ sensors in a specific depth, which reduces the amount of work and soil disturbance in monitoring soil moisture in greater depths.

Using existing monitoring infrastructure such as groundwater observation wells has already been suggested in the context of the active neutron probe [Keller et al., 1990] and is adapted for downhole CRNS in chapter 5. The application of downhole CRNS for estimating soil moisture in the deeper unsaturated soil does not restrict groundwater level measurements and illustrates the potential of using existing monitoring infrastructure for deeper vadose zone monitoring. For instance, Boeing et al. [2022] were not able to evaluate drought simulations in Germany in deeper soil layers due to an insufficient reference soil moisture data availability for greater depths. On a national scale, equipping a sufficient number of existing groundwater observation wells with downhole CRNS would allow for evaluating and improving nationwide hydrological model results, even in deeper soil depths of $\geq 100\,\mathrm{cm}$.

Being a passive approach, downhole CRNS relies on the intensity of hydrogen-sensitive neutrons in the measurement depth. As the source of these secondary cosmic-ray neutrons are high-energy cosmic-ray particles originating from space, the intensity of potentially detectable neutrons decrease with increasing soil depth, raising the question in which depth-range downhole CRNS can be applied. Generally, larger depths result in lower neutron intensities. Here, the same neutron detector requires larger integration times for obtaining a similar statistical accuracy.

Thermal neutrons with an unshielded, bare neutron detector have been observed in a few tens of metres [e.g. Grieger et al., 2020] to several hundreds of metres below the soil surface [e.g. Best et al., 2016]. The origin of these neutrons is dominated by high-energy neutrons and protons in the first few metres. Muons become the dominating source for hydrogen-sensitive neutrons in several tens of metres followed by radioactive decay processes dominating in depths of hundreds of metres [Heusser, 1996; Best et al., 2016]. The presence of thermal neutrons in depths of several hundreds of metres suggests the potential to theoretically obtain information on the amount as well as variations of hydrogen and thus, water in the surrounding rock material in these depths illustrating potential further fields of application.

With a focus on soil moisture, the approach presented in chapter 5 only considered the unsaturated zone of the soil with depths down to 10 m, showing that neutrons can still be observed in these depths. However, a reasonable accuracy with integration times of 24 and 48 hours was only achieved down to 200 cm with a CRNS neutron detector designed for above-ground applications. In larger depths, integration intervals of multiple days to weeks might be required for the same detector to obtain a sufficient statistical accuracy. Given, the generally dampened soil moisture dynamics in larger depths longer integration times and thus, a lower temporal resolution may be still be considered acceptable. The spatio-temporal scale of downhole CRNS relative to other methods is shown in Fig. 6.1. The development and improvement of neutron detectors for CRNS applications is ongoing [e.g., Stevanato et al., 2019; Weimar et al., 2020; Stowell et al., 2021; Patrignani et al., 2021]. More efficient, yet geometrically small neutron detectors tailored to downhole CRNS applications could further improve the method and should be investigated in future.

Although chapter 5 introduces a first methodological framework of downhole CRNS yielding large potential for monitoring soil moisture in the deeper unsaturated zone, several open questions remain. These comprise the general applicability of the method at different observation sites, the impact of vertically heterogeneous soil physical properties as well as different soil chemical compositions including neutrons

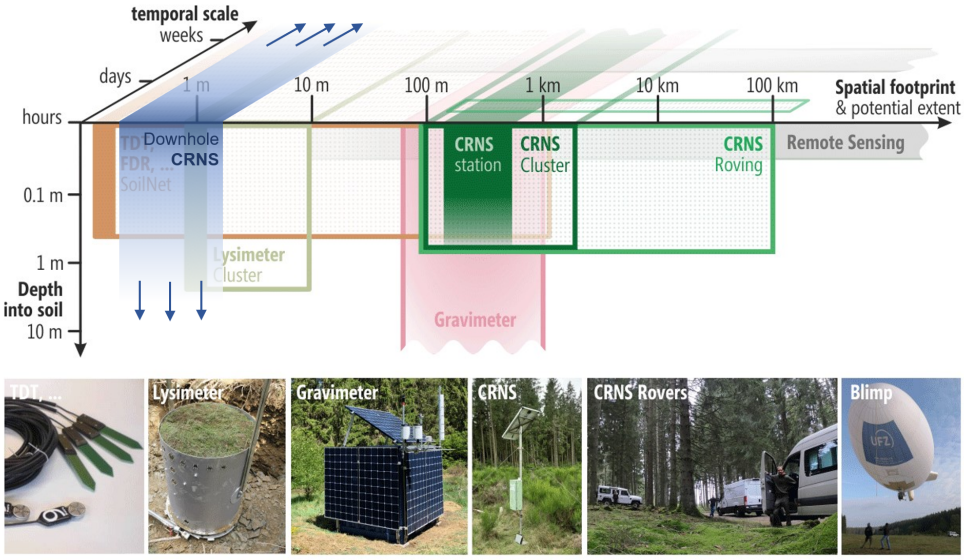

Figure 6.1: Spatio-temporal scale of downhole CRNS relative to other soil moisture measurement techniques. A larger integration time and thus, lower temporal resoltion may allow for a larger measurement depth of downhole CRNS. The footprint of an individual sensor is displayed solid while minimum temporal resolution and maximum spatial extent of typical applications (e.g. clusters of points-scale in situ TDT and FDR sensors) are depicted by frames in the respective colour [Figure modified after Heistermann et al., 2022].

produced by radioactive decay processes of soil components emphasizing the need for further research.

6.2 Conclusions and outlook

Cosmic-Ray Neutron Sensing is a promising measurement technique for monitoring soil moisture at spatio-temporal scales relevant for informing flood and drought risk modelling and forecasting. This becomes especially important in a warming climate with intensifying hydro-meteorological extremes.

Although the methodological framework of CRNS has been introduced more than a decade ago, numerous challenges and questions remained unsolved. Therefore, this thesis aimed for advancing the CRNS method in different aspects ranging from correcting observed neutron signals to the estimation of soil moisture near-surface and deriving soil moisture estimates from larger soil depths.

A major challenge in CRNS research and monitoring applications is the correction of the raw neutron signals observed by the CRNS neutron detector prior soil moisture can be estimated. For the first time, this thesis provides empirical evidence that both epithermal and thermal neutrons are sensitive to the same influencing variables. Thereby confirming the applicability of existing and new correction approaches developed in the scope of this thesis, through the validation of neutron transport models with field experiments. On the one hand, these findings indicate that care needs to be taken when interpreting the results on thermal neutrons for hydrological and environmental applications, but not correcting the neutron signal

sufficiently. On the other hand, confirming the dependence of thermal neutrons to variations of air pressure, incoming primary radiation and absolute air humidity and by presenting an adjusted correction approach for the latter, this thesis sets a benchmark for investigating the potential of thermal neutrons in future studies.

Both thermal and epithermal neutrons respond to variations of incoming primary radiation and a correction is required to obtain most accurate soil moisture estimates. Solely relying on high-energy neutron monitors sparsely distributed across the globe, and with the future operation of specific neutron monitors being uncertain, finding alternatives remains a major challenge in CRNS research. This thesis shows that scaling functions developed in recent studies can improve the correction based on neutron monitor sites in large distances to the respective CRNS site. Nevertheless, the best result would be obtained with information of the high-energy neutron flux close to the site of interest.

The present thesis illustrates the potential of permanently installed neutron detectors above water bodies to monitor variations in the neutron signal caused by variations in incoming primary radiation which could be subsequently used for the correction of neutron signal at terrestrial observation sites. These floating detectors are easier to install and maintain and may be installed close to a specific CRNS monitoring network, for example. Although other approaches including the use of locally observed muons are currently investigated and further research is of utmost importance, the results presented in this thesis represent an important step forward in finding suitable alternatives for the correction of neutron signals for variations in incoming primary radiation observed in the scope of CRNS.

Soil moisture derived from epithermal neutrons requires neutron-to-soil moisture transfer functions. Most studies rely on the standard transfer function introduced with the methodological framework of CRNS. However, more recently introduced transfer functions are expected to provide more accurate estimates of soil moisture. Tested at a terrestrial CRNS monitoring site and above water, newly developed transfer functions accounting for interdependence between soil moisture and absolute humidity provide more accurate representations of observed neutron signals and soil moisture values. Consequently, the results of this thesis indicate the necessity for a shift from the standard transfer function to newly developed approaches for more accurate estimates of field-scale soil moisture.

Strongly heterogeneous, e.g. binary, soil moisture distributions in the sensitive measurement footprint may allow for investigating the sensitive measurement footprint size of epithermal and thermal neutrons. Showing that thermal neutrons have a smaller footprint than epithermal neutrons, but much larger than estimated in previous studies, the results of this thesis shed new light on potential research applications of thermal neutrons but likewise underline the need for further research.

In contrast, heterogeneous soil moisture distributions in the sensitive measurement footprint complicate the estimation of soil moisture with CRNS. This thesis provides an generally applicable approach to reduce CRNS-derived soil moisture observations to the soil moisture regime in the subfootprint area of interest. This is a prerequisite for subsequent soil hydrological modelling applications such as the derivation of soil moisture in larger soil depths.

Despite its large integration radius, the measurement depth of CRNS is limited to the upper decimetres of the soil. The high importance of soil moisture in deeper layers raises the question of increasing the observational window of CRNS in the ver-

tical through soil hydrological modelling approaches of varying complexity. Simple modelling approaches are generally easier to apply and require fewer model input information, but usually require soil moisture information in the depth of interest for model calibration or set-up. This thesis provides a modification of a simple modelling approach, making it applicable without reference information in the depth of interest and solely relying on soil physical and environmental parameters which can be estimated with sufficient accuracy. Although it is shown that valuable first estimates of deeper soil moisture can be derived, an insufficient performance at monitoring sites with complex soil hydraulic processes involved underline the need for in situ measurements of deeper soil moisture.

Against this background, this thesis provides first evidence that CRNS can be used in downhole applications. By applying the introduced methodological concept of downhole CRNS, in situ estimates of soil moisture in depths of below 100 cm and with sufficient accuracy in terms of absolute values and time series dynamics were derived. These findings do not only yield a high potential for national soil moisture monitoring efforts in observing soil moisture in greater depths and utilising existing monitoring infrastructure, but open an entirely new field of CRNS research. With several new research questions raised from these initial investigations, further research is needed to test the introduced methodological framework and investigate the role of varying soil properties as well as soil chemistry to fully assess and exploit the potential of downhole CRNS.

In conclusion, this thesis addresses open research questions and challenges in several different aspects of CRNS research. Providing methodological advancements by testing and introducing new correction approaches, evaluating neutron-to-soil moisture transfer functions and developing new fields of application, it not only contributes to addressing open challenges in hydrological research identified by scientific community. It also underlines the potential of CRNS for national soil moisture monitoring efforts e.g. in the scope of official climate change adaption strategies as well as flood and drought risk modelling and forecasting being of special importance in the context of intensifying hydro-meteorological extremes in a changing climate.

Acknowledgements

First of all I want to thank my supervisors Andreas Güntner and Theresa Blume for their support and commitment in supervising my doctoral thesis. Their advice and knowledge helped me in making progress, especially in difficult times. Likewise, their positive attitude, openness for discussion and giving me the freedom to explore and follow my own research ideas and interests played a key role for the successful completion of this thesis. I would also like to thank Heye Bogena for acting as my mentor during the doctoral studies and, especially, Peter Dietrich for his willingness to be a referee for this thesis.

I feel huge gratitude to all my dear colleagues and fellow doctoral students from the Cosmic Sense project. Especially to Martin Schrön, Markus Köhli and Jannis Weimar for their immense support and acting as unofficial supervisors, being mentors and friends. Regular meetings with my fellow doctoral students Jannis Weimar, Lena Scheiffele, Veronika Döpper, Mandy Kasner, Jannis Jakobi, Nora Krebs and Lasse Hertle for brainstorming ideas, supporting each other with knowledge and advice or lending an ear to those who struggled were a significant help in difficult periods and an important source of motivation. This is also true for the endless chats and coffee breaks with colleagues from the hydrology section at GFZ Potsdam, especially Anne Hartmann and Markus Morgner whose friendship I wouldn't want to miss.

Alongside with Markus Morgner, I would also like to thank my colleagues Stephan Schröder, Heiko Thoss, Jörg Wummel and Knut Günther for their indispensable support regarding technical questions, instrumentation set-ups and in numerous field work campaigns. I would like to express special thanks to Marvin Reich who not only supported me in endless field work campaigns but also with brainstorming new research ideas, methodological concepts, sharing knowledge and gaining motivation when needed.

Last but not least, I am endlessly grateful for my wife, my family and my friends for their endless support during this endeavour as well as the distractions they provided when I needed them most. Always having you at my side is the largest gift there is.

References

A. Abunin, P. Kobelev, M. Abunina, M. Preobragenskiy, D. Smirnov, and A. Lukovnikova. 2016. A wind effect of neutron component of cosmic rays at Antarctic station "Mirny". *Solar-Terrestrial Physics (Solnechno-zemnaya fizika)*, 2(1):71–75. doi: 10.12737/13505.

A. Alaoui, U. Caduff, H. Gerke, and R. Weingartner. 2011. Preferential flow effects on infiltration and runoff in grassland and forest soils. *Vadose Zone Journal*, 10 (1):367–377. doi: 10.2136/vzj2010.0076.

C. Albergel, C. Rüdiger, T. Pellarin, J.-C. Calvet, N. Fritz, F. Froissard, D. Suquia, A. Petitpa, B. Piguet, and E. Martin. 2008. From near-surface to root-zone soil moisture using an exponential filter: an assessment of the method based on in-situ observations and model simulations. *Hydrology and Earth System Sciences*, 12(6): 1323–1337. doi: 10.5194/hess-12-1323-2008.

D. Altdorff, S. E. Oswald, S. Zacharias, C. Zengerle, P. Dietrich, H. Mollenhauer, S. Attinger, and M. Schrön. 2023. Toward large-scale soil moisture monitoring using rail-based Cosmic Ray Neutron Sensing. *Water Resources Research*, 59(3). doi: 10.1029/2022wr033514.

M. Andreasen, K. H. Jensen, M. Zreda, D. Desilets, H. Bogena, and M. C. Looms. 2016. Modeling cosmic ray neutron field measurements. *Water Resources Research*, 52(8):6451–6471. doi: 10.1002/2015wr018236.

M. Andreasen, K. H. Jensen, D. Desilets, T. E. Franz, M. Zreda, H. R. Bogena, and M. C. Looms. 2017a. Status and perspectives on the cosmic-ray neutron method for soil moisture estimation and other environmental science applications. *Vadose Zone Journal*, 16(8):vzj2017.04.0086. doi: 10.2136/vzj2017.04.0086.

M. Andreasen, K. H. Jensen, D. Desilets, M. Zreda, H. R. Bogena, and M. C. Looms. 2017b. Cosmic-ray neutron transport at a forest field site: the sensitivity to various environmental conditions with focus on biomass and canopy interception. *Hydrology and Earth System Sciences*, 21(4):1875–1894. doi: 10.5194/hess-21-1875-2017.

M. Andreasen, K. H. Jensen, H. Bogena, D. Desilets, M. Zreda, and M. C. Looms. 2020. Cosmic ray neutron soil moisture estimation using physically based site-specific conversion functions. *Water Resources Research*, 56(11). doi: 10.1029/2019wr026588.

H. Apel, S. Vorogushyn, and B. Merz. 2022. Brief communication: Impact forecasting could substantially improve the emergency management of deadly floods: case

study July 2021 floods in Germany. *Natural Hazards and Earth System Sciences*, 22(9):3005–3014. doi: 10.5194/nhess-22-3005-2022.

K. Aplin, R. Harrison, and A. Bennett. 2005. Effect of the troposphere on surface neutron counter measurements. *Advances in Space Research*, 35(8):1484 – 1491. doi: 10.1016/j.asr.2005.02.055.

R. Baatz, H. Bogena, H.-J. Hendricks Franssen, J. Huisman, W. Qu, C. Montzka, and H. Vereecken. 2014. Calibration of a catchment scale cosmic-ray probe network: A comparison of three parameterization methods. *Journal of Hydrology*, 516:231–244. doi: 10.1016/j.jhydrol.2014.02.026.

R. Baatz, H. R. Bogena, H.-J. H. Franssen, J. A. Huisman, C. Montzka, and H. Vereecken. 2015. An empirical vegetation correction for soil water content quantification using cosmic ray probes. *Water Resources Research*, 51(4):2030–2046. doi: 10.1002/2014wr016443.

E. Babaeian, M. Sadeghi, S. B. Jones, C. Montzka, H. Vereecken, and M. Tuller. 2019. Ground, proximal, and satellite remote sensing of soil moisture. *Reviews of Geophysics*, 57(2):530–616. doi: 10.1029/2018rg000618.

A. Badiee, J. R. Wallbank, J. P. Fentanes, E. Trill, P. Scarlet, Y. Zhu, G. Cielniak, H. Cooper, J. R. Blake, J. G. Evans, M. Zreda, M. Köhli, and S. Pearson. 2021. Using additional moderator to control the footprint of a COSMOS rover for soil moisture measurement. *Water Resources Research*, 57(6). doi: 10.1029/2020wr028478.

D. Baldwin, S. Manfreda, K. Keller, and E. Smithwick. 2017. Predicting root zone soil moisture with soil properties and satellite near-surface moisture data across the conterminous United States. *Journal of Hydrology*, 546:393–404. doi: 10.1016/j.jhydrol.2017.01.020.

D. Baldwin, S. Manfreda, H. Lin, and E. A. Smithwick. 2019. Estimating root zone soil moisture across the eastern United States with passive microwave satellite data and a simple hydrologic model. *Remote Sensing*, 11(17):2013. doi: 10.3390/rs11172013.

L. R. Barbosa, V. H. R. Coelho, L. M. Scheiffele, G. Baroni, G. M. R. Filho, S. M. G. L. Montenegro, C. das N. Almeida, and S. E. Oswald. 2021. Dynamic groundwater recharge simulations based on Cosmic-Ray Neutron Sensing in a tropical wet experimental basin. *Vadose Zone Journal*, 20(4). doi: 10.1002/vzj2.20145.

G. Baroni and S. Oswald. 2015. A scaling approach for the assessment of biomass changes and rainfall interception using Cosmic-Ray Neutron Sensing. *Journal of Hydrology*, 525:264–276. doi: 10.1016/j.jhydrol.2015.03.053.

G. Baroni, L. Scheiffele, M. Schrön, J. Ingwersen, and S. Oswald. 2018. Uncertainty, sensitivity and improvements in soil moisture estimation with Sosmic-Ray Neutron Sensing. *Journal of Hydrology*, 564:873–887. doi: 10.1016/j.jhydrol.2018.07.053.

A. Belov, L. Baisultanova, E. Eroshenko, H. Mavromichalaki, V. Yanke, V. Pchelkin, C. Plainaki, and G. Mariatos. 2005. Magnetospheric effects in cosmic rays during the unique magnetic storm on November 2003. *Journal of Geophysical Research: Space Physics*, 110(A9). doi: 10.1029/2005JA011067.

W. R. Berghuijs, S. Harrigan, P. Molnar, L. J. Slater, and J. W. Kirchner. 2019. The relative importance of different flood-generating mechanisms across Europe. *Water Resources Research*, 55(6):4582–4593. doi: 10.1029/2019wr024841.

A. Best, J. Görres, M. Junker, K.-L. Kratz, M. Laubenstein, A. Long, S. Nisi, K. Smith, and M. Wiescher. 2016. Low energy neutron background in deep underground laboratories. *Nuclear Instruments and Methods in Physics Research Section A: Accelerators, Spectrometers, Detectors and Associated Equipment*, 812: 1–6. doi: 10.1016/j.nima.2015.12.034.

BKG - German Federal Agency for Cartography and Geodesy. 2018a. Digital landcover model: Atkis-basis-dlm (© geobasis-de/bkg 2018).

BKG - German Federal Agency for Cartography and Geodesy. 2018b. German administrative units atkis-vg2500, scale 1:2,500,000 (© geobasis-de/bkg 2018).

G. Blöschl, J. Hall, J. Parajka, R. A. P. Perdigão, B. Merz, B. Arheimer, G. T. Aronica, A. Bilibashi, O. Bonacci, M. Borga, I. Čanjevac, A. Castellarin, G. B. Chirico, P. Claps, K. Fiala, N. Frolova, L. Gorbachova, A. Gül, J. Hannaford, S. Harrigan, M. Kireeva, A. Kiss, T. R. Kjeldsen, S. Kohnová, J. J. Koskela, O. Ledvinka, N. Macdonald, M. Mavrova-Guirguinova, L. Mediero, R. Merz, P. Molnar, A. Montanari, C. Murphy, M. Osuch, V. Ovcharuk, I. Radevski, M. Rogger, J. L. Salinas, E. Sauquet, M. Šraj, J. Szolgay, A. Viglione, E. Volpi, D. Wilson, K. Zaimi, and N. Živković. 2017. Changing climate shifts timing of European floods. *Science*, 357(6351):588–590. doi: 10.1126/science.aan2506.

G. Blöschl, M. F. Bierkens, A. Chambel, C. Cudennec, G. Destouni, A. Fiori, J. W. Kirchner, J. J. McDonnell, H. H. Savenije, M. Sivapalan, C. Stumpp, E. Toth, E. Volpi, G. Carr, C. Lupton, J. Salinas, B. Széles, A. Viglione, H. Aksoy, S. T. Allen, A. Amin, V. Andréassian, B. Arheimer, S. K. Aryal, V. Baker, E. Bardsley, M. H. Barendrecht, A. Bartosova, O. Batelaan, W. R. Berghuijs, K. Beven, T. Blume, T. Bogaard, P. Borges de Amorim, M. E. Böttcher, G. Boulet, K. Breinl, M. Brilly, L. Brocca, W. Buytaert, A. Castellarin, A. Castelletti, X. Chen, Y. Chen, Y. Chen, P. Chifflard, P. Claps, M. P. Clark, A. L. Collins, B. Croke, A. Dathe, P. C. David, F. P. J. de Barros, G. de Rooij, G. Di Baldassarre, J. M. Driscoll, D. Duethmann, R. Dwivedi, E. Eris, W. H. Farmer, J. Feiccabrino, G. Ferguson, E. Ferrari, S. Ferraris, B. Fersch, D. Finger, L. Foglia, K. Fowler, B. Gartsman, S. Gascoin, E. Gaume, A. Gelfan, J. Geris, S. Gharari, T. Gleeson, M. Glendell, A. Gonzalez Bevacqua, M. P. González-Dugo, S. Grimaldi, A. B. Gupta, B. Guse, D. Han, D. Hannah, A. Harpold, S. Haun, K. Heal, K. Helfricht, M. Herrnegger, M. Hipsey, H. Hlaváčiková, C. Hohmann, L. Holko, C. Hopkinson, M. Hrachowitz, T. H. Illangasekare, A. Inam, C. Innocente, E. Istanbulluoglu, B. Jarihani, Z. Kalantari, A. Kalvans, S. Khanal, S. Khatami, J. Kiesel, M. Kirkby, W. Knoben, K. Kochanek, S. Kohnová, A. Kolechkina, S. Krause, D. Kreamer, H. Kreibich, H. Kunstmann, H. Lange, M. L. R. Liberato, E. Lindquist, T. Link,

J. Liu, D. P. Loucks, C. Luce, G. Mahé, O. Makarieva, J. Malard, S. Mashtayeva, S. Maskey, J. Mas-Pla, M. Mavrova-Guirguinova, M. Mazzoleni, S. Mernild, B. D. Misstear, A. Montanari, H. Müller-Thomy, A. Nabizadeh, F. Nardi, C. Neale, N. Nesterova, B. Nurtaev, V. O. Odongo, S. Panda, S. Pande, Z. Pang, G. Papacharalampous, C. Perrin, L. Pfister, R. Pimentel, M. J. Polo, D. Post, C. Prieto Sierra, M.-H. Ramos, M. Renner, J. E. Reynolds, E. Ridolfi, R. Rigon, M. Riva, D. E. Robertson, R. Rosso, T. Roy, J. H. Sá, G. Salvadori, M. Sandells, B. Schaefli, A. Schumann, A. Scolobig, J. Seibert, E. Servat, M. Shafiei, A. Sharma, M. Sidibe, R. C. Sidle, T. Skaugen, H. Smith, S. M. Spiessl, L. Stein, I. Steinsland, U. Strasser, B. Su, J. Szolgay, D. Tarboton, F. Tauro, G. Thirel, F. Tian, R. Tong, K. Tussupova, H. Tyralis, R. Uijlenhoet, R. van Beek, R. J. van der Ent, M. van der Ploeg, A. F. Van Loon, I. van Meerveld, R. van Nooijen, P. R. van Oel, J.-P. Vidal, J. von Freyberg, S. Vorogushyn, P. Wachniew, A. J. Wade, P. Ward, I. K. Westerberg, C. White, E. F. Wood, R. Woods, Z. Xu, K. K. Yilmaz, and Y. Zhang. 2019a. Twenty-three unsolved problems in hydrology (UPH) – a community perspective. *Hydrological Sciences Journal*, 64(10):1141–1158. doi: 10.1080/02626667.2019.1620507.

G. Blöschl, J. Hall, A. Viglione, R. A. P. Perdigão, J. Parajka, B. Merz, D. Lun, B. Arheimer, G. T. Aronica, A. Bilibashi, M. Boháč, O. Bonacci, M. Borga, I. Čanjevac, A. Castellarin, G. B. Chirico, P. Claps, N. Frolova, D. Ganora, L. Gorbachova, A. Gül, J. Hannaford, S. Harrigan, M. Kireeva, A. Kiss, T. R. Kjeldsen, S. Kohnová, J. J. Koskela, O. Ledvinka, N. Macdonald, M. Mavrova-Guirguinova, L. Mediero, R. Merz, P. Molnar, A. Montanari, C. Murphy, M. Osuch, V. Ovcharuk, I. Radevski, J. L. Salinas, E. Sauquet, M. Šraj, J. Szolgay, E. Volpi, D. Wilson, K. Zaimi, and N. Živković. 2019b. Changing climate both increases and decreases European river floods. *Nature*, 573(7772):108–111. doi: 10.1038/s41586-019-1495-6.

B. Boehrer and M. Schultze. 2008. Stratification of lakes. *Reviews of Geophysics*, 46(2). doi: 10.1029/2006RG000210.

B. Boehrer, U. Kiwel, K. Rahn, and M. Schultze. 2014. Chemocline erosion and its conservation by freshwater introduction to meromictic salt lakes. *Limnologica*, 44:81—-89. doi: 10.1016/j.limno.2013.08.003.

F. Boeing, O. Rakovec, R. Kumar, L. Samaniego, M. Schrön, A. Hildebrandt, C. Rebmann, S. Thober, S. Müller, S. Zacharias, H. Bogena, K. Schneider, R. Kiese, S. Attinger, and A. Marx. 2022. High-resolution drought simulations and comparison to soil moisture observations in Germany. *Hydrology and Earth System Sciences*, 26(19):5137–5161. doi: 10.5194/hess-26-5137-2022.

E. Boergens, A. Güntner, H. Dobslaw, and C. Dahle. 2020. Quantifying the central European droughts in 2018 and 2019 with GRACE Follow-On. *Geophysical Research Letters*, 47(14). doi: 10.1029/2020gl087285.

H. Bogena, C. Montzka, J. Huisman, A. Graf, M. Schmidt, M. Stockinger, C. von Hebel, H. Hendricks-Franssen, J. van der Kruk, W. Tappe, A. Lücke, R. Baatz, R. Bol, J. Groh, T. Pütz, J. Jakobi, R. Kunkel, J. Sorg, and H. Vereecken. 2018.

The TERENO-Rur hydrological observatory: A multiscale multi-compartment research platform for the advancement of hydrological science. *Vadose Zone Journal*, 17(1):180055. doi: 10.2136/vzj2018.03.0055.

H. R. Bogena, J. A. Huisman, R. Baatz, H.-J. H. Franssen, and H. Vereecken. 2013. Accuracy of the cosmic-ray soil water content probe in humid forest ecosystems: The worst case scenario. *Water Resources Research*, 49(9):5778–5791. doi: 10.1002/wrcr.20463.

H. R. Bogena, F. Herrmann, J. Jakobi, C. Brogi, A. Ilias, J. A. Huisman, A. Panagopoulos, and V. Pisinaras. 2020. Monitoring of snowpack dynamics with cosmic-ray neutron probes: A comparison of four conversion methods. *Frontiers in Water*, 2. doi: 10.3389/frwa.2020.00019.

H. R. Bogena, M. Schrön, J. Jakobi, P. Ney, S. Zacharias, M. Andreasen, R. Baatz, D. Boorman, M. B. Duygu, M. A. Eguibar-Galán, B. Fersch, T. Franke, J. Geris, M. G. Sanchis, Y. Kerr, T. Korf, Z. Mengistu, A. Mialon, P. Nasta, J. Nitychoruk, V. Pisinaras, D. Rasche, R. Rosolem, H. Said, P. Schattan, M. Zreda, S. Achleitner, E. Albentosa-Hernández, Z. Akyürek, T. Blume, A. del Campo, D. Canone, K. Dimitrova-Petrova, J. G. Evans, S. Ferraris, F. Frances, D. Gisolo, A. Güntner, F. Herrmann, J. Iwema, K. H. Jensen, H. Kunstmann, A. Lidón, M. C. Looms, S. Oswald, A. Panagopoulos, A. Patil, D. Power, C. Rebmann, N. Romano, L. Scheiffele, S. Seneviratne, G. Weltin, and H. Vereecken. 2022. COSMOS-Europe: a European network of cosmic-ray neutron soil moisture sensors. *Earth System Science Data*, 14(3):1125–1151. doi: 10.5194/essd-14-1125-2022.

B. Böhrer, H. Heidenreich, M. Schimmele, and M. Schultze. 1998. Numerical prognosis for salinity profiles of future lakes in the opencast mine Merseburg-Ost. *International Journal of Salt Lake Research*, 7(3):235–260. doi: 10.1007/BF02441877.

T. Brall, V. Mares, R. Bütikofer, and W. Rühm. 2021. Assessment of neutrons from secondary cosmic rays at mountain altitudes – geant4 simulations of environmental parameters including soil moisture and snow cover. *The Cryosphere*, 15(10):4769–4780. doi: 10.5194/tc-15-4769-2021.

I. Braun, J. Engler, J. Hörandel, and J. Milke. 2009. Forbush Decreases and solar events seen in the 10–20 GeV energy range by the Karlsruhe Muon Telescope. *Advances in Space Research*, 43(4):480–488. doi: 10.1016/j.asr.2008.07.012.

C. Brogi, H. R. Bogena, M. Köhli, J. A. Huisman, H.-J. Hendricks Franssen, and O. Dombrowski. 2022. Feasibility of irrigation monitoring with cosmic-ray neutron sensors. *Geoscientific Instrumentation, Methods and Data Systems*, 11(2):451–469. doi: 10.5194/gi-11-451-2022.

C. Brogi, V. Pisinaras, M. Köhli, O. Dombrowski, H.-J. Hendricks Franssen, K. Babakos, A. Chatzi, A. Panagopoulos, and H. R. Bogena. 2023. Monitoring irrigation in small orchards with cosmic-ray neutron sensors. *Sensors*, 23(5):2378. doi: 10.3390/s23052378.

A. Bronstert, A. Agarwal, B. Boessenkool, I. Crisologo, M. Fischer, M. Heistermann, L. Köhn-Reich, J. A. López-Tarazón, T. Moran, U. Ozturk, C. Reinhardt-Imjela,

and D. Wendi. 2018. Forensic hydro-meteorological analysis of an extreme flash flood: The 2016-05-29 event in Braunsbach, SW Germany. *Science of The Total Environment*, 630:977–991. doi: 10.1016/j.scitotenv.2018.02.241.

J. R. Brooks, F. C. Meinzer, R. Coulombe, and J. Gregg. 2002. Hydraulic redistribution of soil water during summer drought in two contrasting Pacific Northwest coniferous forests. *Tree Physiology*, 22(15–16):1107–1117. doi: 10.1093/treephys/22.15-16.1107.

W. G. Brown, M. H. Cosh, J. Dong, and T. E. Ochsner. 2023. Upscaling soil moisture from point scale to field scale: Toward a general model. *Vadose Zone Journal*, 22(2). doi: 10.1002/vzj2.20244.

G. Brunetti, J. Šimůnek, H. Bogena, R. Baatz, J. A. Huisman, H. Dahlke, and H. Vereecken. 2019. On the information content of cosmic-ray neutron data in the inverse estimation of soil hydraulic properties. *Vadose Zone Journal*, 18(1): 1–24. doi: 10.2136/vzj2018.06.0123.

R. Bütikofer. 1999. Pressure correction of GLE measurements in turbulent winds. In *International Cosmic Ray Conference*, volume 6, page 395.

R. Bütikofer. 2018. *Ground-Based Measurements of Energetic Particles by Neutron Monitors*, pages 95–111. Springer International Publishing, Cham. doi: 10.1007/978-3-319-60051-2_6.

A. Börner. 2015. *Neue Beiträge zum Naturraum und zur Landschaftsgeschichte im Teilgebiet Serrahn des Müritz-Nationalparks - Forschung und Monitoring*, volume 4, chapter Geologische Entwicklung des Gebietes um den Großen Fürstenseer See, page 21–29. Geozon Science Media, Berlin. doi: 10.3285/g.00012.

J. Canadell, R. B. Jackson, J. B. Ehleringer, H. A. Mooney, O. E. Sala, and E.-D. Schulze. 1996. Maximum rooting depth of vegetation types at the global scale. *Oecologia*, 108(4):583–595. doi: 10.1007/bf00329030.

C. Carranza, C. Nolet, M. Pezij, and M. van der Ploeg. 2021. Root zone soil moisture estimation with random forest. *Journal of Hydrology*, 593:125840. doi: 10.1016/j.jhydrol.2020.125840.

T. Chakraborty, S. Saha, and A. Reif. 2016. Biomass equations for european beech growing on dry sites. *iForest - Biogeosciences and Forestry*, 9(5):751–757. doi: 10.3832/ifor1881-009.

K. Chandler, C. Stevens, A. Binley, and A. Keith. 2018. Influence of tree species and forest land use on soil hydraulic conductivity and implications for surface runoff generation. *Geoderma*, 310:120–127. doi: 10.1016/j.geoderma.2017.08.011.

P. Chifflard, J. Kranl, G. z. Strassen, and H. Zepp. 2018. The significance of soil moisture in forecasting characteristics of flood events. a statistical analysis in two nested catchments. *Journal of Hydrology and Hydromechanics*, 66(1):1–11. doi: 10.1515/johh-2017-0037.

M. O. Cimpoiaşu, O. Kuras, T. Pridmore, and S. J. Mooney. 2020. Potential of geoelectrical methods to monitor root zone processes and structure: A review. *Geoderma*, 365:114232. doi: 10.1016/j.geoderma.2020.114232.

J. M. Clem and L. I. Dorman. 2000. Neutron monitor response functions. *Space Science Reviews*, 93(1):335–359. doi: 10.1023/A:1026508915269.

J. M. Clem, J. W. Bieber, P. Evenson, D. Hall, J. E. Humble, and M. Duldig. 1997. Contribution of obliquely incident particles to neutron monitor counting rate. *Journal of Geophysical Research: Space Physics*, 102(A12):26919–26926. doi: 10.1029/97JA02366.

H. M. Cooper, E. Bennett, J. Blake, E. Blyth, D. Boorman, E. Cooper, J. Evans, M. Fry, A. Jenkins, R. Morrison, D. Rylett, S. Stanley, M. Szczykulska, E. Trill, V. Antoniou, A. Askquith-Ellis, L. Ball, M. Brooks, M. A. Clarke, N. Cowan, A. Cumming, P. Farrand, O. Hitt, W. Lord, P. Scarlett, O. Swain, J. Thornton, A. Warwick, and B. Winterbourn. 2021. COSMOS-UK: national soil moisture and hydrometeorology data for environmental science research. *Earth System Science Data*, 13(4):1737–1757. doi: 10.5194/essd-13-1737-2021.

E. Daly and A. Porporato. 2005. A review of soil moisture dynamics: From rainfall infiltration to ecosystem response. *Environmental Engineering Science*, 22(1): 9–24. doi: 10.1089/ees.2005.22.9.

P. Davies, R. Baatz, H. R. Bogena, E. Quansah, and L. K. Amekudzi. 2022. Optimal temporal filtering of the cosmic-ray neutron signal to reduce soil moisture uncertainty. *Sensors*, 22(23):9143. doi: 10.3390/s22239143.

S. M. de Jong, R. A. Heijenk, W. Nijland, and M. van der Meijde. 2020. Monitoring soil moisture dynamics using electrical resistivity tomography under homogeneous field conditions. *Sensors*, 20(18):5313. doi: 10.3390/s20185313.

R. R. S. de Mendonça, C. R. Braga, E. Echer, A. Dal Lago, K. Munakata, T. Kuwabara, M. Kozai, C. Kato, M. Rockenbach, N. J. Schuch, H. K. Al Jassar, M. M. Sharma, M. Tokumaru, M. L. Duldig, J. E. Humble, P. Evenson, and I. Sabbah. 2016. The temperature effect in secondary cosmic rays (muons) observed at the ground: Analysis of the global muon detector network data. *The Astrophysical Journal*, 830(2):88. doi: 10.3847/0004-637x/830/2/88.

G. Demir, B. Michalzik, J. Filipzik, J. C. Metzger, and A. Hildebrandt. 2022. Spatial variation of grassland canopy affects soil wetting patterns and preferential flow. *Hydrological Processes*, 36(12). doi: 10.1002/hyp.14760.

D. Desilets and M. Zreda. 2001. On scaling cosmogenic nuclide production rates for altitude and latitude using cosmic-ray measurements. *Earth and Planetary Science Letters*, 193(1–2):213–225. doi: 10.1016/S0012-821X(01)00477-0.

D. Desilets and M. Zreda. 2013. Footprint diameter for a cosmic-ray soil moisture probe: Theory and Monte Carlo simulations. *Water Resources Research*, 49(6): 3566–3575. doi: 10.1002/wrcr.20187.

D. Desilets, M. Zreda, and T. Prabu. 2006. Extended scaling factors for in situ cosmogenic nuclides: New measurements at low latitude. *Earth and Planetary Science Letters*, 246(3-4):265–276. doi: 10.1016/j.epsl.2006.03.051.

D. Desilets, M. Zreda, and T. P. A. Ferré. 2010. Nature's neutron probe: Land surface hydrology at an elusive scale with cosmic rays. *Water Resources Research*, 46(11). doi: 10.1029/2009wr008726.

U. Dettmann, M. Bechtold, E. Frahm, and B. Tiemeyer. 2014. On the applicability of unimodal and bimodal van Genuchten–Mualem based models to peat and other organic soils under evaporation conditions. *Journal of Hydrology*, 515:103–115. doi: 10.1016/j.jhydrol.2014.04.047.

K. Dimitrova-Petrova, J. Geris, E. M. Wilkinson, R. Rosolem, L. Verrot, A. Lilly, and C. Soulsby. 2020. Opportunities and challenges in using catchment-scale storage estimates from cosmic ray neutron sensors for rainfall-runoff modelling. *Journal of Hydrology*, page 124878. doi: 10.1016/j.jhydrol.2020.124878.

S. L. Dingman. 2015. *Physical hydrology*. Waveland Press, 3 edition.

V. Döpper, T. Jagdhuber, A.-K. Holtgrave, M. Heistermann, T. Francke, B. Kleinschmit, and M. Förster. 2022. Following the cosmic-ray-neutron-sensing-based soil moisture under grassland and forest: Exploring the potential of optical and SAR remote sensing. *Science of Remote Sensing*, 5:100056. doi: 10.1016/j.srs.2022.100056.

W. Dorigo, P. van Oevelen, W. Wagner, M. Drusch, S. Mecklenburg, A. Robock, and T. Jackson. 2011. A new international network for in situ soil moisture data. *Eos, Transactions American Geophysical Union*, 92(17):141–142. doi: 10.1029/2011eo170001.

W. Dorigo, S. Dietrich, F. Aires, L. Brocca, S. Carter, J.-F. Cretaux, D. Dunkerley, H. Enomoto, R. Forsberg, A. Güntner, M. I. Hegglin, R. Hollmann, D. F. Hurst, J. A. Johannessen, C. Kummerow, T. Lee, K. Luojus, U. Looser, D. G. Miralles, V. Pellet, T. Recknagel, C. R. Vargas, U. Schneider, P. Schoeneich, M. Schröder, N. Tapper, V. Vuglinsky, W. Wagner, L. Yu, L. Zappa, M. Zemp, and V. Aich. 2021a. Closing the water cycle from observations across scales: Where do we stand? *Bulletin of the American Meteorological Society*, 102(10):E1897–E1935. doi: 10.1175/bams-d-19-0316.1.

W. Dorigo, I. Himmelbauer, D. Aberer, L. Schremmer, I. Petrakovic, L. Zappa, W. Preimesberger, A. Xaver, F. Annor, J. Ardö, D. Baldocchi, M. Bitelli, G. Blöschl, H. Bogena, L. Brocca, J.-C. Calvet, J. J. Camarero, G. Capello, M. Choi, M. C. Cosh, N. van de Giesen, I. Hajdu, J. Ikonen, K. H. Jensen, K. D. Kanniah, I. de Kat, G. Kirchengast, P. Kumar Rai, J. Kyrouac, K. Larson, S. Liu, A. Loew, M. Moghaddam, J. Martínez Fernández, C. Mattar Bader, R. Morbidelli, J. P. Musial, E. Osenga, M. A. Palecki, T. Pellarin, G. P. Petropoulos, I. Pfeil, J. Powers, A. Robock, C. Rüdiger, U. Rummel, M. Strobel, Z. Su, R. Sullivan, T. Tagesson, A. Varlagin, M. Vreugdenhil, J. Walker, J. Wen, F. Wenger, J. P. Wigneron, M. Woods, K. Yang, Y. Zeng, X. Zhang, M. Zreda, S. Dietrich, A. Gruber, P. van Oevelen, W. Wagner, K. Scipal, M. Drusch, and R. Sabia.

2021b. The International Soil Moisture Network: serving earth system science for over a decade. *Hydrology and Earth System Sciences*, 25(11):5749–5804. doi: 10.5194/hess-25-5749-2021.

L. I. Dorman. 2004. *Cosmic Rays in the Earth's Atmosphere and Underground*. Astrophysics and Space Science Library. Springer Netherlands, 1 edition.

F. Dottori, W. Szewczyk, J.-C. Ciscar, F. Zhao, L. Alfieri, Y. Hirabayashi, A. Bianchi, I. Mongelli, K. Frieler, R. A. Betts, and L. Feyen. 2018. Increased human and economic losses from river flooding with anthropogenic warming. *Nature Climate Change*, 8(9):781–786. doi: 10.1038/s41558-018-0257-z.

T. J. Dunai. 2000. Scaling factors for production rates of in situ produced cosmogenic nuclides: a critical reevaluation. *Earth and Planetary Science Letters*, 176(1):157–169.

M. B. Duygu and Z. Akyürek. 2019. Using cosmic-ray neutron probes in validating satellite soil moisture products and land surface models. *Water*, 11(7):1362. doi: 10.3390/w11071362.

DWD - German Weather Service. 2020a. Multi-annual temperature observations 1981-2010.

DWD - German Weather Service. 2020b. Multi-annual precipitation observations 1981-2010.

J. G. Evans, H. C. Ward, J. R. Blake, E. J. Hewitt, R. Morrison, M. Fry, L. A. Ball, L. C. Doughty, J. W. Libre, O. E. Hitt, D. Rylett, R. J. Ellis, A. C. Warwick, M. Brooks, M. A. Parkes, G. M. H. Wright, A. C. Singer, D. B. Boorman, and A. Jenkins. 2016. Soil water content in southern england derived from a cosmic-ray soil moisture observing system – COSMOS-UK. *Hydrological Processes*, 30 (26):4987–4999. doi: 10.1002/hyp.10929.

J. S. Famiglietti, D. Ryu, A. A. Berg, M. Rodell, and T. J. Jackson. 2008. Field observations of soil moisture variability across scales. *Water Resources Research*, 44(1). doi: 10.1029/2006wr005804.

Y. Fan, G. Miguez-Macho, E. G. Jobbágy, R. B. Jackson, and C. Otero-Casal. 2017. Hydrologic regulation of plant rooting depth. *Proceedings of the National Academy of Sciences*, 114(40):10572–10577. doi: 10.1073/pnas.1712381114.

F. Faridani, A. Farid, H. Ansari, and S. Manfreda. 2017. A modified version of the SMAR model for estimating root-zone soil moisture from time-series of surface soil moisture. *Water SA*, 43(3):492. doi: 10.4314/wsa.v43i3.14.

M. Farokhi, F. Faridani, R. Lasaponara, H. Ansari, and A. Faridhosseini. 2021. Enhanced estimation of root zone soil moisture at 1 km resolution using SMAR model and MODIS-based downscaled AMSR2 soil moisture data. *Sensors*, 21(15): 5211. doi: 10.3390/s21155211.

A. Ferreira, C. Coelho, R. Walsh, R. Shakesby, A. Ceballos, and S. Doerr. 2000. Hydrological implications of soil water-repellency in Eucalyptus globulus forests,

north-central Portugal. *Journal of Hydrology*, 231–232:165–177. doi: 10.1016/s0022-1694(00)00192-x.

V. Ferronsky. 2015. *Nuclear Geophysics*. Springer International Publishing.

B. Fersch, T. Jagdhuber, M. Schrön, I. Völksch, and M. Jäger. 2018. Synergies for soil moisture retrieval across scales from airborne polarimetric SAR, cosmic ray neutron roving, and an in situ sensor network. *Water Resources Research*, 54(11): 9364–9383. doi: 10.1029/2018wr023337.

B. Fersch, T. Francke, M. Heistermann, M. Schrön, V. Döpper, J. Jakobi, G. Baroni, T. Blume, H. Bogena, C. Budach, T. Gränzig, M. Förster, A. Güntner, H.-J. Hendricks Franssen, M. Kasner, M. Köhli, B. Kleinschmit, H. Kunstmann, A. Patil, D. Rasche, L. Scheiffele, U. Schmidt, S. Szulc-Seyfried, J. Weimar, S. Zacharias, M. Zreda, B. Heber, R. Kiese, V. Mares, H. Mollenhauer, I. Völksch, and S. Oswald. 2020. A dense network of cosmic-ray neutron sensors for soil moisture observation in a highly instrumented pre-alpine headwater catchment in Germany. *Earth System Science Data*, 12(3):2289–2309. doi: 10.5194/essd-12-2289-2020.

C. Fischer-Bedtke, J. C. Metzger, G. Demir, T. Wutzler, and A. Hildebrandt. 2023. Throughfall spatial patterns translate into spatial patterns of soil moisture dynamics – empirical evidence. *Hydrology and Earth System Sciences*, 27(15):2899–2918. doi: 10.5194/hess-27-2899-2023.

T. Francke, M. Heistermann, M. Köhli, C. Budach, M. Schrön, and S. E. Oswald. 2022. Assessing the feasibility of a directional Cosmic-Ray Neutron Sensing sensor for estimating soil moisture. *Geoscientific Instrumentation, Methods and Data Systems*, 11(1):75–92. doi: 10.5194/gi-11-75-2022.

T. E. Franz, M. Zreda, T. P. A. Ferre, R. Rosolem, C. Zweck, S. Stillman, X. Zeng, and W. J. Shuttleworth. 2012a. Measurement depth of the cosmic ray soil moisture probe affected by hydrogen from various sources. *Water Resources Research*, 48 (8). doi: 10.1029/2012wr011871.

T. E. Franz, M. Zreda, R. Rosolem, and T. Ferre. 2012b. Field validation of a cosmic-ray neutron sensor using a distributed sensor network. *Vadose Zone Journal*, 11 (4):vzj2012.0046. doi: 10.2136/vzj2012.0046.

T. E. Franz, M. Zreda, T. P. A. Ferre, and R. Rosolem. 2013a. An assessment of the effect of horizontal soil moisture heterogeneity on the area-average measurement of cosmic-ray neutrons. *Water Resources Research*, 49(10):6450–6458. doi: 10.1002/wrcr.20530.

T. E. Franz, M. Zreda, R. Rosolem, and T. P. A. Ferre. 2013b. A universal calibration function for determination of soil moisture with cosmic-ray neutrons. *Hydrology and Earth System Sciences*, 17(2):453–460. doi: 10.5194/hess-17-453-2013.

T. E. Franz, T. Wang, W. Avery, C. Finkenbiner, and L. Brocca. 2015. Combined analysis of soil moisture measurements from roving and fixed cosmic ray neutron probes for multiscale real-time monitoring. *Geophysical Research Letters*, 42(9): 3389–3396. doi: 10.1002/2015gl063963.

T. E. Franz, A. Wahbi, M. Vreugdenhil, G. Weltin, L. Heng, M. Oismueller, P. Strauss, G. Dercon, and D. Desilets. 2016. Using cosmic-ray neutron probes to monitor landscape scale soil water content in mixed land use agricultural systems. *Applied and Environmental Soil Science*, 2016:1–11. doi: 10.1155/2016/4323742.

T. E. Franz, A. Wahbi, J. Zhang, M. Vreugdenhil, L. Heng, G. Dercon, P. Strauss, L. Brocca, and W. Wagner. 2020. Practical data products from Cosmic-Ray Neutron Sensing for hydrological applications. *Frontiers in Water*, 2. doi: 10.3389/frwa.2020.00009.

J. Fäth, J. Kunz, and C. Kneisel. 2022. Monitoring spatiotemporal soil moisture changes in the subsurface of forest sites using electrical resistivity tomography (ERT). *Journal of Forestry Research*, 33(5):1649–1662. doi: 10.1007/s11676-022-01498-x.

X. Gao, X. Zhao, L. Brocca, D. Pan, and P. Wu. 2018. Testing of observation operators designed to estimate profile soil moisture from surface measurements. *Hydrological Processes*, 33(4):575–584. doi: 10.1002/hyp.13344.

W. Gardner and D. Kirkham. 1952. Determination of soil moisture by neutron scattering. *Soil Science*, 73(5):391–402.

W. H. Gardner, 1986. Water content. In *SSSA Book Series, Methods of Soil Analysis, Part 1. Physical and Mineralogical Methods-Agronomy Monograph no. 9 (2nd Edition)*, pages 493–544. Soil Science Society of America, American Society of Agronomy. doi: 10.2136/sssabookser5.1.2ed.c21.

S. Garny, V. Mares, and W. Rühm. 2009. Response functions of a bonner sphere spectrometer calculated with GEANT4. *Nuclear Instruments and Methods in Physics Research Section A: Accelerators, Spectrometers, Detectors and Associated Equipment*, 604(3):612–617. doi: 10.1016/j.nima.2009.02.044.

W. Geller, M. Schultze, B. Kleinmann, and C. Wolkersdorfer. 2013. *Acidic Pit Lakes: The Legacy of Coal and Metal Surface Mines*. Springer Berlin Heidelberg.

A. Germon, J.-P. Laclau, A. Robin, and C. Jourdan. 2020. Tamm review: Deep fine roots in forest ecosystems: Why dig deeper? *Forest Ecology and Management*, 466:118135. doi: 10.1016/j.foreco.2020.118135.

F. Gheybi, P. Paridad, F. Faridani, A. Farid, A. Pizarro, M. Fiorentino, and S. Manfreda. 2019. Soil moisture monitoring in iran by implementing satellite data into the root-zone SMAR model. *Hydrology*, 6(2):44. doi: 10.3390/hydrology6020044.

S. Gianessi, M. Polo, L. Stevanato, M. Lunardon, T. Francke, S. Oswald, H. Ahmed, A. Tolosa, G. Weltin, G. Dercon, E. Fulajtar, L. Heng, and G. Baroni. 2022. Testing a novel sensor design to jointly measure cosmic-ray neutrons, muons and gamma rays for non-invasive soil moisture estimation. *Geoscientific Instrumentation, Methods and Data System Discussions*. doi: 10.5194/gi-2022-20.

S. Glasstone and A. Sesonske, 1981. Nuclear reactor engineering.

T. Goorley, M. James, T. Booth, F. Brown, J. Bull, L. Cox, J. Durkee, J. Elson, M. Fensin, R. Forster, J. Hendricks, H. Hughes, R. Johns, B. Kiedrowski, R. Martz, S. Mashnik, G. McKinney, D. Pelowitz, R. Prael, J. Sweezy, L. Waters, T. Wilcox, and T. Zukaitis. 2012. Initial MCNP6 release overview. *Nuclear Technology*, 180(3):298–315. doi: 10.13182/NT11-135.

M. Grieger, T. Hensel, J. Agramunt, D. Bemmerer, D. Degering, I. Dillmann, L. Fraile, D. Jordan, U. Köster, M. Marta, S. Müller, T. Szücs, J. Taín, and K. Zuber. 2020. Neutron flux and spectrum in the Dresden Felsenkeller underground facility studied by moderated 3He counters. *Physical Review D*, 101(12): 123027. doi: 10.1103/physrevd.101.123027.

M. Grillakis, A. Koutroulis, J. Komma, I. Tsanis, W. Wagner, and G. Blöschl. 2016. Initial soil moisture effects on flash flood generation – a comparison between basins of contrasting hydro-climatic conditions. *Journal of Hydrology*, 541:206–217. doi: 10.1016/j.jhydrol.2016.03.007.

K. Gudima, S. Mashnik, and V. Toneev. 1983. Cascade-exciton model of nuclear reactions. *Nuclear Physics A*, 401(2):329–361. doi: 10.1016/0375-9474(83)90532-8.

R. Gugerli, N. Salzmann, M. Huss, and D. Desilets. 2019. Continuous and autonomous snow water equivalent measurements by a cosmic ray sensor on an alpine glacier. *The Cryosphere*, 13(12):3413–3434. doi: 10.5194/tc-13-3413-2019.

R. Gugerli, D. Desilets, and N. Salzmann. 2022. Brief communication: Application of a muonic cosmic ray snow gauge to monitor the snow water equivalent on alpine glaciers. *The Cryosphere*, 16(3):799–806.

X. Guo, X. Fang, Q. Zhu, S. Jiang, J. Tian, Q. Tian, and J. Jin. 2023. Estimation of root-zone soil moisture in semi-arid areas based on remotely sensed data. *Remote Sensing*, 15(8):2003. doi: 10.3390/rs15082003.

H. V. Gupta, H. Kling, K. K. Yilmaz, and G. F. Martinez. 2009. Decomposition of the mean squared error and NSE performance criteria: Implications for improving hydrological modelling. *Journal of Hydrology*, 377(1-2):80–91. doi: 10.1016/j.jhydrol.2009.08.003.

A. D. P. Hands, F. Baird, K. A. Ryden, C. S. Dyer, F. Lei, J. G. Evans, J. R. Wallbank, M. Szczykulska, D. Rylett, R. Rosolem, S. Fowler, D. Power, and E. M. Henley. 2021. Detecting ground level enhancements using soil moisture sensor networks. *Space Weather*, 19(8):e2021SW002800. doi: 10.1029/2021SW002800.

A. Hawdon, D. McJannet, and J. Wallace. 2014. Calibration and correction procedures for cosmic-ray neutron soil moisture probes located across Australia. *Water Resources Research*, 50(6):5029–5043. doi: 10.1002/2013wr015138.

Q. He, X. Chen, H. Sun, J. Xu, Z. Liu, S. Zhou, and Z. Chen. 2022. Quantitative separation of the local vadose zone water storage changes using the superconductive gravity technique. *Journal of Hydrology*, 609:127734. doi: 10.1016/j.jhydrol.2022.127734.

I. Heidbüchel, A. Güntner, and T. Blume. 2016. Use of cosmic-ray neutron sensors for soil moisture monitoring in forests. *Hydrology and Earth System Sciences*, 20 (3):1269–1288. doi: 10.5194/hess-20-1269-2016.

H. Heidenreich, B. Boehrer, R. Kater, and G. Hennig. 1999. Gekoppelte Modellierung geohydraulischer und limnophysikalischer Vorgänge in Tagebaurestseen und ihrer Umgebung. *Grundwasser*, 4(2):49—-54. doi: 10.1007/s767-1999-8604-4.

I. Heinrich, D. Balanzategui, O. Bens, G. Blasch, T. Blume, F. Böttcher, E. Borg, B. Brademann, A. Brauer, C. Conrad, E. Dietze, N. Dräger, P. Fiener, H. H. Gerke, A. Güntner, I. Heine, G. Helle, M. Herbrich, K. Harfenmeister, K.-U. Heußner, C. Hohmann, S. Itzerott, G. Jurasinski, K. Kaiser, C. Kappler, F. Koebsch, S. Liebner, G. Lischeid, B. Merz, K. D. Missling, M. Morgner, S. Pinkerneil, B. Plessen, T. Raab, T. Ruhtz, T. Sachs, M. Sommer, D. Spengler, V. Stender, P. Stüve, and F. Wilken. 2018. Interdisciplinary geo-ecological research across time scales in the Northeast German Lowland Observatory (TERENO-NE). *Vadose Zone Journal*, 17(1):180116. doi: 10.2136/vzj2018.06.0116.

M. Heistermann, T. Francke, M. Schrön, and S. E. Oswald. 2021. Spatio-temporal soil moisture retrieval at the catchment scale using a dense network of cosmic-ray neutron sensors. *Hydrology and Earth System Sciences*, 25(9):4807–4824. doi: 10.5194/hess-25-4807-2021.

M. Heistermann, H. Bogena, T. Francke, A. Güntner, J. Jakobi, D. Rasche, M. Schrön, V. Döpper, B. Fersch, J. Groh, A. Patil, T. Pütz, M. Reich, S. Zacharias, C. Zengerle, and S. Oswald. 2022. Soil moisture observation in a forested headwater catchment: combining a dense cosmic-ray neutron sensor network with roving and hydrogravimetry at the TERENO site Wüstebach. *Earth System Science Data*, 14(5):2501–2519. doi: 10.5194/essd-14-2501-2022.

M. Heistermann, T. Francke, L. Scheiffele, K. Dimitrova Petrova, C. Budach, M. Schrön, B. Trost, D. Rasche, A. Güntner, V. Döpper, M. Förster, M. Köhli, L. Angermann, N. Antonoglou, M. Zude-Sasse, and S. E. Oswald. 2023. Three years of soil moisture observations by a dense Cosmic-Ray Neutron Sensing cluster at an agricultural research site in north-east Germany. *Earth System Science Data*, 15(7):3243–3262. doi: 10.5194/essd-15-3243-2023.

K. Herbst, A. Kopp, and B. Heber. 2013. Influence of the terrestrial magnetic field geometry on the cutoff rigidity of cosmic ray particles. *Annales Geophysicae*, 31 (10):1637–1643. doi: 10.5194/angeo-31-1637-2013.

W. N. Hess, E. H. Canfield, and R. E. Lingenfelter. 1961. Cosmic-ray neutron demography. *Journal of Geophysical Research (1896-1977)*, 66(3):665–677. doi: 10.1029/JZ066i003p00665.

G. Heusser. 1996. Cosmic ray interaction study with low-level Ge-spectrometry. *Nuclear Instruments and Methods in Physics Research Section A: Accelerators, Spectrometers, Detectors and Associated Equipment*, 369(2–3):539–543. doi: 10.1016/s0168-9002(96)80046-5.

Y. Hirabayashi, R. Mahendran, S. Koirala, L. Konoshima, D. Yamazaki, S. Watanabe, H. Kim, and S. Kanae. 2013. Global flood risk under climate change. *Nature Climate Change*, 3(9):816–821. doi: 10.1038/nclimate1911.

C. Holgate, R. D. Jeu, A. van Dijk, Y. Liu, L. Renzullo, Vinodkumar, I. Dharssi, R. Parinussa, R. V. D. Schalie, A. Gevaert, J. Walker, D. McJannet, J. Cleverly, V. Haverd, C. Trudinger, and P. Briggs. 2016. Comparison of remotely sensed and modelled soil moisture data sets across Australia. *Remote Sensing of Environment*, 186:479–500. doi: 10.1016/j.rse.2016.09.015.

J. W. Hopmans, D. R. Nielsen, and K. L. Bristow. 2002. *How useful are small-scale soil hydraulic property measurements for large-scale vadose zone modeling?*, volume 129, pages 247–258. American Geophysical Union. doi: 10.1029/129gm20.

X. Hu, X. Li, Y. Zhao, Y. Cheng, Z. Gao, and Z. Yang. 2022. Identification of water flow through non-root soil macropores and along roots in shrub-encroached grassland. *European Journal of Soil Science*, 73(4). doi: 10.1111/ejss.13260.

G. Hubert, M. T. Pazianotto, and C. A. Federico. 2016. Modeling of ground albedo neutrons to investigate seasonal cosmic ray-induced neutron variations measured at high-altitude stations. *Journal of Geophysical Research: Space Physics*, 121 (12):12,186–12,201. doi: 10.1002/2016ja023055.

G. Hubert, M. T. Pazianotto, C. A. Federico, and P. Ricaud. 2019. Analysis of the Forbush Decreases and ground-level enhancement on september 2017 using neutron spectrometers operated in Antarctic and midlatitude stations. *Journal of Geophysical Research: Space Physics*, 124(1):661–673. doi: 10.1029/2018ja025834.

IAEA - International Atomic Energy Agency. 1970. Neutron moisture gauges - a guide-book on theory and practive. techreport 112, IAEA - International Atomic Energy Agency, Vienna. URL `https://inis.iaea.org/collection/NCLCollectionStore/_Public/01/001/1001730.pdf`.

J. Iwema, R. Rosolem, R. Baatz, T. Wagener, and H. R. Bogena. 2015. Investigating temporal field sampling strategies for site-specific calibration of three soil moisture–neutron intensity parameterisation methods. *Hydrology and Earth System Sciences*, 19(7):3203–3216. doi: 10.5194/hess-19-3203-2015.

J. Iwema, R. Rosolem, M. Rahman, E. Blyth, and T. Wagener. 2017. Land surface model performance using cosmic-ray and point-scale soil moisture measurements for calibration. *Hydrology and Earth System Sciences*, 21(6):2843–2861. doi: 10.5194/hess-21-2843-2017.

J. Iwema, M. Schrön, J. K. D. Silva, R. S. D. P. Lopes, and R. Rosolem. 2021. Accuracy and precision of the cosmic-ray neutron sensor for soil moisture estimation at humid environments. *Hydrological Processes*, 35(11). doi: 10.1002/hyp.14419.

R. B. Jackson, J. Canadell, J. R. Ehleringer, H. A. Mooney, O. E. Sala, and E. D. Schulze. 1996. A global analysis of root distributions for terrestrial biomes. *Oecologia*, 108(3):389–411. doi: 10.1007/bf00333714.

T. J. Jackson, M. H. Cosh, R. Bindlish, P. J. Starks, D. D. Bosch, M. Seyfried, D. C. Goodrich, M. S. Moran, and J. Du. 2010. Validation of advanced microwave scanning radiometer soil moisture products. *IEEE Transactions on Geoscience and Remote Sensing*, 48(12):4256–4272. doi: 10.1109/tgrs.2010.2051035.

J. Jakobi, J. A. Huisman, H. Vereecken, B. Diekkrüger, and H. R. Bogena. 2018. Cosmic Ray Neutron Sensing for simultaneous soil water content and biomass quantification in drought conditions. *Water Resources Research*, 54(10):7383–7402. doi: 10.1029/2018wr022692.

J. Jakobi, J. A. Huisman, M. Schrön, J. Fiedler, C. Brogi, H. Vereecken, and H. R. Bogena. 2020. Error estimation for soil moisture measurements with Cosmic Ray Neutron Sensing and implications for rover surveys. *Frontiers in Water*, 2. doi: 10.3389/frwa.2020.00010.

J. Jakobi, J. A. Huisman, M. Köhli, D. Rasche, H. Vereecken, and H. R. Bogena. 2021. The footprint characteristics of cosmic ray thermal neutrons. *Geophysical Research Letters*, 48(15). doi: 10.1029/2021GL094281.

J. Jakobi, J. A. Huisman, H. Fuchs, H. Vereecken, and H. R. Bogena. 2022. Potential of thermal neutrons to correct cosmic-ray neutron soil moisture content measurements for dynamic biomass effects. *Water Resources Research*, 58(8). doi: 10.1029/2022wr031972.

J. Jeong, S. Lee, and M. Choi. 2021. Correction efficiency and error characteristics for cosmic-ray soil moisture on mountainous terrain. *Journal of Hydrology*, 601: 126657. doi: 10.1016/j.jhydrol.2021.126657.

Y. Jiang, K. Xuan, C. Gao, Y. Liu, Y. Zhao, H. Deng, X. Li, and J. Liu. 2023. Investigating the potential of Cosmic-Ray Neutron Sensing for estimating soil water content in farmland and mountainous areas. *Water*, 15(8):1500. doi: 10.3390/w15081500.

G. Jost, H. Schume, H. Hager, G. Markart, and B. Kohl. 2012. A hillslope scale comparison of tree species influence on soil moisture dynamics and runoff processes during intense rainfall. *Journal of Hydrology*, 420-421:112–124. doi: 10.1016/j.jhydrol.2011.11.057.

M. Kasner, S. Zacharias, and M. Schrön. 2022. On soil bulk density and its influence to soil moisture estimation with cosmic-ray neutrons. *Hydrology and Earth System Sciences Discussions*. doi: 10.5194/hess-2022-123.

B. R. Keller, L. G. Everett, and R. J. Marks. 1990. Effects of access tube material and grout on neutron probe measurements in the vadose zone. *Groundwater Monitoring & Remediation*, 10(1):96–100. doi: 10.1111/j.1745-6592.1990.tb00326.x.

M. Kemter, B. Merz, N. Marwan, S. Vorogushyn, and G. Blöschl. 2020. Joint trends in flood magnitudes and spatial extents across Europe. *Geophysical Research Letters*, 47(7). doi: 10.1029/2020gl087464.

R. Kiese, B. Fersch, C. Baessler, C. Brosy, K. Butterbach-Bahl, C. Chwala, M. Dannenmann, J. Fu, R. Gasche, R. Grote, C. Jahn, J. Klatt, H. Kunstmann, M. Mauder, T. Rödiger, G. Smiatek, M. Soltani, R. Steinbrecher, I. Völksch, J. Werhahn, B. Wolf, M. Zeeman, and H. Schmid. 2018. The TERENO prealpine observatory: Integrating meteorological, hydrological, and biogeochemical measurements and modeling. *Vadose Zone Journal*, 17(1):180060. doi: 10.2136/vzj2018.03.0060.

P. Kobelev, A. Belov, E. Mavromichalaki, M. Gerontidou, and V. Yanke. 2011. Variations of barometric coefficients of the neutron component in the 22-23 cycles of solar activity. *CD Proc. 32nd ICRC, id0654, Beijing.*

M. Kodama. 1980. Continuous monitoring of snow water equivalent using cosmic ray neutrons. *Cold Regions Science and Technology*, 3(4):295–303. doi: 10.1016/0165-232x(80)90036-1.

M. Kodama, S. Kawasaki, and M. Wada. 1975. A cosmic-ray snow gauge. *International Journal of Applied Radiation and Isotopes*, 26:774–775.

M. Kodama, K. Nakai, S. Kawasaki, and M. Wada. 1979. An application of cosmic-ray neutron measurements to the determination of the snow-water equivalent. *Journal of Hydrology*, 41(1-2):85–92. doi: 10.1016/0022-1694(79)90107-0.

M. Kodama, S. Kudo, and T. Kosuge. 1985. Application of atmospheric neutrons to soil moisture measurement. *Soil Science*, 140(4):237–242.

M. Köhli, M. Schrön, S. Zacharias, and U. Schmidt. 2023. URANOS v1.0 – the Ultra Rapid Adaptable Neutron-Only Simulation for environmental research. *Geoscientific Model Development*, 16(2):449–477. doi: 10.5194/gmd-16-449-2023.

V. K. Korotkov, M. D. Berkova, A. V. Belov, E. A. Eroshenko, P. G. Kobelev, and V. G. Yanke. 2011. Effect of snow in cosmic ray variations and methods for taking it into consideration. *Geomagnetism and Aeronomy*, 51(2):247–253. doi: 10.1134/S0016793211020095.

J. H. Kramer, S. J. Cullen, and L. G. Everett. 1992. Vadose zone monitoring with the neutron moisture probe. *Groundwater Monitoring & Remediation*, 12 (3):177–187. doi: 10.1111/j.1745-6592.1992.tb00058.x.

K. J. Kristensen. 1973. Depth intervals and topsoil moisture measurement with the neutron depth probe. *Hydrology Research*, 4(2):77–85. doi: 10.2166/nh.1973.0007.

E. S. Krueger, T. E. Ochsner, D. M. Engle, J. Carlson, D. Twidwell, and S. D. Fuhlendorf. 2015. Soil moisture affects growing-season wildfire size in the southern Great Plains. *Soil Science Society of America Journal*, 79(6):1567–1576. doi: 10.2136/sssaj2015.01.0041.

E. S. Krueger, M. R. Levi, K. O. Achieng, J. D. Bolten, J. D. Carlson, N. C. Coops, Z. A. Holden, B. I. Magi, A. J. Rigden, and T. E. Ochsner. 2022. Using soil moisture information to better understand and predict wildfire danger: a review of recent developments and outstanding questions. *International Journal of Wildland Fire*, 32(2):111–132. doi: 10.1071/wf22056.

H. Krüger and H. Moraal. 2010. A calibration neutron monitor: Statistical accuracy and environmental sensitivity. *Advances in Space Research*, 46(11):1394–1399. doi: 10.1016/j.asr.2010.07.008.

H. Krüger, H. Moraal, J. W. Bieber, J. M. Clem, P. A. Evenson, K. R. Pyle, M. L. Duldig, and J. E. Humble. 2008. A calibration neutron monitor: Energy response and instrumental temperature sensitivity. *Journal of Geophysical Research: Space Physics*, 113(A8). doi: 10.1029/2008JA013229.

K. Kudela, 2012. Variability of low energy cosmic rays near Earth. In *Exploring the Solar Wind*. IntechOpen. doi: 10.5772/37482.

M. Köhli and J.-P. Schmoldt. 2022. Feasibility of uxo detection via pulsed neutron–neutron logging. *Applied Radiation and Isotopes*, 188:110403. doi: 10.1016/j.apradiso.2022.110403.

M. Köhli, M. Schrön, M. Zreda, U. Schmidt, P. Dietrich, and S. Zacharias. 2015. Footprint characteristics revised for field-scale soil moisture monitoring with cosmic-ray neutrons. *Water Resources Research*, 51(7):5772–5790. doi: 10.1002/2015wr017169.

M. Köhli, M. Schrön, and U. Schmidt. 2018. Response functions for detectors in Cosmic Ray Neutron Sensing. *Nuclear Instruments and Methods in Physics Research Section A: Accelerators, Spectrometers, Detectors and Associated Equipment*, 902: 184–189. doi: 10.1016/j.nima.2018.06.052.

M. Köhli, J. Weimar, M. Schrön, R. Baatz, and U. Schmidt. 2021. Soil moisture and air humidity dependence of the above-ground cosmic-ray neutron intensity. *Frontiers in Water*, 2. doi: 10.3389/frwa.2020.544847.

LAIV-MV - State Agency for Interior Administration Mecklenburg-Western Pomerania. 2011. Digital elevation model: Atkis-dem1 (© geobasis-de/m-v 2011).

B. Laken, D. Kniveton, and A. Wolfendale. 2011. Forbush Decreases, solar irradiance variations, and anomalous cloud changes. *Journal of Geophysical Research: Atmospheres*, 116(D9). doi: 10.1029/2010JD014900.

P. Lal, A. Shekhar, M. Gharun, and N. N. Das. 2023. Spatiotemporal evolution of global long-term patterns of soil moisture. *Science of The Total Environment*, 867:161470. doi: 10.1016/j.scitotenv.2023.161470.

C. Lemmnitz, M. Kuhnert, O. Bens, A. Güntner, B. Merz, and R. F. Hüttl. 2007. Spatial and temporal variations of actual soil water repellency and their influence on surface runoff. *Hydrological Processes*, 22(12):1976–1984. doi: 10.1002/hyp.6782.

B. Li, X. Zhang, S. Morita, N. Sekiya, H. Araki, H. Gu, J. Han, Y. Lu, and X. Liu. 2022a. Are crop deep roots always beneficial for combating drought: A review of root structure and function, regulation and phenotyping. *Agricultural Water Management*, 271:107781. doi: 10.1016/j.agwat.2022.107781.

D. Li, M. Schrön, M. Köhli, H. Bogena, J. Weimar, M. A. J. Bello, X. Han, M. A. M. Gimeno, S. Zacharias, H. Vereecken, and H.-J. H. Franssen. 2019a. Can drip irrigation be scheduled with Cosmic-Ray Neutron Sensing? *Vadose Zone Journal*, 18(1):190053. doi: 10.2136/vzj2019.05.0053.

J. Li and L. Zhang. 2021. Comparison of four methods for vertical extrapolation of soil moisture contents from surface to deep layers in an alpine area. *Sustainability*, 13(16):8862. doi: 10.3390/su13168862.

W. Li, M. Migliavacca, M. Forkel, J. M. C. Denissen, M. Reichstein, H. Yang, G. Duveiller, U. Weber, and R. Orth. 2022b. Widespread increasing vegetation sensitivity to soil moisture. *Nature Communications*, 13(1). doi: 10.1038/s41467-022-31667-9.

X. Li, P. Gentine, C. Lin, S. Zhou, Z. Sun, Y. Zheng, J. Liu, and C. Zheng. 2019b. A simple and objective method to partition evapotranspiration into transpiration and evaporation at eddy-covariance sites. *Agricultural and Forest Meteorology*, 265:171–182. doi: 10.1016/j.agrformet.2018.11.017.

D. Lingri, H. Mavromichalaki, A. Belov, M. Abunina, E. Eroshenko, and A. Abunin. 2019. An extended study of the precursory signs of Forbush Decreases: New findings over the years 2008-2016. *Solar Physics*, 294(6):70. doi: 10.1007/s11207-019-1461-3.

A. López-Comazzi and J. J. Blanco. 2020. Short-term periodicities observed in neutron monitor counting rates. *Solar Physics*, 295(6). doi: 10.1007/s11207-020-01649-5.

A. López-Comazzi and J. J. Blanco. 2022. Short- and mid-term periodicities observed in neutron monitor counting rates throughout solar cycles 20–24. *The Astrophysical Journal*, 927(2):155. doi: 10.3847/1538-4357/ac4e19.

L. Lv, T. E. Franz, D. A. Robinson, and S. B. Jones. 2014. Measured and modeled soil moisture compared with cosmic-ray neutron probe estimates in a mixed forest. *Vadose Zone Journal*, 13(12):vzj2014.06.0077. doi: 10.2136/vzj2014.06.0077.

C. Maan, M.-C. ten Veldhuis, and B. J. H. van de Wiel. 2023. Dynamic root growth in response to depth-varying soil moisture availability: a rhizobox study. *Hydrology and Earth System Sciences*, 27(12):2341–2355. doi: 10.5194/hess-27-2341-2023.

M. Madruga de Brito, C. Kuhlicke, and A. Marx. 2020. Near-real-time drought impact assessment: a text mining approach on the 2018/19 drought in Germany. *Environmental Research Letters*, 15(10):1040a9. doi: 10.1088/1748-9326/aba4ca.

J.-L. Maeght, B. Rewald, and A. Pierret. 2013. How to study deep roots—and why it matters. *Frontiers in Plant Science*, 4. doi: 10.3389/fpls.2013.00299.

S. Manfreda, L. Brocca, T. Moramarco, F. Melone, and J. Sheffield. 2014. A physically based approach for the estimation of root-zone soil moisture from surface measurements. *Hydrology and Earth System Sciences*, 18(3):1199–1212. doi: 10.5194/hess-18-1199-2014.

V. Mares, T. Brall, R. Bütikofer, and W. Rühm. 2020. Influence of environmental parameters on secondary cosmic ray neutrons at high-altitude research stations at Jungfraujoch, Switzerland, and Zugspitze, Germany. *Radiation Physics and Chemistry*, 168:108557. doi: 10.1016/j.radphyschem.2019.108557.

C. Massari, L. Brocca, T. Moramarco, Y. Tramblay, and J.-F. Didon Lescot. 2014. Potential of soil moisture observations in flood modelling: Estimating initial conditions and correcting rainfall. *Advances in Water Resources*, 74:44–53. doi: 10.1016/j.advwatres.2014.08.004.

H. Mavromichalaki, A. Papaioannou, C. Plainaki, C. Sarlanis, G. Souvatzoglou, M. Gerontidou, M. Papailiou, E. Eroshenko, A. Belov, V. Yanke, et al. 2011. Applications and usage of the real-time neutron monitor database. *Advances in Space Research*, 47(12):2210–2222. doi: 10.1016/j.asr.2010.02.019.

J. Maysonnave, N. Delpierre, C. François, M. Jourdan, I. Cornut, S. Bazot, G. Vincent, A. Morfin, and D. Berveiller. 2022. Contribution of deep soil layers to the transpiration of a temperate deciduous forest: Implications for the modelling of productivity. *Science of The Total Environment*, 838:155981. doi: 10.1016/j.scitotenv.2022.155981.

D. McJannet, T. Franz, A. Hawdon, D. Boadle, B. Baker, A. Almeida, R. Silberstein, T. Lambert, and D. Desilets. 2014. Field testing of the universal calibration function for determination of soil moisture with cosmic-ray neutrons. *Water Resources Research*, 50(6):5235–5248. doi: 10.1002/2014wr015513.

D. McJannet, A. Hawdon, B. Baker, L. Renzullo, and R. Searle. 2017. Multiscale soil moisture estimates using static and roving cosmic-ray soil moisture sensors. *Hydrology and Earth System Sciences*, 21(12):6049–6067. doi: 10.5194/hess-21-6049-2017.

D. L. McJannet and D. Desilets. 2023. Incoming neutron flux corrections for cosmic-ray soil and snow sensors using the Global Neutron Monitor Network. *Water Resources Research*, 59(4). doi: 10.1029/2022wr033889.

B. Merz, G. Blöschl, S. Vorogushyn, F. Dottori, J. C. J. H. Aerts, P. Bates, M. Bertola, M. Kemter, H. Kreibich, U. Lall, and E. Macdonald. 2021. Causes, impacts and patterns of disastrous river floods. *Nature Reviews Earth Environment*, 2(9):592–609. doi: 10.1038/s43017-021-00195-3.

R. Merz and G. Blöschl. 2009. A regional analysis of event runoff coefficients with respect to climate and catchment characteristics in Austria. *Water Resources Research*, 45(1). doi: 10.1029/2008wr007163.

A. L. Mishev, L. G. Kocharov, and I. G. Usoskin. 2014. Analysis of the ground level enhancement on 17 May 2012 using data from the global neutron monitor network. *Journal of Geophysical Research: Space Physics*, 119(2):670–679. doi: 10.1002/2013JA019253.

V. Mishra, W. L. Ellenburg, K. N. Markert, and A. S. Limaye. 2020. Performance evaluation of soil moisture profile estimation through entropy-based and

exponential filter models. *Hydrological Sciences Journal*, 65(6):1036–1048. doi: 10.1080/02626667.2020.1730846.

S. Mollerach and E. Roulet. 2018. Progress in high-energy cosmic ray physics. *Progress in Particle and Nuclear Physics*, 98:85–118. doi: 10.1016/j.ppnp.2017.10.002.

C. Montzka, H. Bogena, M. Zreda, A. Monerris, R. Morrison, S. Muddu, and H. Vereecken. 2017. Validation of spaceborne and modelled surface soil moisture products with cosmic-ray neutron probes. *Remote Sensing*, 9(2):103. doi: 10.3390/rs9020103.

N. Nadezhdina, T. S. David, J. S. David, M. I. Ferreira, M. Dohnal, M. Tesař, K. Gartner, E. Leitgeb, V. Nadezhdin, J. Cermak, M. S. Jimenez, and D. Morales. 2010. Trees never rest: the multiple facets of hydraulic redistribution. *Ecohydrology*, 3(4):431–444. doi: 10.1002/eco.148.

National Centers for Environmental Information, 2015. Magnetic field calculators. URL `https://www.ngdc.noaa.gov/geomag/calculators/magcalc.shtml#igrfwmm`.

R. B. Neumann and Z. G. Cardon. 2012. The magnitude of hydraulic redistribution by plant roots: a review and synthesis of empirical and modeling studies. *New Phytologist*, 194(2):337–352. doi: 10.1111/j.1469-8137.2012.04088.x.

H. H. Nguyen, J. Jeong, and M. Choi. 2019. Extension of cosmic-ray neutron probe measurement depth for improving field scale root-zone soil moisture estimation by coupling with representative in-situ sensors. *Journal of Hydrology*, 571:679–696. doi: 10.1016/j.jhydrol.2019.02.018.

M. Nied, Y. Hundecha, and B. Merz. 2013. Flood-initiating catchment conditions: a spatio-temporal analysis of large-scale soil moisture patterns in the Elbe river basin. *Hydrology and Earth System Sciences*, 17(4):1401–1414. doi: 10.5194/hess-17-1401-2013.

M. Nied, T. Pardowitz, K. Nissen, U. Ulbrich, Y. Hundecha, and B. Merz. 2014. On the relationship between hydro-meteorological patterns and flood types. *Journal of Hydrology*, 519:3249–3262. doi: 10.1016/j.jhydrol.2014.09.089.

M. Nied, K. Schröter, S. Lüdtke, V. D. Nguyen, and B. Merz. 2017. What are the hydro-meteorological controls on flood characteristics? *Journal of Hydrology*, 545:310–326. doi: 10.1016/j.jhydrol.2016.12.003.

J. R. Nimmo. 2021. The processes of preferential flow in the unsaturated zone. *Soil Science Society of America Journal*, 85(1):1–27. doi: 10.1002/saj2.20143.

W. Nuntiyakul, A. Sáiz, D. Ruffolo, P.-S. Mangeard, P. Evenson, J. W. Bieber, J. Clem, R. Pyle, M. L. Duldig, and J. E. Humble. 2018. Bare neutron counter and neutron monitor response to cosmic rays during a 1995 latitude survey. *Journal of Geophysical Research: Space Physics*, 123(9):7181–7195. doi: 10.1029/2017JA025135.

S. O, X. Hou, and R. Orth. 2020. Observational evidence of wildfire-promoting soil moisture anomalies. *Scientific Reports*, 10(1). doi: 10.1038/s41598-020-67530-4.

S. Oh, J. W. Bieber, P. Evenson, J. Clem, Y. Yi, and Y. Kim. 2013. Record neutron monitor counting rates from galactic cosmic rays. *J. Geophys. Res. Space Physics*, 118:5431–5436. doi: 10.1002/jgra.50544.

Z. Pang, Y. Jia, X. Peng, X. Ju, and L. Gao. 2021. Applicability of Cosmic-Ray Neutron Sensing for measuring soil water content to heterogeneous landscapes under subtropical hydroclimatic conditions. *Journal of Hydrology*, 596:126068. doi: 10.1016/j.jhydrol.2021.126068.

P. Paschalis, H. Mavromichalaki, V. Yanke, A. Belov, E. Eroshenko, M. Gerontidou, and I. Koutroumpi. 2013. Online application for the barometric coefficient calculation of the NMDB stations. *New Astronomy*, 19:10–18.

A. Pasik, A. Gruber, W. Preimesberger, D. De Santis, and W. Dorigo. 2023. Uncertainty estimation for a new exponential-filter-based long-term root-zone soil moisture dataset from Copernicus Climate Change Service (C3S) surface observations. *Geoscientific Model Development*, 16(17):4957–4976. doi: 10.5194/gmd-16-4957-2023.

A. Patil and R. Ramsankaran. 2018. Improved streamflow simulations by coupling soil moisture analytical relationship in EnKF based hydrological data assimilation framework. *Advances in Water Resources*, 121:173–188. doi: 10.1016/j.advwatres.2018.08.010.

A. Patil, B. Fersch, H.-J. H. Franssen, and H. Kunstmann. 2021. Assimilation of cosmogenic neutron counts for improved soil moisture prediction in a distributed land surface model. *Frontiers in Water*, 3. doi: 10.3389/frwa.2021.729592.

A. Patrignani, T. E. Ochsner, B. Montag, and S. Bellinger. 2021. A novel lithium foil cosmic-ray neutron detector for measuring field-scale soil moisture. *Frontiers in Water*, 3. doi: 10.3389/frwa.2021.673185.

E. Paul-Limoges, S. Wolf, F. D. Schneider, M. Longo, P. Moorcroft, M. Gharun, and A. Damm. 2020. Partitioning evapotranspiration with concurrent eddy covariance measurements in a mixed forest. *Agricultural and Forest Meteorology*, 280:107786. doi: 10.1016/j.agrformet.2019.107786.

J. G. Pausas and J. E. Keeley. 2021. Wildfires and global change. *Frontiers in Ecology and the Environment*, 19(7):387–395. doi: 10.1002/fee.2359.

A. G. Pendergrass, G. A. Meehl, R. Pulwarty, M. Hobbins, A. Hoell, A. AghaKouchak, C. J. W. Bonfils, A. J. E. Gallant, M. Hoerling, D. Hoffmann, L. Kaatz, F. Lehner, D. Llewellyn, P. Mote, R. B. Neale, J. T. Overpeck, A. Sheffield, K. Stahl, M. Svoboda, M. C. Wheeler, A. W. Wood, and C. A. Woodhouse. 2020. Flash droughts present a new challenge for subseasonal-to-seasonal prediction. *Nature Climate Change*, 10(3):191–199. doi: 10.1038/s41558-020-0709-0.

A. M. Peterson, W. D. Helgason, and A. M. Ireson. 2016. Estimating field-scale root zone soil moisture using the cosmic-ray neutron probe. *Hydrology and Earth System Sciences*, 20(4):1373–1385. doi: 10.5194/hess-20-1373-2016.

F. M. Phillips, W. D. Stone, and J. T. Fabryka-Martin. 2001. An improved approach to calculating low-energy cosmic-ray neutron fluxes near the land/atmosphere interface. *Chemical Geology*, 175(3-4):689–701. doi: 10.1016/s0009-2541(00)00329-6.

A. Pierret, J.-L. Maeght, C. Clément, J.-P. Montoroi, C. Hartmann, and S. Gonkhamdee. 2016. Understanding deep roots and their functions in ecosystems: an advocacy for more unconventional research. *Annals of Botany*, 118(4):621–635. doi: 10.1093/aob/mcw130.

L. Poggio, L. M. de Sousa, N. H. Batjes, G. B. M. Heuvelink, B. Kempen, E. Ribeiro, and D. Rossiter. 2021. SoilGrids 2.0: producing soil information for the globe with quantified spatial uncertainty. *SOIL*, 7(1):217–240. doi: 10.5194/soil-7-217-2021.

Y. Pokhrel, F. Felfelani, Y. Satoh, J. Boulange, P. Burek, A. Gädeke, D. Gerten, S. N. Gosling, M. Grillakis, L. Gudmundsson, N. Hanasaki, H. Kim, A. Koutroulis, J. Liu, L. Papadimitriou, J. Schewe, H. Müller Schmied, T. Stacke, C.-E. Telteu, W. Thiery, T. Veldkamp, F. Zhao, and Y. Wada. 2021. Global terrestrial water storage and drought severity under climate change. *Nature Climate Change*, 11(3):226–233. doi: 10.1038/s41558-020-00972-w.

J. Proctor, A. Rigden, D. Chan, and P. Huybers. 2022. More accurate specification of water supply shows its importance for global crop production. *Nature Food*, 3(9):753–763. doi: 10.1038/s43016-022-00592-x.

M. Pätzig, F. Geiger, D. Rasche, P. Rauneker, and A. Eltner. 2020. Allometric relationships for selected macrophytes of kettle holes in northeast Germany as a basis for efficient biomass estimation using unmanned aerial systems (UAS). *Aquatic Botany*, 162:103202. doi: 10.1016/j.aquabot.2020.103202.

Y. Qing, S. Wang, B. C. Ancell, and Z.-L. Yang. 2022. Accelerating flash droughts induced by the joint influence of soil moisture depletion and atmospheric aridity. *Nature Communications*, 13(1). doi: 10.1038/s41467-022-28752-4.

M. Quinta-Ferreira, J. F. Dias, and S. Alija. 2016. False low water content in road field compaction control using nuclear gauges: a case study. *Environmental Earth Sciences*, 75(14). doi: 10.1007/s12665-016-5901-1.

R Core Team, 2018. *R: A Language and Environment for Statistical Computing*. R Foundation for Statistical Computing, Vienna, Austria, r version 3.5.1 (2018-07-02) edition. URL `https://www.R-project.org/`.

R Core Team, 2023. *R: A Language and Environment for Statistical Computing*. R Foundation for Statistical Computing, Vienna, Austria, r version 4.3.2 (2023-10-31 ucrt) edition. URL `https://www.R-project.org/`.

D. Rasche, C. Reinhardt-Imjela, A. Schulte, and R. Wenzel. 2019. Hydrodynamic simulation of the effects of stable in-channel large wood on the flood hydrographs of a low mountain range creek, Ore Mountains, Germany. *Hydrology and Earth System Sciences*, 23(10):4349–4365. doi: 10.5194/hess-23-4349-2019.

D. Rasche, M. Köhli, M. Schrön, T. Blume, and A. Güntner. 2021. Towards disentangling heterogeneous soil moisture patterns in cosmic-ray neutron sensor footprints. *Hydrology and Earth System Sciences*, 25(12):6547–6566. doi: 10.5194/hess-25-6547-2021.

D. Rasche, J. Weimar, M. Schrön, M. Köhli, M. Morgner, A. Güntner, and T. Blume. 2023. A change in perspective: downhole Cosmic-Ray Neutron Sensing for the estimation of soil moisture. *Hydrology and Earth System Sciences*, 27(16):3059–3082. doi: 10.5194/hess-27-3059-2023.

D. Rasche, T. Blume, and A. Güntner. 2024. Depth-extrapolation of field-scale soil moisture time series derived with Cosmic-Ray Neutron Sensing using the SMAR model. *SOIL (submitted)*.

M. Reich, M. Mikolaj, T. Blume, and A. Güntner. 2021. Field-scale subsurface flow processes inferred from continuous gravity monitoring during a sprinkling experiment. *Water Resources Research*, 57(10). doi: 10.1029/2021wr030044.

F. Rezanezhad, J. S. Price, W. L. Quinton, B. Lennartz, T. Milojevic, and P. V. Cappellen. 2016. Structure of peat soils and implications for water storage, flow and solute transport: A review update for geochemists. *Chemical Geology*, 429: 75–84. doi: 10.1016/j.chemgeo.2016.03.010.

J. S. Rieder and C. Kneisel. 2023. Monitoring spatiotemporal soil moisture variability in the unsaturated zone of a mixed forest using electrical resistivity tomography. *Vadose Zone Journal*, 22(3). doi: 10.1002/vzj2.20251.

C. A. Rivera Villarreyes, G. Baroni, and S. E. Oswald. 2011. Integral quantification of seasonal soil moisture changes in farmland by cosmic-ray neutrons. *Hydrology and Earth System Sciences*, 15(12):3843–3859. doi: 10.5194/hess-15-3843-2011.

C. A. Rivera Villarreyes, G. Baroni, and S. E. Oswald. 2014. Inverse modelling of cosmic-ray soil moisture for field-scale soil hydraulic parameters. *European Journal of Soil Science*, 65(6):876–886. doi: 10.1111/ejss.12162.

D. A. Robinson, C. S. Campbell, J. W. Hopmans, B. K. Hornbuckle, S. B. Jones, R. Knight, F. Ogden, J. Selker, and O. Wendroth. 2008. Soil moisture measurement for ecological and hydrological watershed-scale observatories: A review. *Vadose Zone Journal*, 7(1):358–389. doi: 10.2136/vzj2007.0143.

M. Rockenbach, A. Dal Lago, N. J. Schuch, K. Munakata, T. Kuwabara, A. G. Oliveira, E. Echer, C. R. Braga, R. R. S. Mendonça, C. Kato, M. Kozai, M. Tokumaru, J. W. Bieber, P. Evenson, M. L. Duldig, J. E. Humble, H. K. Al Jassar, M. M. Sharma, and I. Sabbah. 2014. Global Muon Detector Network used for space weather applications. *Space Science Reviews*, 182(1–4):1–18. doi: 10.1007/s11214-014-0048-4.

M. Rodell and B. Li. 2023. Changing intensity of hydroclimatic extreme events revealed by GRACE and GRACE-FO. *Nature Water*, 1(3):241–248. doi: 10.1038/s44221-023-00040-5.

U. Rosenbaum, H. R. Bogena, M. Herbst, J. A. Huisman, T. J. Peterson, A. Weuthen, A. W. Western, and H. Vereecken. 2012. Seasonal and event dynamics of spatial soil moisture patterns at the small catchment scale. *Water Resources Research*, 48(10). doi: 10.1029/2011wr011518.

R. Rosolem, W. J. Shuttleworth, M. Zreda, T. E. Franz, X. Zeng, and S. A. Kurc. 2013. The effect of atmospheric water vapor on neutron count in the cosmic-ray soil moisture observing system. *Journal of Hydrometeorology*, 14(5):1659–1671. doi: 10.1175/jhm-d-12-0120.1.

D. Ruffolo, A. Sáiz, P.-S. Mangeard, N. Kamyan, P. Muangha, T. Nutaro, S. Sumran, C. Chaiwattana, N. Gasiprong, C. Channok, C. Wuttiya, M. Rujiwarodom, P. Tooprakai, B. Asavapibhop, J. W. Bieber, J. Clem, P. Evenson, and K. Munakata. 2016. Monitoring short-term cosmic-ray spectral variations using neutron monitor time-delay measurements. *The Astrophysical Journal*, 817(1):38. doi: 10.3847/0004-637x/817/1/38.

D. Sapundjiev, M. Nemry, S. Stankov, and J.-C. Jodogne. 2014. Data reduction and correction algorithm for digital real-time processing of cosmic ray measurements: NM64 monitoring at Dourbes. *Advances in Space Research*, 53(1):71–76. doi: 10.1016/j.asr.2013.09.037.

T. Sato. 2015. Analytical model for estimating terrestrial cosmic ray fluxes nearly anytime and anywhere in the world: Extension of PARMA/EXPACS. *PLOS ONE*, 10(12):e0144679. doi: 10.1371/journal.pone.0144679.

T. Sato. 2016. Analytical model for estimating the zenith angle dependence of terrestrial cosmic ray fluxes. *PLOS ONE*, 11(8):e0160390. doi: 10.1371/journal.pone.0160390.

T. Sato and K. Niita. 2006. Analytical functions to predict cosmic-ray neutron spectra in the atmosphere. *RADIATION RESEARCH*, 166:544–555.

P. Schattan, G. Baroni, S. E. Oswald, J. Schöber, C. Fey, C. Kormann, M. Huttenlau, and S. Achleitner. 2017. Continuous monitoring of snowpack dynamics in alpine terrain by aboveground neutron sensing. *Water Resources Research*, 53(5): 3615–3634. doi: 10.1002/2016wr020234.

P. Schattan, M. Köhli, M. Schrön, G. Baroni, and S. E. Oswald. 2019. Sensing area-average snow water equivalent with cosmic-ray neutrons: The influence of fractional snow cover. *Water Resources Research*, 55(12):10796–10812. doi: 10.1029/2019wr025647.

L. M. Scheiffele, G. Baroni, T. E. Franz, J. Jakobi, and S. E. Oswald. 2020. A profile shape correction to reduce the vertical sensitivity of Cosmic-Ray Neutron Sensing of soil moisture. *Vadose Zone Journal*, 19(1). doi: 10.1002/vzj2.20083.

S. Scherrer, F. Naef, A. O. Faeh, and I. Cordery. 2007. Formation of runoff at the hillslope scale during intense precipitation. *Hydrology and Earth System Sciences*, 11(2):907–922. doi: 10.5194/hess-11-907-2007.

T. Schmidt, M. Schrön, Z. Li, T. Francke, S. Zacharias, A. Hildebrandt, and J. Peng. 2024. Comprehensive quality assessment of satellite- and model-based soil moisture products against the COSMOS network in Germany. *Remote Sensing of Environment*, 301:113930. doi: 10.1016/j.rse.2023.113930.

M. Schrön. 2017. *Cosmic-Ray Neutron Sensing and its Applications to Soil and Land Surface Hydrology*. Phd thesis, University of Potsdam.

M. Schrön, S. Zacharias, M. Köhli, J. Weimar, and P. Dietrich. 2016. Monitoring environmental water with ground albedo neutrons from cosmic rays. In *Proceedings of The 34th International Cosmic Ray Conference — PoS(ICRC2015)*, ICRC2015. Sissa Medialab. doi: 10.22323/1.236.0231.

M. Schrön, M. Köhli, L. Scheiffele, J. Iwema, H. R. Bogena, L. Lv, E. Martini, G. Baroni, R. Rosolem, J. Weimar, J. Mai, M. Cuntz, C. Rebmann, S. E. Oswald, P. Dietrich, U. Schmidt, and S. Zacharias. 2017. Improving calibration and validation of cosmic-ray neutron sensors in the light of spatial sensitivity. *Hydrology and Earth System Sciences*, 21(10):5009–5030. doi: 10.5194/hess-21-5009-2017.

M. Schrön, R. Rosolem, M. Köhli, L. Piussi, I. Schröter, J. Iwema, S. Kögler, S. E. Oswald, U. Wollschläger, L. Samaniego, P. Dietrich, and S. Zacharias. 2018a. Cosmic-ray neutron rover surveys of field soil moisture and the influence of roads. *Water Resources Research*, 54(9):6441–6459. doi: 10.1029/2017wr021719.

M. Schrön, S. Zacharias, G. Womack, M. Köhli, D. Desilets, S. E. Oswald, J. Bumberger, H. Mollenhauer, S. Kögler, P. Remmler, M. Kasner, A. Denk, and P. Dietrich. 2018b. Intercomparison of cosmic-ray neutron sensors and water balance monitoring in an urban environment. *Geoscientific Instrumentation, Methods and Data Systems*, 7(1):83–99. doi: 10.5194/gi-7-83-2018.

M. Schrön, S. E. Oswald, S. Zacharias, M. Kasner, P. Dietrich, and S. Attinger. 2021. Neutrons on rails: Transregional monitoring of soil moisture and snow water equivalent. *Geophysical Research Letters*, 48(24). doi: 10.1029/2021gl093924.

M. Schrön, M. Köhli, and S. Zacharias. 2023a. Signal contribution of distant areas to cosmic-ray neutron sensors – implications for footprint and sensitivity. *Hydrology and Earth System Sciences*, 27(3):723–738. doi: 10.5194/hess-27-723-2023.

M. Schrön, D. Rasche, J. Weimar, M. Köhli, K. Herbst, B. Boehrer, L. Hertle, S. Kögler, and S. Zacharias. 2023b. Buoy-based detection of low-energy cosmic-ray neutrons to monitor the influence of atmospheric, geomagnetic, and heliospheric effects. *Earth and Space Science (submitted)*. doi: 10.22541/au.170319441.16528907/v1.

K. Schröter, M. Kunz, F. Elmer, B. Mühr, and B. Merz. 2015. What made the June 2013 flood in Germany an exceptional event? a hydro-meteorological evaluation. *Hydrology and Earth System Sciences*, 19(1):309–327. doi: 10.5194/hess-19-309-2015.

H. Schume, G. Jost, and K. Katzensteiner. 2003. Spatio-temporal analysis of the soil water content in a mixed norway spruce (Picea abies (l.) karst.)–European

beech (Fagus sylvatica l.) stand. *Geoderma*, 112(3-4):273–287. doi: 10.1016/s0016-7061(02)00311-7.

S. I. Seneviratne, T. Corti, E. L. Davin, M. Hirschi, E. B. Jaeger, I. Lehner, B. Orlowsky, and A. J. Teuling. 2010. Investigating soil moisture–climate interactions in a changing climate: A review. *Earth-Science Reviews*, 99(3-4):125–161. doi: 10.1016/j.earscirev.2010.02.004.

C. Senf and R. Seidl. 2021. Persistent impacts of the 2018 drought on forest disturbance regimes in Europe. *Biogeosciences*, 18(18):5223–5230. doi: 10.5194/bg-18-5223-2021.

P. C. Sentelhas, A. Dalla Marta, and S. Orlandini. 2008. Suitability of relative humidity as an estimator of leaf wetness duration. *Agricultural and Forest Meteorology*, 148(3):392–400. doi: 10.1016/j.agrformet.2007.09.011.

J. Shuttleworth, R. Rosolem, M. Zreda, and T. Franz. 2013. The COsmic-ray soil moisture interaction code (COSMIC) for use in data assimilation. *Hydrology and Earth System Sciences*, 17(8):3205–3217. doi: 10.5194/hess-17-3205-2013.

M. J. Sigouin, M. Dyck, B. C. Si, and W. Hu. 2016. Monitoring soil water content at a heterogeneous oil sand reclamation site using a cosmic-ray soil moisture probe. *Journal of Hydrology*, 543:510–522. doi: 10.1016/j.jhydrol.2016.10.026.

J. A. Simpson. 1983. Elemental and isotopic composition of the galactic cosmic rays. *Annual Review of Nuclear and Particle Science*, 33(1):323–382. doi: 10.1146/annurev.ns.33.120183.001543.

J. Šimůnek, M. T. van Genuchten, and M. Šejna. 2008. Development and applications of the HYDRUS and STANMOD software packages and related codes. *Vadose Zone Journal*, 7(2):587–600. doi: 10.2136/vzj2007.0077.

J. Spinoni, J. V. Vogt, G. Naumann, P. Barbosa, and A. Dosio. 2018. Will drought events become more frequent and severe in Europe? *International Journal of Climatology*, 38(4):1718–1736. doi: 10.1002/joc.5291.

H. Sponagel, W. Grottenthaler, K.-J. Hartmann, R. Hartwich, P. Janetzko, H. Joisten, D. Kühn, K.-J. Sabel, and R. Traidl. 2005. *Bodenkundliche Kartieranleitung KA5*. BGR - German Federal Institute for Geosciences and Natural Resources, Hannover, Germany, 5 edition.

L. Stevanato, G. Baroni, Y. Cohen, F. C. Lino, S. Gatto, M. Lunardon, F. Marinello, S. Moretto, and L. Morselli. 2019. A novel cosmic-ray neutron sensor for soil moisture estimation over large areas. *Agriculture*, 9(9):202. doi: 10.3390/agriculture9090202.

L. Stevanato, G. Baroni, S. E. Oswald, M. Lunardon, V. Mares, F. Marinello, S. Moretto, M. Polo, P. Sartori, P. Schattan, and W. Ruehm. 2022. An alternative incoming correction for cosmic-ray neutron sensing observations using local muon measurement. *Geophysical Research Letters*, 49(6). doi: 10.1029/2021gl095383.

B. D. Stocker, S. J. Tumber-Dávila, A. G. Konings, M. C. Anderson, C. Hain, and R. B. Jackson. 2023. Global patterns of water storage in the rooting zones of vegetation. *Nature Geoscience*, 16(3):250–256. doi: 10.1038/s41561-023-01125-2.

P. Stowell, S. Fargher, C. Steer, and L. Thompson. 2021. Scintillating thermal neutron detectors for cosmic ray soil moisture monitoring. *Journal of Instrumentation*, 16(11):P11039. doi: 10.1088/1748-0221/16/11/p11039.

H. Tabari. 2020. Climate change impact on flood and extreme precipitation increases with water availability. *Scientific Reports*, 10(1). doi: 10.1038/s41598-020-70816-2.

X. Tan, L. Zhang, C. He, Y. Zhu, Z. Han, and X. Li. 2020. Applicability of cosmic-ray neutron sensor for measuring soil moisture at the agricultural-pastoral ecotone in northwest China. *Science China Earth Sciences*, 63(11):1730–1744. doi: 10.1007/s11430-020-9650-2.

J. Tian, Z. Han, H. R. Bogena, J. A. Huisman, C. Montzka, B. Zhang, and C. He. 2020. Estimation of subsurface soil moisture from surface soil moisture in cold mountainous areas. *Hydrology and Earth System Sciences*, 24(9):4659–4674. doi: 10.5194/hess-24-4659-2020.

Z. Tian, Z. Li, G. Liu, B. Li, and T. Ren. 2016. Soil water content determination with cosmic-ray neutron sensor: Correcting aboveground hydrogen effects with thermal/fast neutron ratio. *Journal of Hydrology*, 540:923–933. doi: 10.1016/j.jhydrol.2016.07.004.

D. B. Upadhyaya, J. Evans, S. Muddu, S. K. Tomer, A. A. Bitar, S. Yeggina, T. S, R. Morrison, M. Fry, S. N. Tripathi, M. Mujumdar, M. Goswami, N. Ganeshi, M. K. Nema, S. K. Jain, S. S. Angadi, and B. S. Yenagi. 2021. The indian COSMOS network (ICON): Validating L-band remote sensing and modelled soil moisture data products. *Remote Sensing*, 13(3):537. doi: 10.3390/rs13030537.

J. Urban, J. Čermák, and R. Ceulemans. 2014. Above- and below-ground biomass, surface and volume, and stored water in a mature Scots pine stand. *European Journal of Forest Research*, 134(1):61–74. doi: 10.1007/s10342-014-0833-3.

I. G. Usoskin, G. A. Bazilevskaya, and G. A. Kovaltsov. 2011. Solar modulation parameter for cosmic rays since 1936 reconstructed from ground-based neutron monitors and ionization chambers. *Journal of Geophysical Research: Space Physics*, 116(A2). doi: 10.1029/2010JA016105.

M. Van Camp, O. de Viron, A. Watlet, B. Meurers, O. Francis, and C. Caudron. 2017. Geophysics from terrestrial time-variable gravity measurements. *Reviews of Geophysics*, 55(4):938–992. doi: 10.1002/2017rg000566.

P. van Rüth, K. Schönthaler, S. von Andrian-Werburg, M. Wolf, and M. Gabriel. 2023. *Monitoringbericht 2023 zur Deutschen Anpassungsstrategie an den Klimawandel (www.umweltbundesamt.de/publikationen/monitoringbericht-2023).*

D. Vanella, S. R. Peddinti, and I. Kisekka. 2022. Unravelling soil water dynamics in almond orchards characterized by soil-heterogeneity using electrical resistivity tomography. *Agricultural Water Management*, 269:107652. doi: 10.1016/j.agwat.2022.107652.

T. Vather, C. Everson, and T. E. Franz. 2019. Calibration and validation of the cosmic ray neutron rover for soil water mapping within two South African land classes. *Hydrology*, 6(3):65. doi: 10.3390/hydrology6030065.

T. Vather, C. S. Everson, and T. E. Franz. 2020. The applicability of the cosmic ray neutron sensor to simultaneously monitor soil water content and biomass in an Acacia mearnsii forest. *Hydrology*, 7(3):48. doi: 10.3390/hydrology7030048.

H. Vereecken, J. A. Huisman, H. Bogena, J. Vanderborght, J. A. Vrugt, and J. W. Hopmans. 2008. On the value of soil moisture measurements in vadose zone hydrology: A review. *Water Resources Research*, 44(4). doi: 10.1029/2008wr006829.

H. Vereecken, J. Huisman, Y. Pachepsky, C. Montzka, J. van der Kruk, H. Bogena, L. Weihermüller, M. Herbst, G. Martinez, and J. Vanderborght. 2014. On the spatio-temporal dynamics of soil moisture at the field scale. *Journal of Hydrology*, 516:76–96. doi: 10.1016/j.jhydrol.2013.11.061.

N. Vergopolan, S. Xiong, L. Estes, N. Wanders, N. W. Chaney, E. F. Wood, M. Konar, K. Caylor, H. E. Beck, N. Gatti, T. Evans, and J. Sheffield. 2021. Field-scale soil moisture bridges the spatial-scale gap between drought monitoring and agricultural yields. *Hydrology and Earth System Sciences*, 25(4):1827–1847. doi: 10.5194/hess-25-1827-2021.

P. Väisänen, I. Usoskin, and K. Mursula. 2021. Seven decades of neutron monitors (1951–2019): Overview and evaluation of data sources. *Journal of Geophysical Research: Space Physics*, 126(5). doi: 10.1029/2020ja028941.

W. Wagner, G. Lemoine, and H. Rott. 1999. A method for estimating soil moisture from ERS scatterometer and soil data. *Remote Sensing of Environment*, 70(2): 191–207. doi: 10.1016/s0034-4257(99)00036-x.

N. Wanders, D. Karssenberg, A. de Roo, S. M. de Jong, and M. F. P. Bierkens. 2014. The suitability of remotely sensed soil moisture for improving operational flood forecasting. *Hydrology and Earth System Sciences*, 18(6):2343–2357. doi: 10.5194/hess-18-2343-2014.

C. Wang, B. Fu, L. Zhang, and Z. Xu. 2018. Soil moisture–plant interactions: an ecohydrological review. *Journal of Soils and Sediments*, 19(1):1–9. doi: 10.1007/s11368-018-2167-0.

M. Weber, K. Rinke, M. Hipsey, and B. Boehrer. 2017. Optimizing withdrawal from drinking water reservoirs to reduce downstream temperature pollution and reservoir hypoxia. *Journal of Environmental Management*, 197:96—-105. doi: 10.1016/j.jenvman.2017.03.020.

J. Weimar. 2022. *Advances in Cosmic-Ray Neutron Sensing by Monte Carlo simulations and neutron detector development*. Phd thesis, Heidelberg University.

J. Weimar, M. Köhli, C. Budach, and U. Schmidt. 2020. Large-scale boron-lined neutron detection systems as a 3He alternative for Cosmic Ray Neutron Sensing. *Frontiers in Water*, 2:16. doi: 10.3389/frwa.2020.00016.

C. Werner, J. Bull, C. Solomon, F. Brown1, G. McKinney, M.E.Rising, D. Dixon, R. Martz, H. Hughes, L. Cox, A. J. Zukaitis, J.C.Armstrong, R. A. Forster, and L. Casswell. 2018. Mcnp version 6.2 release notes. techreport LA-UR-18-20808. URL `https://mcnp.lanl.gov/pdf_files/la-ur-18-20808.pdf`.

L. Xu, N. Chen, X. Zhang, H. Moradkhani, C. Zhang, and C. Hu. 2021. In-situ and triple-collocation based evaluations of eight global root zone soil moisture products. *Remote Sensing of Environment*, 254:112248. doi: 10.1016/j.rse.2020.112248.

R. Xu, P. Yu, M. J. Abramson, F. H. Johnston, J. M. Samet, M. L. Bell, A. Haines, K. L. Ebi, S. Li, and Y. Guo. 2020. Wildfires, global climate change, and human health. *New England Journal of Medicine*, 383(22):2173–2181. doi: 10.1056/nejmsr2028985.

X. Yuan, Y. Wang, P. Ji, P. Wu, J. Sheffield, and J. A. Otkin. 2023. A global transition to flash droughts under climate change. *Science*, 380(6641):187–191. doi: 10.1126/science.abn6301.

S. Zacharias, H. Bogena, L. Samaniego, M. Mauder, R. Fuß, T. Pütz, M. Frenzel, M. Schwank, C. Baessler, K. Butterbach-Bahl, O. Bens, E. Borg, A. Brauer, P. Dietrich, I. Hajnsek, G. Helle, R. Kiese, H. Kunstmann, S. Klotz, J. C. Munch, H. Papen, E. Priesack, H. P. Schmid, R. Steinbrecher, U. Rosenbaum, G. Teutsch, and H. Vereecken. 2011. A network of terrestrial environmental observatories in Germany. *Vadose Zone Journal*, 10(3):955–973. doi: 10.2136/vzj2010.0139.

M. Zambrano-Bigiarini, 2017. *hydroGOF: Goodness-of-fit functions for comparison of simulated and observed hydrological time series (R package version 0.3-10)*. URL `http://hzambran.github.io/hydroGOF/`.

M. Zambrano-Bigiarini, 2020. *hydroGOF: Goodness-of-fit functions for comparison of simulated and observed hydrological time series (R package version 0.4-0)*. URL `http://hzambran.github.io/hydroGOF/`.

J. Zhang, J. Guo, M. I. Dobynde, Y. Wang, and R. F. Wimmer-Schweingruber. 2022. From the top of Martian Olympus to deep craters and beneath: Mars radiation environment under different atmospheric and regolith depths. *Journal of Geophysical Research: Planets*, 127(3). doi: 10.1029/2021je007157.

N. Zhang, S. Quiring, T. Ochsner, and T. Ford. 2017. Comparison of three methods for vertical extrapolation of soil moisture in Oklahoma. *Vadose Zone Journal*, 16 (10):vzj2017.04.0085. doi: 10.2136/vzj2017.04.0085.

X. Zhang, K. Wang, M. A. Frassl, and B. Boehrer. 2020. Reconstructing six decades of surface temperatures at a shallow lake. *Water*, 12(2):405. doi: 10.3390/w12020405.

Y. Zheng, G. Coxon, R. Woods, D. Power, M. A. Rico-Ramirez, D. McJannet, R. Rosolem, J. Li, and P. Feng. 2023. Evaluation of reanalysis soil moisture products using cosmic ray neutron sensor observations across the globe. *Hydrology Earth System Sciences Discussions*. doi: 10.5194/hess-2023-224.

X. Zhu, M. Shao, X. Jia, L. Huang, J. Zhu, and Y. Zhang. 2017. Application of temporal stability analysis in depth-scaling estimated soil water content by cosmic-ray neutron probe on the northern Tibetan Plateau. *Journal of Hydrology*, 546:299–308. doi: 10.1016/j.jhydrol.2017.01.019.

R. Zhuang, Y. Zeng, S. Manfreda, and Z. Su. 2020. Quantifying long-term land surface and root zone soil moisture over Tibetan Plateau. *Remote Sensing*, 12(3): 509. doi: 10.3390/rs12030509.

M. Zreda, D. Desilets, T. P. A. Ferré, and R. L. Scott. 2008. Measuring soil moisture content non-invasively at intermediate spatial scale using cosmic-ray neutrons. *Geophysical Research Letters*, 35(21). doi: 10.1029/2008gl035655.

M. Zreda, W. J. Shuttleworth, X. Zeng, C. Zweck, D. Desilets, T. Franz, and R. Rosolem. 2012. COSMOS: the COsmic-ray soil moisture observing system. *Hydrology and Earth System Sciences*, 16(11):4079–4099. doi: 10.5194/hess-16-4079-2012.

C. Zweck, M. Zreda, and D. Desilets. 2013. Snow shielding factors for cosmogenic nuclide dating inferred from monte carlo neutron transport simulations. *Earth and Planetary Science Letters*, 379:64–71. doi: 10.1016/j.epsl.2013.07.023.

Author's declaration

I hereby declare that this doctoral thesis has not been submitted to any other university. I have completed this thesis independently and only with the indicated means.

Signature of doctoral candidate